DISS. ETH NO. 24627

STATISTICAL METHODS FOR DAM BEHAVIOUR ANALYSIS

A thesis submitted to attain the degree of

DOCTOR OF SCIENCES of ETH ZURICH

(Dr. sc. ETH Zurich)

presented by

MARIUS BÜHLMANN

MSc ETH Civil Eng

born on 20.11.1982

citizen of Maschwanden (ZH) and Guggisberg (BE)

accepted on the recommendation of

Prof. Dr. Robert M. Boes

Prof. Dr. Frédéric Dufour

Dr. Benedikt Weber

Dr. Georges R. Darbre

Dr. David F. Vetsch

2018

Acknowledgements

I would like to thank all people who supported me during the work of this thesis.

A special thank goes to my supervisor and first examiner Prof. Dr. R. M. Boes, director at VAW, who gave me the opportunity to carry out this interesting thesis at his institute. Moreover, I wish to thank my co-supervisor and co-examiner Dr. D. F. Vetsch for the interesting discussions, the valuable inputs and the review of the manuscript. Furthermore, I would like to thank all my colleagues at VAW for the interesting discussions.

The original idea for this work stems from the dam safety department of the Swiss Federal Office of Energy (BFE). I would like to thank for their financial support of this thesis (project S1/500834-01) and their valuable inputs on the semi-annual meetings.

I am very grateful to Dr. B. Weber for his input during the thesis, the valuable input to the manuscript and acting as co-examiner of this thesis. Sincere thanks also goes to Prof. Dr. F. Dufour and Dr. G. R. Darbre for acting as co-examiners of this thesis.

Indispensable were the discussions with the people from the consulting group of the Seminar for Statistics (SfS) at the ETH Zurich. In particular I would also like to deeply thank Dr. Lukas Meier.

Further thanks go to F. Schiefer and F. R. Hauser who wrote their Master's theses under the umbrella of this project. Their ideas and inputs were valuable for this thesis.

A special thanks goes to my friends S. Gianora and M. Vogt who were proofreading some parts of this manuscript.

Last but not least I wish to thank my family; in particular my wife Fabienne who supported me during this time and my parents Markus and Regula who supported me during my education.

Zurich, Fabruary 2018 Marius Bühlmann

"Essentially, all models are wrong, but some are useful" (George Box)

Abstract

Concrete dams can be affected by long-term processes such as alkali aggregate reaction, concrete ageing and irreversible rock mass deformation, from which they can suffer serious damage. Therefore, an early detection of deficiencies by the use of a proper monitoring system in combination with a dam behaviour analysis model is essential. A dam behaviour analysis model links measured behaviour indicators, e.g. displacements, with the environmental conditions, i.e. mainly the water level and the temperature distribution in the dam body. This is usually done empirically by statistical methods. The effects of the environmental conditions are represented by model equations. A common approach to represent the effects of the water level are polynomials and there are several approaches proposed in the literature to represent the effects of temperature. Nevertheless, the different temperature variables are likely to be correlated. Thus, multicollinearity and unstable models result.

The goal of this thesis is to evaluate existing statistical approaches used in the field of dam behaviour analysis and to improve them if necessary. The thesis is divided in the following main parts: (i) heat transfer analysis, (ii) evaluation of existing models and (iii) the presentation of new approaches and its (iv) application.

In concrete dams, heat conduction can be regarded as a one-dimensional problem between the upstream and the downstream boundary. The analysis is done by the use of the frequency domain solution of the heat conduction equation. Usually the thermometers are embedded in the concrete body. Therefore, inverse heat conduction analysis has to be performed. Since this is an ill-conditioned problem, stabilising procedures are needed. Besides the evaluation of existing approaches, a new approach, based on the limitation of the amplification of high frequencies, is proposed. It is successfully applied to several case studies.

In a next step, well known statistical approaches are assessed. The evaluation of the behaviour analysis procedures shows that the observation-prediction comparison, which is commonly applied, can lead to results that are not robust. Hence, wrong conclusions about the structural behaviour might be drawn. Thus, it is recommended to use adjusted behaviour indicators. The latter are obtained by subtracting the reversible effects from the measured behaviour indicator. It is shown that this approach is very robust and the results are independent of the chosen calibration period.

Moreover, the evaluation of the approaches to consider temperature effects shows that their performance mainly depends on the data and less on the models itself. All models are able to detect artificial behaviour changes previously applied to the data. It is shown that the magnitude of the behaviour changes found by a model correlates with its residual standard error.

Finally, new approaches are presented. Beam models are introduced to create physically based shape functions that can be used to create hybrid models. For gravity dams, a cantilever beam model with an elastic abutment and for arch dams an arch-cantilever model is set up. The models have been applied to several dams. Due to the fact that only few uncorrelated variables result, multicollinearity does not occur. Therefore, beam models are very robust. Furthermore, the beam model for gravity dams is used to perform multi-objective calibration with the Markov Chain Monte Carlo method in a Bayesian framework. The advantage of multi-objective calibration is that the measured displacements are simultaneously matched with the model output on several levels. This leads to simple models that allow for drawing comprehensible conclusions based on engineering judgement. Moreover, due to the simultaneous analyses of the displacement at different levels, a potential abnormal behaviour can be detected and correctly located.

Because the adjusted behaviour indicators are very robust with respect to different calibration periods, it is recommended to use all available measurement data for model calibration. Consequently, extrapolations that may result in unstable predictions can be avoided. This change in the concept of behaviour analysis can be seen as a paradigm shift from a statistical prediction to a statistical inference problem.

Kurzfassung

Talsperren können Langzeitprozessen wie Alkali-Aggregat-Reaktionen, Betonalterung und Taldeformationen ausgesetzt sein. Durch die Talsperrenüberwachung sollen solche sicherheitsrelevanten Prozesse möglichst frühzeitig erkannt werden. Für die Überwachung werden Verhaltensmodelle, welche gemessene Verhaltensindikatoren, z.B. die Verformung auf Kronenniveau, mit den einwirkenden Umweltbedingungen in Relation setzen, verwendet. Für die Überwachung der Deformation von Betonsperren sind der Wasserspiegel und die Betontemperatur die Haupteinflussgrössen. In der Regel werden statistische Verhaltensmodelle, welche die Grössen empirisch in Beziehung setzen, verwendet. Die Beziehung wird dabei durch Modellgleichungen beschrieben und für die Einwirkung des Wasserstands wird normalerweise ein Polynomansatz verwendet. Für die Temperatureffekte gibt es verschiedene Ansätze aus der Literatur. Jedoch sind die verschiedenen Temperaturvariablen, welche alle von der selben Umgebungstemperatur abhängen, oft korreliert. Daher tritt bei diesen Modellen üblicherweise Multikollinearität auf, was in instabilen Modellen resultiert.

Das Ziel dieser Dissertation ist, die existierenden statistischen Verfahren, welche im Bereich der Verhaltensanalyse von Talsperren angewendet werden, zu evaluieren und weiter zu entwickeln. Die Arbeit ist in die folgenden Hauptteile gegliedert: (i) Wärmetransport, (ii) Evaluierung der bestehenden Ansätze, (iii) Entwicklung neuer Ansätze und (iv) Anwendung an Fallbeispielen.

Die Wärmeleitung in Betontalsperren kann als eindimensionales Problem zwischen der Wasser- und der Luftseite betrachtet werden. Die Lösung der Wärmeleitungsgleichung kann im Frequenzbereich durchgeführt werden. Da die Thermometer mit einem bestimmten Abstand zur Oberfläche im Beton eingebaut sind, muss inverse Wärmeleitung angewendet werden, um die Temperaturinformation über die gesamte Mauer zu kennen. Da inverse Wärmeleitung ein schlecht konditioniertes Problem ist, sind Stabilisierungsverfahren notwendig. Neben der Anwendung von bestehenden Stabilisierungsverfahren wurde ein neuer Ansatz entwickelt. Dieser beruht auf der Limitierung der Amplifikation der hohen Frequenzen. Der Ansatz wird erfolgreich an verschiedenen Fallstudien angewendet.

In einem nächsten Schritt werden die aus der Literatur bekannten statistischen Verfahren evaluiert. Die Analyse zeigt auf, dass der oft verwendete Soll-Ist-Vergleich zu nicht robusten Resultaten und demzufolge zu falschen Aussagen führen kann. Daher wird empfohlen, das Konzept des korrigierten Verhaltensindikators zu verwenden. Letzterer wird durch die Subtraktion der reversiblen Effekte (z.B. aus Wasserstand und Temperatur) vom gemessenen Verhaltensindikator erhalten. Es kann gezeigt werden, dass dieser Ansatz sehr robust ist und die Resultate unabhängig von der Kalibrierungsperiode sind.

Die Analyse der Ansätze zur Berücksichtigung der Temperatureffekte zeigt, dass die Modellgüte vor allem von den Messdaten und nicht von den eingesetzten Modellen abhängig ist. Alle untersuchten Modelle sind imstande, den Daten hinzugefügte, bekannte Verhaltensänderungen zu finden. Des Weiteren kann gezeigt werden, dass die Grössenordnung von Verhaltensänderungen, die mit einem Modell erkannt werden können, mit dem Standardfehler der Modelle korreliert.

In einem letzten Schritt werden neue Ansätze aufgezeigt. Auf Stabstatik basierende Modelle können dazu verwendet werden, physikalisch basierte statistische Ansatzfunktionen zu erhalten. Dies führt zu hybriden Modellen. Für Gewichtsstaumauern wurde ein Modell mit Kragarm mit einer elastischen Einspannung entwickelt und für Bogenstaumauern ein Balkenrostmodell aufgesetzt. Die Modelle werden an verschiedenen Fallstudien angewendet. Da bei solchen Modellen wenige Variablen resultieren, die nicht korreliert sind, tritt keine Multikollinearität auf. Dies führ zu sehr robusten Modellen. Darüber hinaus wurde das Balkenmodell für Gewichtstaumauern dazu benutzt, um eine statistische Optimierung auf mehrere Zielfunktionen durchzuführen. Der Vorteil dabei ist, dass die Deformation auf verschiedenen Höhenlagen gleichzeitig an die Messdaten angepasst wird. Dazu wurde die sog. Markov Chain Monte Carlo Methode verwendet. Dies führt zu einfachen Modellen, welche für Ingenieure gut nachvollziehbare Resultate liefern. Durch die gleichzeitige Analyse des Verhaltens auf mehreren Höhenlagens kann ein abnormales Verhalten nicht nur gefunden, sondern auch lokalisiert werden.

Da bei der Verwendung von korrigierten Verhaltensindikatoren von der Kalibrierungsperiode unabhängige, sehr robuste Resultate erhalten werden, wird empfohlen, alle verfügbaren Daten für die Kalibrierung zu verwenden. Dadurch können Extrapolationen vermieden werden. Dieser Konzeptwechsel kann als Paradigmenwechsel von einem statistischen Voraussageproblem hin zu einem statistischen Inferenzproblem gesehen werden.

Contents

1 Introduction

1.1 Background

Dams are manmade structures that impound water by closing a valley. In general, they are used to manage available water resources for the purpose of hydropower electricity production, drinking water supply, irrigation, flood protection, low flow control and tourism (Boes, 2015a). Many of them are built for multiple purposes. Usually, these structures are located in mountainous or hilly areas upstream of villages and cities. The collapse of a large dam would lead to an immense flood wave and to devastation downstream. To guarantee safety throughout their service lives, it is essential to monitor such structures.

One can basically distinguish between concrete and embankment dams. The difference is not only due to the material that was used for construction but also due to the behaviour during the lifetime of the structure. Concrete dams can be influenced by various phenomena that can affect their safety. These are mainly alkali aggregate reactions (AAR), concrete ageing and valley deformations. AAR, the most common phenomenon, is a chemical reaction between the components of the aggregates and the pore solutions in concrete. It leads to concrete swelling which causes volume expansion or stress changes. Additionally, the tensile strength and the Young's modulus of the concrete can decrease. The maximal expansion that can take place lies in the order of 0.2 - 0.5%, corresponding to a thermal expansion of 200 - 500 °C (Saouma, 2014). Thus, as a worst-case scenario AAR can lead to the deterioration of a structure. There is a number of dams worldwide that were demolished and had to be rebuilt due to the effects of AAR. A recent study of the Swiss Committee on Dams in Switzerland leads to the conclusion that around 50% of the large concrete dams experience an irreversible displacement. In most of the cases, an AAR is supposed to be the origin and it is estimated that 50% of the AAR affected dams have to be rehabilitated in the future (Amberg, 2015). Since the developing progress of an AAR is very slow, it becomes visible not before 20 - 30 years after the construction (Amberg, 2011). While concrete dams, especially arch dams, are sensitive to valley deformations, embankment dams are not. The failure of embankment dams can mostly be related to internal erosion (Johansson, 1997). Internal erosion means that the fine core material that is important for the impermeability is washed out. This leads to increasing drainage flow and turbidity of the drainage water at the bottom of the dam. Thus, it is essential to monitor these parameters at embankment dams.

Generally, it is important to recognise an abnormal behaviour of the structure at early stage to prevent failure. Therefore, the behaviour of dams must be monitored frequently. The behaviour is expressed by measurable variables that represent the global behaviour of the structure, called behaviour indicators. These are for instance the displacements at the top level or the drainage flow at the bottom of the structure.

A safety assessment can be done by comparing observed and predicted values of behaviour indicators. The predicted value can be calculated using a model based on input variables such as environmental conditions (e.g. water level, temperatures). Basically, there are two modelling approaches; the deterministic method links the behaviour of the structure and input variables on the basis of physical laws, and the statistical method links it by regression analysis. In dam behaviour analysis, statistical models are frequently used since their implementation is straightforward. In 2004, the Swiss Federal Office of Energy (SFOE) launched the Software DamReg (Weber, 2004), in which statistical models can be set-up and evaluated. DamReg has recently been re-engineered at VAW and is now called DamBASE (Gerber *et al.*, 2015). In doing so, the R environment (R Core Team, 2013) has been integrated in the software to facilitate the application and testing of various procedures for statistical analysis.

1.2 Research gap

The application of common statistical modelling approaches in dam behaviour analysis can be challenging. For a behaviour analysis, a regressor model equation has to be defined. It approximatively describes the relationship between the environmental conditions and the behaviour of the structure. The model accuracy and the prediction accuracy particularly depend on the chosen model equation.

Regarding the monitoring of displacements of concrete dams, the most difficult part is to choose functions that consider the effect of the concrete temperature on the displacement (Swiss Committee on Dams, 2003). There are various approaches in the literature. Many of them work well for some dams, whereas they may lead to physically meaningless results for other dams. Since usually a large set of correlated temperature measurements is available, multicollinearity likely occurs. This can lead to prediction instabilities and consequently to wrong conclusions. There are different statistical approaches to consider multicollinearity in the literature. Until now, there is no study in which these approaches are systematically evaluated. Another approach to reduce the number of variables and hence the effect of multicollinearity are physically-based models. Due to the integration of the temperature variables, the individual weights of the temperature measurements are considered by physical laws. Good results by the use of finite element models were obtained in Obernhuber and Perner (2005) or De Sortis and Paoliani (2007), for example. Unfortunately, the set-up of finite element models is time-consuming and has to be done individually for each structure. The use of simplified beam models representing the behaviour of concrete dams for the purpose of dam behaviour analysis would allow a more general use.

Furthermore, dam behaviour models are commonly set up and calibrated to fit the displacement at one level above ground. If several levels are analysed, different sets of

parameters are estimated. The instantaneous observation of several levels with a multi-objective calibration would lead to the same parameters for the whole structure and therefore allow for drawing comprehensible conclusions based on engineering judgement.

In addition, there is a lot of discussion among practitioners about which part of the data should be considered for model calibration. Some engineers say, if a good working model has been achieved, its coefficients shall be fixed. Otherwise, behaviour changes would be included in the new regression coefficients and thus be part of the model. Others say that also newly available data shall be included for calibration, since the model precision increases the more data are considered. Currently, there is no study that prefers either strategy.

1.3 Objectives and research approach

The focus of the current research project lies on statistical models predicting the crest displacement of concrete dams. Mainly, the following goals are aimed at:

- evaluate state-of-the-art models by use of prototype data of different Swiss dams and dam types
- improve robustness
- develop new models considering the effect of temperature on the displacement
- define data part that shall be used for model calibration

These research objectives are tackled as described in the following. Firstly, established procedures for dam behaviour analysis and models from literature will be studied and evaluated by the use of prototype data of different Swiss dams and dam types. Secondly, new approaches shall be developed and tested with the same data sets. The main goal is to improve the robustness of the models. This can be achieved using physically-based model equations for the effects of the water level and temperature. The goal is to use flexible models that can be applied to several dams. Thus, simplified beam models shall be used instead of finite element models. Since these models can be used to evaluate the displacement on several levels, multi-objective calibration shall be investigated.

For the use of physically-based models, the temperature field in the dam has to be known. Based on this, the mean temperature and the linear temperature difference between the upstream and the downstream side of the dam, which are physically causing the deformation, can be estimated. Since the thermometers are usually embedded inside the concrete body, inverse heat conduction analysis is necessary. Due to the fact that inverse heat conduction is an ill-conditioned problem, stabilisation procedures are applied. Established procedures from the literature shall be evaluated and a new approach shall be developed if necessary.

Finally, it is investigated which part of the data shall be used for the model calibration. The findings of this project shall be used to extend the software DamBASE (Gerber *et al.*, 2015).

1.4 Thesis outline

In Chapter 2, the physical fundamentals are introduced, and the literature review is presented. In Chapter 3, the heat transfer analysis is introduced. The calibration of the thermal conductivity is presented and applied for several case studies. In addition, the need of inverse heat conduction analysis and stabilisation procedures are discussed.

In a next step, presented in Chapter 4, existing modelling approaches are evaluated. The focus lies on models that allow for displacement monitoring of concrete dams. At the beginning, different procedures to perform the behaviour analysis are compared. Then, the approaches to consider the effects of the water level, temperature and time are evaluated separately. Finally, approaches to consider multicollinearity and autocorrelation are analysed.

Based on the experience of the existing approaches, new approaches are presented in Chapter 5. First of all, beam models to create hybrid models for gravity- and arch dams are introduced. These are a cantilever model with an elastic abutment to model the behaviour of gravity dams and an arch-cantilever model for arch dams. Then, the multi-objective calibration of the beam model for gravity dams with the Markov Chain Monte Carlo method is presented. In a next step, the advantage of using Generalized Additive Models (GAM) is presented. Finally, the difference between prediction and inference, where all data are used for calibration, is discussed.

In Chapter 7, a work flow for dam behaviour analysis is summarised in a flow chart. Based on this flow chart, two case studies are presented. In Chapter 8. the main findings of this work are summarised in the conclusions. The thesis closes with an outlook on further research.

2 Literature review and fundamentals

2.1 Dams

2.1.1 Dam types

Different types of dams can be distinguished (Fig. 2.1). There are two main categories, (i) concrete dams and (ii) embankment dams. Concrete dams are typically grouped in four main categories, arch dams, gravity dams, arch-gravity dams and buttress dams. Further, gravity dams can be sub-classified in gravity dams and hollow gravity dams. Embankment dams are grouped in homogenous embankment dams, central core dams and upstream faced dams.

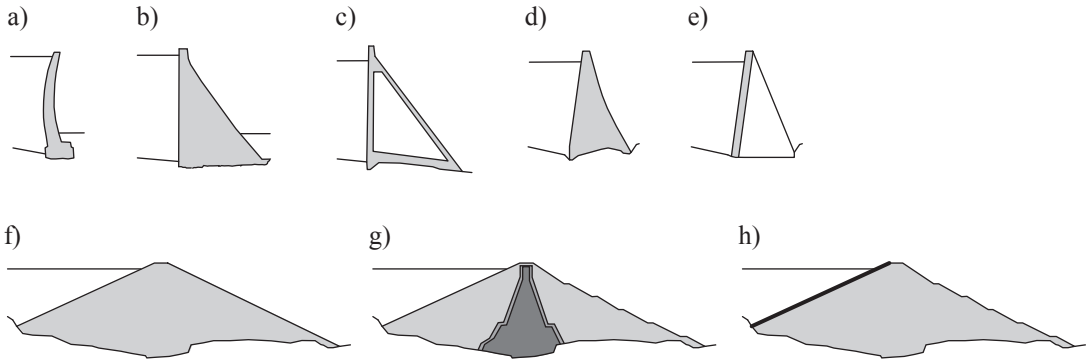

Fig. 2.1 Side view of different dam types: a) arch dam; b) gravity dam; c) hollow gravity dam; d) arch-gravity dam; e) buttress dam f) homogenous embankment dam; g) central core embankment dam; h) embankment dam with upstream facing.

Arch dams carry the load by the arch effect in horizontal direction and by the cantilever effect in vertical direction. Thus, the valley must be narrow enough and the rock of good quality. Gravity dams carry the load in vertical direction into the foundation. They can be thought as rigid concrete bodies that counter the water load by their weight. To reduce the weight and therefore the concrete mass, hollow gravity dams are built. To increase the resistance against tilting, the inclination of the upstream surface can be adapted, which leads to a vertical component of the water pressure. In addition, there are buttress dams which lead to an even lower concrete volume but additional work in concrete formwork construction. Since there are only two buttress dams in Switzerland, they are not treated in this thesis. There is also a combination of arch- and gravity dams, the so-called arch-gravity dams.

Homogenous embankment dams are usually limited to a height of around 30 m. Due to impermeability they should consist of compacted material with a Darcyan velocity $k_F < 10^{-7}$ m/s. Central core dams are the most used embankment dams. The shoulders guarantee the stability and the core guarantees the impermeability. Since the core zone

is small compared to the shoulders, very compact material with $k_F < 10^{-9}$ m/s must be used. Besides the natural cores, artificial cores such as asphaltic concrete cores or sheet piles in the case of smaller dams can be used. An upstream facing can consist of cementitious or asphaltic concrete. In recent years, concrete faced rock-fill dams (CFRD) became very popular. Since concrete is a brittle material, the requirements to limit settling are high. The choice for a certain dam type depends on several aspects. These are mainly the topography, the rock quality, the available material and further the design of the spillway and the seismicity (Boes, 2015b). More information about the different dam types and their advantages and disadvantages can be found in Boes (2015b) and Schleiss and Pougatsch (2011).

2.1.2 Influences quantities on dams

2.1.2.1 Loads for structural safety assessment

Considering structural safety, permanent, varying and exceptional loads should be distinguished. The different loads are shown in Table 2.1. Schleiss and Pougatsch (2011) give more details about these loads and their estimation.

Table 2.1 Loads on dams (adapted from Schleiss and Pougatsch, 2011).

permanent loads	varying loads	exceptional loads
self-weight	water pressure	floods
earth pressure	sediment pressure	earth quakes
anchors	uplift force	avalanches
	temperature	mudflows
	seepage flow force	(plane crash)
	pore pressure	
	snow load	
	ice load	
	traffic load	

2.1.2.2 Influence quantities on dam behaviour

With respect to the monitoring of dam behaviour, not all loads listed in Table 2.1 are of importance. Constant loads do not lead to a variation of the monitored variables and exceptional loads rarely occur. The behaviour of dams is expressed by recordable variables such as deformations and drainage flows (Schleiss and Pougatsch, 2011). These variables are mainly influenced by the water pressure which is given by the water level elevation, the temperature distribution inside the structure, precipitation and snow melt. In addition, the displacement can be influenced by creep, concrete ageing, deformation of the valley or an alkali aggregate reaction. In the following, these influences are described briefly.

Water level

The water body causes hydrostatic pressure that acts on the surface of the structure. In addition, the reservoir filling has an effect on the valley widening and valley bottom rotation and therefore also on the dam displacement (Herzog, 1988a).

Temperature

The displacement due to temperature is caused by the temperature field inside the concrete dam body. This in term depends on the air- and water temperature and the solar radiation. The heat exchange between the air temperature and the concrete surface is influenced by convection that is a function of wind speed and topography (Çengel and Ghajar, 2015). Due to the thermal diffusivity, the temperature change in the middle of the dam is delayed with respect to the change of the boundary temperatures. The theory of heat transport and the different processes at the boundary are described in Section 2.3.

Precipitation and snow melt

Precipitation (rain and snow) influences the drainage flow measured at the dam toe. Since the infiltration and the seepage flow is a slow process, these effects are not instantaneous (Simon *et al.*, 2013). In the case of snow fall, the snow melt is actually the representative variable since it causes the infiltrating water.

Hydration heat

The setting of placed concrete causes hydration heat caused by chemical processes. In thick mass concrete structures, the heat flow is restrained and the temperature rises. The heat flow induces temperature gradients which in turn lead to tensile stresses. As a consequence, cracks can occur (Schackow *et al.*, 2016).

Bofang (2014) describes the temperature variation inside concrete in time (Fig. 2.2). After the concrete was placed at temperature T_p, the concrete temperature rises until it reaches its peak value $T_p + T_r$. After a first cooling, the temperature rises again due to the covering by new placed concrete. After some time, the steads temperature T_f which is only influenced by the air temperature and the water temperature is reached. This can take a very long time and depends on the thickness of the structure. In the example of Amberg (2003), it takes nine years until the steady temperature is reached. According to Bofang (2014), it even can take decades.

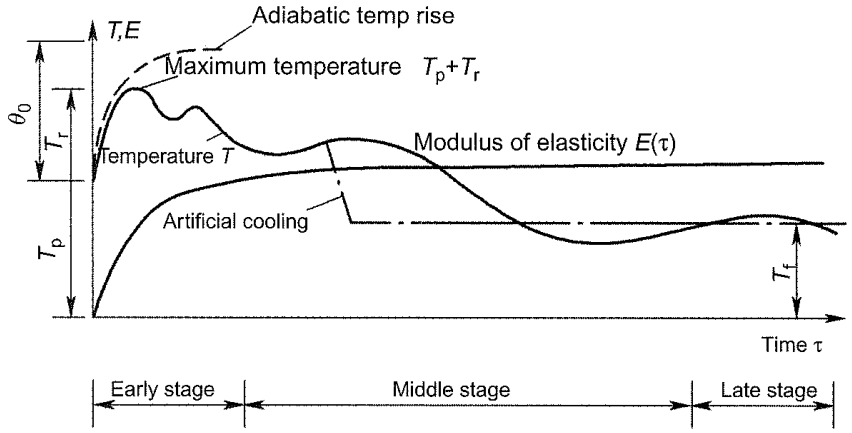

Fig. 2.2 Temperature variation of mass concrete with time. In addition, the development of the Young's modulus E is given (Bofang, 2014).

Creep

The mechanical definition of creep is an increasing contracting deformation under constant load. In the case of concrete, the mechanism is explained by chemical unbounded pore water that is squeezed out. There are several factors that influence the speed and amount of concrete creeping: Properties of the concrete mixture, conditions when concreting, age of the concrete by first loading, temperature, humidity and stress level (Serra *et al.*, 2012).

Concrete ageing

The properties of concrete change with the age of the structure. If no AAR is present, compressive strength, tensile strength and the Young's modulus E_c rise with the age. In Table 2.2, the Young's modulus for three dams in Austria is given for tests 90 d or 180 d after concreting and for core sample tests years later (Pichler, 2009). All of the dams have experienced a rise of the Young's modulus with time.

Table 2.2 Young's modulus of concrete E_c [N/mm^2] for tests after construction (at 90 d or 180 d after placement) and of core samples (12 a or 32 a later) (Pichler, 2009).

	test after construction	core samples
Weisssee	18.3 (90 d)	28.8 (32 a)
Tauernmoos	20.0 (90 d)	26.9 (12 a)
Schlegeis	23.2 (180 d)	28.2 (12 a)

The concrete can also be affected by a deterioration. This can happen if the water to cement ratio was high during concreting. This leads to a high porosity in the concrete and therefore this concrete is susceptible to freezing and thawing (Bossoney and Balissat, 2005).

Valley deformation

Valley closing or opening may occur due to geological processes or tunnelling and can lead to irreversible displacements. By tunnelling, water can be drained and the ground water table is lowered what may lead to settlements (Bremen, 2005). Fig. 2.3 shows that the valley location in respect of the subsidence cavity controls whether the valley opens or closes. Gravity dams and embankment dams are less sensitive to valley deformations than arch dams (Kobelt *et al.*, 2004).

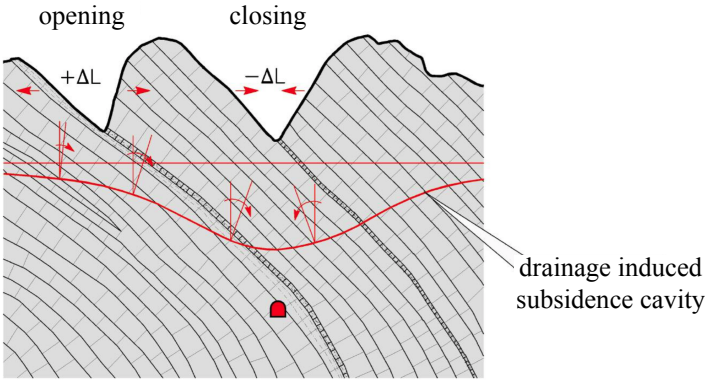

Fig. 2.3 Valley closing due to tunnelling (adapted from Bremen, 2005).

A famous case where a dam was influenced by tunnelling is the Zeuzier arch dam in Switzerland. By constructing a test tunnel that was 1500 m away and 500 m below the dam, high drainage flows up to 1000 l/s occurred. This led to massive settling of the rock mass and therefore valley deformations. The progress of the drainage flow and the dam displacement at crest level is shown in Fig. 2.4. Within one year, the crest deformed around 70 mm.

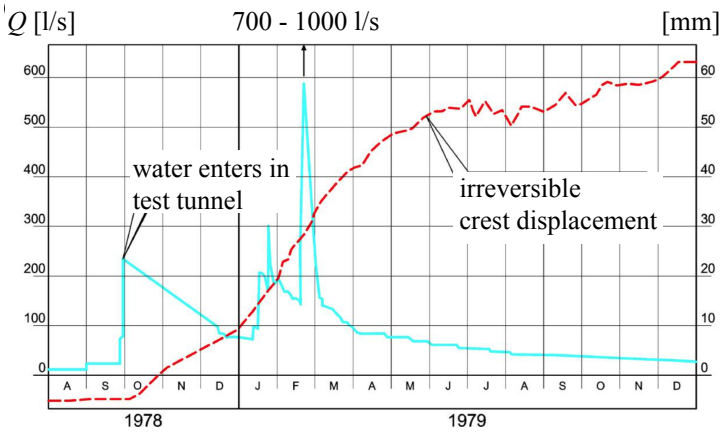

Fig. 2.4 Drainage flow in test tunnel and irreversible crest displacement of Zeuzier arch dam (adapted from Bremen, 2005).

Alkali aggregate reaction

Alkali aggregate reaction (AAR) is a chemical reaction between the components of the aggregates and the pore solutions in concrete. Three reaction types can be distinguished (Holcim Schweiz AG, 2008). The alkali silica reaction (ASR), the slow rate alkali-silicate reaction (ASSR) and the alkali-carbonate reaction (ACR) (Amberg, 2011). Three conditions must be fulfilled so that an AAR can occur: (i) a content of reactive aggregates that is greater than the threshold value, (ii) enough available alkali, and (iii) sufficient moisture (Léger *et al.*, 1996). AAR leads to concrete swelling which causes volume expansion or stress changes in the case of restrained structures. In addition, the Young's modulus and the tensile strength of concrete can decrease (Saouma *et al.*, 2007), possibly leading to cracks in the dam (Amberg, 2011). The maximal expansion that can be achieved by an AAR lies in the order of $0.2 \div 0.5$. This can be compared to a thermal expansion of $200 \div 500$ °C (Saouma, 2014).

2.1.3 Effects on dam behaviour

2.1.3.1 Separation into reversible and irreversible effects

The influence quantities described in Section 2.1.2.2 have an effect on the structure that can be expressed in the form of deformation (displacement or rotation) or drainage flow at different locations. The effects are a superposition of different influences (Bianchi and Bremen, 2000). The influences can have a reversible (elastic) or an irreversible (plastic) effect to the structure (Swiss Committee on Dams, 2003). Therefore, it is common to separate between reversible and irreversible effects. Generally, they can be grouped as shown in Table 2.3. In addition, they can also be grouped in instantaneous and deferred effects (Swiss Committee on Dams, 2003). In the following, the effects of the different influences are discussed separately for concrete dams and embankment dams.

Table 2.3 Reversible or irreversible effects on the structure.

reversible effects	irreversible effects
water level	hydration heat
temperature	creep
precipitation	concrete ageing
snow melt	valley deformation
	alkali aggregate reaction (AAR)

2.1.3.2 Concrete dams

Displacement

If the material behaviour is linear elastic, the mechanical pressure that acts on the dam leads to an instantaneous elastic displacement of the structure. In addition to this elastic

behaviour, a delayed viscous response may occur. Lombardi *et al.* (2008) describe this phenomenon for a large arch dam with a height of $H = 220$ m. They assumed that the observed viscous behaviour comes from the concrete properties that are not linear elastic for large stresses and the drainage of the rock foundation.

The influence of the concrete temperature on the displacement is different for arch- and gravity dams. The main difference comes from the different structural behaviour and the difference in the thermal inertia. The core temperature changes faster in a thin arch dam than in a thick gravity dam. The contribution due to temperature to the total displacement is different for small and large dams. For small arch dams, temperature is the controlling influence for displacement (Perner and Obernhuber, 2009) whereas for large arch dams it is the water level.

Tatin (2014) modelled the displacement of a gravity dam and an arch dam with finite elements. Fig. 2.5 shows the result of his simulations. For the gravity dam, the temperature difference between the upstream and the downstream side (gradient) is the important quantity. The mean temperature has only a minor influence. For the arch dam, it is vice versa. The mechanical decomposition into the mean temperature T_m and the temperature difference T_d is explained in Section 2.2.2.3.

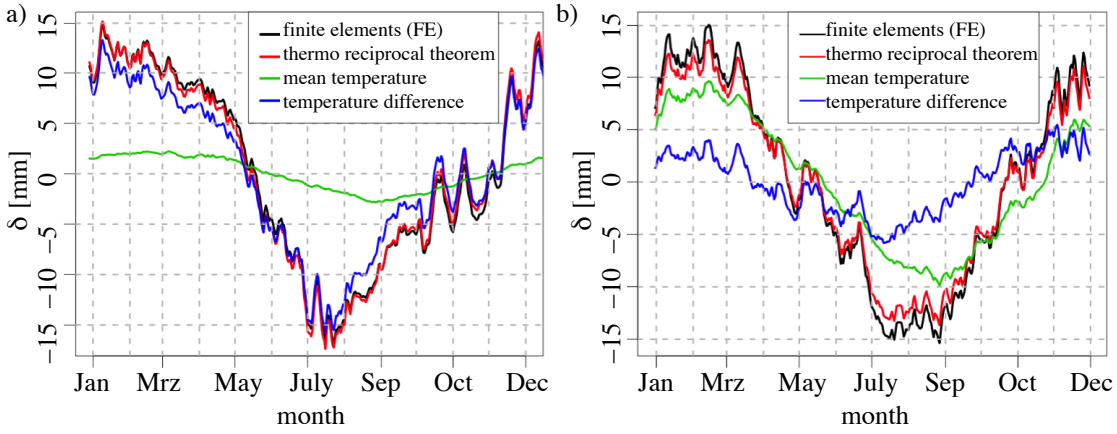

Fig. 2.5 a) Modelled temperature displacement for a gravity dam and b) for an arch dam for a period of one year. The parts of the mean temperature (green) and temperature difference (blue) are separately displayed (adapted from Tatin, 2014).

Tatin *et al.* (2013a) identified the main factors of temperature displacement in a case study of a gravity dam. They were interested in the deviation of a complex FE-model to monitoring data. Fig. 2.6 shows the results of this analysis. Going from number 1 to 10, different thermal phenomenons were added to the model. The larger the increase of the standard deviation of the residuals from one step to the next, the more important was the influence of an added thermal phenomenon. It can be concluded that the water temperature and the solar radiation have a significant effect on the displacement. In contrast,

the convection and the radiative exchanges are negligible. In addition, Tatin *et al.* (2015) showed that accounting for the water temperature could lower the standard deviation of the residuals for seven out of eight dams.

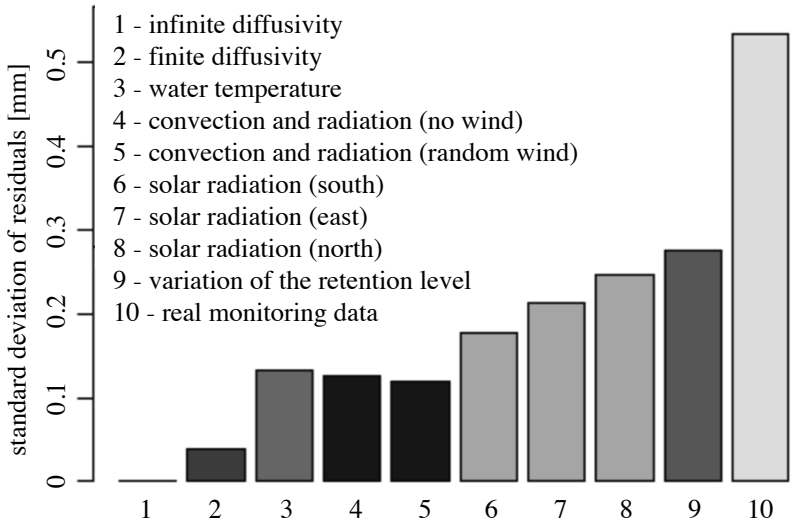

Fig. 2.6 Different thermal phenomenon (1-10) were added in sequence to a finite element model. Then, the difference to a statistical model (standard deviation) was regarded. The larger the increase of the standard deviation of the residuals from one step to the next, the more important was the effect (adapted from Tatin *et al.*, 2013a).

Irreversible displacements can be caused by valley creep, concrete ageing, valley deformation or an AAR. As described in Section 2.1.2, valley deformations can lead to displacements in both directions, AAR leads to a volume expansion, creep to a compression and concrete ageing to a stiffer structure. The common characteristic of these influences is that all are functions of time. Since they can occur simultaneously, the separation is difficult (Bossoney and Balissat, 2005). An AAR can be hidden due to creep, shrinkage and thermal cooling in the early years (Amberg, 2009). Fig. 2.7 shows that the evolution of an AAR can be hidden due to creep for several years.

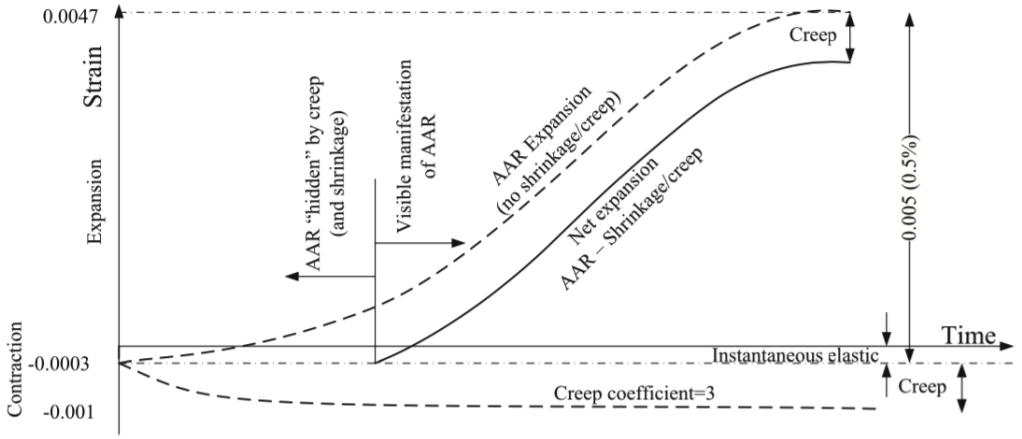

Fig. 2.7 AAR expansion can be hidden by creeping (Saouma, 2014).

Drainage flow

The water level is the main influence on drainage flow that is measured at the dam toe. Since the seepage flow is a very slow process, the effect is deferred. Simon *et al.* (2013) observed in a case study that the measured uplift force was not the same in summer and in winter since it is affected by the crack opening in the foundation that is influenced by the dam displacement which in turn depends on the temperature variation and the reservoir operation. The cracks can also influence the amount of drainage flow.

2.1.3.3 Embankment dams

Displacement

The water level has both a direct and an indirect effect on the displacement of an embankment dam. The mechanical pressure to the dam body acts directly on the displacement. In addition, the water level affects the seepage line and therefore the effective stress of the soil inside an embankment dam. This stress change leads to displacements (Lang *et al.*, 2011). Loading and unloading leads to permanent displacement in early years.

Drainage flow

As in the case of concrete dams, the water level is the main influence on the amount of drainage flow. In addition, depending on the measurement location and due to infiltration in the dam body, precipitation can become a major influence as well.

2.1.4 Surveillance

In Switzerland, dam surveillance is based on three pillars (Bundesamt für Energie, 2015):

- structural safety
- monitoring and maintenance
- emergency concept

The structural safety must be checked periodically according to the recent state of the art. For instance, since 2004 all Swiss dams have to be assessed by applying the new earth quake code. Due to a proper monitoring and maintenance, the risk of a serious accident can be minimised but it will not vanish. Therefore, the operators must have an emergency concept for each dam. This concept includes flood wave propagation calculations for dam break scenarios (Bundesamt für Energie, 2015).

The monitoring can be divided into three groups (Fig. 2.8). The visual control gives a general statement about the condition, e.g. concrete cracking or movements of blocks, of the structure. This is done by the dam wardens. The functional control involves the control of regulated spillways and bottom outlets, the check of measurement equipment, the check of communication lines to the operational office and the sirens. The influence quantities and the effects are measured to evaluate whether the behaviour of the structure is normal or abnormal (BWG, 2002). The link between the influence quantities and the effects is done by dam behaviour analysis models (see Section 2.5). If an abnormal behaviour is detected, its origin should be identified. This can be a time-consuming process. Sometimes additional measurement equipment has to be installed (Bossoney and Balissat, 2005).

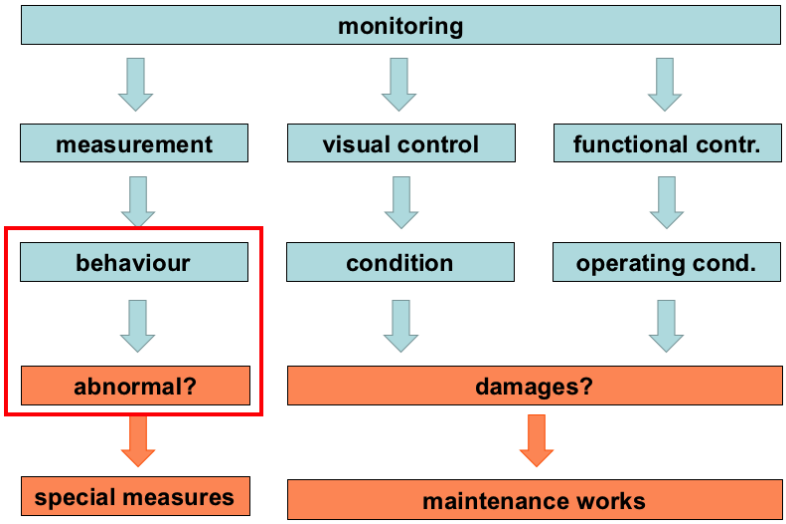

Fig. 2.8 Monitoring of dams according to Swiss guidelines for dam safety (adapted from BWG, 2002).

2.1.4.1 Measurements

The aim of an appropriate monitoring system is to measure the influence quantities and the effects on dams. The measurement equipment should be robust, simple to use and insensitive to temperature and moisture changes (Schleiss and Pougatsch, 2011). In the following, the established equipment to measure the effects and the causing influences are presented.

Displacement

Displacements can be measured by direct and inverted pendulums, inclinometers, extensometers, geodesy instruments etc. (Schleiss and Pougatsch, 2011). The most common equipment to measure horizontal displacements in concrete dams is a pendulum. its advantage is that the relative displacement between different levels can be measured directly with a high precision. The pendulum wire is installed in a vertical shaft. Direct pendulums (2) (Fig. 2.9a and 2.10) are fixed on the top (3) and a pendulum weight in a stabilising vessel is at the bottom (9). The displacement can be measured on different levels manually by a coordiscope and electronically by a telelot (7) (Huggenberger AG, 2016). With the latter, a permanent monitoring is possible whereas the manual readings are performed by the dam wardens. In the case of an inverted pendulum (4) (Fig. 2.9b and 2.10), the wire is fixed at a reference point at the bottom (5) and a float rot and a float vessel at the top (8). Usually, several pendulums are installed at one site (Fig. 2.10). The accuracy is given to ± 0.2 mm (Schleiss and Pougatsch, 2011). In Fig. 2.11, photos of a pendulum are shown.

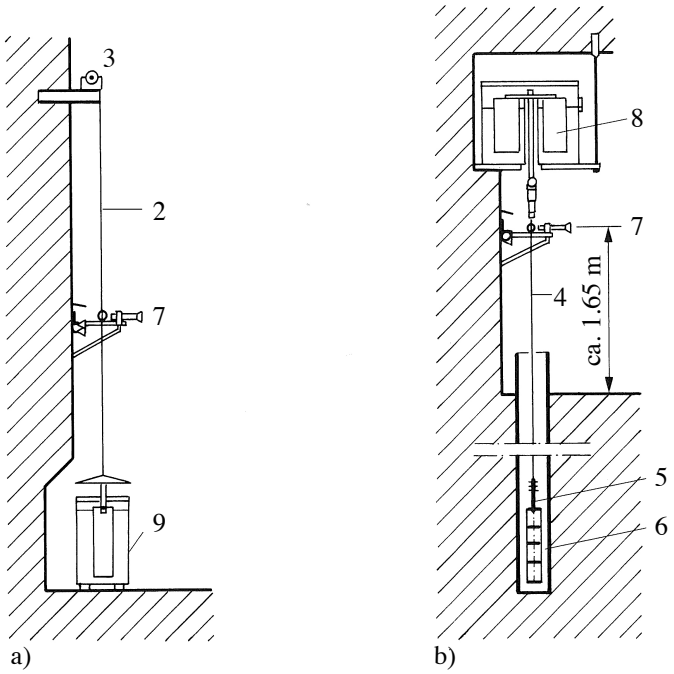

Fig. 2.9 Schematic display of pendulums; a) (2) direct pendulum fixed on the top (3), with (7) coordiscope and (9) stabilising vessel; b) (4) inverted pendulum fixed at a reference point at the bottom (5,6) and a (8) float vessel at the top. The measurements are taken with a (7) coordiscope (adapted from Schleiss and Pougatsch, 2011).

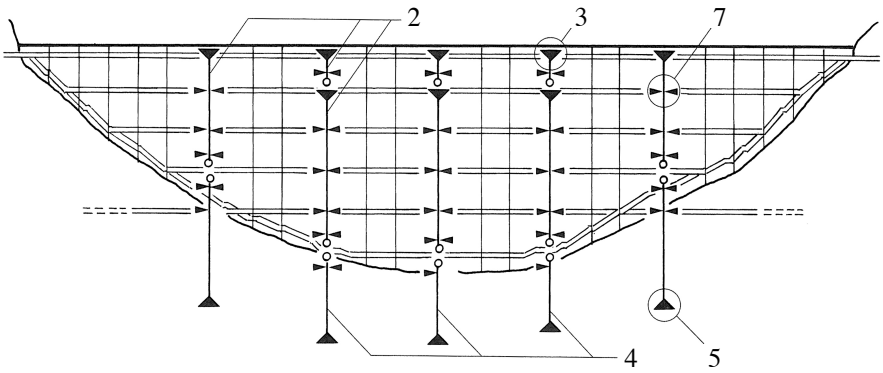

Fig. 2.10 Layout of five direct pendulums (2) fixed at the top (3) and five inverted pendulums (4) fixed at the bottom (5). The readings are taken by a coordiscope (7) (adapted from Schleiss and Pougatsch, 2011).

Fig. 2.11 Equipment to measure displacements by pendulum: a) fixed pendulum at the top; b) direct pendulum with electronic reading at the top; c) inverted pendulum; d) vertical shaft with pendulum wire; e) device for manual pendulum reading (photos: M. Bühlmann).

Drainage flow

The discharge of the drainage water can be measured with a measuring weir (e.g. Thompson weir) or by measuring the amount of drainage water over a certain time (BWG, 2002). Measurement weirs where the water level of the backwater is measured and converted to

a discharge are commonly used. The water level elevation is measured manually or with an ultrasonic sound that allows continuous and remote monitoring.

a) b) c)

Fig. 2.12 Measurement of drainage flow: a) collection of drainage flow in channel; b) measuring weir; c) ultrasonic sound to measure backwater level (photos: M. Bühlmann).

Water level

The most reliable way to measure the water level is a precision balance (Fig. 2.13). The accuracy is about ± 10 cm. It is essential to calibrate the precision balance by other measurement equipment (Schleiss and Pougatsch, 2011). The readings can be taken manually from the display or are recorded by an electronic monitoring system. Alternatively, pneumatic level measurements by the bubbling-through method can be done where the counter pressure created by an air compressor is measured.

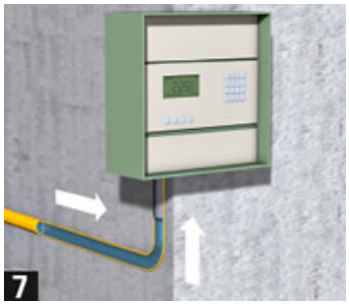

Fig. 2.13 Schematic display of precision balance to measure the water level (Strom-online, 2018).

Temperature

The temperature can be measured with an electrical resistance thermometer. They can be used to measure the temperature in concrete, water and air. In the case of air temperature measurements, a weather and radiation protection is available. The accuracy is given to ± 0.2 °C (Huggenberger AG, 2016). In Fig. 2.14, the temperature sensors to measure the concrete, water and air temperature, respectively, are shown.

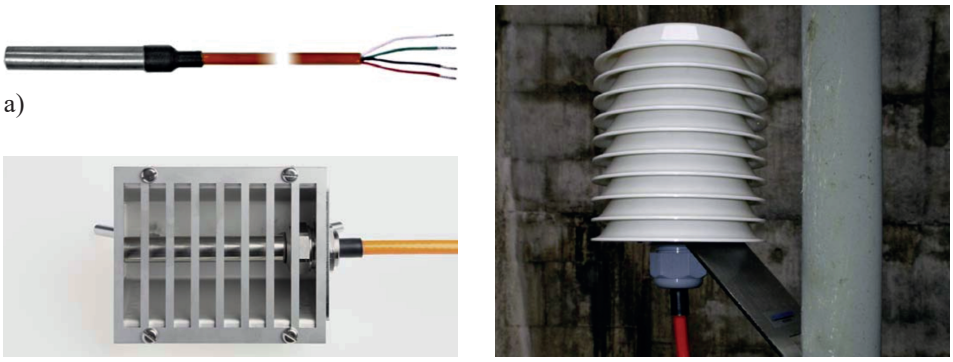

a) b) c)

Fig. 2.14 Temperature sensor for a) concrete, b) water and c) air (adapted from Huggenberger AG, 2016).

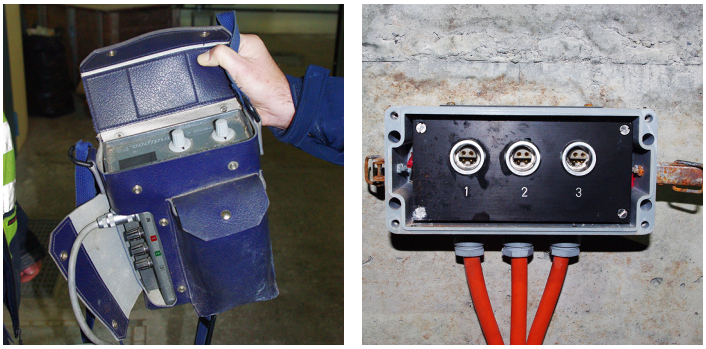

a) b)

Fig. 2.15 Measurement of temperature; a) measuring device to connect to the b) plug that is connected to the sensors (photos: M. Bühlmann).

Temperature measurements can be influenced by the position of the thermometers. Obernhuber and Perner (2005) give an example of two distances, i.e. (i) 40 cm and (ii) 80 cm away from the boundary. The surface amplitude of daily temperature variation decreases to 10% at 40 cm and to 1% at 80 cm inside the concrete. Based on this fact, they suggest placing the thermometer at least 80 cm away from the concrete surface if the measurements are taken at an arbitrary time during the day. If the daily temperature variations are of interest, the thermometers should not be more than 40 cm inside the concrete. Amberg (2009) also gives some advices about the positioning of thermometers in concrete dams:

- The temperature distribution is more or less uniform in horizontal direction in the case of a constant dam concrete thickness on the levels. Hence, the placement in the central section is sufficient. In addition, the central section corresponds to the mean orientation of the solar radiation in arch dams.
- In the vertical direction, the varying thickness and the moving water level have influence on the thermal distribution in the concrete. Therefore, the thermometers should be placed on at least three to five levels.

- Since the temperature gradient is higher near the boundaries, the distance between the thermometers should be small at the boundaries and larger in the middle of the dam. The optimal placement along a section can be obtained by a thermal analysis.

Inadequate positioning of the thermometers leads to deviations in the estimated temperature field and thus also in the displacement that is calculated based on this (Amberg, 2009).

Precipitation and snow

The precipitation can be measured by a weather station close to the dam site. The snowfall can be measured as new snow or as total compressed amount. The melt is difficult to measure on site. Therefore, the difference in water content and snow height between two days can be estimated leading to the mass balance (Simon *et al.*, 2013).

2.1.4.2 Plausibility check of measurements

The recorded measurement data should be checked for plausibility (BWG, 2002) to identify errors in the readings, inaccuracies in the measurement equipment or outliers. Lombardi (1992) presented methods for the plausibility check of measurement data. One proposed method is based on the history of a time series. The measurement data, e.g. the temperature, is plotted for every year on the same axis (Fig. 2.16a). In addition, based on the past measurement data, a confidence band is created. The new data are added to this plot and it is checked if they lie within the created confidence band. Another method is based on the empirical correlation between two measurements. For instance, the pendulum displacement is plotted versus inclinometer readings measured at the same location (Fig. 2.16b).

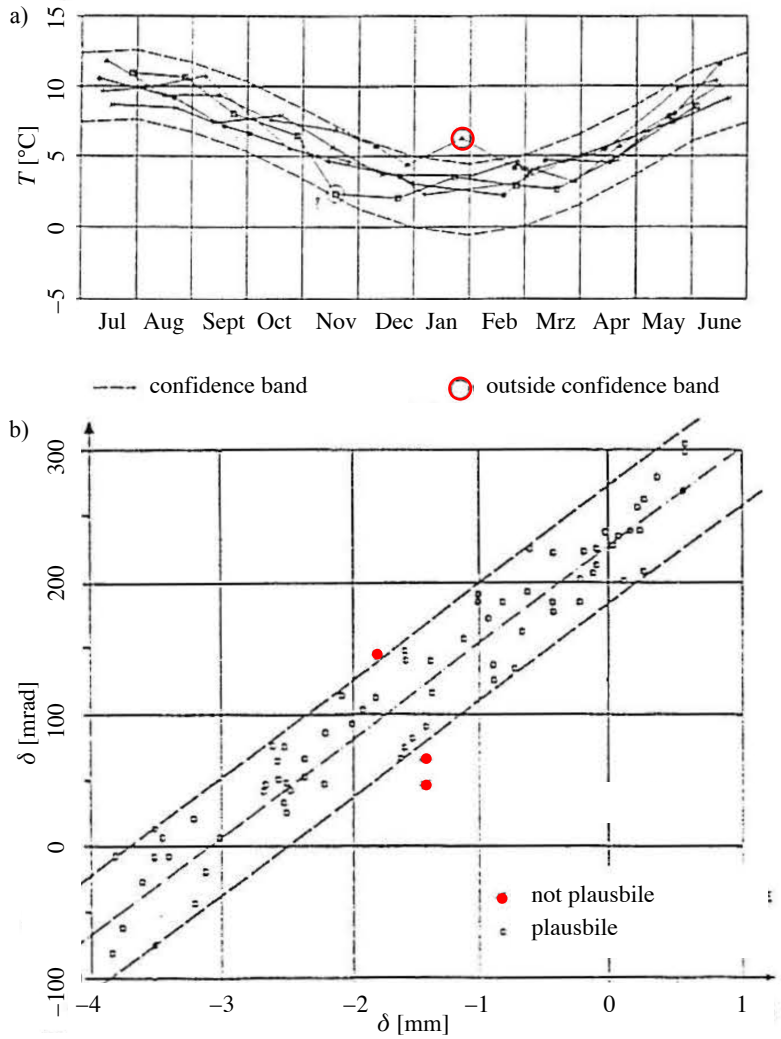

Fig. 2.16 Plausibility test for measurement data: a) test based on time series history; b) test based on correlation between two measurements (adapted from Lombardi, 1992).

2.1.5 Abnormal behaviour

One goal of the monitoring is to evaluate whether the behaviour of the structure is normal or abnormal. Normal behaviour is present if the behaviour is similar to the past behaviour under the same loading conditions (Mata, 2011). In addition, irreversible displacement such as deformation due to valley deformation or a AAR should be detected since it may deteriorate the dam.

2.2 Statics

2.2.1 Introduction

The fundamentals of statics are the definition of stress, equilibrium, the kinematic relationships and the constitutive laws. Their combination leads to the known equations used in statics. A solid description of these fundamentals is given in Marti (2013). Here, a selection of statics methods that can be used to calculate the deformation of dams is briefly described. The focus lies on analytical models based on the linear elastic beam theory since they are applied later herein. After the introduction of dam specific methods, framed structures are discussed. The work theorem that can be used to calculate the deformation of beams and the force method to calculate statically indeterminate systems are introduced. In addition, grillages are introduced. They connect different beams by compatibility conditions.

2.2.2 Deformation calculation of dams

2.2.2.1 Analytical models for arch dams

Until the 1920s, arch dams had been calculated using the ring tube formula. Since then it became common to use beam models with arches and cantilevers (Herzog, 1988b). In the so-called arch-cantilever models, the arch dam is modelled as a grillage that consists of arches and cantilevers (Fig. 2.17). The arches can be modelled as circles, parabolas or ellipses. The loads that act on the structure are carried by both the arches and the cantilevers (or consoles). The load distribution is estimated with the compatibility condition (equal displacements) that needs to be satisfied on all the nodes. Furthermore, linear elastic material behaviour is assumed.

The cantilevers distribute the loads to the different arches that are exposed to different water pressure. In Fig. 2.18, the load distribution between the arches and a cantilever is shown exemplarily. It can be recognised that the loading of the top arch is larger than solely from the water pressure. This is due to the load distribution by the cantilevers. There are several publications (e.g. USBR (1938) or Bosshard (1949)) about the arch-cantilever model. The general idea of these models is the same but different equations and solution procedures are used.

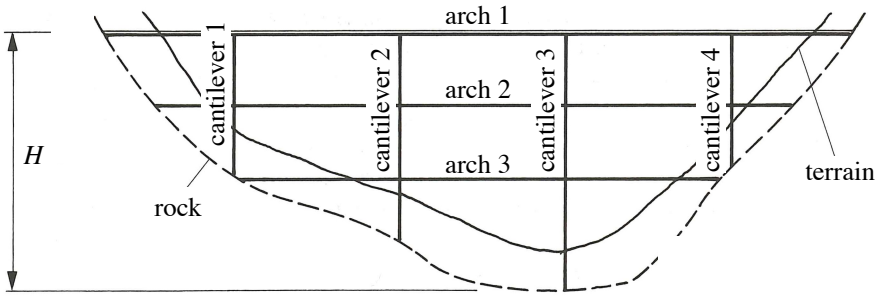

Fig. 2.17 Modelling an arch dam by arches and cantilevers (consoles) (adapted from Schleiss and Pougatsch, 2011).

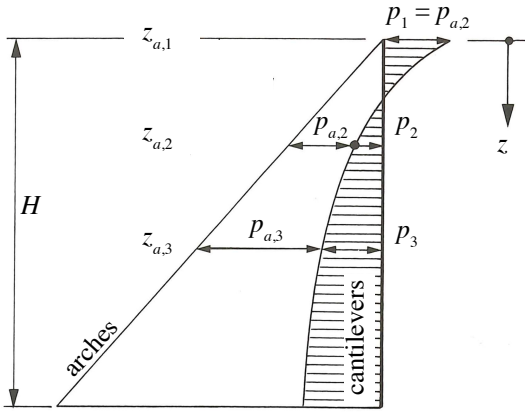

Fig. 2.18 Load distribution between arches and cantilevers. The load of the water level is given by the triangle, the load of the cantilevers is shaded and the difference between these is acting on the arches. The arch on the top receives more load due to the cantilever that is supported elastically by the arches (Schleiss and Pougatsch, 2011).

2.2.2.2 Analytical models for gravity dams

Based on an elastic slab equation, an analytical solution for the displacement at crest level (subscript *cr*) δ_{cr} due to a full reservoir can be derived (deep beam model) (Schleiss and Pougatsch, 2011):

$$\delta_{cr} = \frac{\gamma_w h^2}{2E_c}\left(\frac{1+(1+\tan^2(\phi))^2}{\tan^3(\phi)} + \frac{\nu_c}{\tan(\phi)}\right) \tag{2.1}$$

γ_w is the unit weight of water, h the water level about the abutment, E_c the Young's modulus of concrete, ν_c the Poisson's ratio of concrete and ϕ the opening angle of the triangle at crest level. Eq. (2.1) assumes a rigid support at the toe. According to Rescher (1965), the rigid support can be moved to $0.3 \div 0.4h$ below the toe to consider an elastic foundation.

Unfortunately, the equation presented above can only be used to calculate the displacement of a full reservoir. For monitoring purposes, the displacement due to a varying water

level is of interest. Rescher (1965) states that the displacement of a gravity dam can be calculated approximately by a cantilever beam. An elastic foundation can also be considered by a stiff support below the bottom of the dam. Léger and Seydou (2009) use a beam model for the monitoring of gravity dams. They use springs to consider an elastic foundation.

2.2.2.3 Thermal deformation

Changes in the temperature field lead to deformations in the dam body. It can be shown that a mean (subscript m) temperature T_m and a linear temperature difference (subscript d) T_d between the upstream and downstream sides cause the deformation (Obernhuber and Perner, 2005). In the following, it is shown how T_m and T_d are estimated and how they can be used to calculate the displacement.

Temperature decomposition

Consider a 1D bar of length L (Fig. 2.19). A given thermal field $T(x)$ can be decomposed in a uniform temperature T_m, a linear temperature difference T_d, and a nonlinear part T_n(x) (Amberg, 2009).

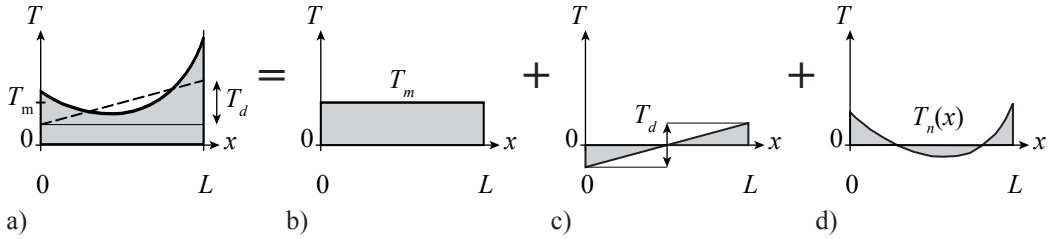

Fig. 2.19 Decomposition of temperature field $T(x)$ in a uniform temperature T_m, a linear temperature difference T_d, and a nonlinear part T_n(x) (adapted from Amberg, 2009).

T_m can be derived by the equilibrium condition $\sum N = 0$. Integrating the normal forces, which are caused by expansions leads to

$$T_m = \frac{1}{L}\int_0^L T(x)\mathrm{d}x. \tag{2.2}$$

The temperature difference T_d can be derived by equilibrium of the bending moments $\sum M = 0$:

$$T_d = \frac{12}{L^2}\int_0^L T(x)\left(\mathrm{x}-\frac{\mathrm{L}}{2}\right)\mathrm{d}x. \tag{2.3}$$

One dimensional analysis

For a 1D-section with homogenous and isotropic material, with a linear temperature difference T_d and a mean temperature T_m, the deformation due to temperature can expressed by the strain ε, which is affected by the mean temperature, and the curvature χ resulting from the linear temperature difference (Dallmann, 2009):

$$\varepsilon(x) = \alpha_T \, T_m(x) \tag{2.4}$$

$$\chi(x) = \alpha_T \, \frac{T_d(x)}{L} \tag{2.5}$$

The thermal expansion coefficient α_T is a material constant. For concrete and steel, it is in the range of 10^{-5} 1/K. In statically indeterminate systems, temperature changes lead to restraints (Marti, 2013). The displacement is calculated by integrating the strain or the bending over the whole section.

Three-dimensional analysis

In the case of 3D bodies, the deformation due to temperature can be calculated by the thermo-elastic reciprocal theorem (Timoshenko and Goodier, 1970):

$$\delta = \alpha_T \int_V \Theta(x,y,z) \, T(x,y,z) \, \mathrm{d}V \tag{2.6}$$

The temperature field $T(x,y,z)$ is multiplied with the first invariant of the stress tensor $\Theta(x,y,z) = \sigma_{xx} + \sigma_{yy} + \sigma_{zz}$ and integrated over the whole body (Obernhuber and Perner, 2005). The stress tensor is the result of the unit load acting on the location and in the direction of the displacement that needs to be calculated.

Obernhuber and Perner (2005) used the thermo-elastic reciprocal theorem (Eq. (2.6)) to show that T_m and T_d are the important quantities to calculate the displacements due to temperature variation in dams and the nonlinear part T_n(x) can be neglected. By assuming constant temperature in lateral direction, the displacement at an arbitrary point can be calculated with the thermo-elastic reciprocal theorem:

$$\delta(x,y,z) = \int_0^H \int_0^{L_a} \left(\Theta_m \, T_m + \frac{L}{3} \Theta_\mathrm{d} \, T_d \right) \mathrm{d}x \, \mathrm{d}z \tag{2.7}$$

where Θ_m and Θ_d are the respective influence functions for a unit load applied at the point and in the direction of the displacement of interest. The integration is performed across the whole dam height H and arch length L_a.

2.2.2.4 Considering the elasticity of the foundation

The elastic deformation of a rock foundation can be calculated by the Vogt's method which is well described in USBR (1938). The method is based on the Boussinesq formula and isotropic linear elastic material behaviour. Since this is a crude assumption, this approach can only be seen as a rough approximation of the real problem.

The loaded portion of the foundation surface is approximated by a rectangle with width b and height a (Fig. 2.20b). For an element with unit width and of thickness t_a at the abutment, the spring constants to consider an elastic foundation can be calculated with Eq. (2.8) - (2.10) (USBR, 1938).

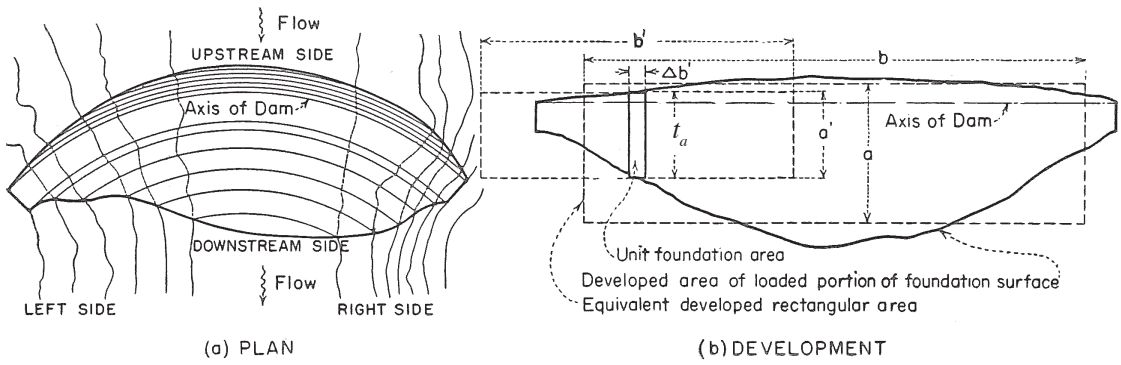

Fig. 2.20 a) Situation of dam with topography; b) loaded foundation area (solid) and corresponding equivalent rectangular area (dashed) (USBR, 1938).

$$k_N = \frac{f_{k,N}}{E_r} \tag{2.8}$$

$$k_V = \frac{f_{k,V}}{E_r} \tag{2.9}$$

$$k_M = \frac{f_{k,M}}{E_r t_a^2} \tag{2.10}$$

E_r is the Young's modulus of the elastic rock (subscript r) foundation. The factors $f_{k,N}$, $f_{k,V}$ and $f_{k,M}$ are given in the tables in Appendix A.1.1 or can be calculated by Eq. (2.11) - (2.16) where $X = b/a$ and ν_c is the Poisson's ratio of rock.

$$f_{k,N} = \frac{2(1-\nu_r^2)}{\pi} A \tag{2.11}$$

$$f_{k,V} = \frac{2}{\pi}\left((1-\nu_r^2)A + (\nu_r+\nu_r^2)B\right) \tag{2.12}$$

$$f_{k,M} = \frac{24(1-\nu_r^2)}{\pi} C \tag{2.13}$$

$$A = \ln(X+\sqrt{1+X^2}) + X\ln\left(\frac{1+\sqrt{1+X^2}}{X}\right) - \frac{\sqrt{1+X^2}^3 - 1 - X^3}{3X} \tag{2.14}$$

$$B = X\ln\left(\frac{1+\sqrt{1+X^2}}{X}\right) - \frac{\sqrt{1+X^2}(2X^2-1) - 2X^3 + 1}{3X} \tag{2.15}$$

$$C = \frac{\sqrt{1+X^2}(3-14X^2-2X^4) + 15X^3 + 2X^5 - 3}{15X} + X\ln\left(\frac{1+\sqrt{1+X^2}}{X}\right) \tag{2.16}$$

2.2.2.5 Numerical models

The use of numerical methods, such as finite elements (FE), is the standard in dam engineering today. A good overview on state of the art methods used in dam engineering is given in ICOLD (2013). Commonly FE-models are used to evaluate the structural safety of dams. In a FE-model, the structure is discretised by a finite number of elements in which the displacement is described by governing equations. The single elements are joined to the global model under preserving the kinematic compatibility and the equilibrium conditions. The relation between the force and the displacement is given by chosen constitutive laws (Werkle, 2008). This can be the elastic models based on Hook's law or even nonlinear models that allow for plastic strains. Further information about FE-models can be found in Bathe (1996) and Werkle (2008).

2.2.3 Framed structures

Framed structures consist of bar elements that are connected by nodes and that end on supports. The cross-section of the structure is assumed to be small compared to its span. They can be grouped to straight bar elements, beams and columns, and curved bar elements known as arches. Combining bar elements leads to trusses which can be distinguished between plane structures (2D) and spatial structures (3D) (Marti, 2013).

The stress resultants can be determined by the equilibrium and the compatibility conditions. For statically determinate systems, only the equilibrium condition is needed, for statically indeterminate systems both. There are the force method, the slope deflection

method or integral solutions to solve statically indeterminate systems. In the following, the first method is described shortly. More details about these methods can be found in Marti (2013). Usually linear-elastic material behaviour and plain remaining cross-sections are assumed and the calculation of the internal forces is done by first order, which means that they are calculated for the non-deformed system.

2.2.3.1 Work theorem

To calculate a deformation δ_{ij} at a certain position of a beam due to a load X_j, the work theorem (Eq. (2.17)) can be applied. In doing so, a virtual load $X_i = 1$ in the direction of the displacement of interest is applied. The displacement is calculated by integrating the stress resultants due to X_j multiplied with the stress resultants due to X_i .

$$\begin{aligned}\delta_{ij} \;=\; & \int \left[N_i \left(\frac{N_j}{EA} + \alpha_T T_m \right) + \frac{V_{y,i} V_{y,j}}{GA_{v,y}} + \frac{V_{z,i} V_{z,j}}{GA_{v,z}} \right. \\ & \left. + \frac{T_i T_j}{GI_x} + M_{y,i} \left(\frac{M_{y,j}}{EI_y} + \alpha_T \frac{T_{d,z}}{h_b} \right) + M_{z,i} \left(\frac{M_{z,j}}{EI_z} + \alpha_T \frac{T_{d,y}}{B_b} \right) \right] \mathrm{d}x \\ & + \sum \frac{R_{N,i} R_{N,j}}{k_N} + \sum \frac{R_{V,i} R_{V,j}}{k_V} + \sum \frac{R_{M,i} R_{M,j}}{k_M}\end{aligned} \tag{2.17}$$

Here, N, V_y, V_z, T, M_y and M_z are the stress resultants due to X_j and X_i , respectively, $A = B_b h_b$ is the cross-sectional area, $A_v = \alpha_v A$ the shear area with the area shear factor α_v (α_v=5/6 for rectangular cross-sections) , $G = E/(2(1+\nu))$ is the shear modulus, I_x the torsional moment of inertia, I_y the moment of inertia around the y-axis and I_z the moment of inertia around the z-axis (Fig. 2.21). R_N, R_V and R_M are the supporting forces and k_N, k_V and k_M the corresponding spring constants. They lead to a displacement at the supporting. T_m and T_d are the mean temperature and the linear temperature difference, respectively.

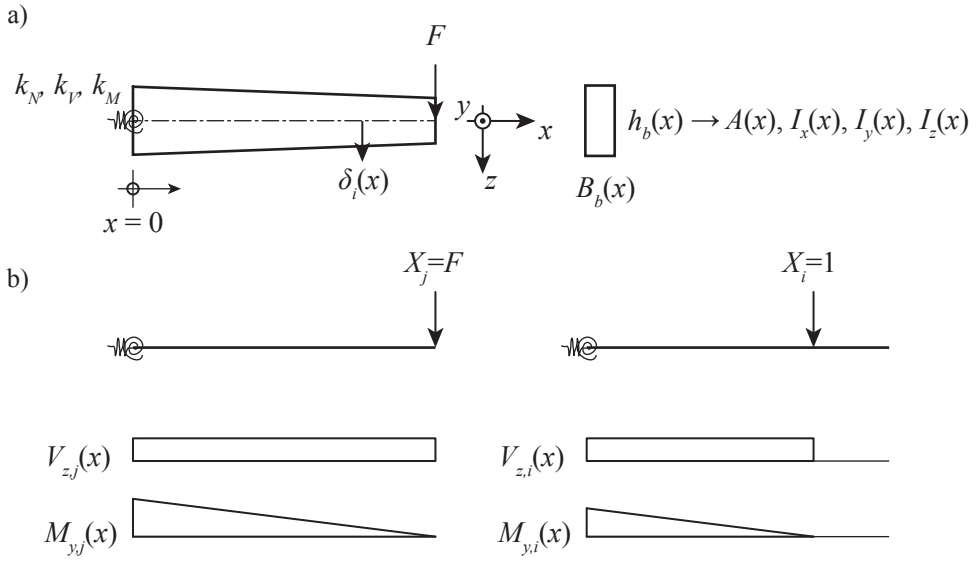

Fig. 2.21 Application of the work theorem to a cantilever beam with axis in x-direction. The load F is applied and the displacement $\delta_i(x)$ is calculated. a) geometry of cantilever beam; b) stress resultants due to the load $X_j = F$ and the virtual load X_i.

2.2.3.2 Force method

The force method can be applied to estimate the resultants of statically indeterminate systems and based on them also the corresponding displacements. Basically, the principle of the force method to is to define a statically determinate system by releasing constraints and replacing them with redundant variables X_i=1. The number of redundant variables corresponds to the degree of static indeterminacy. On the statically determinate system, the displacement due to the load X_0 and the redundant variables X_i is calculated by using the work theorem (Eq. (2.17)). Since the deformations δ_i at the supporting are known, the following linear equation system of compatibilities can be solved to obtain the redundant variables X_i:

$$\delta_i \quad = \quad \delta_{i0} + \Delta_{ij} X_i \quad = \quad 0 \tag{2.18}$$

δ_{i0} are the displacements at the location of the removed support i (in direction of support force) due to the load X_0, Δ_{ij} is the displacement matrix due to the redundant variables X_i in direction of themselves. The matrix Δ_{ij} can be used for several different load cases X_0. If all the resulting forces and the redundant variables are known, the support forces and the resultants can be calculated. If the displacement shall be calculated, the work theorem can be used by introducing a load $X_j = 1$.

The procedure of the force method consists of the following steps (Marti, 2013):

1. `Determination of the degree of static indeterminacy` r

2. Selection of a stable, statically determinate basic system and introducing r redundant variables $X_i = 1$
3. Determine the support forces and the stress resultants on the basic system for all X_i and the on the static system acting load X_0
4. Determine the deformations (incompatibilities) δ_{ij} (e.g. deformation in direction of X_1 due to X_2) and the deformations δ_{i0} due to the load X_0 in direction of X_i.
5. Calculate redundant variables X_i with Eq. (2.18)
6. Calculate support forces and stress resultants of the statically indeterminate system by the superposition of the supporting forces and the stress resultants of all X_i and X_0
7. Calculate the displacement by using the work theorem and introducing a virtual force $X_j = 1$

2.2.3.3 Grillages

A grillage is a static system that consists of different beams that are firmly interconnected. The static system can be a grillage as such or used as an approximation for plates or shells. In contrary to the last two, grillages can carry only normal forces, shear forces and bending moments but no membrane forces. The idea of a grillage is that the load is distributed to the different beams so that the compatibility of the displacement at the intersection points $P_{i,j}$ is satisfied. In the following, the application of a grillage is demonstrated by an example.

Consider the grillage with the two beams $B_{x,1}$ and $B_{x,2}$ in x-direction and $B_{y,1}$ in y-direction (Fig. 2.22a). A load F_z on the intersection point $P_{1,1}$ acts on the grillage. This load is carried by all of the three beams. Since the static system is statically indeterminate, the load distribution must be found by the compatibility condition. In this example, the compatibility condition of the displacement in z-direction is formulated. Thus, the unit loads $F_{1,1}$ and $F_{2,1}$ are introduced on the corresponding nodes (Fig. 2.22b). Then the displacement due to these unit loads at every intersection point is calculated for every beam, with results summarised in Table 2.4.

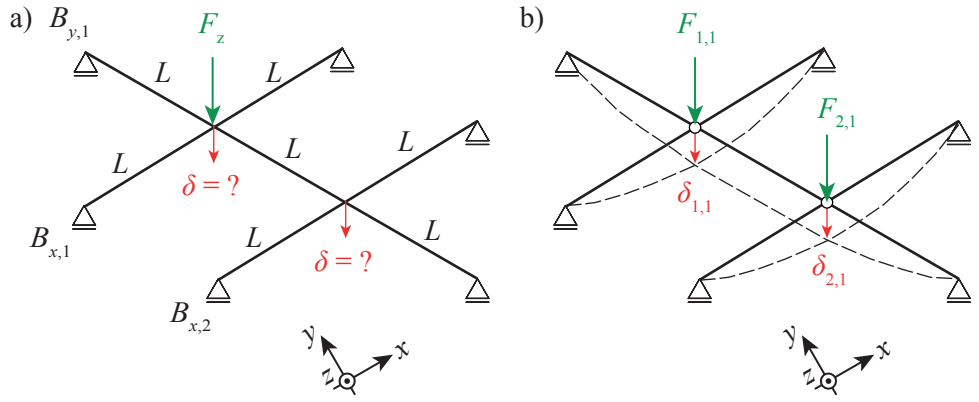

Fig. 2.22 Application of the work theorem to a cantilever beam with axis in x-direction. The load F is applied and the displacement $\delta_i(x)$ is calculated. a) Geometry of cantilever beam; b) stress resultants due to the load $X_j = F$ and the virtual load X_i.

Table 2.4 Displacements $\delta F_{i,j}$ for the unit loads $F_{i,j}$ and the load F_z loaded to beam $B_{x,1}$.

		$\delta F_{1,1}$	$\delta F_{2,1}$
	$B_{x,1}$	$1/(6EI)\,L^3\,F_{1,1}$	0
$F_{1,1}$	$B_{x,2}$	0	0
	$B_{y,1}$	$4/(9EI)\,L^3\,F_{1,1}$	$7/(18EI)\,L^3\,F_{1,1}$
	$B_{x,1}$	0	0
$F_{2,1}$	$B_{x,2}$	0	$1/(6EI)\,L^3\,F_{2,1}$
	$B_{y,1}$	$7/(18EI)\,L^3\,F_{2,1}$	$4/(9EI)\,L^3\,F_{2,1}$
	$B_{x,1}$	$1/(6EI)\,L^3\,F_z$	0
F_z	$B_{x,2}$	0	0
	$B_{y,1}$	0	0

The displacements listed in Table 2.4 are used to formulate the compatibility condition. In direction and at the location of each load $F_{i,j}$ that was introduced, a compatibility condition can be formulated:

$$\begin{aligned} \frac{11}{18}\frac{L^3}{EI}F_{1,1} + \frac{7}{18}\frac{L^3}{EI}F_{2,1} &= \frac{1}{6}\frac{L^3}{EI}F_z \\ \frac{11}{18}\frac{L^3}{EI}F_{1,1} + \frac{7}{18}\frac{L^3}{EI}F_{2,1} &= 0 \end{aligned} \tag{2.19}$$

Eq. (2.19) can be written in the general matrix notation

$$\Delta_G F_{i,j} = \delta_F, \tag{2.20}$$

where Δ_G is the matrix of compatibility conditions of the grillage, $F_{i,j}$ is the vector of loads to satisfy the compatibility conditions and δ_F the vector of displacements of the load F. To calculate the load distribution $F_{i,j} = \Delta_G^{-1}\delta_F$ the matrix Δ_G needs to be inverted. As soon as the loads $F_{i,j}$ are known, the displacement and the stress resultants of the grillage can be calculated for the single beams. The matrix Δ_G remains constant for the same static system. As a consequence, different load cases can be studied by changing only the displacement vector due to the load δ_F.

2.3 Heat transfer

The knowledge of the mean temperature T_m and the linear temperature difference T_d is of major importance to calculate the temperature deformation of concrete dams (see Section 2.2.2.3). Since the temperature is measured only at certain locations in the dam, the temperature field and therefore also T_m and T_d are not known a priori. Therefore, they have to be estimated based on the available measurements. In Switzerland, most dams are equipped with concrete temperature sensors whereas in some other countries they are not measured (Tatin *et al.*, 2015). In the case of no inner temperature measurements, the air temperature is used as a boundary condition. In addition, the water temperature and the boundary processes of convection and solar radiation can be taken into account. Unfortunately, there is considerable uncertainty in the calculation of convection and radiation. If some temperature measurements inside the concrete body are available, these processes at the boundary do not need to be taken into account (Amberg, 2009). Due to the fact that the installed concrete thermometers are not located at the boundary but at a certain distance inside the dam, a zone where no information is available exists. To estimate the surface temperature from inner measurements, inverse heat conduction analysis can be carried out. The goal of this chapter is to present the basics of heat transport analysis and having a closer look on methods that are applied to estimate the mean and the temperature difference.

2.3.1 Introduction to heat transport mechanisms

The first law of thermodynamics states that energy can neither be created nor destroyed (also known as the conservation of energy principle). Energy can be transferred by the two mechanisms heat transfer and work (Çengel and Ghajar, 2015). From the second law of thermodynamics it follows that the heat must flow from higher to lower temperature levels, and that it stops when the two levels are equal (Poulikakos, 2011; Çengel and Ghajar, 2015). Heat can be transferred in three different ways: conduction, convection and radiation. Heat conduction (diffusion) is the energy transfer from more to less energetic particles. In solids, it is caused by the vibrations of the molecules and the energy transport of free electrons. The rate is dependent on the material, the geometry and the temperature profile inside the body. Heat convection is the energy transfer between a solid surface and adjacent liquid or gas that is in motion. A faster motion leads to greater convective heat transfer. Radiation is the energy that is emitted in the form of electromagnetic waves. It is a result of the change in the electromagnetic configuration of the atoms or molecules. In contrast to conduction and convection, radiation does not need an intervening medium. This means that two bodies in a vacuum will reach a temperature equilibrium in time (Çengel and Ghajar, 2015).

Related to dams the three heat transfer processes described above are shown in Fig. 2.23. Heat conduction leads to temperature changes inside the dam body, convention can lead to a gain or loss of heat at the surface, the dam can lose heat by radiation and the solar radiation leads to heating.

In the following sections, the three transport processes are described more in detail. At first, the general heat conduction equation is derived and some simplifications of it are shown. Then the frequency domain solution procedures for the direct and the inverse heat conduction analysis are presented. Furthermore, the equations for convection and solar radiation are briefly discussed.

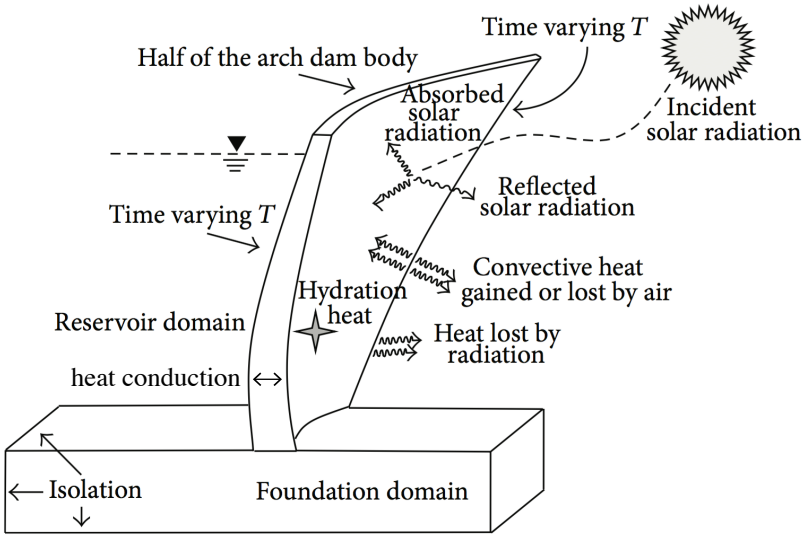

Fig. 2.23 Processes of heat transfer at a dam (adapted from Mirzabozorg *et al.*, 2014).

2.3.2 Conduction

2.3.2.1 Fourier's Law

The French mathematician Jean Baptiste Fourier stated in 1822 that a heat flux $\dot{q}$ through a plane with normal direction n is proportional to the temperature gradient ∇T:[1]

$$\dot{q} = -\lambda \nabla T \tag{2.21}$$

The proportionality constant λ is called thermal conductivity. The negative sign of Eq. (2.21) leads to positive heat flux in positive x-, y- and z-direction. Based on Eq. (2.21), it follows that for double temperature gradients ∇T the heat flux is also doubled.

[1] $\nabla = \left(\frac{\partial}{\partial x}, \frac{\partial}{\partial y}, \frac{\partial}{\partial z}\right)^T$ Nabla operator

2.3.2.2 Heat conduction equation

The content of this section is based on Çengel and Ghajar (2015) and Poulikakos (2011). The heat conduction equation can be derived by the conservation of energy principle. Regarding the energy balance over a small time step dt in a control volume dxdydz (Fig. 2.24) the energy balance Eq. (2.22) can be stated. The sum of all the heat fluxes $\dot{Q}_i$ and the source term $\dot{Q}_s$ equals the energy change in the control volume.

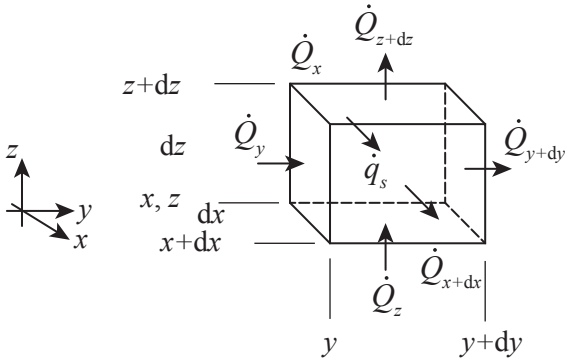

Fig. 2.24 Heat flux in control volume (adapted from Poulikakos, 2011).

$$\frac{\partial E}{\partial t} = \dot{Q}_x + \dot{Q}_y + \dot{Q}_z - \dot{Q}_{x+dx} - \dot{Q}_{y+dy} - \dot{Q}_{z+dz} + \dot{Q}_s \tag{2.22}$$

Applying Taylor series expansions to Eq. (2.22), the terms $\dot{Q}_{x+dx}$, $\dot{Q}_{y+dy}$ and $\dot{Q}_{z+dz}$ can be expressed as:

$$\dot{Q}_{x+dx} = \dot{Q}_x + \frac{\partial \dot{Q}_x}{\partial x}dx + (\frac{1}{2!}\frac{\partial^2 \dot{Q}_x}{\partial x^2}dx^2 + ...) \tag{2.23}$$

$$\dot{Q}_{y+dy} = \dot{Q}_y + \frac{\partial \dot{Q}_y}{\partial y}dy + \mathscr{O} \tag{2.24}$$

$$\dot{Q}_{z+dz} = \dot{Q}_z + \frac{\partial \dot{Q}_z}{\partial z}dz + \mathscr{O} \tag{2.25}$$

Neglecting terms with orders > 2 $\mathscr{O}$ and inserting Eq. (2.23) - (2.25) into Eq. (2.22) and setting the source term $\dot{Q}_s$ to $\dot{q}_s\,dx\,dy\,dz$ leads to

$$\frac{\partial E}{\partial t} = \frac{\partial \dot{Q}_x}{\partial x}dx + \frac{\partial \dot{Q}_y}{\partial y}dy + \frac{\partial \dot{Q}_z}{\partial z}dz + \dot{q}_s\,dx\,dy\,dz \tag{2.26}$$

Furthermore, the heat fluxes of Eq. (2.21) can be written as

$$\dot{Q}_x = -\lambda \, \mathrm{d}y \, \mathrm{d}z \frac{\partial T}{\partial x} \tag{2.27}$$

$$\dot{Q}_y = -\lambda \, \mathrm{d}x \, \mathrm{d}z \frac{\partial T}{\partial y} \tag{2.28}$$

$$\dot{Q}_z = -\lambda \, \mathrm{d}x \, \mathrm{d}y \frac{\partial T}{\partial z} \tag{2.29}$$

The energy E can be expressed as function of temperature:

$$E = \rho \, \mathrm{d}x \, \mathrm{d}y \, \mathrm{d}z \, c \, T, \tag{2.30}$$

where ρ is the density of the medium and c its specific heat capacity.

By setting Eq. (2.27) to (2.29) and the derivative of Eq. (2.30) with respect to time t into Eq. (2.26), the general form of the heat conduction equation is obtained:

$$\rho \, c \frac{\partial T}{\partial t} = \nabla \bullet (\lambda \nabla T) + \dot{q}_s \tag{2.31}$$

The source term $\dot{q}_s$ in Eq. (2.31) is expressed as volume source term. For many practical applications, the temperature dependency of the thermal conductivity λ can be neglected and Eq. (2.31) simplifies to the general heat conduction equation with constant thermal conductivity:

$$\frac{\partial T}{\partial t} = a \Delta T + \frac{1}{\lambda} \dot{q}_s, \tag{2.32}$$

where $a = \lambda / (\rho \, c)$ is the thermal diffusivity and Δ the Laplace operator [2]. If no internal heat is generated, Eq. (2.32) reduces to the transient heat conduction equation with no sources and constant thermal conductivity (Eq. (2.33)). This equation can be used to calculate the temperature field in a three-dimensional body that is free of heat sources.

$$\frac{\partial T}{\partial t} = a \Delta T \tag{2.33}$$

For (1D) problems, Eq. (2.33) simplifies to the one-dimensional transient heat conduction equation (1D transient HCE):

$$\frac{\partial T}{\partial t} = a \frac{\partial^2 T}{\partial x^2} \tag{2.34}$$

[2] $\Delta = \frac{\partial^2}{\partial x^2} + \frac{\partial^2}{\partial y^2} + \frac{\partial^2}{\partial z^2}$ Laplace operator

Considering a steady-state solution, Eq. (2.33) reduces to the Laplace equation

$$\Delta T = 0. \tag{2.35}$$

2.3.3 Solution procedures for the 1D transient HCE

The 1D transient heat conduction equation (Eq. (2.34)) can be solved analytically or numerically. Analytical solutions are limited to simple geometries and boundary conditions whereas numerical solutions can be obtained for more complex situations (Çengel and Ghajar, 2015). Analytical solutions can be found by the method of separation of variables for instance. Another possibility to solve the 1D transient HCE is to use Fourier- or Laplace transformation to transform the equation into the frequency domain. In doing so, the partial differential equation (PDE) is transformed to an ordinary differential equation (ODE) that is based on the principle of superposition of different frequencies (Baehr and Stephan, 2008). The resulting ODE can be solved using standard procedures. Since the solution is based on the principle of superposition, the original PDE must be linear, which means that it has a constant thermal diffusivity. Here, the frequency domain solution by the Fourier transform will be described and applied. An extensive collection of analytical solutions can be found in Carslaw and Jaeger (1986).

There are different ways for the numerical implementation, such as the finite difference method, the finite element method or the control volume method. Finite differences replace the derivatives of the PDE by discretised versions using a discretisation in space and time (Çengel and Ghajar, 2015). The variables are considered to exist only at the grid points (Tannehill *et al.*, 1997). The method of finite elements approximates the solution of the PDE using shape (polynomial) functions. The space is divided into elements and the shape function approximates the solution inside the element and the equations are balanced at the nodes (Bathe, 1996). The control volume method results in the same set of algebraical equations regarding the 1D transient HCE (Çengel and Ghajar, 2015).

In the following, the frequency domain solution by Fourier transformation is explained in detail. Additionally, numerical implementation of the finite difference solution is shown in Appendix A.2.1.1.

2.3.3.1 Frequency domain solution by Fourier transformation

The one-dimensional transient heat conduction equation (Eq. (2.34)) can be solved by a transformation into the frequency domain. The Fourier transform of Eq. (2.34) is

$$i\,\omega\,\hat{T}(x,\omega) = a\,\frac{\partial^2 \hat{T}(x,\omega)}{\partial x^2} \tag{2.36}$$

where i is the imaginary unit, $\omega = 2\pi/T_h$ is the angular frequency with period T_h of the harmonic and $\hat{T}(x,\omega)$ is the temperature transformed into the frequency domain. This transformation can be done by a fast Fourier transformation (FFT). On the contrary to Eq. (2.34), this is an ordinary differential equation with the general solution

$$\hat{T}(x,\omega) = A(\omega)\exp(-kx) + B(\omega)\exp(kx), \tag{2.37}$$

where $A(\omega)$ and $B(\omega)$ are complex constants that can be determined with the boundary conditions. The complex auxiliary quantity k is defined by

$$k = \sqrt{\frac{i\omega}{a}} = (1+i)\sqrt{\frac{\omega}{2a}}. \tag{2.38}$$

Consider a 1D slab with length L and $\hat{T}(x=0,\omega) = \hat{T}_{b,l}(\omega)$ as left boundary condition and $\hat{T}(x=L,\omega) = \hat{T}_{b,r}(\omega)$ as right boundary condition (Fig. 2.25a). By using Eq. (2.37), the two constants $A(\omega)$ and $B(\omega)$ can be determined to

$$\begin{pmatrix} A \\ B \end{pmatrix} = \begin{bmatrix} \dfrac{1}{\exp(2kL)-1} + 1 & -\dfrac{1}{2\sinh(kL)} \\ -\dfrac{1}{\exp(2kL)-1} & \dfrac{1}{2\sinh(kL)} \end{bmatrix} \begin{pmatrix} \hat{T}_{b,l}(\omega) \\ \hat{T}_{b,r}(\omega) \end{pmatrix}. \tag{2.39}$$

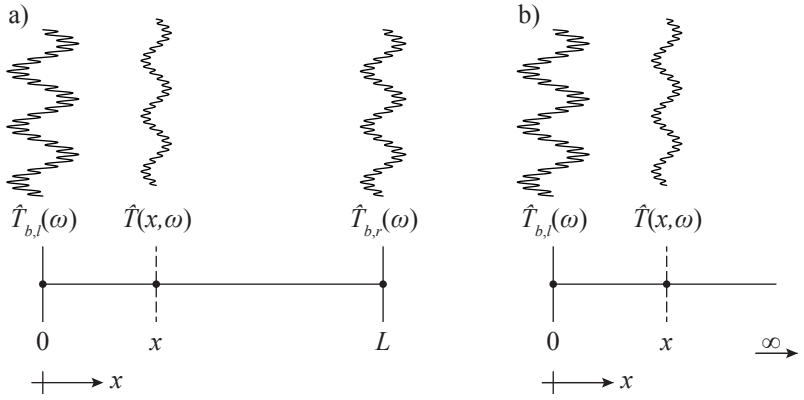

Fig. 2.25 a) 1D slab, b) semi-infinite space.

Inserting Eq. (2.39) into Eq. (2.37) leads to the solution of the temperature field $\hat{T}(x,\omega)$ in an one-dimensional slab with boundary temperatures $\hat{T}_{b,l}(\omega)$ and $\hat{T}_{b,r}(\omega)$

$$\hat{T}(x,\omega) = \frac{1}{\sinh(kL)}\left(\sinh(k(L-x)\,\hat{T}_{b,l}(\omega) + \sinh(kx)\,\hat{T}_{b,r}(\omega)\right) \tag{2.40}$$

In a semi-infinite space (Fig. 2.25b) the constants can be determined with the boundary conditions $\hat{T}(x=0,\omega)=\hat{T}_b(\omega)$ and $\hat{T}(x=\infty,\omega)=0$ which leads to the solution of the temperature field in a semi-infinite slab

$$\hat{T}(x,\omega)=\hat{T}_b(\omega)\exp(-kx) \tag{2.41}$$

For the semi-infinite slab, it can be shown that the measurable penetration of low frequencies is higher as for fast ones (see Appendix A.2.2.2).

Properties of complex numbers

The form of Eq. (2.41) can be modified as follows:

$$\begin{aligned}\hat{T}(x,\omega) &= \hat{T}_b(\omega)\exp(-kx) = \hat{T}_b(\omega)\exp\left(-(1+i)\sqrt{\frac{\omega}{2a}}x\right) \\ &= \hat{T}_b(\omega)\exp\left(-\sqrt{\frac{\omega}{2a}}x\right)\exp\left(-i\sqrt{\frac{\omega}{2a}}x\right)\end{aligned} \tag{2.42}$$

According to the exponential form for complex numbers $z=r\exp(i\phi)$, where r is the absolute value of the complex number z and ϕ is the argument (angle) (Fig. 2.26a), one obtains

$$r = \exp\left(-\sqrt{\frac{\omega}{2a}}x\right) \tag{2.43}$$

$$\phi = \sqrt{\frac{\omega}{2a}}x \tag{2.44}$$

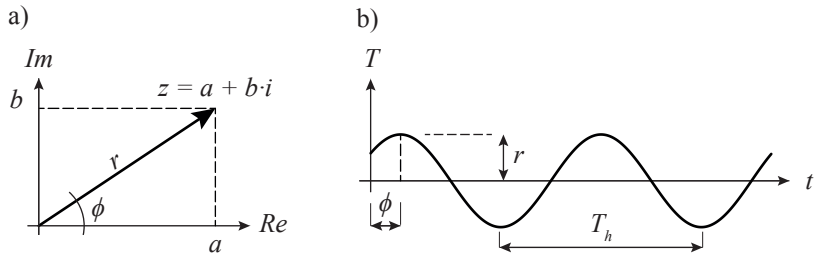

Fig. 2.26 Properties of complex numbers, a) absolute value r and argument ϕ; b) harmonic with amplitude r, phase shift ϕ and period T_h .

The absolute value r represents the amplitude of the harmonic with frequency ω and the argument ϕ the phase shift. Thus, the properties of the harmonics can easily be obtained

from the complex temperatures. Furthermore, it can be shown that the propagation velocity of the signals is frequency-dependent (see Appendix A.2.2.1).

Mean temperature and temperature difference in the frequency domain

In the frequency domain, the mean temperature T_m and the temperature difference T_d read:

$$\hat{T}_m(\omega) = \frac{1}{L}\int_0^L \hat{T}(x,\omega)\mathrm{d}x \tag{2.45}$$

$$\hat{T}_d(\omega) = \frac{12}{L^2}\int_0^L \hat{T}(x,\omega)\,(x-L/2)\mathrm{d}x \tag{2.46}$$

By substitution of Eq. (2.40) in Eq. (2.45) and integration along the slab, T_m can be directly calculated from the two boundary temperatures $\hat{T}_{b,l}$ and $\widehat{T}_{b,r}$

$$\hat{T}_m(\omega) = \frac{2}{kL}\tanh\left(\frac{kL}{2}\right)\left(\frac{\hat{T}_{b,l}+\hat{T}_{b,r}}{2}\right) = G_m(\omega)\left(\frac{\hat{T}_{b,l}+\hat{T}_{b,r}}{2}\right) \tag{2.47}$$

with

$$G_m(\omega) = \frac{2}{kL}\tanh\left(\frac{kL}{2}\right) \tag{2.48}$$

The same can be done by substitution of Eq. (2.40) in Eq. (2.46)

$$\hat{T}_d(\omega) = \frac{6}{(kL)^2}\left(\frac{kL}{2\tanh\left(\frac{kL}{2}\right)}-1\right)\left(\frac{\hat{T}_{b,r}-\hat{T}_{b,l}}{2}\right) = G_d(\omega)\left(\frac{\hat{T}_{b,r}-\hat{T}_{b,l}}{2}\right) \tag{2.49}$$

with

$$G_d(\omega) = \frac{6}{(kL)^2}\left(\frac{kL}{2\tanh\left(\frac{kL}{2}\right)}-1\right) \tag{2.50}$$

From Eq. (2.47) it follows that the mean temperature depends on the average of the two boundary values and from Eq. (2.49) that the temperature difference depends on the difference of the boundary values (Weber *et al.*, 2010). The transfer functions $G_m(\omega)$ and $G_d(\omega)$ contain the information of the thickness L, the frequency ω and the thermal diffusivity a and do not depend on the boundary temperatures. They can be seen as a kind of transfer function from the boundary temperatures to the mean temperature and the temperature difference.

2.3.4 Inverse heat conduction analysis

By estimating the surface temperatures with inverse heat conduction analysis, the problem of uncertainties related to convection and solar radiation can be overcome. To obtain accurate results, temperature information should be available not too far from the surface (Amberg, 2009).

In Section 2.3.3, two procedures to determine the temperature field inside a solid body with given boundary temperatures were presented. However, the temperature field in the boundary regions cannot be determined with these procedures, but with inverse heat conduction analysis. Since the solution of an inverse heat conduction problem in not unique and not stable under small changes, it is a mathematically ill-conditioned problem (Özisik and Orlande, 2000). In this section, the stability of the inverse heat conduction analysis is briefly discussed first. Then, a solution procedure in the frequency domain is presented.

2.3.4.1 Stability of inverse HC

Due to the diffusivity of the heat flow, the amplitudes of the temperature signals are damped exponentially inside the solid body. Higher frequencies are damped within a shorter distance from the surface than lower frequencies, which can be verified with Eq. (2.41). At a certain depth, only low frequencies can be recorded with thermometers since the amplitudes of the high frequencies are smaller than the measurement noise (Obernhuber and Perner, 2005). Suppose a semi-infinite concrete body with a thermometer placed 1.5 m away from the boundary. On the boundary, a temperature with a frequency that has a daily period and an amplitude of 10 °C is applied. The total daily temperature variation is damped to 0.02 °C at the measurement location (by assuming a mean value of $a = 0.15$ m^2/d for the thermal diffusivity). Compared to measurement errors of $\pm$ 0.2 °C, this can be neglected. If these measurements were used for an inverse analysis, physically meaningless results would be expected. Doing an inverse calculation, this would mean that measurement noise would be amplified by a factor of 1000 to $\pm$ 200 °C on the boundary. A general problem of inverse heat conduction analysis is that the noise is magnified at the surface (Raynaud and Beck, 1988). Therefore, methods to stabilise the influence of the measurement noise are necessary. Extensive research in this field was carried out in the 1980's (e.g. Raynaud and Bransier (1986); Raynaud and Beck (1988)).

2.3.4.2 Frequency domain solution for 1D transient HCE

Obernhuber and Perner (2005) and Weber *et al.* (2010) describe a solution for the inverse heat conduction problem in the frequency domain and applied it with success to concrete dams. The present section follows these two publications. The properties of the inverse

heat conduction problem can nicely be shown on a simple example of a semi-infinite space (Fig. 2.27b) and then adapted to the case of a 1D slab with two thermometers next to each surface (Fig. 2.27a).

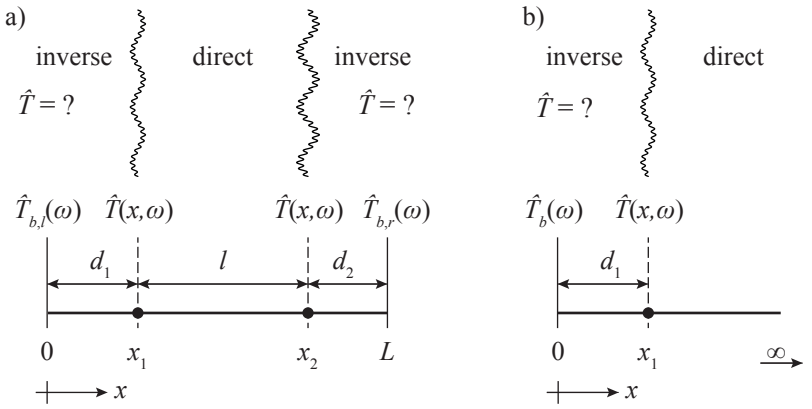

Fig. 2.27 a) One dimensional slab with two thermometers at locations x_1 and x_2 b) semi-infinite slab with thermometer at location x_1 .

Semi-infinite space

Considering the situation depicted in Fig. 2.27b, Eq. (2.41) results in

$$\hat{T}(x_1,\omega) = \hat{T}_b(\omega)\exp(-kx_1) = \hat{T}_b(\omega)\,G(\omega), \tag{2.51}$$

where $G = \exp(-kx_1)$ is the transfer function. Inverse heat conduction analysis means that Eq. (2.51) needs to be rearranged and the inverse G^{-1} estimated:

$$\hat{T}_b(\omega) = \hat{T}(x_1,\omega)\exp(kx_1) = \hat{T}(x_1,\omega)\exp\left(\sqrt{\frac{i\omega}{a}}x_1\right) \tag{2.52}$$

From Eq. (2.52) it follows that the solution is unbounded for high frequencies ω. This is not only a theoretical but also a numerical problem. Thus, Obernhuber and Perner (2005) and Weber *et al.* (2010) make use of a low pass filter that damps high frequencies. They use a Gaussian distribution as mollifier function m_γ (Eq. (2.53)) that can be implemented as a convolution integral in the time domain. The regularisation parameter γ defines the width of the pulse and therefore the smoothing.

$$m_\gamma(t) = \frac{1}{\gamma\sqrt{2\pi}}\exp\left(-\frac{t^2}{2\gamma^2}\right) \tag{2.53}$$

In the frequency domain, a convolution integral corresponds to a multiplication of the Fourier transformed mollifier function $\hat{m}_\gamma$ (Eq. (2.55)) with the temperature measurements:

$$\hat{T}_{b,\gamma}(\omega) = \hat{T}_b(\omega)\hat{m}_\gamma(\omega) \tag{2.54}$$

$$\hat{m}_\gamma(\omega) = \exp\left(-\frac{\omega^2\gamma^2}{2}\right) \tag{2.55}$$

In Fig. 2.28, the mollifier function in the time and in the frequency domain is presented for different values of γ.

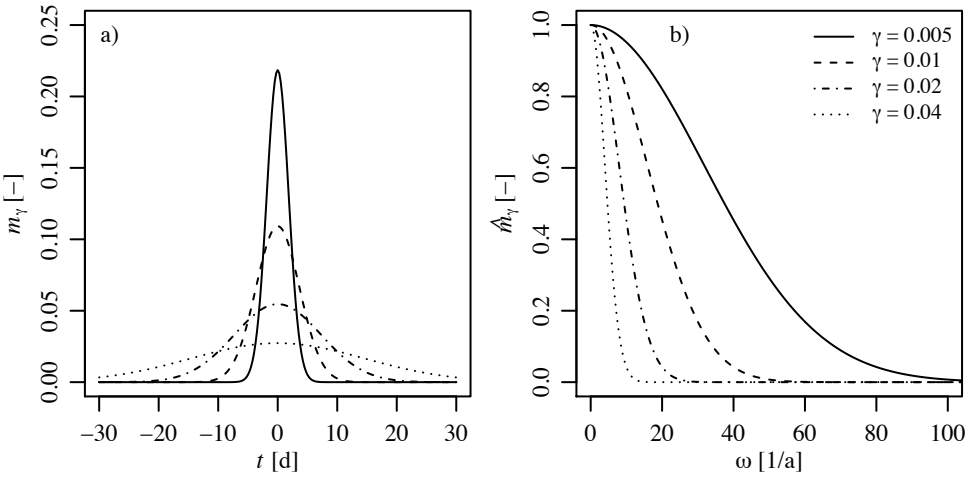

Fig. 2.28 Mollifier function for different regularisation parameters γ for a) time domain and b) frequency domain (adapted from Weber *et al.*, 2010).

In the time domain (Fig. 2.28a), the regularisation parameter γ defines the pulse width and therefore the smoothing. Low values lead to a narrow Gaussian distribution and consequently to less smoothing then high values. The same can be observed in the frequency domain (Fig. 2.28b). Since the mollifier function is multiplied with the corresponding frequencies, all high frequencies are wiped out.

Combining Eq. (2.52) and (2.55) leads to Eq. (2.56) that can be used to calculate the surface temperature from smoothed measurement values of an inner thermometer.

$$\hat{T}_{b,\gamma}(\omega) = \hat{T}(x_1,\omega)G^{-1}\hat{m}_\gamma(\omega) \tag{2.56}$$

1D slab with two thermometers next to each surface

The same analysis as for the semi-infinite space can be carried out for the slab with two thermometers next to each boundary (Fig. 2.27a). This results in a matrix for the inverse transfer function G^{-1}:

$$G^{-1} = \frac{1}{\sinh(k\,l)} \begin{bmatrix} \sinh(k\,(l+d_1)) & -\sinh(k\,d_1) \\ -\sinh(k\,d_2) & \sinh(k\,(l+d_2)) \end{bmatrix} \tag{2.57}$$

The two boundary temperatures $\hat{T}_{b,l,\gamma}(\omega)$ and $\hat{T}_{b,r,\gamma}(\omega)$ smoothed with the mollifier $\hat{m}_\gamma(\omega)$ read:

$$\begin{pmatrix} \hat{T}_{b,l,\gamma}(\omega) \\ \hat{T}_{b,r,\gamma}(\omega) \end{pmatrix} = \hat{m}_\gamma(\omega)\, G^{-1} \begin{pmatrix} \hat{T}_{x1}(\omega) \\ \hat{T}_{x2}(\omega) \end{pmatrix} \tag{2.58}$$

The choice of the regularisation parameter depends on the frequency of measurement data recording and the thermometer location. Therefore, no general suggestion can be given and each case must be assumed individually. Weber *et al.* (2010) state that $\gamma = 0.1$ works well for $d = 0.20$ m and 0.35 m, while $\gamma = 1.5$ works well for $d = 1.50$ m.

2.3.5 Convection

The principle of convection along a solid body is shown in Fig. 2.29. The surface temperature of the solid body is T_b and the temperature of the fluid away from the surface is $T_{fl,\infty}$. At the surface, the fluid temperature is equal to the temperature of the solid body (Çengel and Ghajar, 2015). Between the boundary temperature and the fluid temperature, a nonlinear temperature profile that depends on the flow profile appears. The flow field of the fluid has a laminar boundary layer, which has parallel stream lines (Poulikakos, 2011). The convection consists of two processes. First, the heat is transferred by conduction through the laminar boundary layer and then the motion of the fluid replaces the hot fluid near the surface by cold one (Poulikakos, 2011; Çengel and Ghajar, 2015).

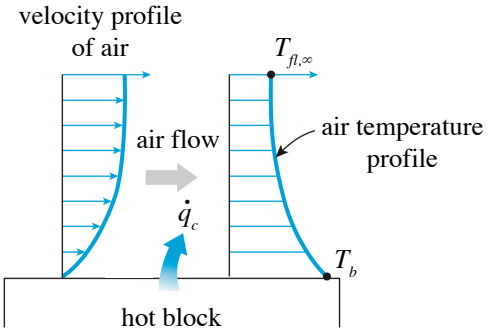

Fig. 2.29 Heat transfer by convection (adapted from Çengel and Ghajar, 2015).

Two different types of convection are distinguished. When the fluid motion is caused by fans, pumps or wind, it is called forced convection. Natural convection is caused by density currents in the fluid and occurs on vertical oriented surfaces. The rate of the convective heat transfer $\dot{q}_c$ is observed to be proportional to the temperature difference

between T_b and $T_{fl,\infty}$ and can be expressed by Newton's law of cooling (Çengel and Ghajar, 2015).

$$\dot{q}_c = \alpha_c(T_b - T_{fl,\infty}) \tag{2.59}$$

The convection heat transfer coefficient α_c is an empirical parameter and not a thermodynamic property (Moran and Shapiro, 2010). It depends on the fluid motion, the properties of the fluid, the surface geometry (dimension, orientation and roughness) and the phase transition (Poulikakos, 2011).

2.3.6 Radiation

The energy emitted by electromagnetic waves between a body with boundary temperature T_b and a surrounding air temperature T_{air} can be estimated by:

$$\dot{q}_{emit} = -\varepsilon\sigma(T_{air}^4 - T_b^4) \tag{2.60}$$

where $\sigma = 5.670 \cdot 10^{-8}\ W/m^2K$ is the Stefan-Boltzmann constant and ε the emissivity of the surface ($\varepsilon = 1$ corresponds to a black body) (Léger *et al.*, 1993; Çengel and Ghajar, 2015). In Eq. (2.60), the unit of the temperatures is Kelvin.

2.3.7 Solar radiation

The energy of the sun comes in the form of electromagnetic waves. The energy that reaches the atmosphere is called solar irradiance and has a power of 1373 W/m^2. In the atmosphere, a part of the radiation is scattered. Hence, beam radiation and diffusive radiation can be distinguished (Çengel and Ghajar, 2015). In addition, the beam radiation can further be classified into sky diffusive radiation and ground diffusive radiation (Léger *et al.*, 1993). The proportion depends on the weather, e.g. on a clear day only 10% are diffusive radiation and on a cloudy day up to 100% (Çengel and Ghajar, 2015). One part of the solar radiation I_t that arrives at the earth's surface is absorbed by objects and the other part is reflected. The solar absorptivity α_a defines the amount of absorbed energy $\dot{q}_s$ as:

$$\dot{q}_s = -\alpha_a I_t \tag{2.61}$$

2.3.8 Heat transfer analysis of concrete dams

In dam engineering, heat transfer analysis is applied for three different purposes: (i) for the design of the structure, (ii) the analysis of hydration heat and (iii) the structural monitoring. For the structural design, temperature is expressed as a load case. Historic readings

of the air temperature can be used as boundary condition. If no readings are available, a sinusoidal function can be used instead (Léger *et al.*, 1993). Today, finite element models that are used for the analysis of the structural safety are also used for the heat conduction analysis. Before construction, an analysis of hydration heat has to be carried out (see Section 2.1.2.2). Based on this analysis, the progress of concreting and a possible cooling is designed. In these calculations, the hydration heat is considered as source term. In the case of dam engineering, the thermal field inside the concrete body is of interest. Due to the fact that the thermometers are usually grouped on different levels, one-dimensional heat conduction analysis is performed in many cases. In the following, some approaches that are used in the scope of dam behaviour analysis are briefly discussed.

2.3.8.1 Conduction

Léger and Leclerc (2007) present a frequency domain solution for the one-dimensional direct- and indirect heat conduction analysis in a concrete dam cross-section. They suggest stabilising the inverse heat conduction analysis by cutting the frequencies that have eigenvalues > 8 in the thermal impedance matrix. The performance of this approach is shown in a case study of the Schlegeis arch dam data. Their approach is implemented in the software TADAM that is freely available (Leclerc and Léger, 2004).

A similar approach, also in the frequency domain, was proposed by Obernhuber and Perner (2005) and Weber *et al.* (2010). Instead stabilising by removing large eigenvalues, a mollifier function is used. This approach is explained in Section 2.3.4.2.

Léger and Seydou (2009) compare a one-dimensional heat conduction analysis performed with the software TADAM (Leclerc and Léger, 2004) with the results of a 2D FE-solution for a gravity dam. The results are in very good agreement with the measurement data. Nevertheless, Léger and Seydou (2009) state to take caution since the presence of galleries can disturb the 1D results and a 2D calculation might be necessary.

Amberg (2009) used an explicit finite difference scheme that is not stabilised to extrapolate the surface temperatures from inner readings. Therefore, he proposes to do this analysis only for thermometers that are installed close to the boundary.

Bofang (2014) gives a good overview of heat conduction analysis for hydration heat due to mass concrete.

2.3.8.2 Convection

For dams, the conductivity between the air temperature and the concrete surface mainly depends on the wind velocity. For the upstream surface that is below the water level, the surface temperature can be assumed to be the water temperature (Amberg, 2003). He also mentions that convection is of secondary importance for thick dams. This statement is supported by the analysis of Tatin *et al.* (2013a). The convection heat transfer coefficient

α is in the order of $15 \div 45$ W/(m^2 K) (Stucky and Derron, 1957). Instead of considering a convective boundary condition, they proposed to add an additional fictitious concrete part of $0.04 \div 0.17$ m to the dam body to consider convection.

2.3.8.3 Radiation

Since the difference of the absolute temperature (in Kelvin) between the boundary and the air temperature is small, radiation is not significant in the case of concrete dams (Léger *et al.*, 1993).

2.3.8.4 Solar radiation

According to Amberg (2003) and Tatin *et al.* (2013a), the solar radiation has a significant influence on the concrete temperature of dams. The solar radiation that reaches the dam surface depends on the site latitude, the orientation of the surface, the slope of the surface, the cloud cover and the topography that may cause mountain effect (Léger *et al.*, 1993). In the case of arch dams, the geometry is variable and thus also the solar radiation over the surface. As the temperature, the solar radiation follows a seasonal variation (Léger *et al.*, 1993). Since the solar radiation depends not only on the geometry but also on the weather conditions (cloud cover), it is measured at certain weather stations. Unfortunately, the solar radiation is measured for horizontal surfaces and thus transformation equations must be used (Léger *et al.*, 1993). Due to all these different influences, the implementation of solar radiation is complex. A well described implementation for arch dams can be found in Santillán *et al.* (2014).

For preliminary analysis, according to the curves published in Copen *et al.* (1977) can be used to estimate the mean annual increase in surface temperature (compared to the air temperature) due to solar radiation. The values are provided as a function of the latitude, the angle of the surface and the orientation.

2.4 Statistics

The goal of this section is to explain the basics of statistics that are used in the field of dam behaviour analysis. These are mainly multiple linear regression models with related analysis tools. Regression analysis is a statistical technique to investigate and model the relationship between variables. There are applications in almost every discipline in science and engineering and it might be the most used statistical tool (Montgomery *et al.*, 2012). The statistics are explained from an engineering point of view based on an example. If the reader is interested in the theory, the derivations and the proofs, the standard works of Montgomery *et al.* (2012) or James *et al.* (2013) are suggested.

The chapter follows more or less the workflow for the regression model building process (Fig. 2.30). At the beginning, the basics of linear regression models are introduced and based on this, multiple linear regression models are discussed. Moreover, measures for the goodness of fit and tools for the model adequacy checking to assess the models are introduced. Afterwards, the model validation, which is the application of the model to new data, is explained. Furthermore, there are two chapters where autocorrelation and multicollinearity are discussed. At the end of this section, some special statistical methods that go beyond the scope of linear models such as artificial neural networks are introduced.

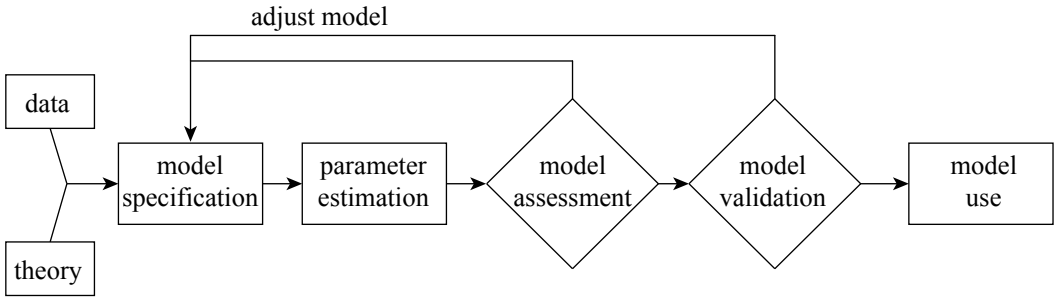

Fig. 2.30 Workflow for model building process (adapted from Montgomery *et al.*, 2012).

The content of this section is mainly based on the works Montgomery *et al.* (2012), James *et al.* (2013) and Dettling (2015).

2.4.1 Linear regression analysis

2.4.1.1 Illustrative example

In this section, the basics of linear regression analysis are introduced and illustrated by a case study of drainage flow monitoring of an arch dam in Switzerland. At this dam, the total drainage flow at the bottom Q_{tot} is measured monthly. Additionally, the water level is recorded. A description of the dam and the data is given in Appendix A.5.5. The amount of drainage flow is monitored because it is an indicator for dam safety. An increasing amount of drainage flow could indicate a damage of the grout curtain, while a

decreasing amount indicates a blockage of the drainage system (BWG, 2002). To quantify if the amount of the drainage flow is on a normal level, it must be somehow related to the environmental conditions. It seems to be obvious that the water level might play a major role and that there might be some further effects such as the season, snow melt, rain fall and possible irreversible changes depending on the age of the structure. Unfortunately, it is not clear which of these variables have a significant influence on Q_{tot}. The data from 2000 - 2009 is used for the calibration of the model coefficients and the data from 2010 - 2013 for model validation.

In Fig. 2.31, the scatter diagram of the drainage flow Q_{tot} versus the third power of the normalised water level h^3 is shown. The scatter shows a linear relationship between the variables. Therefore, the drainage flow could be modelled as a linear function of the scaled water level h^3, which would be a simple linear regression (SLR) model. SLR are explained in Section 2.4.1.2. As described above, other variables might also play a role. Including more than two variables leads to a multiple linear regression (MLR) model. They are presented in Section. 2.4.1.3.

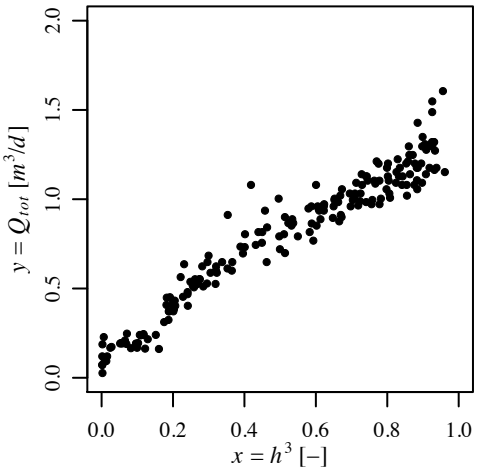

Fig. 2.31 Scatter plot of the drainage flow Q_{tot} versus the scaled water level h^3.

2.4.1.2 Simple linear regression

The relationship between an independent variable x and dependent variable y can be approximated with the following linear relationship:

$$y = \beta_0 + \beta_1 x + \varepsilon \tag{2.62}$$

The intercept β_0 and the slope β_1 are the model parameters and the error term ε represents the difference between the observations of y and the linear approximation $y = \beta_0 + \beta_1 x$. The error term can be considered as a statistical error that accounts for the stochastic

variation of the process and error of the model. If the independent variable is assumed to be constant, the error depends only on the properties of y. The error term ε can be assumed to be normally distributed with mean 0 and a variance σ^2 that determines the variability or noise in the response variable y (Montgomery *et al.*, 2012). The values of the model parameters β_0 and β_1 are not known in real applications but they can be estimated from an observed data set with n observations by regression analysis. The so called fitted model is

$$\hat{y} = \hat{\beta}_0 + \hat{\beta}_1 x \tag{2.63}$$

The hat (ˆ) symbol denotes that coefficients $\hat{\beta}_i$ are estimates of the true coefficients β_i and $\hat{y}$ stands for the estimates of y. The differences $e = y - \hat{y}$ between the observed values and its estimates are called residuals. In statistics, the following nomenclature is commonly used:

- x = regressor or predictor variable
- y = response variable
- $\hat{\beta}_i$ = regression coefficients

Estimation of the regression coefficients

The regression coefficients β_0 and β_1 are commonly estimated by the least square approach. In this approach, the sum of the squared residuals is minimised. The so called residual sum of squares SS_{res} can be written in function of the intercept β_0 and the slope β_1:

$$SS_{res}(\beta_0, \beta_1) = \sum_{i=1}^{n} e_i^2 = \sum_{i=1}^{n} (y_i - \beta_0 - \beta_1 x_i)^2 \tag{2.64}$$

To obtain the least squares estimate of the model parameters β_i, SS_{res} must be minimised. This is done by differentiating Eq. (2.64) with respect to β_0 and β_1. This leads to the least squares estimators for the simple linear regression model

$$\hat{\beta}_0 = \bar{y} - \hat{\beta}_1 \bar{x} \tag{2.65}$$

$$\hat{\beta}_1 = \frac{\sum_{i=1}^{n} y_i (x_i - \bar{x})^2}{\sum_{i=1}^{n} (x_i - \bar{x})^2}, \tag{2.66}$$

where $\bar{x}$ and $\bar{y}$ are the mean values of all x_i and y_i, respectively. There also exist other estimators than the least squares, as the maximum likelihood estimation for example. A description about this estimator can be found in Montgomery *et al.* (2012).

The variance σ^2 can be estimated from the residual sum of squares SS_{res}. Since two parameters are estimated, SS_{res} has $n-2$ degrees of freedom.

$$MS_{res} = \hat{\sigma}^2 = \frac{SS_{res}}{n-2} \tag{2.67}$$

The estimated variance $\hat{\sigma}^2$ is also called the residual mean square MS_{res}. Due to the fact that MS_{res} depends on the residuals of the model, its usefulness is reduced if the model assumptions are violated, e.g. normal distribution of errors or non-correlated errors (Montgomery *et al.*, 2012). The assumptions are listed in the following and the detection of potential violations is treated in Section 2.4.1.6.

Assumptions for least squares

There are several assumptions behind the least squares approach. The theoretical background can be found in James *et al.* (2013) or Montgomery *et al.* (2012). These assumptions are (Dettling, 2015):

- the expected value of the error is 0 ($E(\varepsilon_i) = 0$)
- the variance of the error is σ^2 ($\text{Var}(\varepsilon_i) = \sigma^2$)
- the errors are not correlated ($\text{Cov}(\varepsilon_i, \varepsilon_j) = 0$ for $i \neq j$)
- the errors are (at least) normally distributed ($\varepsilon_i \sim N(0, \sigma^2)$)

A single value for $E(\varepsilon_i)$ is not 0 by definition but for a large number of data $E(\varepsilon_i)$ should converge to 0. After developing a model, these assumptions must be checked. This is mainly done by the analysis of the residuals (see Section 2.4.1.6).

Properties of least squares

The least square estimators $\hat{\beta}_0$ and $\hat{\beta}_1$ are unbiased estimators of the model parameters β_0 and β_1. This means that for a specific data set the estimates can be over- or underestimated, but in average for a large number of data sets, $\hat{\beta}_i$ would be equal to β_i. Therefore, an unbiased estimator does not systematically over- or underestimate the true model parameters. Under assumption of $E(\varepsilon_i) = 0$, $\text{Var}(\varepsilon_i) = \sigma^2$ this can be proofed by the Gauss-Markov theorem (see Montgomery *et al.*, 2012). Based on this theorem it can also be stated that a least square estimator has minimal variance. Therefore, it can be said that the least squares estimators are the estimators that lead to minimal variance. Furthermore, based on Eq. (2.65) and (2.66) it follows that the resulting model always goes through the centroid point ($\bar{x}$, $\bar{y}$) of the regression line.

Extrapolation

Regression analysis is only an approximation of the real behaviour that can be expressed by physical laws. Fig. 2.32 shows an example of a true relationship and a linear approximation, where data between x_1 and x_2 was available only for fitting. The linear relationship seems to approximate the true relation well within this range. Generally, linear regression models are valid within the range of the observed regressor values (Montgomery *et al.*,

2012). Caution must be paid to extrapolations. In the example of Fig. 2.32, extrapolation leads to a considerable overestimation of the true relationship between x_2 and x_3.

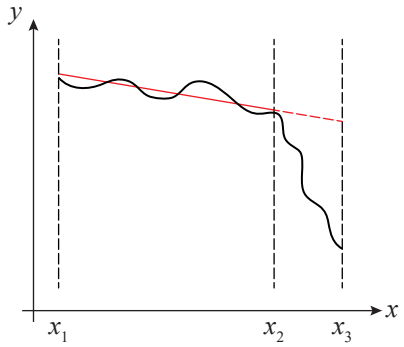

Fig. 2.32 Comparison of a true functional relationship (black) and a linear approximation (red) (adapted from Montgomery *et al.*, 2012).

Drainage flow SLR example

For the drainage flow example, the estimation of the regression coefficients leads to the following SLR model:

$$\hat{Q}_{tot} = 0.165 + 1.22\,h^3 \tag{2.68}$$

The error was estimated to $\hat{\sigma} = 0.093$ which corresponds to an error variance of $\hat{\sigma}^2 = 0.0087$. In Fig. 2.33, the fitted model given by Eq. (2.68) is shown by a straight line. In addition, the error variance is shown by a normal distribution. The 95% interval (corresponding to $2\hat{\sigma}$) is marked with dashed lines. In addition, the time series of the measured values Q_{tot} and the fitted values $\hat{Q}_{tot}$ are shown in Fig. 2.34. Generally, a good agreement is recognisable.

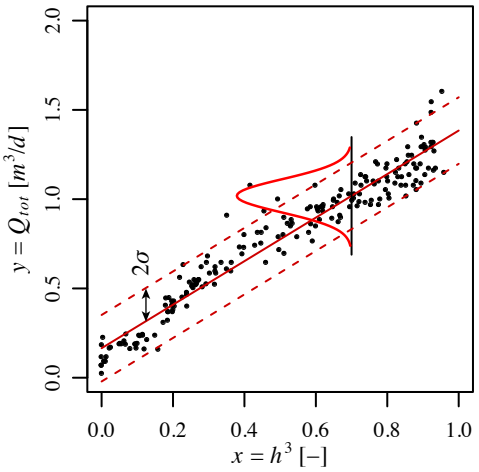

Fig. 2.33 Linear relationship between the predictor variable h^3 and the response variable Q_{tot}. The error variance is shown by a normal distribution and the corresponding 95% interval by dashed lines.

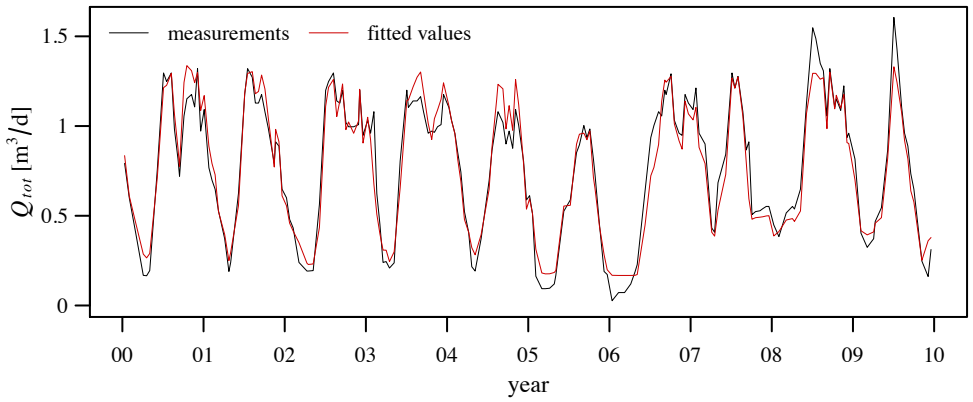

Fig. 2.34 Time series for the measurement values and the fitted values for the SLR example.

2.4.1.3 Multiple linear regression

Regression models with more than one regressor variable are called multiple linear regression (MLR) models. Linear stands for the response, which is a linear function of the regressor variables x_j. As a consequence, MLR models can be solved with the methods of linear algebra. An MLR model with k regressor variables reads:

$$y = \beta_0 + \beta_1 x_1 + \beta_2 x_2 + \ldots + \beta_k x_k + \varepsilon \tag{2.69}$$

and in matrix notation,

$$\mathbf{y} = \mathbf{X}\beta + \varepsilon \tag{2.70}$$

Estimation of regression coefficients

As for the simple linear regression models, the coefficients are usually determined by the method of least squares. The residual sum of squares in matrix notation can be written as

$$SS_{res}(\beta) = \sum_{i=1}^{n} \varepsilon_i^2 = \varepsilon'\varepsilon = (\mathbf{y} - \mathbf{X}\beta)'(\mathbf{y} - \mathbf{X}\beta) \tag{2.71}$$

Differentiating Eq. (2.71) with respect to all β_i leads to the least squares estimator in matrix notation

$$\hat{\beta} = (\mathbf{X}'\mathbf{X})^{-1}\mathbf{X}'y \tag{2.72}$$

The residual sum of squares SS_{res} has $n-p$ degrees of freedom, where p is the number of parameters β_i that are included in the model. The intercept β_0 counts for p as far as included in the model. The total variance $\hat{\sigma}^2$ and the residual mean square MS_{res} can be obtained by

$$MS_{res} = \hat{\sigma}^2 = \frac{SS_{res}}{n-p}. \tag{2.73}$$

Based on the total variance $\hat{\sigma}^2$, the standard errors of the individual regression coefficients can be estimated:

$$\mathrm{se}(\beta_i) = \sqrt{\hat{\sigma}^2 C_{ii}} \tag{2.74}$$

where C_{ii} are the diagonal element of the matrix $(\mathbf{X}'\mathbf{X})^{-1}$ corresponding to β_i.

Drainage flow example

Now, the dam operator wants to improve his simple linear regression model for the drainage flow monitoring. In doing so, he adds information by adding polynomial coefficients for the water level h, inserting a sinusoidal function for seasonal effects with the period of one year (this is represented by the seasonal function $S = j\,2\pi/365.25$ where j represents the number of the day in the year) and adding the time of measurement t:

$$Q_{tot} = \beta_0 + \beta_1 h + \beta_2 h^2 + \beta_3 h^3 + \beta_4 \sin(S) + \beta_5 \cos(S) + \beta_6 t + \varepsilon \tag{2.75}$$

Since more than one regressor variable is present, this is an MLR model. The least squares estimation leads to

$$\hat{Q}_{tot} = 0.078 - 1.46h + 3.72h^2 - 1.14h^3 + 0.036\sin(S) - 0.033\cos(S) + 0.012t \quad (2.76)$$

In Fig. 2.35, the time series of the measured values Q_{tot} and the fitted values $\hat{Q}_{tot}$ are shown for the MLR model. Compared to the SLR model (Fig. 2.34), the agreement of the MLR model with the measured values is better for low drainage flows. The error of the MLR model is estimated to $\hat{\sigma} = 0.078$ and the corresponding MS_{Res} to 0.0061, which is lower than for the SLR example.

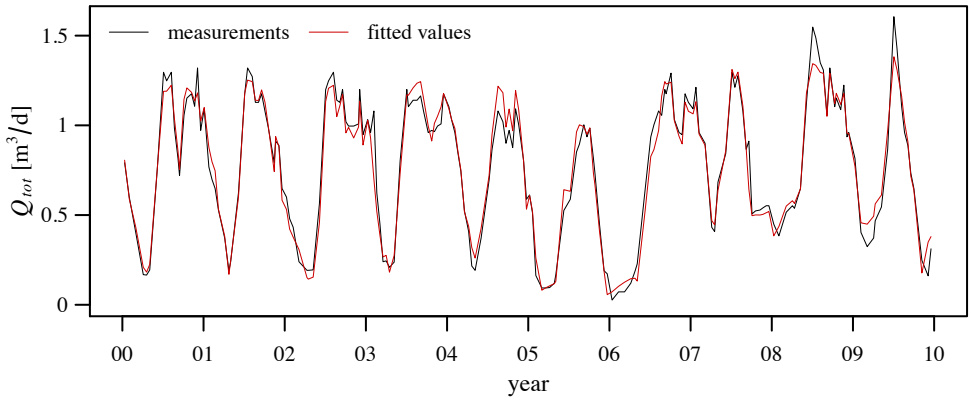

Fig. 2.35 Time series for the measurement values and the fitted values for the MLR example.

2.4.1.4 Assessment of model accuracy

After setting up and fitting a model, it is of interest how good the model fits the data. Typically, two related quantities are used to measure the goodness of fit. One is the residual standard error (*RSE*) that makes a statement in the unit of the predictor variable and the other is the dimensionless coefficient of determination R^2. In addition, the test error and the cross-validation test error can also be used to make a statement about the goodness of fit.

Residual standard error

The residual standard error is an estimate of the standard deviation of the model error ε:

$$RSE = \sqrt{MS_{res}} = \sqrt{\frac{SS_{res}}{n-p}} \quad (2.77)$$

Since the *RSE* has the unit of the response variable y, it is not always clear what values are good and not. It depends on the problem at hand. Therefore, the coefficient of determination can be a good alternative (James *et al.*, 2013).

Coefficient of determination

A quite common approach to measure the goodness of fit is the coefficient of determination R^2 (Eq. (2.78)). It is a measure which portion of the total variance can be explained by the model and which remains stochastic (James *et al.*, 2013). The value of the R^2 lies by definition between 0 and 1. A value of 1 stands for a perfect fit whereas 0 indicates that the model is not able to describe the total variance of the predictor variable at all.

$$R^2 = 1 - \frac{SS_{res}}{SS_t} \tag{2.78}$$

The total sum of squares SS_t is defined by

$$SS_t = \sum_{i=1}^{n} (y_i - \bar{y})^2 \tag{2.79}$$

Applying Eq. (2.78) to the simple linear regression model of the drainage flow example leads to a R^2 value of 0.939. Fig. (2.36) visualises the idea behind the coefficient of determination R^2 of this example. It measures the proportion between the variance of the residuals and the total variance of the response variable.

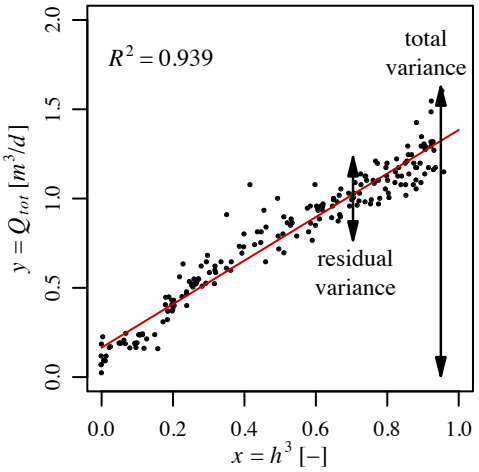

Fig. 2.36 Visualisation of the idea behind the coefficient of determination R^2 for the simple linear regression model of the drainage flow example (adapted from Dettling, 2015).

For multiple linear regression models, also Eq. (2.78) can be applied to calculate the coefficient of determination R^2. Due to the fact that adding predictors to an MLR model leads to a lower residual sum of squares by definition, the R^2 value will always be higher when adding predictors (Dettling, 2015). This can be overcome by the use of the adjusted coefficient of determination R^2_{adj} that considers the degrees of freedom:

$$R^2_{adj} = 1 - \frac{n-1}{n-p}\frac{SS_{res}}{SS_t} \tag{2.80}$$

For the MLR drainage flow example, the coefficient of determination is estimated to $R^2 = 0.962$ and the adjusted coefficient of determination to $R^2_{adj} = 0.961$. Since $n = 199$ observations are used, the difference is small. Compared to the SLR model, the amount that is expressed by the model rises by about 2%.

Test error

If the model is used for prediction, its prediction performance is of main interest. The most effective method to quantify the prediction performance is to keep one part of the data with n_p values as test data (not used for fitting of the model) and use it only to calculate the test error (Montgomery *et al.*, 2012). The test error is calculated by the difference between the predictions of the response variable and the corresponding measurement values. It can be expressed as the mean squared residuals of the prediction $MS_{res,p}$ or the root mean squared prediction error *RMSPE* that has the unit of the response variable:

$$MS_{res,p} = \frac{\sum_{i=1}^{n_p}(y_i - \hat{y}_i)^2}{n_p} \tag{2.81}$$

$$RMSPE = \sqrt{MS_{res,p}} \tag{2.82}$$

Since the test data set was not used to fit the model, the test error $MS_{res,p}$ is expected to be larger than the error of the fitted model MS_{res}. By checking the test error, the danger of overfitting can be controlled. Overfitting means that the model follows the errors too closely and for a new sample, other coefficient estimates result (James *et al.*, 2013). The disadvantage is that a part of the data is not used for the fitting. In addition, since more data could have been used, the test error rate is overestimated with this approach (James *et al.*, 2013). The cross-validation approach addresses this issue.

The test error for the drainage flow example was calculated by a data split of 2/3 for fitting and 1/3 to calculate the test error. For the SLR, the *RMSPE* is 0.113 m^3/d and for the MLR model it is 0.087 m^3/d. For the calibration, they were estimated to 0.093 m^3/d for the SLR and 0.078 m^3/d for the MLR. As expected, they are lower as the estimated test error.

Prediction coefficient of determination

Since the test error depends on the unit of the response variable y, it cannot be used as a measure to compare different data sets. To overcome this problem, the dimensionless prediction coefficient of determination R^2_{pred} can be calculated (Montgomery *et al.*, 2012):

$$R^2_{pred} = 1 - \frac{\sum_{i=1}^{n_p}(y_i - \hat{y}_i)^2}{SS_t} \tag{2.83}$$

As for the test error, R^2_{pred} of the drainage flow example was calculated by a data split of 2/3 for fitting and 1/3 for prediction. For the SLR, the R^2_{pred} is 0.899 and for the MLR model 0.942. This is lower than the R^2 of the calibration.

Cross-validation

The idea behind the cross-validation approach is that all of the data can be used to estimate the test error. By this approach, the data are divided in k folds (groups) of approximately the same size (Fig. 2.37). Then each fold is used to calculate the test error whereas the others are used to fit the model. This procedure leads to k estimates of the test error. The average of these test errors leads to the cross-validation test error:

$$RMSPE_{CV} = \frac{1}{k}\sum_{i=1}^{k} RMSPE_i \tag{2.84}$$

By this procedure, each data point can be used to estimate the test error rate. James *et al.* (2013) suggest using $k = 5$ or $k = 10$ folds, since it was shown empirically that there is not a too high bias and variance for these values. In the past, R^2_{adj} was preferred since the cross-validation approach is computationally intensive. For the 5-fold cross-validation for instance, five MLR models must be fitted and predicted. Due to the gain of computational power in recent years, this approach has become attractive (James *et al.*, 2013). Besides the test error, also the prediction coefficient of determination $R^2_{pred,CV}$ can be determined by cross-validation.

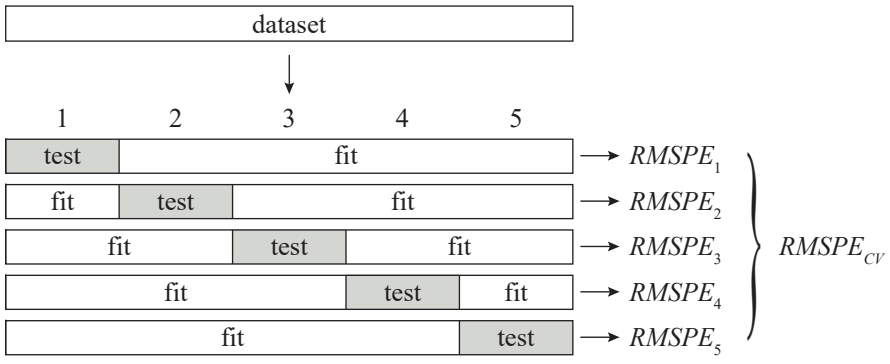

Fig. 2.37 Schematic example of a 5-fold cross-validation. The data set is split into folds of approximately the same size. Each fold is once used to calculate the test error $RMSPE_i$ whereas the rest of the data is used for fitting. The mean value of all test errors is the cross-validation prediction error $RMSPE_{CV}$ (adapted from James *et al.*, 2013).

Performing 5-fold cross-validation for the drainage flow example leads to $RMSPE_{CV} = 0.099$ m^3/d for the SLR model and $RMSPE_{CV} = 0.082$ m^3/d for the MLR model. As the test error, the $RMSPE_{CV}$ are higher than the calibration error.

2.4.1.5 Hypothesis tests

There are different hypothesis tests that are usually done in MLR; two of the most popular are presented here. Considering Eq. (2.75) of the MLR drainage flow example, the question arises if it makes sense to add the time t and the sinusoidal function $\sin(S)+\cos(S)$ to the model. This question can be answered by hypothesis tests. The presence of the time t can be tested by a hypothesis test on individual coefficients. Unfortunately, this test does only work if the coefficients are removed individually step by step. A check for adding or removing a subset of two or more regressor variables can be done by a partial F-test. Detailed information about test statistics can be found in Stahel (2008) and Montgomery *et al.* (2012).

Hypothesis tests on individual coefficients

In this test, the goal is to find out if an arbitrary value of a coefficient β_i is reasonable. The most popular procedure is to check if it could be 0, i.e. having no influence on the response y (Dettling, 2015), and therefore can be deleted from the model (Montgomery *et al.*, 2012). This can be tested with the null hypothesis $H_0 : \beta_i = 0$. If this hypothesis can be rejected, it can be inferred that a relation between the predictor variable x_i and the response y exists. To perform this test, the t-test statistics is calculated by dividing the value of the coefficient by its standard error:

$$t = \frac{\beta_i}{\mathrm{se}(\beta_i)} \tag{2.85}$$

The t-value is an indicator for the number of standard deviations where β_i is not zero (James *et al.*, 2013). On the basis of the t-value, the p-value is calculated by using integral tables of distribution functions or statistical software. A small p-value indicates that a relation between the predictor variable and the response variable due to chance is unlikely. Typically, the significance level α for the p-values is chosen to 0.05 or 0.01 (James *et al.*, 2013). The choice of the significance level has an influence on the type I error (H_0 true, but rejected) and type II error (H_0 false, but retained). The type I error increases when doing several tests. If for example 10 predictors are in a model and they are tested with a significance level of $\alpha = 0.05$, the chance of at least one false rejection is 0.40. On the other hand, if the significance level is chosen too low, the chance of a type II error increases. This means that the test fails in rejecting the null hypothesis although the predictor variable is related to the response. It even can be that all individual hypothesis tests fail in rejecting the null hypothesis, even though some predictor variables have a

known significant effect. This may happen due to the collinearity between the predictor variables. Their values are distributed to several coefficients with less influence each (Dettling, 2015). The detection and treatment of such collinearities, called multicollinearity, is discussed in Section 2.4.2.

As an example, consider a normally distributed coefficient β_i with mean value of 0.5 and standard error of 0.1 (Fig. 2.38a). This results in a p-value of 0 and a relation between the predictor and the response can be inferred. In contrary, consider a coefficient β_i with mean value of 0.5 and standard error of 0.4 (Fig. 2.38b). A relation between the predictor and the response due to chance is likely since the p-value is 0.18.

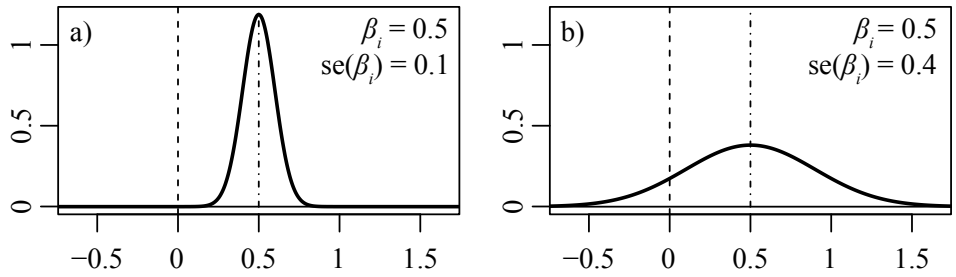

Fig. 2.38 Example cases with a) $\beta_i = 0.5$ and $\text{se}(\beta_i) = 0.1$; b) $\beta_i = 0.5$ and $\text{se}(\beta_i) = 0.4$.

Considering the MLR drainage flow example, the coefficient estimates, their standard errors, the resulting t-values and the corresponding p-values are given in Table 2.5. The p-values indicate high significance except for the intercept and the water level h^3. Nevertheless, the water level h^3 is still significant with $p = 0.02$ but one might think about a reduced model with $h + h^2$ to represent the influence of the water level. The intercept is not significant, but should generally be included according to Montgomery *et al.* (2012).

Table 2.5 Coefficient estimates ($\hat{\beta}$), standard errors $\text{se}(\hat{\beta})$, t-values and p-values of the MLR model for drainage flow example.

type		$\hat{\beta}$	$\text{se}(\hat{\beta})$	t	p
	Intercept	-0.0798	0.0755	1.1	0.29
β_1	h	-1.46	0.451	-3.2	$1.4 \cdot 10^{-3}$
β_2	h^2	3.72	0.867	4.3	$2.3 \cdot 10^{-5}$
β_3	h^3	-1.14	0.486	-2.3	0.02
β_4	$\sin(S)$	0.0360	0.0105	3.4	0.0038
β_5	$\cos(S)$	-0.0331	0.00802	-4.1	$7.0 \cdot 10^{-4}$
β_6	t	0.0116	0.00195	5.9	$1.4 \cdot 10^{-8}$

Caution is advised if the excluding of predictors is decided on the basis of p-values. The estimated coefficient values $\hat{\beta}$ and their standard error $\text{se}(\hat{\beta})$ depend on the other predictor

variables that were included for model fitting. Therefore, it is tested if a certain predictor x_j has a significant effect to the response y in presence off all other predictor variables. To check if adding a subset of predictors has a significant effect on the response, a partial F-test can be done.

Hypothesis tests on subset of coefficients, the partial F-test

A partial F-test allows to compare two different MLR models with different size. The larger model must contain all predictors that are contained in the small model. It is tested if at least one of the removed variables has a significant effect on the response. The test is based on the residual sum of squares SS_{res}. Thus, the question whether the additional subset of predictors will lower the SS_{res} enough will be answered with this test. The test statistic F can be calculated as:

$$F = \frac{n-p}{q} \frac{SS_{res,small} - SS_{res,large}}{SS_{res,large}} \tag{2.86}$$

where q is the number of additional coefficients. The test statistic can be compared to the values of the F-distribution of a chosen significance level α. These values can be found in statistical tables or calculated by statistical tools such as R (R Core Team, 2013).

Now, the described procedure is applied to check if adding a sinusoidal function is worth in case of the MLR drainage flow example. The results of the analysis are summarised in Table 2.6. The residual sum of squares can be reduced by 0.36 by the model including a sinusoidal function. Eq. (2.86) gives an F-value of 16.04 what leads to a p-value of $3.6 \cdot 10^{-6}$. Thus, adding the sinusoidal function significantly improves the model.

Table 2.6 Results of F-test for a small and a large model with a sinusoidal function for the drainage flow example.

model	SS_{res}	F	p
$\beta_0 + \beta_1 h + \beta_2 h^2 + \beta_3 h^3 + \beta_4 t$	1.254	16.04	$3.6 \cdot 10^{-7}$
$\beta_0 + \beta_1 h + \beta_2 h^2 + \beta_3 h^3 + \beta_4 \sin(S) + \beta_5 \cos(S) + \beta_6 t$	1.074		

2.4.1.6 Model adequacy checking

The validity of the assumptions for the least squares approach must be checked (see Section 2.4.1.2,), because serious violations lead to unstable models. This means that a different sample of the same data could lead to a totally different model and therefore to other conclusions. Usually the checking is done visually by a plot of the residuals (Dettling, 2015).

The Tukey-Anscombe plot allows to check if (i) the expected value of the residuals is zero ($E(\varepsilon_i) = 0$), (ii) the variance is constant and (iii) if there are nonlinear effects that

are not considered in the model. A scale-location-plot is similar to the Tukey-Anscombe-plot, but it is a bit simpler to detect non-constant variance (Dettling, 2015). In addition, a plot of the partial residuals can be used to check if the linear assumption is satisfied by all regressors in the model. This may help to detect if a variable transformation might be useful. Furthermore, with a normal probability plot (also called quantile-quantile plot or Q-Q-plot), the assumption of the normal (Gaussian) distribution of the residuals can be checked. Finally, the presence of potential leverage points that heavily influence the result of the analysis, can be detected by a plot of the Cook's distance. In addition, the assumption that the residuals are not correlated by themselves ($\mathrm{Cov}(\varepsilon_i, \varepsilon_j) = 0$ for $i \neq j$) should also be checked. A method how this can be done and also two methods that can be applied if a correlation was detected are explained in Section 2.4.3.

The plots listed above are explained in Appendix A.3.1 or in Montgomery *et al.* (2012) and Dettling (2015). Some of the plots are based on scaled residuals since they allow for better detecting outliers and extreme values. Thus, they will be introduced before the description of the different diagnosis tools.

2.4.1.7 Variable selection

Too many predictor variables can cause different problems in MLR-models. Irrelevant variables can lead to unnecessary complexity what reduces the interpretability (James *et al.*, 2013) and they can add noise to the estimated coefficients of the other predictors (Dettling, 2015). If some of the predictor variables are correlated, instabilities in prediction can occur (this is addressed in Section 2.4.2).

Therefore, the question which variables shall be included and in which form arises when setting up MLR models. For the drainage flow case study presented here, the water level in arbitrary form, the season, the time or even more information could be used to set up a model. In models where the displacement is used as response variable, the choice between different thermometer readings can be necessary. In this section, an approach how a subset of regressor variables can be selected is presented.

There are different established procedures that help to decide which variables shall be taken into the model. One of these, the best subset selection, is presented here. The idea behind it is very simple. All possible combinations of variables are determined and the corresponding model is fitted. The best model is chosen by the assessment of the model accuracy. Due to the fact that this procedure is computational intensive, stepwise selection procedures such as the forward selection, the backward selection and some mixed algorithms were developed. Usually, these algorithms do not find the best of all models since the influence of some variables can be less important by adding other variables. Montgomery *et al.* (2012) suggest performing best subset selection whenever it is feasible. For a data set with p predictors, 2^p models must be considered. For $p = 10$, there

are 1024 models, for $p = 20$ there are $1.05 \cdot 10^6$ models and for $p = 30$ there are $1.07 \cdot 10^9$ models.

Best subset selection

The implementation of the best subset algorithm is straightforward. It can be performed in three main steps:

1. `Define null model` M_0`, which contains no predictors and predicts the sample mean.`
2. `(a) For` $k = 1,2,3,\ldots,(p-1)$`: Fit` $\binom{p-1}{k}$ `models that contain` k `predictors. (b) Pick the best of these models and call it` M_k`. The best can be chosen by a goodness of fit criteria such as` R^2`,` RSE `or` $RMSE_{CV}$`.`
3. `Select the best models among` $M_0,\ldots,M_k$`, using goodness of fit criteria that account for the number of predictors (`R^2_{adj}`) or do not suffer from overfitting (`$RMSE_{CV}$`). Alternatively, cross validation can be performed.`

In Fig. 2.39 the results of the best subset selection analysis for the drainage flow example are shown. The variables h, h^2, h^3, h^4, $\sin(S)$, $\cos(S)$, $\sin(2S)$, $\cos(2S)$ and t were given to the selection algorithm. This resulted in 512 different MLR models. To compare the models, the cross-validation *RMSPE* was calculated. All $RMSPE_{CV}$ are displayed against the model order p in Fig. 2.39. For model orders up to 6, the cross-validation test error decreases and for higher orders it increases again due to overfitting. The best model has the order $p = 6$ and reads:

$$\begin{aligned} \hat{Q}_{tot} &= -0.027 - 0.46h + 1.70h^2 \\ &\quad +0.023\sin(S) - 0.034\cos(S) + 0.029\cos(2S) + 0.012t \end{aligned} \tag{2.87}$$

This model is similar to the MLR model presented before. The influence of the water level is represented by a polynomial of second-order instead of third order. According to Table 2.5, the p-value for h^3 was not highly significant. Thus, the model of the best subset selection seems to be plausible. In addition, a second order sinusoidal function was added.

A closer look to the best models for each order (red dots in Fig. 2.39) indicates that the difference between the 4^{th} and the 6^{th} order is small. Applying the so called one-standard-error rule considers this.

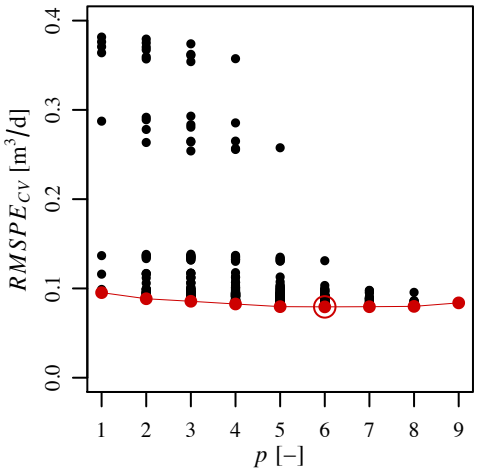

Fig. 2.39 Best subset selection for drainage flow example. The estimated $RMSPE_{CV}$ are shown for all possible regressor combinations separately for the number of coefficients in the model p.

One-standard-error rule

The idea of the one-standard-error rule is, if there are some models that are more or less equally good, the smallest shall be chosen (James *et al.*, 2013). As a measure of equal goodness, the standard error of the goodness of fit criteria of the best model, e.g. the standard error of $RMSPE_{CV}$, is taken. This standard error is added to the criteria and is seen as a cut-off value. The smallest model with a $RMSPE_{CV}$ below the cut-off value is chosen.

2.4.1.8 Model validation

Before a developed model is used for prediction, its performance should be validated. This shall not be confused with the model adequacy checking where basic assumption for the least squares approach and potential leverage points are checked. A model can be validated by looking at the regression coefficients and assess the prediction performance by using new data.

The signs and the values of the regression coefficients β_i shall be checked for plausibility. This can be done by the knowledge of analytical solutions or physical behaviour. Coefficients with a wrong sign or too large values are an indicator for an inappropriate model or poor coefficient estimates. Furthermore, the stability of the estimated coefficients shall be checked. One option is to use a new data sample and compare these coefficients to the fitted ones, another is to split the existing sample in different parts and compare them (Montgomery *et al.*, 2012).

The prediction performance can be analysed with fresh data that have not yet been used for model calibration and variable selection. Even if a test data set was used to create the

model, this should not be used to validate the model; this would lead to a bias. If two or more models have been developed, they can be compared and the final model decision can be made on the basis of an unbiased test error.

2.4.2 Multicollinearity

2.4.2.1 Introduction

Multicollinearity occurs if two or more of the predictor variables are correlated to each other (James *et al.*, 2013). In the context of dam behaviour analysis, this is mainly related to temperature measurements at different positions in the dam body. The temperature measurements are different due to the varying boundary conditions (e.g upstream and downstream side) and the diffusive nature of the heat transport. However, from a global point of view, all the temperature readings are driven by the air temperature at the site. Thus, correlations likely occur. In Fig. 2.40, temperature data of a gravity dam (gravity dam G1, see Appendix A.5.7 for details) are shown as an example. In Fig. 2.40a, the correlation plot of the temperatures $T_{262,6}$ and $T_{283,4}$, both near the downstream surface, are shown. There is a high correlation, except for the spring time marked by red dots. In Fig. 2.40b, the correlation plot of the temperatures $T_{262,6}$ on the downstream side and $T_{262,2}$ on the upstream side, is shown. A hysteresis is recognisable and the correlation is weaker.

Multicollinearity can cause stability problems when estimating the regression coefficients (James *et al.*, 2013). This can be illustrated by Fig. 2.40c and d, where the SS_{Res} is shown as a function of the regression coefficients corresponding to the temperatures of the correlation plots. In Fig. 2.40c, it can be identified that for the temperatures $T_{262,6}$ and $T_{283,4}$ different pairs of regression coefficient estimates lead to the same SS_{Res} of 76 mm^2, which is close to the optimum value. This means that a slight modification of the data set may lead to different coefficient estimates. In Fig. 2.40d, it can be recognised that there is still a linear dependency, but it is weaker due to the weaker correlation of the temperatures.

In the case of dams, other sources of multicollinearity can occur. If the progress of the water level is similar to the temperature measurements multicollinearity may occur, e.g. in the case of a seasonally operated reservoir. According to Amberg (2009), this can be avoided by a calibration period that is long enough. In addition, multicollinearity can occur between different polynomial terms of the water level approach and between different shape functions considering irreversible effects. Fortunately, this does not cause any problems since they are treated as one piece by definition (Montgomery *et al.*, 2012). In the following, it is shown how multicollinearity can be detected and treated.

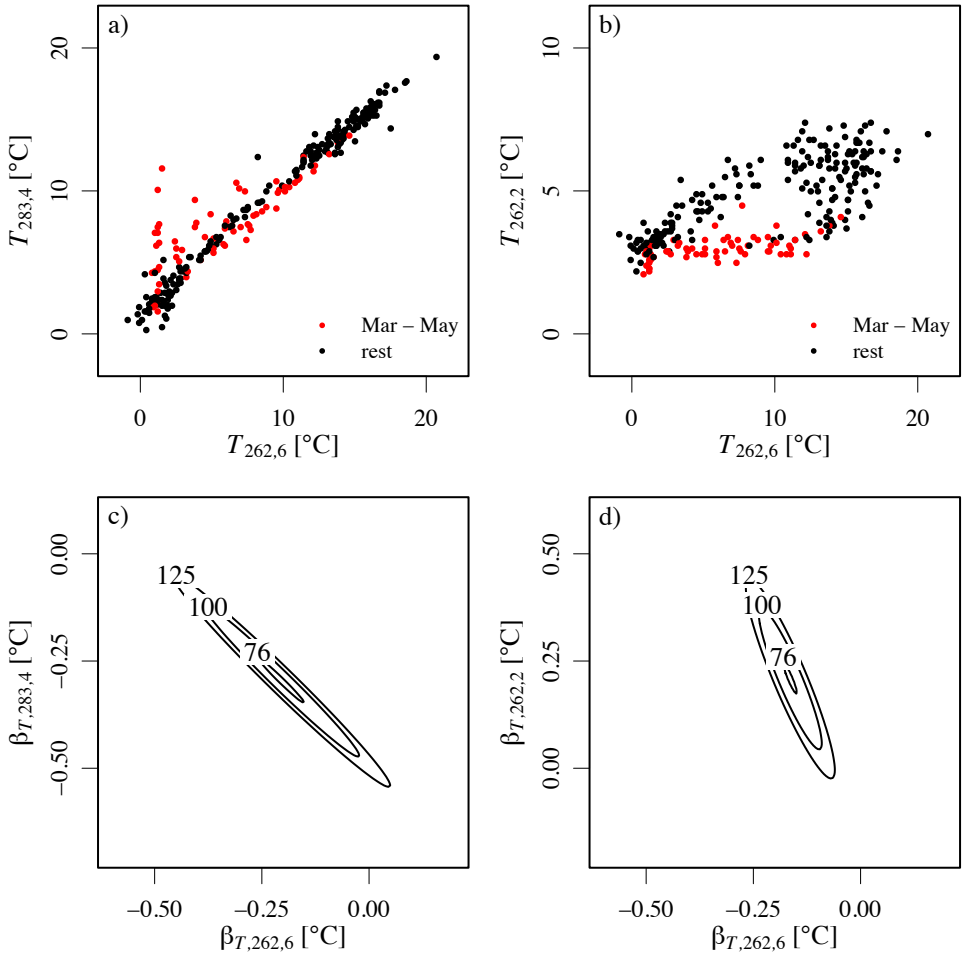

Fig. 2.40 Data of gravity dam G1: a) correlation plot of the temperatures $T_{262,6}$ and $T_{283,4}$; b) correlation plot of the temperatures $T_{262,6}$ and $T_{262,2}$; c) and d) SS_{Res} in function of the regression coefficients of the temperatures $T_{283,4}$, $T_{262,6}$ and $T_{262,2}$.

2.4.2.2 Detection

Multicollinearity can be detected by the variance inflation factor VIF. It can be calculated by

$$VIF = \text{diag}\left((\mathbf{X}'\mathbf{X})^{-1}\right) S_{jj}, \tag{2.88}$$

with S_{jj} as the corrected sum of squares for regressor x_j (Montgomery *et al.*, 2012):

$$S_{jj} = \sum_{i=1}^{n} (x_{ij} - \bar{x_j})^2 \tag{2.89}$$

Alternatively, the VIF of the j^{th} regression coefficient can be written as

$$VIF_j = \frac{1}{1 - R_j^2}, \tag{2.90}$$

where R_j^2 is the coefficient of determination from a regression of the regressor x_j as target variable to the other regressors (Montgomery *et al.*, 2012; James *et al.*, 2013). VIF values larger than $5 \div 10$ are said to cause serious multicollinearity (Montgomery *et al.*, 2012; James *et al.*, 2013).

2.4.2.3 Treatment

There are different approaches to deal with multicollinearity. There are established statistical procedures such as ridge regression (RR), lasso regression (LR) or principal component regression (PCR). Nevertheless, the simplest approach is to eliminate some of the correlated temperatures from the model since they contain the same information as others. This is often applied in the practice of dam behaviour analysis (Amberg, 2009) (see Weber (2002), for example). In the following, RR and PCR are briefly discussed. More details can be found in James *et al.* (2013) and Montgomery *et al.* (2012). RR is a modified least squares approach with a tuning parameter λ. The ridge estimator is

$$\hat{\beta}_R = (\mathbf{X}'\mathbf{X} + \lambda\mathbf{I})^{-1}\mathbf{X}'y, \tag{2.91}$$

with $\mathbf{I}$ as the identity matrix. For $\lambda = 0$, the estimator is the same as for the common least squares approach. For $\lambda > 0$, the regression coefficients are shrunken towards 0. This leads to a decreasing variance but an increasing bias. In Fig. 2.41 the distribution of an estimated coefficient $\hat{\beta}$ with variance V is shown exemplarily. Since the MLR approach was used, the estimate is unbiased ($E(\hat{\beta}) = \beta$). When applying RR, the variance reduces but a bias is introduced ($E(\hat{\beta}) \neq \beta$).

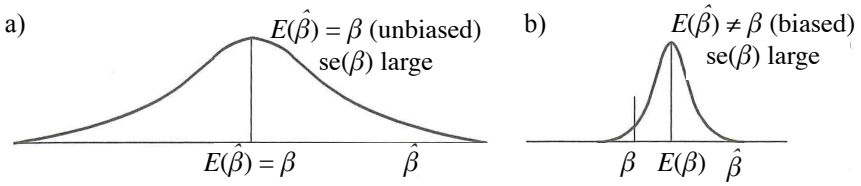

Fig. 2.41 a) Resulting distribution of an MLR-estimated coefficient $\hat{\beta}$; b) distribution of the RR-estimated coefficient, a bias is introduced and $E(\hat{\beta}) \neq \beta$ (adapted from Montgomery *et al.*, 2012).

The choice of the tuning parameter λ is difficult. James *et al.* (2013) use the cross-validation procedure to determine the best choice. Due to the shrinkage of the coefficients, RR can also be seen as a variable selection procedure. Not important variables result in

very small coefficients close to 0 (James *et al.*, 2013). In the field of dam behaviour analysis, RR was applied by Weber (2002).

The PCR is based on dimension reduction. The principal components of the data are estimated and used as predictor variables of an MLR model. The idea behind this approach is that usually a small number of principal components explain most of the variability of the response variable (James *et al.*, 2013). As usual for MLR models, adding more principal components to the model, leads to a reduction of the SS_{Res} by definition. Thus, the number of required principal components is usually estimated by cross-validation (James *et al.*, 2013). When performing PCR, it is recommended to standardise the variables (Montgomery *et al.*, 2012; James *et al.*, 2013). There are two popular scalings, *unit normal scaling* and *unit length scaling*. Both of them are described in Montgomery *et al.* (2012).

2.4.3 Autocorrelation

2.4.3.1 Introduction

One of the general assumptions for a least square estimate is that the residuals are uncorrelated. When using time-series data in regression models, this assumption will likely be violated and the errors can be autocorrelated. Autocorrelation means that the errors are correlated by themselves at different times (Montgomery *et al.*, 2012). An intuitive visualisation can be done by temporally lagged scatterplots of the residuals. In doing so, the residuals of the current time step e_t are plotted against the corresponding residuals some time-lags back e_{t-lag}. In Fig. 2.42, a lagged scatterplot for 1 time-lag for the residuals of the simple linear regression model of the drainage flow example is shown. It is visible that there is a weak positive correlation (cor $= 0.59$, $R^2 = 0.34$) between the residuals of one time lag.

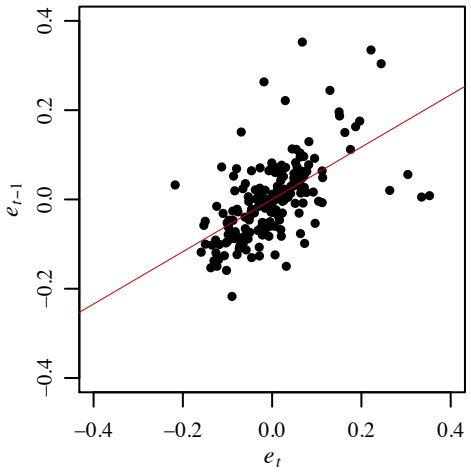

Fig. 2.42 Lagged scatterplot of the residuals of the SLR drainage flow example for 1 time-lag.

Autocorrelation can have two different origins. The first is the absence of one or more important predictor variables in the model (Montgomery *et al.*, 2012). This leads to systematic deviations and wrong estimates of the other regression coefficients. The second concerns data that are recorded in sequence. For example, consider a data set that was doubled. The content of the information will be the same but instead of n observations, there are $2n$ observations available. The estimates of the regression coefficients will be exactly the same for both data sets when doing MLR analysis but the standard errors $\mathrm{se}(\beta)$ will be different since they depend on the number of observations n that are used to fit the model (James *et al.*, 2013). The standard errors will become smaller as more times the data set is doubled. Unfortunately, many test procedures (see Section 2.4.1.5) are based on the p-values, which depend on the ratio between the coefficient estimate and the standard error.

Now, consider the measurements of time series that are recorded at relatively short intervals compared to their variation. This means that almost the same quantities are measured multiple times. As in the example described above, this will result in smaller standard errors and smaller p-values of the regression coefficients compared to data with a larger measurement interval. If conclusions are made based on the result of hypothesis tests, wrong conclusions may be drawn. Thus, it is important to check for autocorrelation of the residuals and to eliminate this phenomenon if the standard errors of the coefficients and the p-values are of interest.

2.4.3.2 Detection

Autocorrelation can be detected visually by plotting the autocorrelation function (ACF) and the partial autocorrelation function (PACF) or by a Durbin-Watson test. The visual detection is straightforward. It is explained in Appendix A.3.2.

2.4.3.3 Treatment

There are statistical methods as the Cochrane-Orcutt method or the Prais-Winsten algorithm. They are well described in general in Montgomery *et al.* (2012), and specifically with regard to dam behaviour analysis in Weber (2002). These procedures can lead to meaningless results if strong autocorrelation is detected.

Furthermore, a crude but effective approach to reduce autocorrelation is thinning out the data set (see Bühlmann *et al.* (2015)). This reduces the correlation of the residuals. If the chosen sampling rate is long enough, the residuals will be uncorrelated. Unfortunately, because the data is thinned out, some information is lost.

A more sophisticated approach to estimate correct standard errors of the regression coefficients is the block bootstrap (BBS) method (Gonçalves and White, 2005). In the BBS method, the data are divided into blocks of size l (Gonçalves and White, 2005). Then,

new data sets are created by sampling with replacement (Fig. 2.43). As a consequence, a block can be used more than once, and therefore some of the original data might not be present in the new dataset. This procedure is usually repeated 200 to 1'000 times (Montgomery *et al.*, 2012). Ordinary least square regression (OLS) is performed to all of these datasets. Every regression will lead to slightly different regression coefficients. On the basis of these different coefficients a mean value β_i and a standard error $\mathrm{se}(\beta_i)$ can be calculated. Since the sampled data sets depend on the block length, it should be selected with care and a sensitivity analysis is recommended.

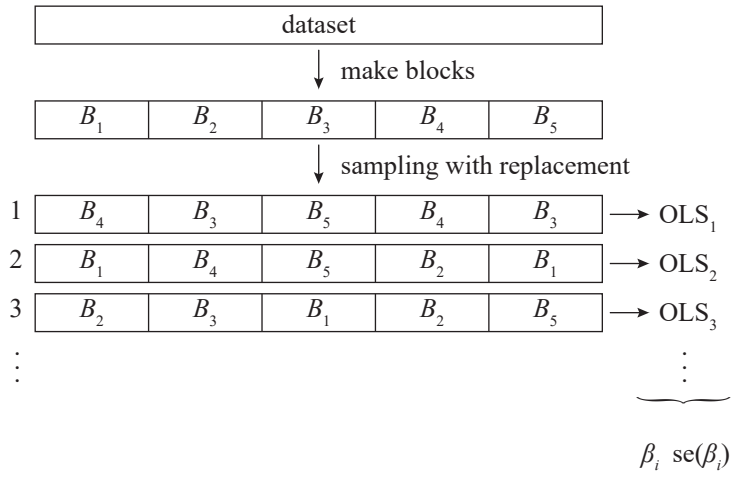

Fig. 2.43 Principle of the block bootstrap (BBS) approach.

2.4.4 Generalized Additive Models

MLR models are limited to linear relationships. Generalized Additive Models (GAM) are an extension of MLR models that allow for nonlinear relationships between the predictor variables and the response. The response y is formulated as a sum of (smooth) nonlinear functions f_j (James *et al.*, 2013):

$$y = \beta_0 + \sum_{j=1}^{p} f_j(x_j) + \varepsilon \tag{2.92}$$

The model is called additive since the functions f_j are added and independent from each other. They can be determined by smoothing splines. The degree of smoothing can be determined by the generalised cross-validation criterion described in Wood (2004). This approach is implemented in the R-package "mgcv" that allows for convenient application (Wood, 2006).

The advantages and disadvantages of GAM are (James *et al.*, 2013):

+ GAM allow for nonlinear functions to represent the effects of the predictor variables
+ potentially more accurate predictions than a linear relationship

+ since the model is additive, the individual effect of each predictor variable can still be analysed individually when keeping the others fixed
- the model is restricted to be additive which means interactions cannot be considered
- in terms of dam behaviour analysis, the description of the relationship is statistical but not physical

2.4.5 Markov Chain Monte Carlo method

2.4.5.1 Introduction

Bayesian inference allows for the use of prior knowledge of the parameters when fitting to the observed data. One of the standard procedures to observe the most probable parameters is the use of the Markov Chain Monte Carlo (MCMC) method that samples from the posterior distribution. Here, the basic idea about Bayesian inference and the MCMC algorithm used in this work is described. Further, the applied diagnosis is shortly described. More information about the theory can be found in Robert and Casella (2010) or Brooks *et al.* (2011).

2.4.5.2 Bayesian inference

Consider a deterministic model, for example a cantilever beam made of concrete with material properties E_c and ν_c and an elastic supporting with a spring constant k_M. From material tests and engineering knowledge, the mean value and the standard deviation of the material properties and the spring constant are known. With this knowledge, the deformation can be calculated. However, if there is further knowledge, e.g. measurements of the displacement for certain loading conditions, the material properties and the spring constant can be adjusted. The simplest way would be to adjust material constants by a least squares procedure rather than using the prior knowledge. However, if there are some collinearities, this may lead to physically meaningless results. This problem can be overcome by the use of the Bayesian inference.

Bayes' rule (Eq. (2.93)) says that the prior distribution $\pi(\theta|y)$ of the parameters θ (the material properties and the spring constant in the example mentioned above) given the measured data y is proportional to the likelihood $\mathscr{L}(y|\theta)$ of observing the data y given the parameters θ multiplied by the prior distribution of the parameters $\pi(\theta)$ (van Ravenzwaaij *et al.*, 2016).

$$\pi(\theta|y) \propto \mathscr{L}(y|\theta)\,\pi(\theta) \tag{2.93}$$

Eq. (2.93) can be examined for arbitrary parameter sets θ. Ideally, every possible combination of parameters would be used but this would be computationally very extensive. A common way to approximate the posterior distribution is to draw samples from it by the MCMC method (van Ravenzwaaij *et al.*, 2016).

2.4.5.3 Markov Chain Monte Carlo algorithm

Markov Chains define the path of the walk through the parameter space from which the samples are drawn. By definition, they follow an autoregressive process of first-order (AR(1)). There are different algorithms how the path of the Markov Chains can be described, the simplest one is a common random walk (Hastie *et al.*, 2009). In this thesis, the algorithm of Braak (2006) with parallel Markov Chains is used. This algorithm considers the genetic algorithm differential evolution algorithm of Storn and Price (1997) (DE-algorithm, see below) for the update. The advantages of this algorithm are the simple implementation and the convergence and therefore the good efficiency even if collinear parameters are present (Braak, 2006). The pseudo-code of the DE-MCMC algorithm is given below (for details see Braak (2006)):

```
Define prior distributions π of θ including a lower and upper limit

Choose a number of parallel chains P

Draw P random samples from the prior distributions π as initial values

Calculate likelihood 𝓛(y|θ) for the initial values

# loop with N steps

for ( i in 1:N ){

  for ( j in 1:P ){

    Randomly select two chains c1 and c2 unequal to j

    Apply DE-algorithm of Storn and Price (1997):

    θ_j = θ_{j-1} + γ_de (θ_c1 − θ_c2) + e  (see Fig. 2.44)

    Mirror points outside parameter interval at the limits

    Calculate 𝓛(y|θ_j) π(θ)

    Selection process based on the Metropolis-Hastings update

      r = π(θ_j|y) / π(θ_{j-1}|y)

      if ( log(r) > T_mh log(unif(0,1)){ θ_j = θ_j } # keep

      else { θ_j = θ_{j-1} } # reject

    }

  }

}
```

The parameter γ_{de} scales the step size to get accurate acceptance rates. According to Braak (2006), it can be chosen to $\gamma_{de} = 2.38/\sqrt{2\,p}$, where p is the number of parameters in the model. The so-called temperature T_{mh} has an influence on the convergence as well. It can be set as a variable or fixed, here a fixed value is used.

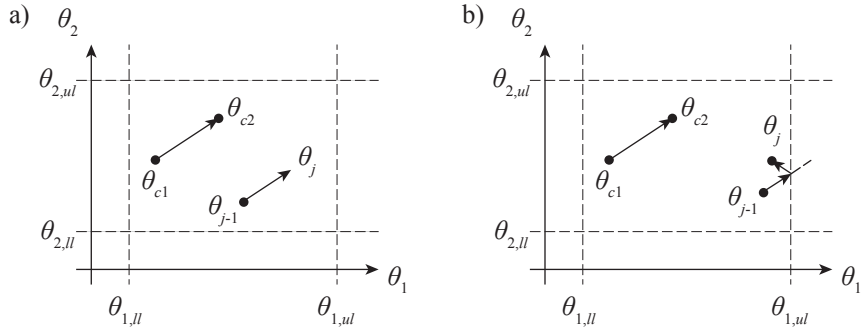

Fig. 2.44 DE-algorithm of Storn and Price (1997); a) step to next parameters θ_j (tuple of θ_2 and θ_2) is defined by the difference between the parameters of the two randomly chosen chains θ_{c1} and θ_{c2}; b) if the resulting parameters lie outside the range $[\theta_{ll}, \theta_{ul}]$, the vector is mirrored at the limit (adapted from Braak, 2006).

2.4.5.4 Diagnosis

The resulting samples shall be checked for convergence. Further, the autocorrelation and the acceptance rates should be checked.

Convergence

The Markov chains start from the random sampled initial values. Until a stationary ergodic distribution is reached, several sampling steps are needed. This period is called burn-in and must be removed before the distribution is analysed (Robert and Casella, 2010). The length of the burn-in period can be determined by the potential scale reduction factor *PSRF* of Brooks and Gelman (1998) that should be less than 1.1.

Autocorrelation

The Markov chain samples of the posterior distribution are autocorrelated by definition. To obtain independent samples, the resulting Markov chains have to be thinned out. The lag that has to be applied can be determined by the use of an ACF-plot.

Acceptance rate

The acceptance rate defines how much of the sampled parameter sets θ are accepted by the Metropolis-Hastings algorithm. According to Gelman *et al.* (1996), an acceptance rate of around 0.25 shall be targeted for multi-dimensional parameter spaces. A high acceptance rate is an indicator for poor convergence and there might be some regions that are not explored by the chains. On the contrary, a low acceptance rate indicates that the

chains move fast through the parameter space and therefore the borders of the parameter space are reached frequently (Robert and Casella, 2010).

2.4.6 Inference versus prediction

The statistical models can be used for two purposes: (i) inference and (ii) prediction. In the case of inference, the relation between the predictor variables and the response variable is of special interest. The important questions are (James *et al.*, 2013):

- Which of the predictor variables are significantly related to the response?
- How is the relationship between these significant predictors and the response? How is the response affected by a change of the predictor variable?
- Is a linear relationship adequate?

When doing pure prediction, the interpretation of the relations is not of interest. The goal is to have a function that approximates the data as well as possible. Generally, more flexible approaches such as boosting, support vector machines or artificial neural networks give very good predictions but they are hardly interpretable. On the contrary, less flexible approaches such as the linear regression, are better interpretable but they usually lead to a larger prediction error (James *et al.*, 2013). The flexibility and the interpretability for different approaches are shown in Fig. 2.45.

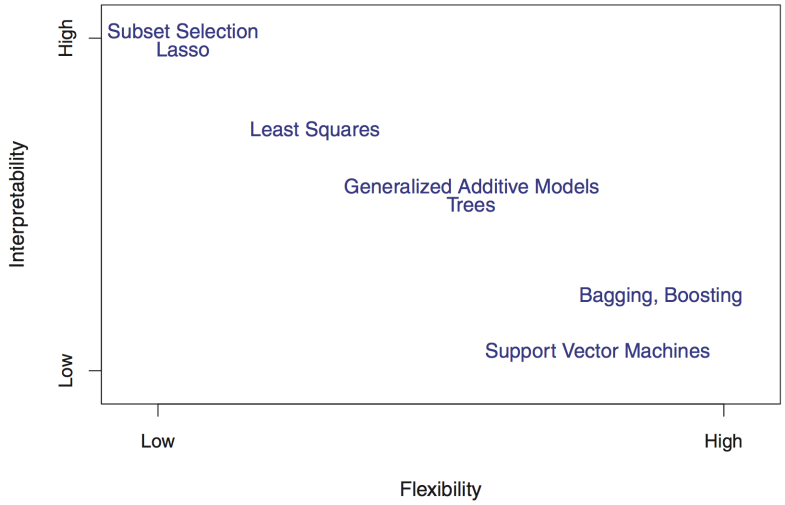

Fig. 2.45 Flexibility and interpretability of different statistical approaches. Generally, the more flexible, the harder interpretable are the approaches (James *et al.*, 2013).

On the one hand, there are fields where only inference or prediction is of interest. On the other hand, there are fields where both are needed. James *et al.* (2013) give the nice example of a real estate model, where house prices are estimated in function of zoning, air quality, distance from the river, etc. The question how much extra a house with river view is worth can be seen as an inference problem. Nevertheless, the same model can be used to predict the price of a certain house for sales purposes.

2.5 Dam behaviour analysis

2.5.1 Introduction

The monitoring of dams is essential to recognise an abnormal behaviour at an early stage. This gives enough time for the development, design and implementation of rehabilitation works. A common way to analyse the behaviour of dams is to set up a model that links the influence quantities and their effects. In dam behaviour analysis (DBA) the effects that are used for monitoring purposes are called behaviour indicator (Swiss Committee on Dams, 2003). Fig. 2.46 gives an overview of commonly used models for dam behaviour analysis. Generally, there are two different modelling approaches: (i) deterministic models link the influence quantities and the behaviour indicator based on physical laws and (ii) statistical models relate them by statistical procedures. In addition, there are also hybrid and mixed models, which are a combination of deterministic and statistical models (Swiss Committee on Dams, 2003). The different models with their advantages and disadvantages are presented in Section. 2.5.2. For each model that is set up, a behaviour indicator must be chosen. To this end, variables that represent the global behaviour of the structure, such as the displacement at crest level or the drainage flow at the bottom, are taken. The commonly used behaviour indicators are presented in Section 2.5.3. The set-up of the model depends on the chosen form. Deterministic models are based on structural analysis whereas for statistical models a model equation is needed. The model equation provides the shape of the relation between the influence quantities and the behaviour indicator. There exist a large number of different shape functions for model equations, which are described in Section 2.5.4. For statistical models, a wide range of solution procedures is available. Commonly multiple linear regression models (MLR) are used. In recent years also more sophisticated machine learning based methods such as artificial neural networks (ANN) or classification based methods became popular (Mata, 2011). The solution procedures are briefly described in Section 2.5.4.5. In Section 2.5.5, two procedures to perform the behaviour analysis are presented. These are (i) the observation-prediction comparison and (ii) the adjusted behaviour indicator.

2.5.2 Model types

2.5.2.1 Deterministic models

Deterministic models link the influences and the behaviour by physical laws. Usually they are set up as 2D or 3D FE-models (Swiss Committee on Dams, 2003; Léger and Seydou, 2009). The geometry of the structure is usually known. However, for the constitutive laws and the belonging material parameters assumptions have to be made. In the case where no information about the behaviour is known, the assumptions can be made based on punctual measurements such as drill-hole logs, tests with core samples or plate tests in

galleries (Swiss Committee on Dams, 2003). If information about the behaviour is present, material parameters, such as the Young's modulus of concrete E_c, can be calibrated. However, this does not mean that this coefficient is optimised in a statistical procedure like in a hybrid model. The quality of deterministic models depends on the discretisation, the ability of the constitutive laws to reproduce the structural behaviour and the knowledge about material parameters and model simplifications (Swiss Committee on Dams, 2003). If the relationship between the influence quantities and the behaviour cannot be described physically, as for the case of drainage flow and uplift pressure as behaviour indicators, a deterministic model cannot be taken into account and a statistical model must be set up (Salazar *et al.*, 2015).

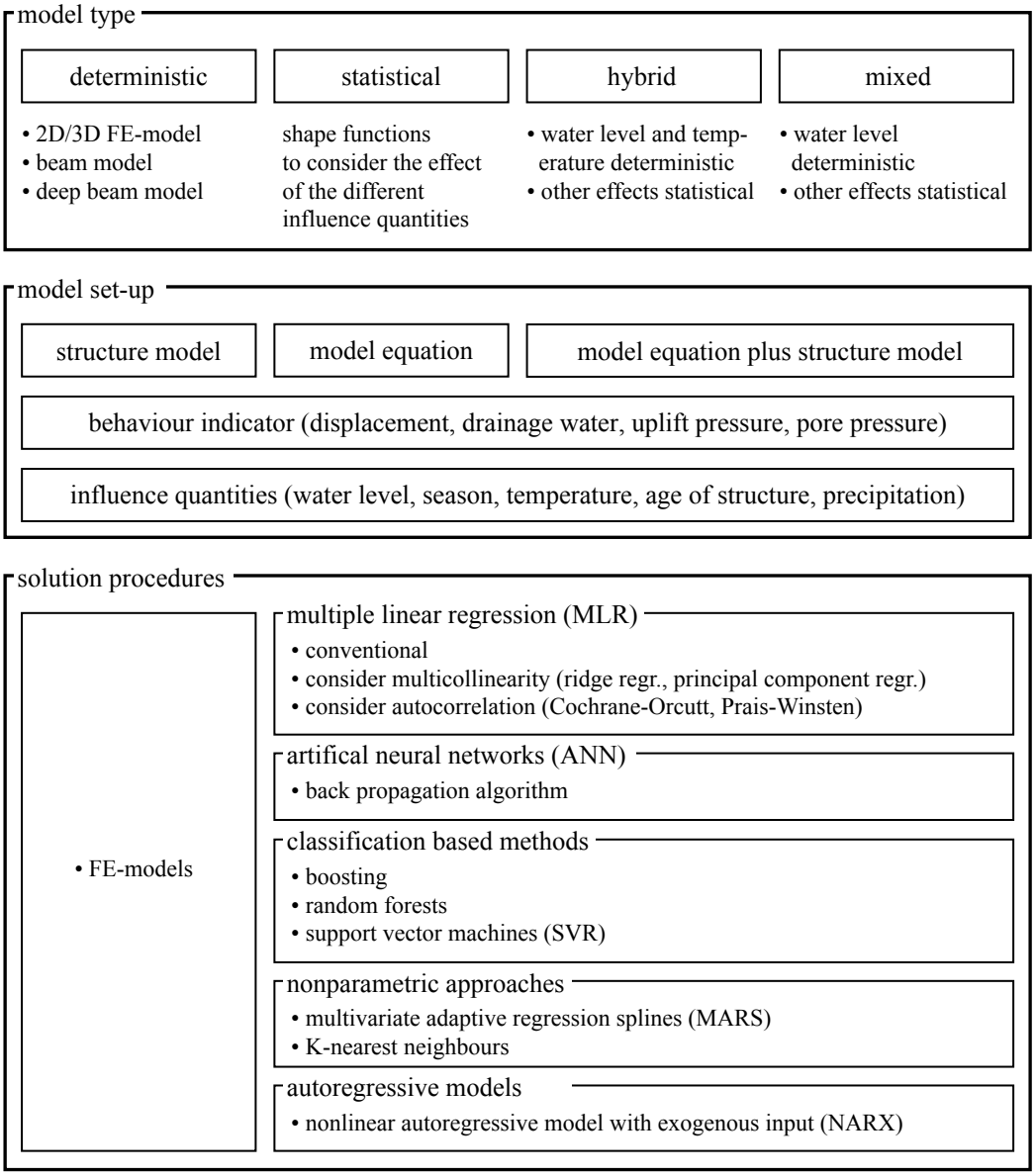

Fig. 2.46 Overview of models for dam behaviour analysis.

On the one hand, deterministic models are a powerful tool to assess the effects of first impounding and to detect long-term non-reversible displacements. They have quasi no limits in the extrapolation of load cases not yet experienced (Bianchi and Bremen, 2000). On the other hand, the set-up of FE-models is time-consuming and it has to be done individually for each structure.

2.5.2.2 Statistical models

Statistical models relate the influence quantities and the behaviour by statistical procedures. To set up a statistical model, a model equation that defines the shape of the relation between the influences and the behaviour indicator has to be chosen. The model equation is a sum of shape functions that consider the effects of different influences. These shape functions are multiplied by the calibration parameters. In regression analysis, the latter are called regression coefficients (Montgomery *et al.*, 2012). The efficiency and adequacy of the shape function can be tested by different statistical procedures (see Section 2.4). In contrast to deterministic models, statistical models are straightforward to set up and easy to implement. Thus, different models can be compared with an acceptable effort, and they are used widely in dam behaviour analysis (Mata *et al.*, 2013). Statistical models can be used to evaluate if the current behaviour of the structure corresponds to its behaviour in the past (Bianchi and Bremen, 2000). Therefore, statistical models are not suitable during the first life phase of a dam where hydration heat still causes permanent displacements and no knowledge about the behaviour in the past is available. Furthermore, statistical models do not provide reliable results for conditions that were not experienced in the past (Léger and Seydou, 2009).

2.5.2.3 Hybrid models

Hybrid models, also called adjusted deterministic models, are statistically optimised deterministic models. Instead of statistical shape functions, the results of a deterministic model are taken as shape functions (Swiss Committee on Dams, 2003). Thus, the hybrid model can be seen as a deterministic model with adjustment of the global stiffness and the thermal expansion coefficient (Swiss Committee on Dams, 2003; Amberg, 2009). Delayed effects and non-reversible effects can be added statistically.

2.5.2.4 Mixed models

The influence of the water level can be modelled quite simple in deterministic models. However, the modelling of the temperature effect needs more effort. Thus, the so called mixed models, where the influence of the water level is deterministically modelled and the temperature statistically, can be set up. As in hybrid models, delayed effects and non-reversible effects can be added statistically (Swiss Committee on Dams, 2003).

2.5.3 Behaviour indicators

Behaviour indicators are measurable variables that represent the global behaviour of the structure. These are (i) the displacement at different levels, particularly the crest level, since every abnormal behaviour in the structure itself or in the foundation has an effect on the displacement, or (ii) the drainage flow at the bottom of the structure (Amberg, 2009). Variables such as the stresses, joint openings, the uplift pressure and the pore pressure are especially influenced by local effects. Thus, they are not representative for the analysis of the global behaviour (Amberg, 2009). Although the uplift pressure and the pore pressure are influenced by local effects, sometimes they are used as behaviour indicator in dam behaviour analysis. This is because they have a direct influence on the stability of the structure.

2.5.4 Statistical models

2.5.4.1 Introduction

In Section 2.1.2 the different influence quantities acting on dams have been presented. In this section, it is shown how the effect of these influences are considered in statistical model equations. The approaches are presented separately for the different behaviour indicators in historical order.

There is a common naming convention for model equations in the field of dam behaviour analysis: The first letters of the influences considered in the model are combined to an acronym. H stands for the influence of the hydrostatic load, S for the seasonal influence, T stands either for the temperature or time influence (age of the structure) and R for rainfall and snow melt.

For the displacement of concrete dams, it is assumed that the water level, the temperature and the age of the structure have a significant influence. In the case of drainage flow, the water level, the age and the precipitation are significant (Swiss Committee on Dams, 2003).

2.5.4.2 Displacement of concrete dams

In the following, a selection of important dam behaviour analysis models for monitoring the displacement of concrete dams is presented. The established models are presented as originally published. Furthermore, these models are evaluated in Section 4. More models are explained in Appendix A.4.

The first two publications where dam behaviour models based on MLR analysis are mentioned are those of Willm and Beaujoint (1967) and Widmann (1967). The model of Willm and Beaujoint (1967), the so called HST-model (hydrostatic, seasonal, time) is the most common statistical model and therefore the basic form of statistical models (Tatin

et al., 2015). In this model, the displacement of the structure is related to the hydrostatic load h, some seasonal effects S and irreversible time-dependent effects. The hydrostatic influence is modelled as a fourth-order polynomial function of the water level h. The seasonal effects, which represent the temperature effect in particular, are described by a sinusoidal function of second order. In the model of Willm and Beaujoint (1967), the irreversible effects are considered with a logarithmic function and an exponential function of the time t.

$$\begin{aligned} P(h,S,t) &= \beta_0 + \beta_1 h + \beta_2 h^2 + \beta_3 h^3 + \beta_4 h^4 \\ &\quad + \beta_5 \sin(S) + \beta_6 \cos(S) + \beta_7 \sin(2S) + \beta_8 \cos(2S) \\ &\quad + \beta_9 \log(t) + \beta_{10} \exp(t) \end{aligned} \tag{2.94}$$

The seasonal function S reads

$$S = \frac{j\,2\pi}{365.25}, \tag{2.95}$$

where j is the number of the day in the year starting on the 1st of January. The total number of the days is either set to 365.25 (Swiss Committee on Dams, 2003) or 365 (Breitenstein *et al.* (1985)).

In a case study, where 8 pendulums were analysed, Willm and Beaujoint (1967) compared the seasonal approach to the use of air temperature measurements. In most of the cases, the seasonal approach performed nearly as well as the air temperature measurements; in one case even better. Thus, they suggested to use a seasonal function instead of the air temperature measurements.

Widmann (1967) used both a seasonal function and air temperature measurements. He proposed to determine at first an average annual temperature curve:

$$T_{air} = \tau_0 + \tau_1 \sin(S) + \tau_2 \cos(S) + \Delta T_a \tag{2.96}$$

The coefficients τ_i represent the first order sinusoidal function of T_{air}. They are estimated by regression analysis. The deviation between T_{air} and sinusoidal function is ΔT_a. They are used to calculate delayed deviations $\Delta T_{a,i}$. For this, the mean value over a chosen period in the past is calculated. Widmann (1967) proposed to use 5, 20 and 50 days. The effect of the water level is considered as a third-order polynomial function. The water

level does not only influence the displacement due to hydrostatic pressure on the dam, but also the change of the water pressure in the rock foundation. Since the latter is influenced by the seepage flow in the underground that reacts with a delay to changes in the water level, Widmann (1967) suggests considering a delayed water level Δh_{20} which is the difference between the actual water level and the mean water level during the preceding 20 days. Regarding this phenomenon, it does matter if the water level rises or sinks. To consider the irreversible displacements, he suggested to use a linear function and a natural logarithmic function. Because this model contains hydrostatic, seasonal, temperature and irreversible effects in function of time, it is a so called HSTT-model:

$$\begin{aligned} P(h,S,T,t) &= \beta_0 + \beta_1 h + \beta_2 h^2 + \beta_3 h^3 + \beta_4 \Delta h_{20} \\ &\quad + \beta_5 \sin(S) + \beta_6 \cos(S) + \beta_7 \sin(2S) + \beta_8 \cos(2S) \\ &\quad + \beta_9 \Delta T_5 + \beta_{10} \Delta T_{20} + \beta_{11} \Delta T_{50} \\ &\quad + \beta_{12} t + \beta_{13} \ln(t) \end{aligned} \tag{2.97}$$

Schnitter (1969) published the idea of a model in which the water level and the temperature is considered with a hybrid approach:

$$P(h,T) = \beta_0 + \beta_1 \delta_h(h) + \beta_2 \delta_T(T) \tag{2.98}$$

The influence functions for the water level δ_h and for the temperature δ_T were determined by the use of an arch-cantilever model. In this model, the regression coefficient β_1 mainly corresponds to a correction of the Young's-moduli of concrete (subscript c) E_c and rock E_r (subscript r) and β_2 mainly to a correction of the thermal expansion coefficient α_c. Schnitter (1969) applied this procedure successfully to several arch dams.

The Swiss Committee on Dams (2003) published a report about the methods of analysis for the prediction and the verification of dam behaviour. The goal of this report was to summarise the methods in the field of dam behaviour analysis applied in Switzerland. In addition, the advantages and disadvantages of the different approaches are discussed.

Because the HST-model performs not well in periods with weather conditions that strongly differ from the average value of the corresponding season, Penot *et al.* (2005) improved the model of Willm and Beaujoint (1967). They introduced the thermal correction function

$$\Delta T_R(t+\mathrm{d}t) = \Delta T_a(t+\mathrm{d}t)\left(1-\exp\left(-\frac{\mathrm{d}t}{t_c}\right)\right)+\Delta T_R(t)\exp\left(-\frac{\mathrm{d}t}{t_c}\right), \quad (2.99)$$

where $\Delta T_R(t)$ and $\Delta T_R(t+\mathrm{d}t)$ are the thermal correction at the current and the next time step and $\Delta T_a(t+\mathrm{d}t)$ is the deviation of the annual average temperature (as in Widmann (1967)) at the next time step. The constant t_c represents the characteristic time of the thermal inertia of the structure. Penot *et al.* (2005) suggested to use $t_c = \ln(10)\,L^2/(a\,\pi^2)$, later Tatin *et al.* (2013b) proposed to adjust t_c to optimise the result of the MLR model. In addition, Penot *et al.* (2005) provide information on how to calculate a physically-based estimate for the regression coefficient of ΔT_R for arch dams. Adding the thermal correction to the HST-model leads to the HSTT-model presented in Eq. (2.100). Instead of the logarithmic and exponential function for the irreversible effects, Penot *et al.* (2005) use a fourth-order polynomial approach plus an exponential decay function.

$$\begin{aligned} P(h,S,T,t) = {} & \beta_0+\beta_1 h+\beta_2 h^2+\beta_3 h^3+\beta_4 h^4 \\ & +\beta_5\sin(S)+\beta_6\cos(S)+\beta_7\sin(2S)+\beta_8\cos(2S)+\beta_9\Delta T_R \\ & +\beta_{10}t+\beta_{11}t^2+\beta_{12}t^3+\beta_{13}t^4+\beta_{14}\exp(-t/c_1) \end{aligned} \quad (2.100)$$

A model that considers internal temperature measurements was published by Léger and Leclerc (2007). They calculate the mean temperature T_m and the temperature difference T_d from a temperature field that was calculated by a thermal analysis (see Section 2.3.8 for a description of their method). This procedure can be done for a number of levels n_l. Léger and Leclerc (2007) proposed the HTT-model given by Eq. (2.101). For the reference temperature T_{ref} the temperature at the grouting of the joints or the long-term average temperature can be taken.

$$\begin{aligned} P(h,T,t) = {} & \beta_0+\beta_1 h+\beta_2 h^2+\beta_3 h^3+\beta_4 h^4 \\ & +\sum_{i=1}^{i=n_l}\left(\beta_{m,i}(T_m-T_{ref})+\beta_{d,i}T_d\right) \\ & +\beta_{5+n_l}t+\beta_{6+n_l}\exp(-t) \end{aligned} \quad (2.101)$$

A fully statistical approach based on the principal component analysis (PCA) without need of a thermal analysis was published by Mata *et al.* (2013). They suggest a procedure how to select a number of thermometers n_T on the basis of the PCA. The measurement data of the selected thermometers can be used in the raw form (Eq. (2.102)) or in the form

of the principal components (Eq. (2.103)). For the irreversible displacement, they used a linear and an exponential decay function.

$$\begin{aligned} P(h,T,t) &= \beta_0 + \beta_1 h + \beta_2 h^2 + \beta_3 h^3 + \beta_4 h^4 \\ &\quad + \sum_{i=5}^{i=5+n_T} \beta_i T_i \\ &\quad + \beta_{5+n_T} t + \beta_{6+n_T} \exp(-t) \end{aligned} \tag{2.102}$$

$$\begin{aligned} P(h,T,t) &= \beta_0 + \beta_1 h + \beta_2 h^2 + \beta_3 h^3 + \beta_4 h^4 \\ &\quad + \sum_{i=5}^{i=5+n_{PC}} \beta_i T_{PC,i} \\ &\quad + \beta_{5+n_{PC}} t + \beta_{6+n_{PC}} \exp(-t) \end{aligned} \tag{2.103}$$

The French HSTT-model (Eq. (2.100)) was improved by Tatin *et al.* (2015). Due to their knowledge that the water temperature has a significant influence on the displacement (Tatin *et al.*, 2013a), they omit the corrective term ΔT_R and propose the following approach:

$$\delta_T = \sum_{i=1}^{i=nLev} \left(\beta_{m,i} \Delta T_{m,i} + \beta_{d,i} \Delta T_{d,i} \right) \tag{2.104}$$

where ΔT_m is the difference between the average mean temperature T_m and its seasonal component, and ΔT_d the same for the temperature difference. The temperatures T_m and T_d are computed by a thermal analysis with the upstream temperature T_{up} and the downstream temperature T_{do} as boundary conditions. For the downstream temperature, the measurements of the air temperature are taken whereas for the upstream temperature a weighted average of the water temperature and the air temperature is taken. Despite the fact that T_m and T_d vary over the height, they are assumed to be constant due the reason of multicollinearity. The 1D-section used in the heat conduction analysis is not the geometrical length of the dam but a fictitious length of which the thermal inertia can be calibrated. For the influence of the water level, Tatin *et al.* (2015) assumed a polynomial 4^{th} order. The irreversible displacement is considered linear since it is assumed that the creep phenomenon is cushioned:

$$
\begin{aligned}
P(h,S,T,t) \;=\; & \beta_0 + \beta_1 h + \beta_2 h^2 + \beta_3 h^3 + \beta_4 h^4 \\
& + \beta_5 \sin(S) + \beta_6 \cos(S) + \beta_7 \sin(2S) + \beta_8 \cos(2S) + \beta_9 \Delta T_m + \beta_{10} \Delta T_d \\
& + \beta_{10} t
\end{aligned} \tag{2.105}
$$

In Tables. 2.7 - 2.9, the different shape functions for model equations are summarised separately for (i) the influence of the water level, (ii) the seasonal and the temperature influence and (iii) the irreversible displacement in function of time t. The models explained in Appendix A.4 are included as well.

Table 2.7 Summary of different approaches to consider the influence of the water level.

type	approach	used in
statistical	$h + h^2 + h^3$	Widmann (1967), Breitenstein *et al.* (1985)
	$h + h^2 + h^3 + h^4$	Willm and Beaujoint (1967), Penot *et al.* (2005), Léger and Leclerc (2007), Mata *et al.* (2013), Tatin *et al.* (2015)
hybrid	analytical model (beam model)	Rocha *et al.* (1958), Schnitter (1969), Léger and Seydou (2009)
	FE-model	Bonaldi *et al.* (1977), Perner and Obernhuber (2009)

Table 2.8 Summary of different approaches to consider seasonal and temperature influences. Models marked with an asterisk (*) are evaluated in Section 4.5.2.

type	approach	used in
statistical	$\beta_1 \sin(S) + \beta_2 \cos(S) + \beta_3 \sin(2S) + \beta_4 \cos(2S)^*$	Willm and Beaujoint (1967)
	$\beta_1 \sin(S) + \beta_2 \cos(S) + \beta_3 \sin(2S) + \beta_4 \cos(2S) + \beta_4 \cos(2S) + \sum \beta_i \Delta T_i^*$	Widmann (1967), Breitenstein *et al.* (1985)
	$\beta_1 \sin(S) + \beta_2 \cos(S) + \beta_3 \sin(2S) + \beta_4 \cos(2S) + \Delta T_R{}^*$	Penot *et al.* (2005)
	$\sum \beta_i T_i^*$	Swiss Committee on Dams (2003), Mata *et al.* (2013)
	$\sum \beta_i T_{m,i} + \sum \beta_j T_{m,j}$	Rocha *et al.* (1958)
	$\sum_{i=1}^{i=nLev} \left(\beta_{m,i}(T_m - T_{ref}) + \beta_{d,i} T_d\right)^*$	Léger and Leclerc (2007)
	$\sum \beta_i T_{PC,i}{}^*$	Mata *et al.* (2013)
	$\beta_1 \sin(S) + \beta_2 \cos(S) + \beta_3 \sin(2S) + \beta_4 \cos(2S) + \beta_5 \Delta T_m + \beta_6 \Delta T_d{}^*$	Tatin *et al.* (2015)
hybrid	analytical model (beam model)	Schnitter (1969), Léger and Seydou (2009)
	FE-model	Bonaldi *et al.* (1977), Perner and Obernhuber (2009)

Table 2.9 Summary of different approaches to consider the irreversible displacement as a function of time t.

type	approach	used in
statistical	$\beta_1 \log(t) + \beta_2 \exp(t)$	Willm and Beaujoint (1967)
	$\beta_1 t + \beta_2 \ln(t)$	Widmann (1967)
	$\beta_1 \sum d_i \exp(m_i(t-t_0))$	Bonaldi *et al.* (1977)
	$\beta_1 t + \beta_2 (\ln(1+t/c_1))^{1/c_2} + \beta_3 (1-\exp(-t/c_3))$	Breitenstein *et al.* (1985)
	$\beta_1 t + \beta_2 t^2 + \beta_3 t^3 + \beta_4 t^4 + \beta_5 \exp(-t/c_1)$	Penot *et al.* (2005)
	$\beta_1 t + \beta_2 \exp(-t)$	Léger and Leclerc (2007), Mata *et al.* (2013)
	$\beta_1 (1-\exp(-\kappa t))$	Mata *et al.* (2013)
	$\beta_1 t$	Tatin *et al.* (2015)

2.5.4.3 Drainage flow

For the monitoring of drainage flow, less models have been published than for displacements of concrete dams. One of the first published models is that of Breitenstein *et al.* (1985):

$$P(h) = \beta_0 + \beta_1 h + \beta_2 h^d \tag{2.106}$$

The model depends only on the water level h. Since the exponent d can be calibrated as well, the model needs to be calibrated in a nonlinear or linear way for different values of d.

An adaption to the HST-model (Eq. (2.94)) was developed by Simon *et al.* (2013):

$$\begin{aligned} P(h,S,T,t) = {} & \beta_0 + \beta_1 h + \beta_2 h^2 + \beta_3 h^3 + \beta_4 h^4 \\ & + \beta_5 \sin(S) + \beta_6 \cos(S) + \beta_7 \sin(2S) + \beta_8 \cos(2S) \\ & + \beta_{10} t + \beta_{11} t^2 + \beta_{12} t^3 + \beta_{13} t^4 + \beta_{14} \exp(-t/c_1) \\ & + \beta_{13} R_{sm} + \beta_{12} R_d \end{aligned} \tag{2.107}$$

The snow melt R_{sm} and the daily rain fall R_d were added to the standard HST-model. The snow melt was considered by the difference of the water content between two consecutive days. Since the data had a high variability over time, it was smoothed by a fast Fourier Transform (FFT), considering only low frequencies.

2.5.4.4 Scaling the influences

For numerical reasons, the scaling of regressor variables before the analysis is a common procedure. For example, if an analysis for the years 2000 to 2010 is carried out and the time would be used without scaling, the evaluation of $\exp(-t)$ will converge to 0 for the entire time span. Therefore, a scaling is needed. In the case of the water level, there are different approaches in literature. The French school of EDF (Penot *et al.*, 2005; Tatin *et al.*, 2015) uses the approach $h = (z_{FSL} - z)/(z_{FSL} - z_e)$, where z_{FSL} is the full supply level (FSL) of the reservoir, z is the current reservoir level and z_e is the empty reservoir level. This leads to an interval of $h = [0, 1]$, with $h = 0$ for a full and $h = 1$ for an empty reservoir. Weber (2002) uses Chebyshev polynomials based on a centred and scaled water level h. The advantage of these polynomials is that they are orthogonal, and therefore low VIF-values are expected. There are other scalings for the water level, but most of them scale between 0 and 1. For the time t, it is common to scale the total number of days of one year to 1 and to set $t = 0$ at the starting point of the regression analysis. The temperature measurement values are usually not scaled. In some cases, the temperature that was measured when the joints were grouted or the long-term average temperature is subtracted from the measured values (Léger and Leclerc, 2007).

2.5.4.5 Solution procedures

There is a wide range of solution procedures to analyse dam behaviour based on measurements with statistical models. Commonly, multiple linear regression (MLR) models are used for dam behaviour analysis (see Section 2.5.4). Some of the key publications are those of the Widmann (1967), Willm and Beaujoint (1967), Swiss Committee on Dams (2003), Penot *et al.* (2005), Léger and Leclerc (2007), Mata *et al.* (2013) and Tatin *et al.* (2015). On the one hand, MLR models are straightforward in application, easy to interpret and many statistical tests are available. On the other hand, the shape functions have to be defined which may not a priori represent the correct behaviour. Furthermore, nonlinear relationships between the different variables cannot be reproduced (Salazar *et al.*, 2015).

There are extensions of the standard MLR algorithm as the Cochrane-Orcutt and the Prais-Winsten algorithm to consider autocorrelation or ridge regression and principal component regression to consider multicollinearity, for example. They are well described in Weber (2002). In addition, there are different procedures to select the best fitting variables. Weber (2002) suggests performing forward selection and backward selection on the basis of the t-values. Saouma *et al.* (2001) perform best subset selection, where all possible combinations of regressors are determined and the corresponding models are compared.

The second most widely used approach are artificial neural networks (ANNs). They consist of single neurons that are operators with a nonlinear transfer function between the

input and the output (Fig. 2.47a) (Mata, 2011). The connection of the neurons arranged in different layers leads to an ANN. There is an input layer, a number of hidden layers and a output layer (Fig. 2.47b). The functionality of ANN is inspired by the human brain (Liu *et al.*, 2008). The output of each neuron is generated by a linear combination of the weights w_{ij} multiplied with the input variable and the application of the transfer function. The training of the network is done by finding the optimal weights w_{ij}. The most common algorithm to find the weights is the so called back-propagation algorithm (Mata, 2011). Overfitting is avoided by splitting the learning into a training, a cross-validation and a test set (Mata, 2011). ANNs allow for complex interaction between the different parameters (Simon *et al.*, 2013). However, the result depends on the chosen network architecture and the initialisation weights. Furthermore, the optimisation can result in a local minimum (Salazar *et al.*, 2015). Thus, different runs with random initialisation and different network architectures are performed (Mata, 2011). Some of the key publication in the field of dam behaviour analysis are from Liu *et al.* (2008), Mata (2011) and Simon *et al.* (2013).

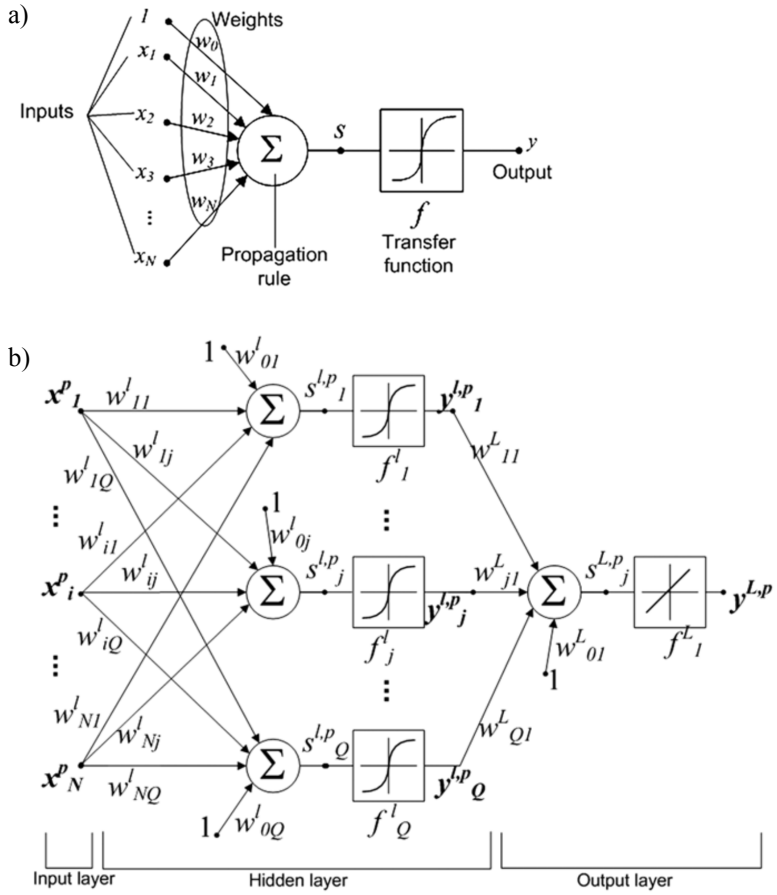

Fig. 2.47 Structure of artificial neural network; a) single neuron with nonlinear transfer function; b) network consisting of different interconnected neurons (Mata, 2011).

Less frequently used are classification based methods like boosting, random forests and support vector machines. Boosting and random forests are based on the classification of the data in trees. The trees are segmenting the data in different branches (James *et al.*, 2013). To prevent overfitting, the calibration is done by a cross-validation approach. Salazar *et al.* (2015) apply both methods in the scope of dam behaviour analysis. Support vector machines are based on a nonlinear transformation of the variables to a high dimensional space. In this space, MLR is performed (Salazar *et al.*, 2015). An application of support vector machines can be found in Su *et al.* (2016) or Salazar *et al.* (2015). Furthermore, there are nonparametric approaches as multivariate adaptive regression splines (MARS). They are based on data depending on piecewise linear functions. Besides the estimation of the shape function, variable selection is performed (Salazar *et al.*, 2015). An application can be found in Salazar *et al.* (2015). Another nonparametric approach is the K-nearest neighbours approach which was used by Saouma *et al.* (2001). Palumbo *et al.* (2001) and Piroddi and Spinelli (2003) use a nonlinear autoregressive model with exogenous input (NARX) in combination with an identification algorithm. In this autoregressive approach, delayed measurement values of a pendulum and also the water level and the temperature are taken into account. A combination of NARX and support vector machines is used by Ranković *et al.* (2014). Salazar *et al.* (2015) explain and empirically compare the concept of the MLR with a seasonal approach, ANN, random forests, boosting and MARS by means of a case study of an arch dam. They used the displacement in radial and tangential direction as well as the drainage flow as behaviour indicators.

2.5.5 Behaviour analysis concepts

There are different ways to carry out behaviour analysis. The simplest approach is a graphical method based on envelope curves that does not need a model describing the behaviour indicator. More advanced methods are based on dam behaviour analysis models. These are the observation-prediction comparison and the adjusted behaviour indicator.

2.5.5.1 Graphical method based on envelope curve

Many of the Swiss dam operators use an envelope curve approach complementary to the more advanced models. In this approach, the measured radial displacement is plotted versus the measured tangential displacement for instance. In addition, the measured displacement can be plotted versus the water level. Due to the influence of the concrete temperature a hysteresis results. Biedermann (1997) compared the observation-prediction comparison with the graphical method for the Zeuzier arch dam. For the graphical method the abnormal behaviour appears two months later (6.12.1978) than it would have been observed by the observation-prediction comparison (6.10.1978) (Fig. 2.48).

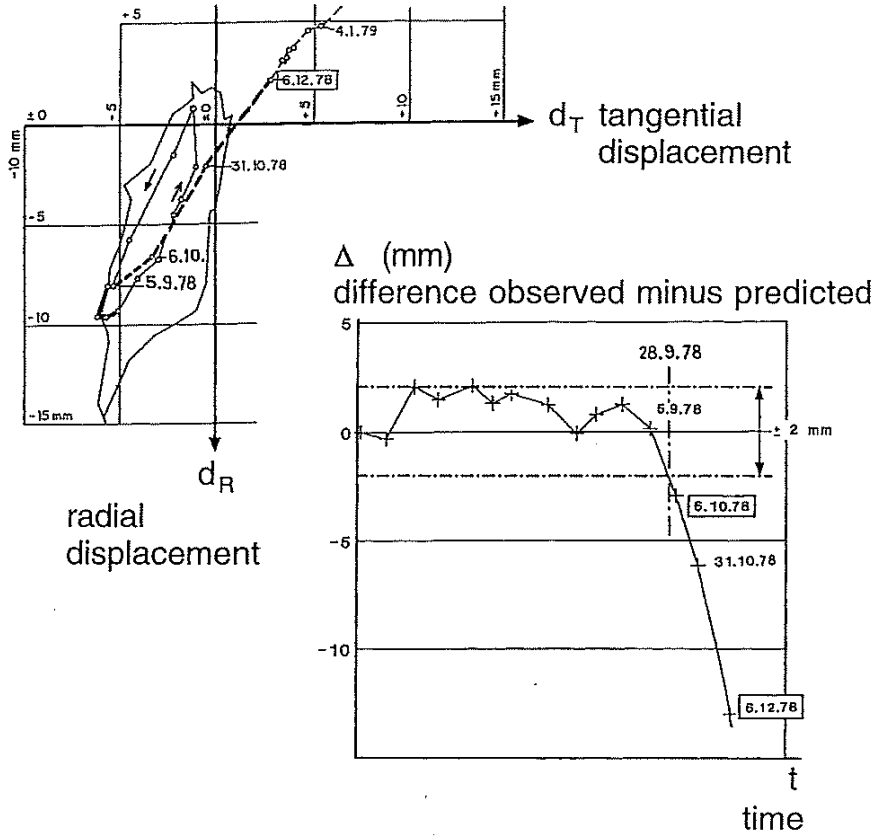

Fig. 2.48 Detection of abnormal behaviour at Zeuzier arch dam by envelope approach and observation-prediction comparison (Biedermann, 1997).

2.5.5.2 Observation-prediction comparison

A common way to analyse the behaviour of dams is the observation-prediction comparison (OPC) of measurements M of a behaviour indicator to their corresponding predicted values P (Swiss Committee on Dams, 2003). The workflow is divided in three parts: (i) observation, (ii) modelling and (iii) behaviour analysis. A schematic display of the workflow is given in Fig. 2.49. The observation is done as described in Section 2.1.4.1. Then a model equation is chosen and calibrated and validated with one part of the available data. This step also includes statistical model adequacy checking and optimising the chosen model equation. If a satisfying model is reached, the modelled displacements for the different effects (water level, temperature, irreversible) are calculated. This is also done for data used for prediction.

To analyse the behaviour with the OPC, the difference D between the observation M and the prediction P is estimated and analysed. Here, prediction is meant in terms of statistics where predicted values were not used for calibration and not in terms of prediction to future displacements. The difference D is the sum of measurement errors, modelling errors and the actual deviation from the expected behaviour. These three components are not

treated separately (Swiss Committee on Dams, 2003). To analyse the behaviour, a prediction band is commonly used (Weber, 2002; Swiss Committee on Dams, 2003; De Sortis and Paoliani, 2007). Points that are outside this prediction band indicate a possible abnormal behaviour. On the one hand, the band width should be small to recognise a possible abnormal behaviour as early as possible. On the other hand, it should not be too small to avoid that it is exceeded too frequently (Weber, 2002). Commonly a 95% prediction interval is used.

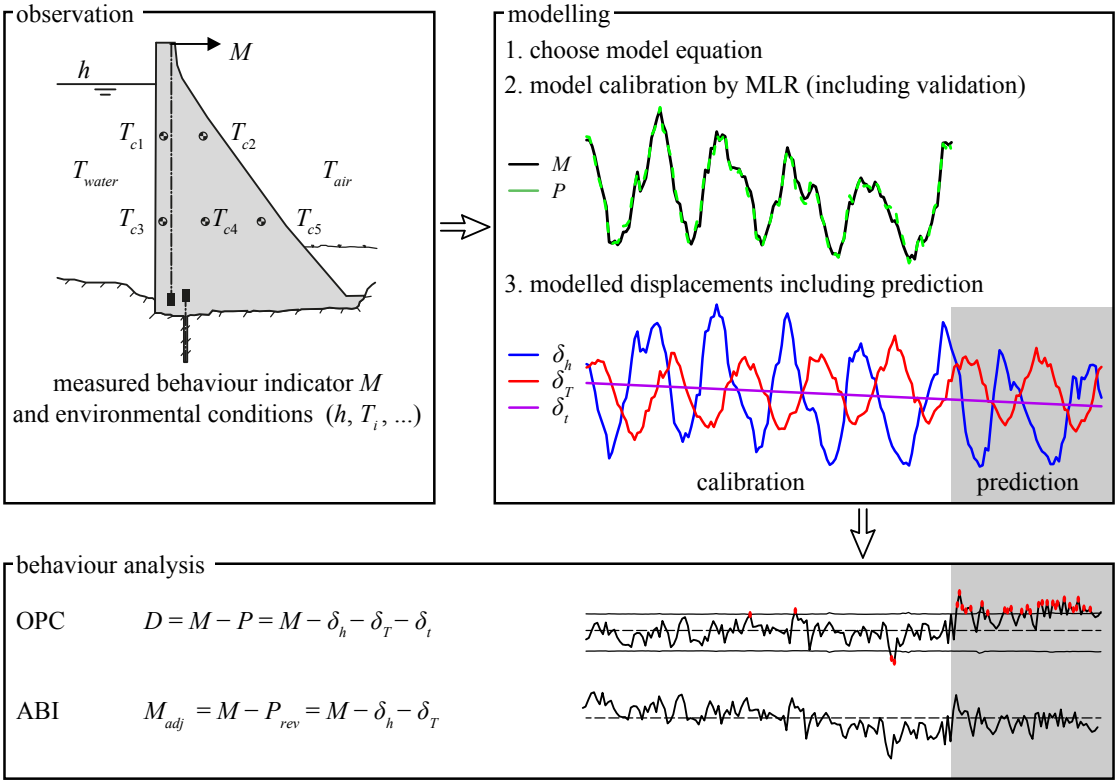

Fig. 2.49 Workflow of DBA summarised in three steps: observation, modelling and behaviour analysis (OPC and ABI).

2.5.5.3 Adjusted behaviour indicator

A similar way to perform behaviour analysis is the adjusted behaviour indicator approach (ABI). The observation and the modelling are equal to the OPC but the behaviour analysis part is different (Fig. 2.49). The concept of the ABI is to highlight irreversible changes of a behaviour indicator by subtraction of the modelled reversible variables P_{rev} from the measurements of the behaviour indicator M (Penot *et al.*, 2005; Amberg, 2009):

$$M_{adj} = M - P_{rev} = \beta_0 + f(t) + e \tag{2.108}$$

The remaining part is the herein called adjusted behaviour indicator M_{adj}. It is the sum of the intercept β_0, the irreversible displacements $f(t)$ and the residuals e. The analysis of the behaviour can be done by checking for trends and behaviour changes of the structure in M_{adj}.

2.6 Software tools for dam behaviour analysis

In 2004, the Swiss Federal Office of Energy (SFOE) launched the Software DamReg (Weber, 2004), in which MLR models can be set up and evaluated. DamReg has recently been re-engineered at the Laboratory of Hydraulics, Hydrology and Glaciology VAW of ETH in Zurich and is now called DamBASE. In doing so, the R environment (R Core Team, 2013) has been integrated in the software to facilitate the application and testing of various procedures for statistical analysis. Besides the option to set up common HST and HTT models, there is a simple method for the heat conductivity and the option to define splines defining a hybrid model by the import of results from FE models. In addition to standard regression procedures, the software provides special case treatment such as dealing with autocorrelation with extended concepts like ridge and principal component regression to handle multicollinearity.

In this thesis, the calculations have been done by the use of the R environment (R Core Team, 2013). Some of the developed scripts will be implemented in the software DamBASE.

3 Heat transfer analysis

3.1 Introduction

In dam behaviour analysis, the information of the thermometers shall be linked to the measured displacement to estimate the thermal effects. There are approaches where the temperature readings are directly linked to the displacement by regression analysis. However, the heat transport in the dam is a diffusive process. This means that the thermal signals from external influence quantities such as solar radiation arrive delayed and damped inside the dam. As a consequence, the measured temperatures only give local information (Tatin *et al.*, 2015). Therefore, the thermometer locations influence the result of a statistical analysis when using the measurements without any pre-processing. However, there are statistical approaches that use the mean temperature T_m and the temperature difference T_d as a basis for the regression model. These quantities physically cause the displacement of the structure (for details see Section 2.2.2.3). In addition, these quantities can be used to calculate the displacement by a mechanical model. In concrete dams, heat transport can often be simplified as a one-dimensional problem between the upstream and the downstream surfaces (Obernhuber and Perner, 2005). Hence, the thermometers in concrete dams are usually grouped on different levels. Different levels are needed to (i) consider the effect of the water level on the temperature field of the dam (Tatin *et al.*, 2015) and (ii) to consider the different thermal inertia of dam sections varying with dam height.

In this chapter, procedures to calculate the mean temperature T_m and the temperature difference T_d are presented and analysed. At the beginning, it is shown how the thermal diffusivity can be calibrated if more than two sensors are available at one level. In a next step, inverse heat conduction analysis is discussed. This is needed, since the thermometers are commonly embedded in the concrete body 0.25 - 2 m away from the boundaries. As a consequence, regions where no temperature information can be obtained by the direct heat conduction analysis (DHCA) exist. By the use of inverse heat conduction analysis (IHCA), the temperature between the boundary and the first thermometer can be estimated. Unfortunately, due to measurement errors, IHCA can be affected by stability problems (Raynaud and Beck, 1988). Besides the evaluation of a stabilising procedure from literature, a new approach is presented.

In this thesis, two solution procedures, (i) finite differences and (ii) the frequency domain solution are used to perform heat conduction analysis. Both of them have their advantages and disadvantages. For direct heat conduction analysis, equal results were obtained when comparing the two procedures. On the one hand, the calculation of the finite difference approach with a Crank-Nicolson scheme (see Appendix A.2.1.1 for details) was slightly faster than the frequency domain solution where a fast Fourier transformation (FFT) has to be performed for several temperatures. On the other hand, the frequency domain solu-

tion is more intuitive when applying stabilisation criteria for IHCA. Since the different frequencies of the thermal signals have different amplitude decays and propagation velocities, a frequency-dependent filter criterion can be formulated. In the finite difference approach, the calculation is stabilised by the discretisation, more precisely by the choice of the spatial discretisation and the time step. No general valid discretisation could be found, however. Thus, data of the boundary temperatures had to be used to prevent from artificial amplifications. Therefore, the frequency domain approach is presented here. For the sake of consistency, the frequency domain approach is used for both the direct and the inverse heat conduction analysis.

3.2 Calibration of thermal diffusivity

3.2.1 Introduction

In most cases, more than two thermometers are placed on one level between the upstream and the downstream face of a concrete dam. This allows to use the two outermost thermometers close to the surfaces as boundary condition and the inner thermometers to calibrate the thermal diffusivity. The thermal diffusivity determines how fast the temperature propagates inside the concrete body. In the next sections, it is described how this calibration can be done. In addition, the results of the calibration for different reference dams are shown.

3.2.2 Methodology

3.2.2.1 Optimisation procedure

Consider a one-dimensional slab with length L and two thermometers T_1 and T_n at the left and the right boundary (Fig 3.1). The one-dimensional heat conduction equation in the frequency domain (Eq. 2.40) with T_1 ($x = 0$) and T_n ($x = L$) as boundary temperatures can be used to calculate the temperature at any location in the interval [0, L]. As a consequence, the temperature T_i in the inner part can be calculated and compared to available measurements. Thus, the thermal diffusivity a of the concrete slab can be optimised in the way that the sum of the squared errors between the measurements and the calculation is minimised. The same weights were given to all temperature sensors T_i. In most cases, this is suitable since the distribution of the measurement locations is more or less equal along the slab. If there is a non-symmetrical distribution, the individual *RMSE* can be weighted by the distance in x-direction of the sensors.

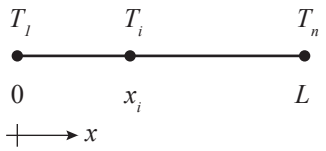

Fig. 3.1 One-dimensional slab with thermometers T_1 and T_n at the boundaries.

If only two thermometer readings are available on a level, the thermal diffusivity cannot be calibrated. If there is another level with more than two thermometers, the calibrated thermal diffusivity of this level can be used as an approximation. If this is not the case, the thermal diffusivity a can be optimised in an iterative, or even more sophisticated, in a nonlinear optimisation procedure by means of the dam behaviour analysis model.

3.2.2.2 Initial phase

Besides seasonal information, temperature measurements can contain small trends. These may be induced by global warming (Santillán *et al.*, 2015) or naturally colder and warmer periods. For gravity dam G2 (see Appendix A.5.2), a linear trend of 0.02 °C/a has been observed between 2000 - 2016 and for another dam not further used in this thesis, a linear increase of 0.12 °C/a has been measured during the last decade.

To show the effect of a trend in the temperature data, a 25 m thick concrete slab with a thermal diffusivity of a = 0.15 m^2/d is considered. On both surfaces a linear temperature drift $T_{\mathrm{b,drift}} = 0.1$ °C/a over a time period of 20 years is applied (Fig. 3.2a). When using the heat conduction equation in the frequency domain (Eq. (2.40)), the signal has to be transformed by a Fourier transform. In Fig. 3.2a, the sum of the five lowest frequencies $T_{b,\mathrm{FFT},1-5}$ is shown. In addition, the individual of the five lowest frequencies are shown in Fig. 3.2b. Applying Eq. (2.40) to calculate the temperature $T_{12.5}$ in the middle of the slab leads to a damping and phase shift $\Delta\phi$ of these signals (Fig. 3.2c). The sum of the damped and the phase shifted signals is shown in Fig. 3.2a (red). The linear trend in the mean temperature can be reproduced well even only the five lowest frequencies are shown. If the sum over all frequencies is taken, a smooth straight line results. In Fig. 3.2d, the boundary temperature $T_{b,\mathrm{dirft}}$ and the temperature in the middle $T_{12.5}$ are shown. It can be recognised that the gradient of the drift in the middle of the slab is the same as on the boundary with a delay. Unfortunately, a deviation occurs during the first years. This deviation comes from the phase shift of the low frequencies. Consequently, this leads to a reduction of the data that can be used for further analysis. As a countermeasure, an initial phase can be inserted before the data. The length of this initial phase depends mainly on the thickness of the slab and the gradient of the drift function. In addition, the thermal diffusivity a has an influence as well. In this thesis, the length of the initial phase was determined so that the temperature in the middle of the slab does no longer significantly change when adding additional years before the data.

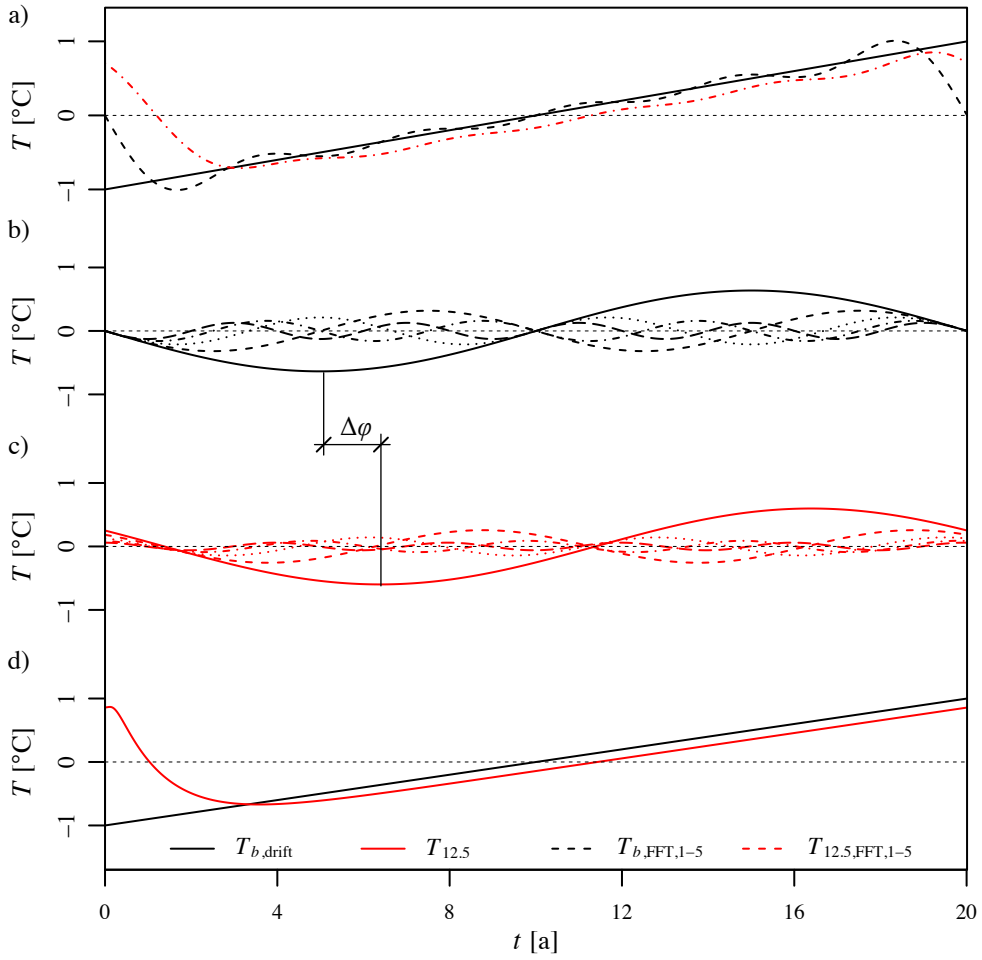

Fig. 3.2 Example of a 25 m thick concrete slab; a) linear temperature drift (solid black line), linear temperature drift approximated by the five lowest frequencies (dashed black line) and the same five frequencies that were used to calculate the temperature in the middle $T_{12.5}$ of a 25 m thick concrete slab (dashed red line); b) five lowest frequencies at the boundary; c) damped and phase shifted frequencies in the middle of the slab; d) linear temperature drift at the boundary $T_{b,\mathrm{dirft}}$ (solid black line) and estimated temperature in the middle of the slab $T_{12.5}$ (solid red line).

Since no temperature measurements are available for the initial phase, artificial temperature data are created by a regression model that is fitted to the measurement data. A first order seasonal function and a linear trend are used as regressor variables:

$$T = \beta_0 + \beta_1 \sin(S) + \beta_2 \cos(S) + \beta_3 t. \tag{3.1}$$

The predicted temperatures are inserted before the measured data. Due to the fact that the initial phase is principally necessary in thick slabs, where only the low frequencies can be measured in the middle, this approach proofed to work well. In Fig. 3.3, the results of a heat conduction analysis of gravity dam G2 are shown for the level of 250 m a.s.l. T_1

and T_5 are the measured temperatures close to the boundaries (Fig. 3.3a). The length of the initial phase was determined to four years. The resulting temperature in the middle of the slab $T_{17.4,ini}$ is shown in Fig. 3.3b. In addition, the resulting temperature $T_{17.4}$ for the calculation without the use of an initial phase is shown. By comparing the two results, the need of an initial phase becomes obvious. The duration was estimated to 4 years by rising its duration and comparing the results.

An initial phase is also necessary for the finite difference approach. Its length can be determined by adding initial years before the data and check whether there are any changes in the calculated temperature in the middle of the slab.

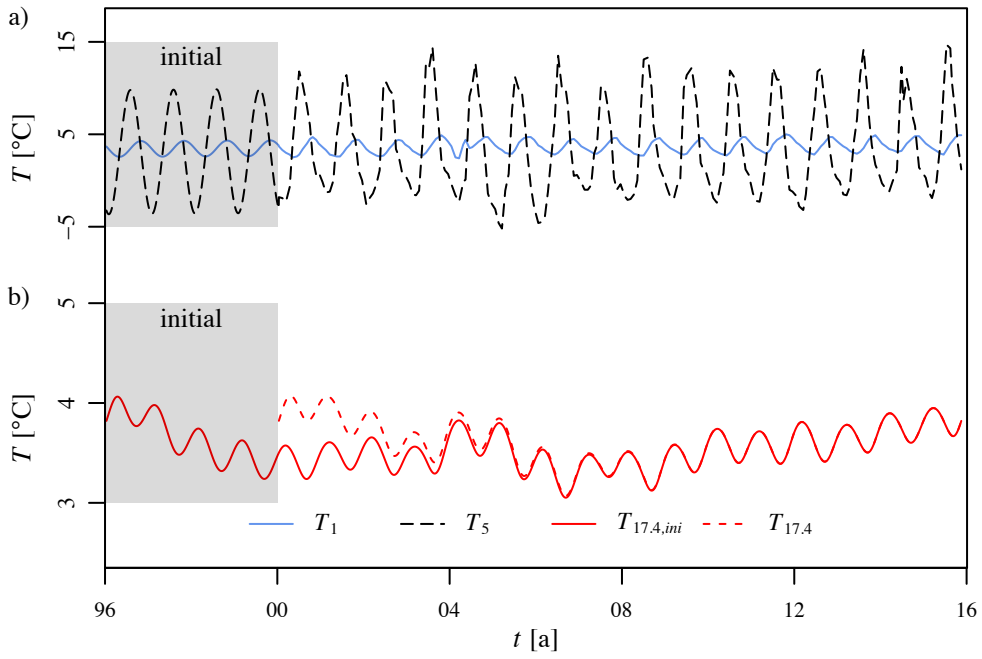

Fig. 3.3 Heat conduction applied for gravity dam G2 at level 250 m a.s.l.; a) temperature measurements T_1 and T_5 located close to the upstream and downstream boundaries are used as input data; b) the temperature $T_{17.4,ini}$ in the middle was calculated with the use of an initial phase of 4 years (solid red line). The need of an initial phase is obvious when comparing with the calculation of $T_{17.4}$, where no initial phase was used (dashed red line).

3.2.3 Results

For all concrete dams used for the model evaluation later in this thesis (see Appendix A.5), the thermal diffusivity was calibrated for different levels. Table 3.1 shows the resulting thermal diffusivity a and the *RMSE* of the calibration as a measure of accuracy. In addition, the number of inner temperature sensors and the duration of the estimated initial phase t_I is given.

Table 3.1 Calibrated thermal diffusivity a for different concrete dams. In addition, the *RMSE* of the calibration, the number of thermometers available for the calibration n_i, the slab length L and the estimated duration of the initial phase t_I are given.

dam	level [m a.s.l.]	a [m^2/d]	*RMSE* [°C]	n_i [-]	L [m]	t_I [a]
G1	283	0.156	0.30	1	12.29	1
	262	0.161	0.30	3	27.74	2
	241	0.243	0.80	6	44.99	10
G2	272	0.174	0.19	2	19.20	1
	250	0.196	0.33	3	35.80	4
	223	0.270	0.16	4	56.50	12
A1	293	0.109	0.84	2	3.80	2
	284	0.126	0.73	3	5.20	3
	272	0.102	0.74	3	6.60	3
	260	0.109	0.59	3	7.40	3
A2	299	0.278	1.48	3	9.80	2
	281	0.135	1.36	3	14.29	4
	251	0.100	0.96	4	17.63	4
	203	0.122	0.35	4	21.19	4
	158	0.168	0.51	4	28.80	4
A3	297	0.129	0.75	1	5.63	1
	276	0.121	0.49	1	8.75	1
	255	0.076	0.38	1	10.88	1
AG1	292	0.138	0.22	1	11.50	1
	273	0.157	0.26	1	19.95	1
	284	0.123	0.62	2	63.00	4
HG1	292	0.126	0.52	1	6.40	2
	280	0.185	0.38	2	16.30	2
	263	0.216	0.52	3	30.60	4

3.2.4 Discussion

When doing heat conduction analysis, an initial phase is needed. Otherwise, some of the data may not be used for further analysis since the temperature evolution in the middle of the dam needs some time. Because the duration of the initial phase depends on several parameters, a general definition is not possible. Nevertheless, its duration can easily be determined by checking whether the calculated mean temperature does no longer change when inserting years of artificial temperature data before the measurement data.

The calibration of the thermal diffusivity works fine for most of the herein considered cases. Tatin (2014) provides a list with maximum and minimum values of the thermal diffusivity for mass concrete based on eleven literature sources. The values vary between

0.036 and 0.181 m^2/d. There are five estimated values herein that are higher than this range. A closer look at the data and the geometry of the structure helps to explain these deviations. The temperature sensors of the topmost level of arch dam A2 are situated 2.5 m below the crest level. Since the distance to the crest level is smaller than the slab length, the one-dimensional assumption is violated. The heat flow from the crest level results in a higher temperature diffusivity. The hollow gravity dam HG1 is affected by a similar process. The temperature sensors at levels 280 and 263 m a.s.l. are influenced by the temperature in the hollow section which also results in slightly higher temperature diffusivities. The two bottom levels of the gravity dams G1 and G2 are influenced by another phenomenon. The measured temperatures in the core vary little during a year (0.3 - 0.8 °C). A comparison of the yearly peak values of the sensors with different distance to the boundary shows that there is no phase shift and the amplitude differs not much. This stands in contrast to the theory of heat conduction. The remarkable high values in the core of the dams can be explained by the perturbation of the galleries (Léger and Seydou, 2009). Nevertheless, experience has shown that such results still can be used to estimate the mean temperature T_m and the temperature difference T_d. The high thermal diffusivity compensates the additional temperature gain. Furthermore, considerations of the mechanical behaviour show that the temperatures at the bottom of the dam have less influence on the displacement than those on the upper levels.

3.3 Inverse heat conduction analysis

3.3.1 Introduction

Concrete temperature sensors are usually located 0.20 - 2.50 m away from the boundaries. As a consequence, a region where no temperature information can be calculated by DHCA exists. By the use of IHCA, the temperature in the outer region can be estimated. Since IHCA is a mathematical ill-conditioned problem, stabilisation procedures are necessary (for details see Section 2.3.4.1). First, it is discussed how large the influence of the inverse region on the quantities of interest T_m and T_d is. Second, two stabilisation procedures are discussed. One approach is taken from literature (Obernhuber and Perner, 2005; Weber *et al.*, 2010) and the other one is a new development.

3.3.2 The need for inverse heat conduction analysis

For IHCA, two regions inside the concrete slab are distinguished. The direct region between the thermometers where DHCA can be applied and the region between the boundary and the first thermometer where IHCA has to be applied (see Fig. 2.27). The question now is how big the influence of the outer or inverse region on the quantities of interest T_m and T_d is. Intuitively, for small distances d_i from the boundary to the first thermometer, the influence might be small and vice versa. In addition, in long concrete slabs,

the influence might be less than in short ones. This intuitive statement can be checked by applying Eq. (2.45) and (2.46). The mean temperature of the total region $\hat{T}_{m,tot}$ in the interval [0, L] can be calculated by

$$\hat{T}_{m,tot} = \frac{1}{L}\int_0^L \hat{T}(x,\omega)\mathrm{d}x = \frac{\cosh(kL)-1}{kL\sinh(kL)}\left(\hat{T}_{b,l}(\omega)+\hat{T}_{b,r}(\omega)\right). \tag{3.2}$$

The mean temperature $\hat{T}_{m,dir}$ of the direct region in the interval $[x_1, x_2]$ is

$$\begin{aligned}\hat{T}_{m,dir} &= \frac{1}{L}\int_{x_1}^{x_2}\hat{T}(x,\omega)\mathrm{d}x \qquad (3.3)\\ &= \frac{\cosh(k(L-x_1))-\cosh(k(L-x_2))}{kL\sinh(kL)}\hat{T}_{b,l}(\omega)+\frac{\cosh(kx_2)-\cosh(kx_1)}{kL\sinh(kL)}\hat{T}_{b,r}(\omega).\end{aligned}$$

for $d_1 = d_2 = d$, which is often satisfied or almost satisfied, it simplifies to

$$\hat{T}_{m,dir} = \frac{\cosh(k(L-d))-\cosh(kd)}{kL\sinh(kL)}\left(\hat{T}_{b,l}(\omega)+\hat{T}_{b,r}(\omega)\right) \tag{3.4}$$

Now, the ratio r_{Tm} between the mean temperature in the total region $\hat{T}_{m,tot}$ and the mean temperature in the direct region $\hat{T}_{m,dir}$ can be defined as follows:

$$r_{Tm} = \frac{\hat{T}_{m,tot}}{\hat{T}_{m,dir}} = \frac{\cosh(kL)-1}{\cosh(k(L-d))-\cosh(kd)} \tag{3.5}$$

By introducing the dimensionless temperature sensor position $d^* = d/L$ and the dimensionless slab length $L^* = \sqrt{\omega/a}L$, Eq. (3.5) becomes

$$r_{Tm} = \frac{\hat{T}_{m,tot}}{\hat{T}_{m,dir}} = \frac{\cosh(\sqrt{i}L^*)-1}{\cosh(\sqrt{i}L^*(1-d^*))-\cosh(\sqrt{i}L^*d^*))} \tag{3.6}$$

The same analysis can be done for the temperature difference $\hat{T}_d$. The temperature difference of the total region can be found by

$$\hat{T}_{d,tot} = \frac{12}{L^2}\int_0^L \hat{T}(x,\omega)(\mathrm{x}-\frac{\mathrm{L}}{2})\mathrm{d}x = \frac{12}{(kL)^2}\left(\frac{kL}{2\tanh\left(\frac{kL}{2}\right)}-1\right)\left(\hat{T}_{b,l}(\omega)-\hat{T}_{b,r}(\omega)\right) \tag{3.7}$$

The temperature difference of the direct region can be found by

$$\begin{aligned}
\hat{T}_{d,dir}(\omega) &= \frac{12}{L^2}\int_{x_1}^{x_2}\hat{T}(x,\omega)(x-\frac{L}{2})\mathrm{d}x && (3.8)\\
&= \frac{12}{(kL)^2\sinh(kL)}\left(A(x_1,x_2)\,\hat{T}_{b,l}(\omega)+B(x_1,x_2)\,\hat{T}_{b,r}(\omega)\right) && (3.9)\\
A(x_1,x_2) &= k\left(x_1-\frac{L}{2}\right)\cosh(k(L-x_1)-k\left(x_2-\frac{L}{2}\right)\cosh(k(L-x_2) && (3.10)\\
&\quad +\sinh(k(L-x_1))-\sinh(k(L-x_2))\\
B(x_1,x_2) &= k\left(x_2-\frac{L}{2}\right)\cosh(kx_2)-k\left(x_1-\frac{L}{2}\right)\cosh(kx_1) && (3.11)\\
&\quad +\sinh(kx_1)-\sinh(kx_2)
\end{aligned}$$

If again the simplification $d_1 = d_2 = d$ is used, the ratio r_{Td} results:

$$r_{Td}=\frac{\hat{T}_{d,tot}}{\hat{T}_{d,dir}}=\frac{\sinh(kL)\left(\dfrac{kL}{2\tanh(kL/2)}-1\right)}{k\left(\dfrac{L}{2}-d\right)\left(\cosh(k(L-d))+\cosh(kd)\right)+\sinh(kd)-\sinh(k(L-d))} \tag{3.12}$$

In dimensionless form Eq. (3.12) can be transformed to

$$r_{Td}=\frac{\dfrac{\sinh(\sqrt{i}L^*)}{\sqrt{i}L^*\left(\dfrac{1}{2}-d^*\right)}\left(\dfrac{\sqrt{i}L^*}{2\tanh(\sqrt{i}L^*/2)}-1\right)}{\left(\cosh(\sqrt{i}L^*(1-d^*))+\cosh(\sqrt{i}L^*d^*)\right)+\dfrac{\sinh(\sqrt{i}L^*d^*)-\sinh(\sqrt{i}L^*(1-d^*))}{\sqrt{i}L^*\left(\dfrac{1}{2}-d^*\right)}}. \tag{3.13}$$

The moduli of the ratios r_{Tm} and r_{Td} represent the ratio between the amplitudes of the total and the direct region. In Fig. 3.4a and b the moduli of the two dimensionless equations Eq. (3.6) and (3.13), are plotted for varying dimensionless parameters L^* and d^*. In addition, L^* and d^* of the investigated concrete slabs of Table 3.1 are shown by red dots. For the frequency ω, the measurement sampling rate was used. It can be seen that considering the inverse region leads to up to 3 times higher amplitudes for $\hat{T}_m$ and up to 10 times higher amplitudes for $\hat{T}_d$. The argument of r_{Tm} and r_{Td} leads to the phase shift due to the inverse region. In Fig. 3.4c and d, the arguments of Eq. (3.6) and (3.13) are shown. For

the investigated data, the phase shift is between 0 and 0.25, which corresponds to about two weeks.

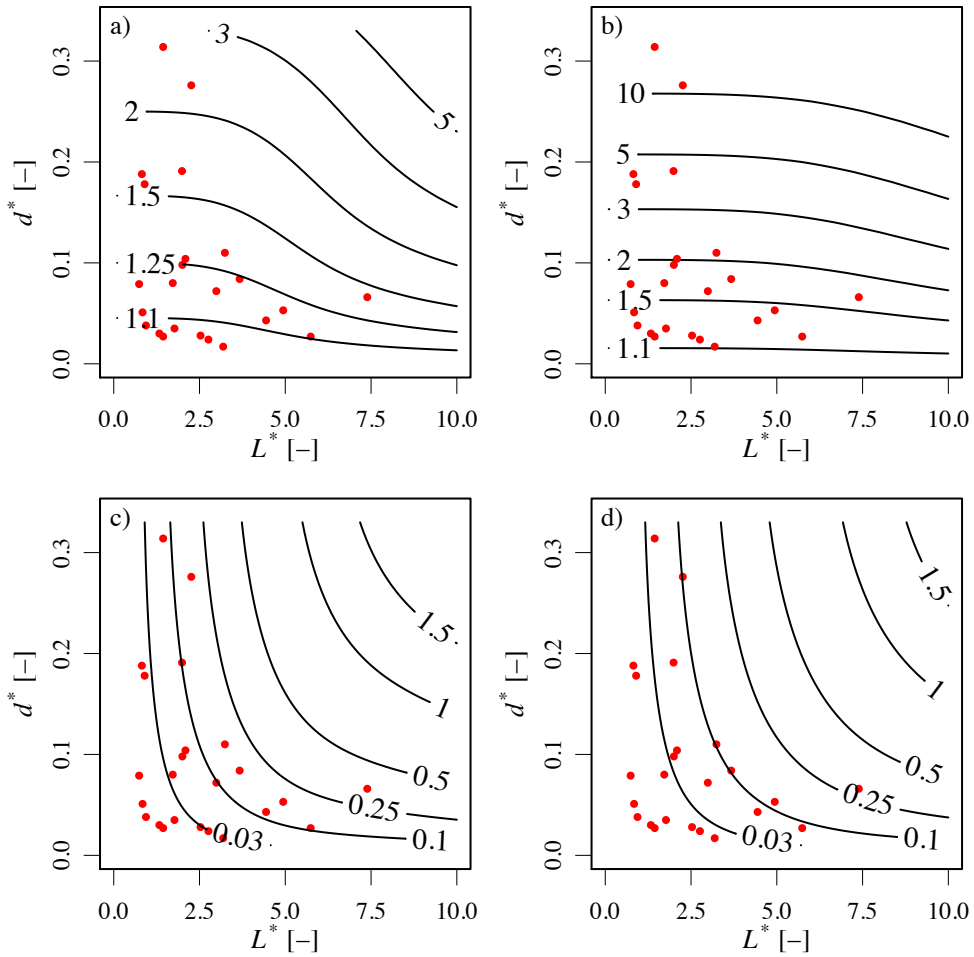

Fig. 3.4 Influence of the inverse region on the mean temperature $\hat{T}_m$ and the temperature difference $\hat{T}_d$: ratio between the amplitude of the total region and the direct region for a) $\hat{T}_m$ and b) $\hat{T}_d$; phase shift due to considering the inverse region for c) $\hat{T}_m$ and d) $\hat{T}_d$. L^* and d^* of the investigated concrete slabs of Table 3.1 are shown by the red dots. For the frequency ω, the measurement sampling rate was used.

As a result, the consideration of the inverse region seems to be important. Besides an amplification of the mean temperature $\hat{T}_m$ and the temperature difference $\hat{T}_d$, a phase shift is considered. A phase shift of two weeks represents about the shift of one measurement time lag. In most of the case studies, significant differences result. Generally, a smaller dimensionless temperature sensor location leads to less difference. Moreover, the higher the frequency is, the larger are the amplification and the phase shift. This means that the signal of the yearly variation is less affected by changes than the monthly or bi-weekly fluctuations.

3.3.3 Methodology to evaluate stabilising procedures

As mentioned in Section 3.3.1, stabilising procedures are necessary when performing IHCA. To evaluate stabilising procedures for IHCA, measurement data at different locations near the boundary should be available. Inner temperature measurements can be used as input data to calculate the temperature in the outer regions. The calculated outer temperatures can be compared to the corresponding measurements. As a consequence, dams with at least two thermometers within the first 3 m can be used for the evaluation. Since the air temperature is not equal to the boundary temperature because of convection and radiation, only concrete temperature measurements and water temperature measurements were considered. The water temperature is assumed to be equal to the boundary temperature (Amberg, 2003). The arch dams A1 and A2 have such a thermometer layout (Fig. 3.5a and b). In addition, arch dam A3 was used because of the available water temperature measurements (Fig. 3.5c).

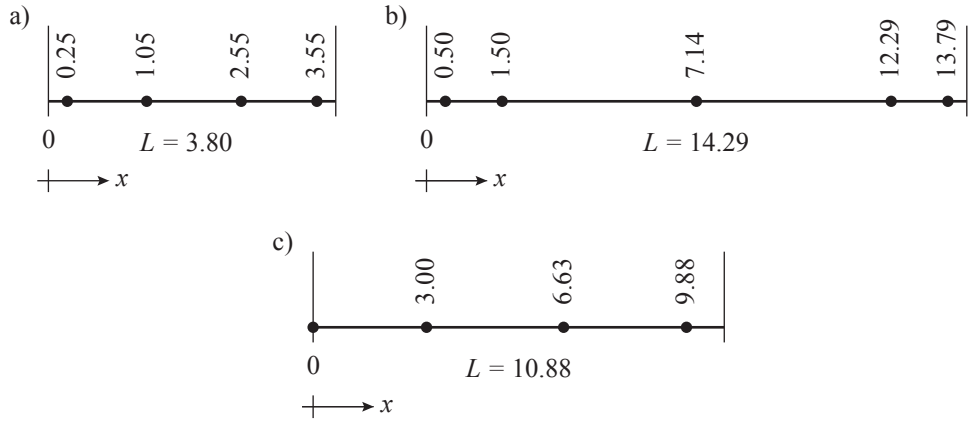

Fig. 3.5 Thermometer positioning of a) arch dam A1 at 293 m a.s.l.; b) arch dam A2 at 281 m a.s.l.; c) arch dam A3 at 255 m a.s.l.

3.3.4 Stabilisation procedure with mollifier function

For the data sets described above, the stabilising procedure by a mollifier function proposed by Obernhuber and Perner (2005) or Weber *et al.* (2010) was applied. To determine the regularisation parameter γ, the data of the outer measurements was used. In doing so, the $RMSE_{cal}$ between the measured and the calculated outer temperatures was minimised. The calibrated γ and the corresponding $RMSE_{cal}$ are given in Table 3.2. In addition, the $RMSE_{Tm}$ and $RMSE_{Td}$ that represent the difference between the quantities calculated by the IHCA using outer and inner thermometers are provided for arch dam A1 and A2. This was not done for arch dam A3 since the boundary temperature on the air side is not known.

Table 3.2 Calibrated regularisation parameter γ for different inverse heat conduction analyses. In addition, the difference $RMSE_{Tm}$ and $RMSE_{Td}$ to T_m and T_d calculated by the outer measurements is given.

dam	level [m a.s.l.]	data	γ [-]	$RMSE_{cal}$ [°C]	$RMSE_{Tm}$ [°C]	$RMSE_{Td}$ [°C]
A1	293	weekly	0.029	1.2	0.8	1.2
	293	monthly	0.017	1.5	1.0	1.6
A2	281	monthly	0.033	1.6	0.5	1.0
A3	255	monthly	0.17	1.4	-	-

The larger the distance over which IHCA was applied, the larger are the observed regularisation parameters. The case study of A1 nicely shows that γ does not only depend on the distance but also on the measurement time step. Therefore, its value is difficult to determine if no outer measurements are available. Unfortunately, this is usually the case. The $RMSE_{cal}$ between the calibrated and measured temperatures is between 1.2 and 1.6 °C for the investigated data sets. In addition, the $RMSE_{Tm}$ and the $RMSE_{Td}$ are in the same order. $RMSE_{Td}$ is generally larger than $RMSE_{Tm}$.

3.3.5 New stabilisation procedure

Since the choice of the stabilising parameter γ is difficult if no outer measurement data are available, a new procedure was developed. The idea behind this approach is that measurement deviations (noise, errors) recorded by the thermometers are not amplified when calculating the quantities of interest T_m and T_d.

3.3.5.1 Derivation

In Section 3.3.2, the ratio r_{Tm} that expresses the ratio between the mean temperature of the total and the direct region was introduced. The ratio can be defined individually for the left boundary temperature $\hat{T}_{b,l}(\omega)$ and the right boundary temperature $\hat{T}_{b,r}(\omega)$:

$$r_{Tm,l} = \frac{\hat{T}_{m,tot}(\hat{T}_{b,l})}{\hat{T}_{m,dir}(\hat{T}_{b,l})} = \frac{\cosh(kL)-1}{\cosh(k(L-x_1))-\cosh(k(L-x_2))}, \tag{3.14}$$

$$r_{Tm,r} = \frac{\hat{T}_{m,tot}(\hat{T}_{b,r})}{\hat{T}_{m,dir}(\hat{T}_{b,r})} = \frac{\cosh(kL)-1}{\cosh(kx_1)-\cosh(kx_2)}. \tag{3.15}$$

The mean temperature of the direct region can alternatively be expressed in function of the measured inner temperatures $\hat{T}_{x1}$ and $\hat{T}_{x2}$ and their distance l between them:

$$\hat{T}_m(\hat{T}_{x1},\hat{T}_{x2}) = \frac{\tanh\left(\frac{kl}{2}\right)}{kL}(\hat{T}_{x1}+\hat{T}_{x2}). \tag{3.16}$$

Thus, the mean temperature of the total region $\hat{T}_{m,tot}$ can directly be estimated by $r_{Tm,i}\,\hat{T}_m(\hat{T}_{xi})$, applying the superposition principle:

$$\hat{T}_{m,tot}(\hat{T}_{x1}) = \frac{\tanh\left(\frac{kl}{2}\right)}{kL}\frac{(\cosh(kL)-1)}{\cosh(k(L-x_1))-\cosh(k(L-x_2))}\hat{T}_{x1}, \tag{3.17}$$

$$\hat{T}_{m,tot}(\hat{T}_{x2}) = \frac{\tanh\left(\frac{kl}{2}\right)}{kL}\frac{(\cosh(kL)-1)}{\cosh(kx_1)-\cosh(kx_2)}\hat{T}_{x2}, \tag{3.18}$$

$$\hat{T}_{m,tot} = \hat{T}_{m,tot}(\hat{T}_{x1})+\hat{T}_{m,tot}(\hat{T}_{x2}). \tag{3.19}$$

With Eq. (3.17) - (3.19) the mean temperature can directly be estimated from two inner thermometer readings $\hat{T}_{x1}$ and $\hat{T}_{x2}$. The inverse heat conduction is considered implicitly.

The same derivation as for the mean temperature can be done for the temperature difference. It results in the following equations that can be used to calculate the temperature difference $\hat{T}_d$ from two inner thermometers $\hat{T}_{x1}$ and $\hat{T}_{x2}$ and their distance l:

$$\hat{T}_{d,tot}(\hat{T}_{x1}) = \frac{12\left(k\left(x_1-\frac{L}{2}\right)\cosh(kl)-k\left(x_2-\frac{L}{2}\right)+\sinh(kl)\right)}{(kL)^2\sinh(kl)}\hat{T}_{x1}, \tag{3.20}$$

$$\hat{T}_{d,tot}(\hat{T}_{x2}) = \frac{12\left(-k\left(x_1-\frac{L}{2}\right)+k\left(x_2-\frac{L}{2}\right)\cosh(kl)-\sinh(kl)\right)}{(kL)^2\sinh(kl)}\hat{T}_{x2}, \tag{3.21}$$

$$\hat{T}_{d,tot} = \hat{T}_{d,tot}(\hat{T}_{x1})+\hat{T}_{d,tot}(\hat{T}_{x2}). \tag{3.22}$$

3.3.5.2 Limitation of the measurement noise amplification

The equations (3.17) - (3.18) and (3.20) - (3.21) can be seen as transfer functions multiplied with the measurements of the inner temperature sensors $\hat{T}_{xi}$. Potential measurement deviations which are disturbing the result are multiplied with these transfer functions. Thus, the amplification of the measurement deviations can be avoided if the modulus of these transfer functions is limited to a certain threshold value Mod_{th}. Obviously, a threshold value of 1 means no amplification of the measurement deviations. However, for certain thermometer configurations, the value of the transfer function exceeds 1 even for low frequencies ω. In Fig. 3.6, the transfer functions of $\hat{T}_{x1}$ for the three examples of the arch dams A1, A2 and A3 are shown for $\hat{T}_m$ and $\hat{T}_d$ separately. Due to the large distance from the boundary, the modulus of the transfer functions of arch dam A3 is much higher than for the arch dams A1 and A2. Moreover, the amplification of $\hat{T}_d$ is higher than for $\hat{T}_m$. Good experience was gained with a threshold value equal to the modulus of the

transfer function at the measurement sampling rate, larger or equal to 1. This leads to no information loss for all frequencies that are lower than the measurement sampling rate. For the examples, this is shown by the thin red lines in Fig. 3.6. In addition, the estimated threshold values are given in Table 3.3. For the arch dams A1 and A2, the threshold modulus of the mean temperature can be set to 1. For the temperature difference, it is slightly higher than 1 for arch dam A2 and around 3 for arch dam A1. This means that a measurement deviation of 0.2 °C is amplified to 0.6 °C. For arch dam A3, where the thermometer is 3 m away from the boundary, the threshold modulus is 7.85. This means that a measurement deviation of 0.2 °C is amplified to almost 1.6 °C when calculating the temperature difference. For $\hat{T}_{x2}$, other values that are not discussed here are obtained.

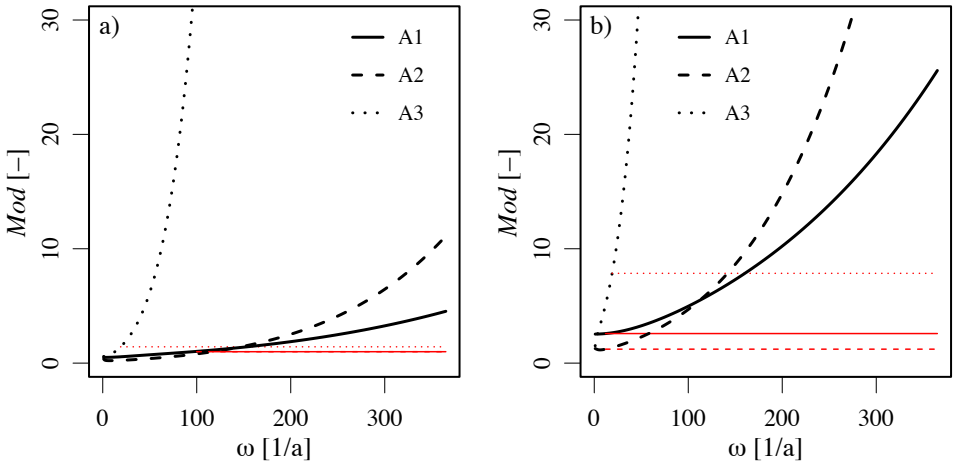

Fig. 3.6 Transfer functions for direct calculation of $\hat{T}_m$ and $\hat{T}_d$ with implicit inverse heat conduction analysis for the examples of the arch dams A1, A2 and A3. The black lines show the modulus Mod of a) $\hat{T}_m$ and b) $\hat{T}_d$. The proposed threshold values Mod_{th} are shown by the thin red lines.

Table 3.3 Estimated threshold values Mod_{th} for different dams and data.

dam	level [m a.s.l.]	data	$Mod_{th,Tm}$ [-]	$Mod_{th,Td}$ [-]
A1	293	weekly	1	3.31
	293	monthly	1	2.58
A2	281	monthly	1	1.22
A3	255	monthly	1.43	7.85

3.3.5.3 Theoretical example with measurement deviation

To show the functionality of the developed stabilisation procedure, a theoretical example is considered (Fig. 3.7). A 10 m thick concrete slab with two temperature sensors, each located 2.5 m away from the boundary, is considered. A constant temperature with a

single measurement deviation of 0.2 °C and a varying measurement time step t_m (28, 14, 7 and 1 day) is assumed for T_1. In addition, the temperature T_2 is set constant.

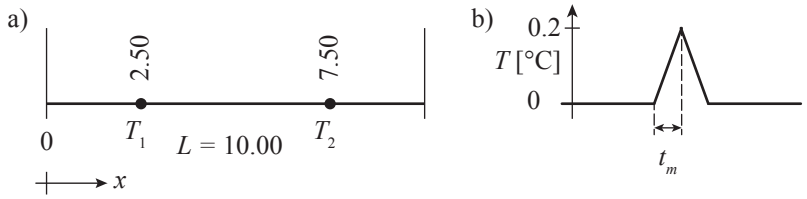

Fig. 3.7 Theoretical example with measurement noise; a) cross section of the concrete slab; b) single measurement error with measurement time step t_m.

For this set up, the mean temperature T_m and the temperature difference T_d were calculated by the use of Eq. (3.19) and (3.22). In a first step, the threshold value of the amplification Mod_{th} was set to 1 and in all other steps it was not limited. The results are shown in Fig. (3.8). The smaller the measurement time step, the more the artificial measurement deviation is amplified (dashed lines). Moreover, the amplification is higher for the calculation of the temperature difference (red) than for the mean temperature (black). The application of the proposed stabilisation procedure (solid lines) limits the amplification to the order of magnitude of the considered measurement deviation 0.2 °C. Moreover, if Mod_{th} is limited to 2 for example, the deviation in the quantities of interest is limited to 0.4 °C. In the case of the mean temperature, the stabilisation only had to be applied for the measurement time step of 1 d. On the contrary, for the temperature difference the stabilisation was necessary for all measurement time steps.

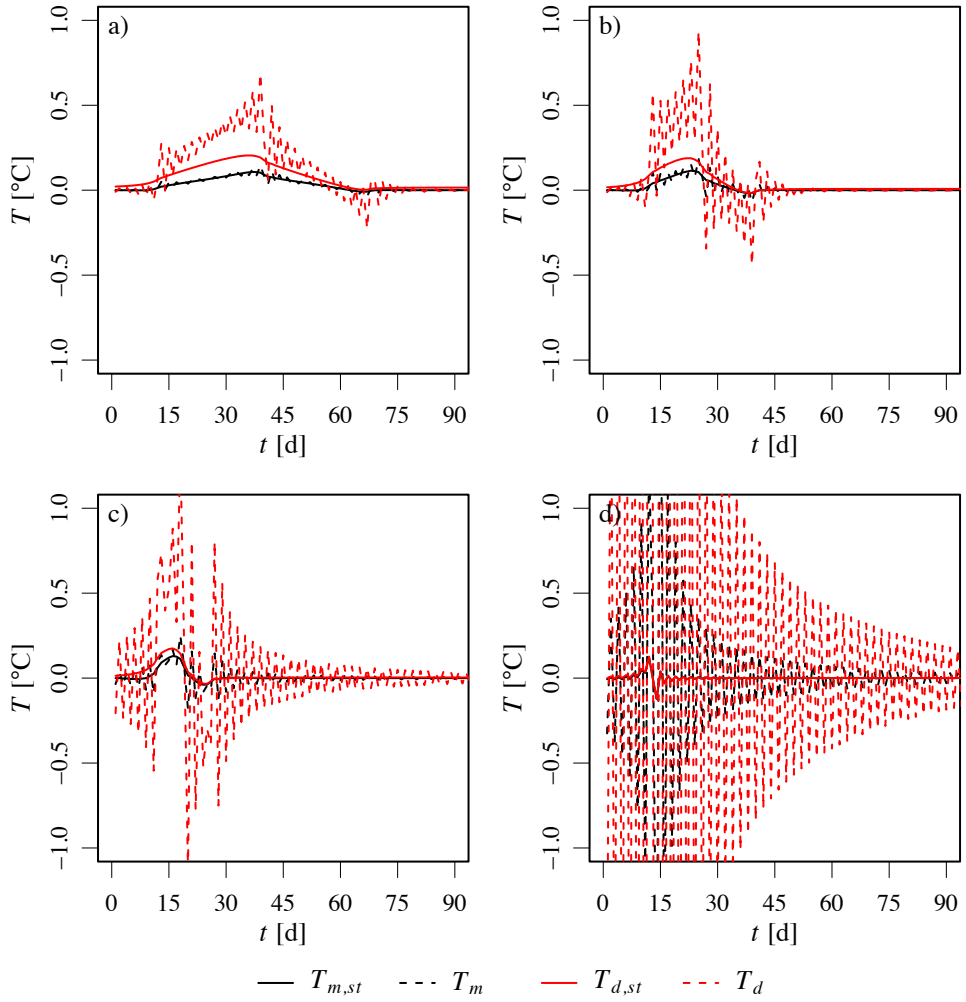

Fig. 3.8 Results of theoretical example for a) t_m = 28 d; b) t_m = 14 d; c) t_m = 7 d; d) t_m = 1 d.

3.3.5.4 Comparison to mollifier approach

In Table 3.4, the results of the same analysis as with the mollifier approach in Section 3.3.4 are presented. The $RMSE_{Tm}$ and $RMSE_{Td}$ of the original data of T_m and T_d are given. A comparison to the mollifier approach shows that the difference between the two stabilisation procedures is small for T_m and larger for T_d. To highlight this fact, the $RMSE_{Tm,\gamma}$ and $RMSE_{Td,\gamma}$ between the new approach and the mollifier approach are given in Table 3.4. For the arch dams A1 and A2, the $RMSE$ between these approaches is very small for T_m. It has the order of the measurement precision. On the other hand, the difference is larger for the temperature difference T_d. This is due to the fact that the outer region where inverse heat conduction is performed has the largest influence on T_d. Compared to a yearly variation of 10 - 15 °C this difference is acceptable. Nevertheless, for arch dam A3 the difference is larger. In Fig. 3.9, the mean temperature and the temperature difference of the mollifier approach (subscript γ) and the new approach with implicit inverse heat conduction (subscript impl), respectively, are shown. Due to the high regularisation

parameter, the result of the mollifier approach is very smooth compared to the result of the new approach. For the mollifier approach, the regularisation parameter is the same for both thermometers T_1 and T_2 whereas in the new approach the limitation of the amplification is estimated individually for both thermometers. In the case of arch dam A3, where T_1 is 3 m away from the boundary and T_2 only 1 m, this plays a major role. By the use of the superposition principle and two different regularisation parameters γ, this problem could possibly be overcome.

Table 3.4 Comparison of new stabilisation approach to mollifier approach and the use of the outer thermometer data.

dam	level [m a.s.l.]	data	$RMSE_{Tm}$ [°C]	$RMSE_{Td}$ [°C]	$RMSE_{Tm,\gamma}$ [°C]	$RMSE_{Td,\gamma}$ [°C]
A1	293	weekly	0.9	1.6	0.2	1.0
	293	monthly	0.8	1.5	0.2	1.0
A2	281	monthly	0.6	1.1	0.1	0.3
A3	255	monthly			1.2	3.3

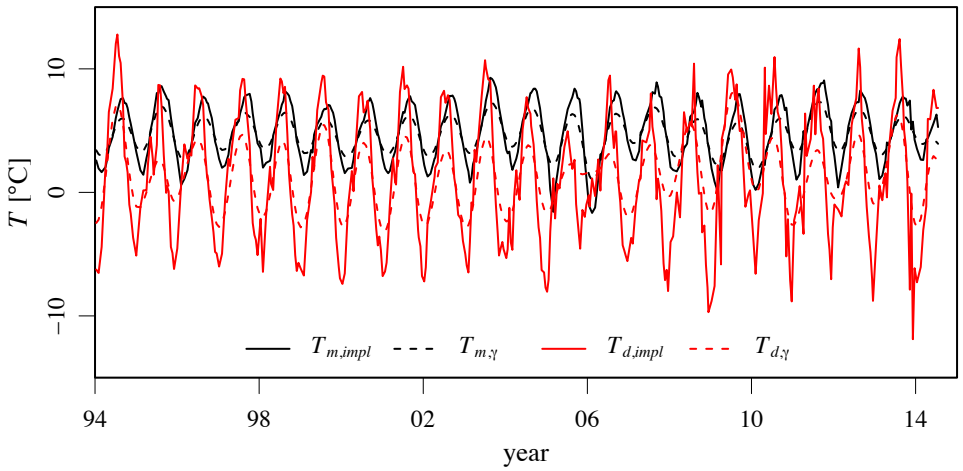

Fig. 3.9 Comparison of T_m and T_d of stabilising approaches for arch dam A3.

3.3.6 Discussion of inverse hat conduction analysis

The analysis in this section has shown that the consideration of the inverse region is essential for most of the examples investigated in this thesis. The consideration leads to an amplification and a phase shift. Whereas the amplification can be compensated by the regression coefficients in a regression analysis, the phase shift cannot. This can lead to periodical errors in the dam behaviour analysis model. Thus, the application of IHCA is recommended.

The proposed new stabilising procedure for the direct estimation of the quantities of interest T_m and T_d, based on the limitation of the amplification for high frequencies, performs well. For the arch dams A1 and A2, the results are comparable to the mollifier

approach. In the case of arch dam A3, the performance is even better since the filtering is done individually for the thermometers T_1 and T_2. Nevertheless, this individual filtering could also be applied to the mollifier approach. The main advantage of this new approach is that no regularisation parameter and corresponding calibration is necessary. Therefore, the application is straightforward.

Another approach could be to use measurements of the water and the air temperature instead of performing IHCA. The water temperature is seldom recorded; only two of the dams described in Appendix A.5 are equipped with such sensors. In contrast, air temperature measurements are usually available, at least from a weather station in the region of the dam. Nevertheless, the air temperature cannot directly be used as boundary condition because of the influences of convection and solar radiation at the surface (Léger *et al.*, 1993). The modelling of these processes is difficult and cumbersome, therefore IHCA is the preferred approach.

3.4 Proposed workflow

The workflow of a heat conduction analysis can be summarised by the following steps:

1. Plausibility check of measurement data (see Section 2.1.4.2)
2. Calibration of thermal diffusivity a, adjustment of the initial phase duration so that the temperature in the middle no longer changes
3. Direct estimation of T_m and T_d with Eq. (3.19) and (3.22), limitation of the amplification with the use of the measurement sampling rate

3.5 Discussion and Conclusion

One-dimensional heat conduction analysis works fine for most of the analysed concrete slabs. Nevertheless, deviations are observed for sections close to the crest level, in hollow gravity dams and in thick sections of gravity dams where the yearly temperature variation is very low. Furthermore, galleries disturb the one-dimensional approach. Despite these 2D- or 3D-effects, the results of the 1D analysis are a useful approximation.

If more than two sensors are available at a given level, the inner readings can be used to calibrate the thermal diffusivity. Since the temperature evolution in the middle of the slab needs time, especially if a temperature drift is present, an initial phase is beneficial. Otherwise some of the data cannot be used for the further analysis.

The frequency domain solution was identified as an intuitive tool to perform direct and inverse heat conduction analysis. It could be shown that inverse heat conduction analysis is necessary for most of the investigated slabs. The consideration of the inverse part leads to an amplification and a phase shift in the mean temperature T_m and the temperature

difference T_d. While the amplification can be compensated by the regression coefficients, the phase shift cannot. Due to amplification of the measurement noise in inverse heat conduction analysis, a stabilisation procedure is necessary. The mollifier approach, described in Obernhuber and Perner (2005) or Weber *et al.* (2010), leads to good results if the calibration of the regularisation parameter γ is possible. Unfortunately, if a calibration is not possible, the application of this approach is difficult. This is the usual case since water temperature measurements are rarely recorded. Therefore, a new approach, based on the frequency amplification is proposed. The idea behind this approach is that the quantities of interest T_m and T_d can be directly estimated from the outermost inner temperature readings T_1 and T_2. The limitation of the amplification of the high frequencies leads to stable results. In addition, a statement about how large the amplification of the measurement deviation is can be made. It can be shown that the new approach performs as well as the mollifier approach. The advantage of the new approach is that the stabilising parameter is given by the thermometer layout and the measurement sampling rate.

4 Evaluation of existing modelling approaches

4.1 Introduction

The goal of this chapter is to evaluate models and procedures from the literature that are used for dam behaviour analysis. All models and procedures applied in the scope of this thesis are described in Chapter 2. First, two common procedures for dam behaviour analysis are compared: (i) the observation-prediction comparison (OPC) and (ii) the adjusted behaviour indicator. Secondly, models for monitoring the displacement of concrete dams are evaluated. The approaches to represent the effects o the (i) water level, (ii) temperature and (iii) time are evaluated separately. In addition, the topic of multicollinearity is discussed. This is an important issue when modelling the displacement of concrete dams. Further, the influence of autocorrelation on the results is discussed.

4.2 Reference dams

This section gives a brief overview of the measurement data used for the model evaluation. To achieve a high evidence, data of eight different prototype dams from Switzerland and of one Austrian dam are used. Furthermore, different dam types were considered: gravity (G), arch (A), arch-gravity (AG) and hollow gravity (HG) dams.

The operators agreed to the publication of the data in anonymised graphical form. Hence, the dams are named by identifiers containing the abbreviation of the dam type. In addition, the water level is transferred to a full supply level of 300 m a.s.l. for every dam, and the year of construction end is provided in decades only. Non-essential data, e.g. the crest length for gravity dams, are not provided due to distinctiveness. Table 4.1 gives an overview of the dams used for the study. In addition, the period of data acquisition and the corresponding measurement sampling rate is given. The description of the dams and the available data sets is provided in Appendix A.5.

Table 4.1 Overview of reference dams.

id	type	H [m]	L_{cr} [m]	constr. end	data	meas. sampl. rate
G1	gravity	68		1960's	1999 - 2012	monthly / bi-weekly
G2	gravity	104		1950's	2000 - 2016	monthly
A1	arch	61	75	1980's	1986 - 2014	monthly / bi-weekly
A2	arch	180	554	1970's	1976 - 2015	monthly
A3	arch	111	320	1960's	1994 - 2014	19 meas. / a
A4	arch	131	725	1970's	1992 - 1998	daily
AG1	arch-gravity	130	363	1950's	1999 - 2014	bi-weekly
HG1	hollow gravity	92		1950's	1999 - 2014	monthly

4.3 Behaviour analysis procedure

4.3.1 Introduction

The way of carrying out dam behaviour analysis was found to play a major role to obtain robust results. There are two commonly used quantitative procedures, (i) the observation-prediction comparison and (ii) the analysis of the adjusted behaviour indicator (see Section 2.5.5). The aim of this section is to analyse and compare both procedures concerning the robustness of the results. The robustness refers to similar results regarding the behaviour evaluation for different calibration periods.

4.3.2 Methodology

The results of the before-mentioned procedures are presented for the case study of gravity dam G2. The pendulum displacement at crest level in block no. 5 (Fig. 4.1) is used as behaviour indicator. First, the behaviour of the original data is analysed for different models and calibration periods. Then, simulated behaviour changes in the form of shifts and drifts are added to the measured pendulum displacement. It is checked if the procedures are able to detect the simulated behaviour changes and thus are suitable for dam behaviour analysis.

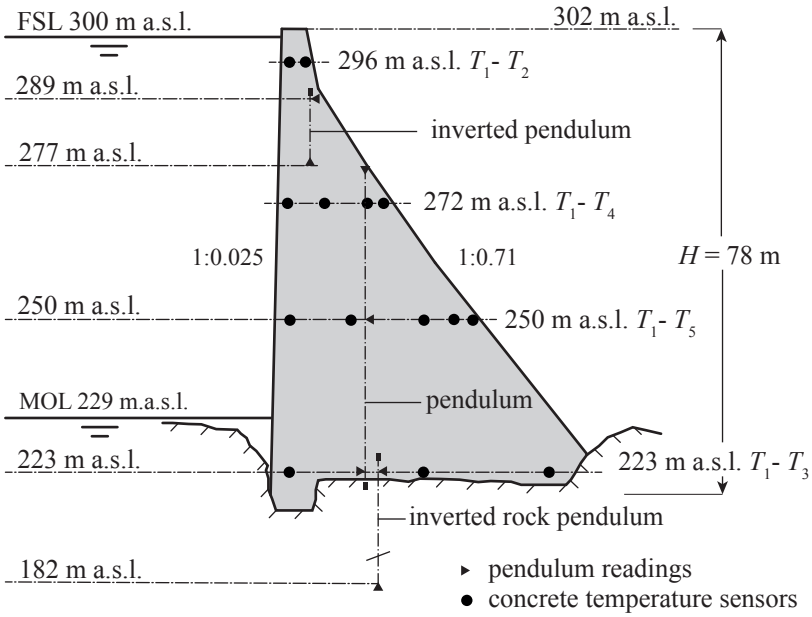

Fig. 4.1 Cross section through block no. 5 of gravity dam G2.

Three different statistical models to represent the effects of the water level, temperature and time are used: A HST, a HTT and a hybrid model (compare Section 2.5.4). The HST model is set up with a third-order polynomial function to represent the effect of the scaled water level h, a second order sinusoidal function for the seasonal effects and a linear function to approximate the irreversible displacement in function of the time t:

$$\begin{aligned} P(h,S,t) &= \beta_0 + \beta_1 h + \beta_2 h^2 + \beta_3 h^3 \\ &\quad + \beta_4 \sin(S) + \beta_5 \cos(S) + \beta_5 \sin(2S) + \beta_6 \cos(2S) + \beta_7 t \end{aligned} \tag{4.1}$$

For the HTT model, a third-degree polynomial function for the effect of the water level and a linear function for the time-dependent irreversible effects are used. The used temperature approach is based on a thermal analysis and decomposition into the mean temperature T_m and the linear temperature difference T_d of the four levels with temperature sensors (Fig. 4.1). A preliminary analysis has shown that the use of $T_{d,250}$, $T_{m,296}$ and $T_{m,272}$ leads to the most accurate model (Eq. (4.2)). This was evaluated by minimising the *RMSPE* in a 10-fold cross-validation procedure for the whole data available. In addition, the constraint $VIF \leq 10$ was defined to avoid multicollinearity.

$$P(h,T,t) = \beta_0 + \beta_1 h + \beta_2 h^2 + \beta_3 h^3 + \beta_4 T_{d,250} + \beta_5 T_{m,296} + \beta_6 T_{m,272} + \beta_7 t \tag{4.2}$$

The hybrid model is based on a cantilever beam model with an elastic abutment. Material properties of concrete (E_c and ν_c) and geometrical properties such as the beam thickness $t(z)$, the upstream surface inclination $y_{usf}(z)$, the abutment level and the crest level have to be allocated. Furthermore, the spring constants can be estimated by the Vogt's method described in Section 2.2.2.4. The model can be used to calculate the deformation δ_h due to the water level h and δ_T due to the temperatures T_m and T_d. More details about this model are presented in Section 5.2. The model output is used as input data for the hybrid regression model:

$$P(\delta_h, \delta_T, t) = \beta_0 + \beta_h \delta_h + \beta_T \delta_T + \beta_t t \tag{4.3}$$

The whole available data set from 2000 - 2016 was used for this analysis. For the calibration of the models, four different periods were compared (2000 - 2005, 2000 - 2010, 2005 - 2010 and 2000 - 2016). The first three have in common that they are all used for prediction from 2010 - 2016. For the last one, all data are used for calibration.

Artificial behaviour changes (Fig. 4.2) are added after 2010 in the prediction period of the data sets 1 - 3 and inside the calibration period of data set 4, respectively. As a consequence, the model calibration for data set 1 - 3 has to be done once whereas it has to be done three times for data set 4. The first added behaviour change is a shift of 1.2 mm on the 1.1.2011. The size of the shift was chosen to be about $2 \cdot RSE$ of the models. Such a

shift may occur due to a mechanical damage of the measurement equipment. The second one is a drift of 0.2 mm/a starting on the 1.1.2010. After the prediction period of six years, the total deviation is 1.2 mm. Such a drift is similar to a pattern of AAR or deformation due to rock mass movement.

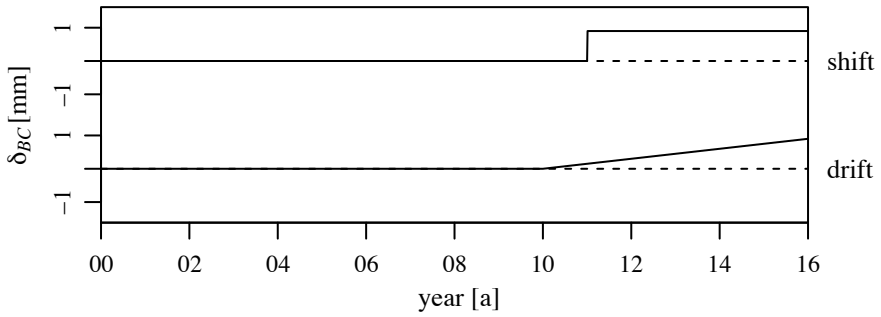

Fig. 4.2 Artificial behaviour changes added to the behaviour indicator of the data sets.

4.3.3 Observation-prediction comparison

The models described in Section 4.3.2 were fitted for four calibration periods and three data sets (original, shift and drift). This leads to 12 fits for each model. In Table 4.2, the estimated regression coefficients are shown for the hybrid model. After calibration, the rest of the data was used for prediction. The differences D between the observed pendulum displacement and the prediction of the hybrid model are shown in Fig. 4.3. The differences of the HST and the HTT models are shown in Appendix A.6.1.

On the basis of these differences, the behaviour analysis is carried out. Regarding the hybrid model with the original data (Fig. 4.3a), the interpretation of the differences leads to other conclusions for different calibration periods. Using the data from 2000 - 2005 for calibration, only few data points of the differences lie outside the prediction band and no abnormal behaviour is recognisable. Using the data from 2000 - 2010 for calibration, several points lie outside the prediction band and a small drift in negative direction is recognisable. However, if only the data from 2005 - 2010 is used, many points lie outside the prediction band and a clear drift in negative direction is visible. In addition, if all available data are used for calibration, only three points are outside the prediction band.

The interpretation of the modified data also leads to different conclusions for the considered calibration periods. In Fig. 4.3b, the differences D of the data with the added artificial shift are shown for the different calibration periods. For the calibration periods of 2000 - 2005 and 2000 - 2010, the added shift is recognisable. On the other hand, for the calibration data from 2005 - 2010, only few points lie outside the prediction band and a normal behaviour can be interpreted. Furthermore, in the case of all data is used for calibration the added artificial drift is hardly detectable (Fig. 4.3c)). The results of the HST and the HTT models are similar (see Appendix A.6.1).

Table 4.2 Regression coefficients of the hybrid model for different data sets and calibration periods. The standard errors of the coefficients are given in brackets behind their mean values.

	calibration	β_h [-]	β_T [-]	β_t [-]
normal	2000 - 2005	1.06 (±0.02)	1.07 (±0.04)	0.09 (±0.05)
	2000 - 2010	1.07 (±0.02)	1.05 (±0.03)	0.07 (±0.02)
	2005 - 2010	1.09 (±0.02)	1.06 (±0.03)	0.20 (±0.05)
	2000 - 2016	1.04 (±0.01)	1.03 (±0.02)	0.03 (±0.01)
shift	2000 - 2016	1.04 (±0.01)	1.03 (±0.02)	0.11 (±0.01)
drift	2000 - 2016	1.04 (±0.01)	1.02 (±0.02)	0.10 (±0.01)

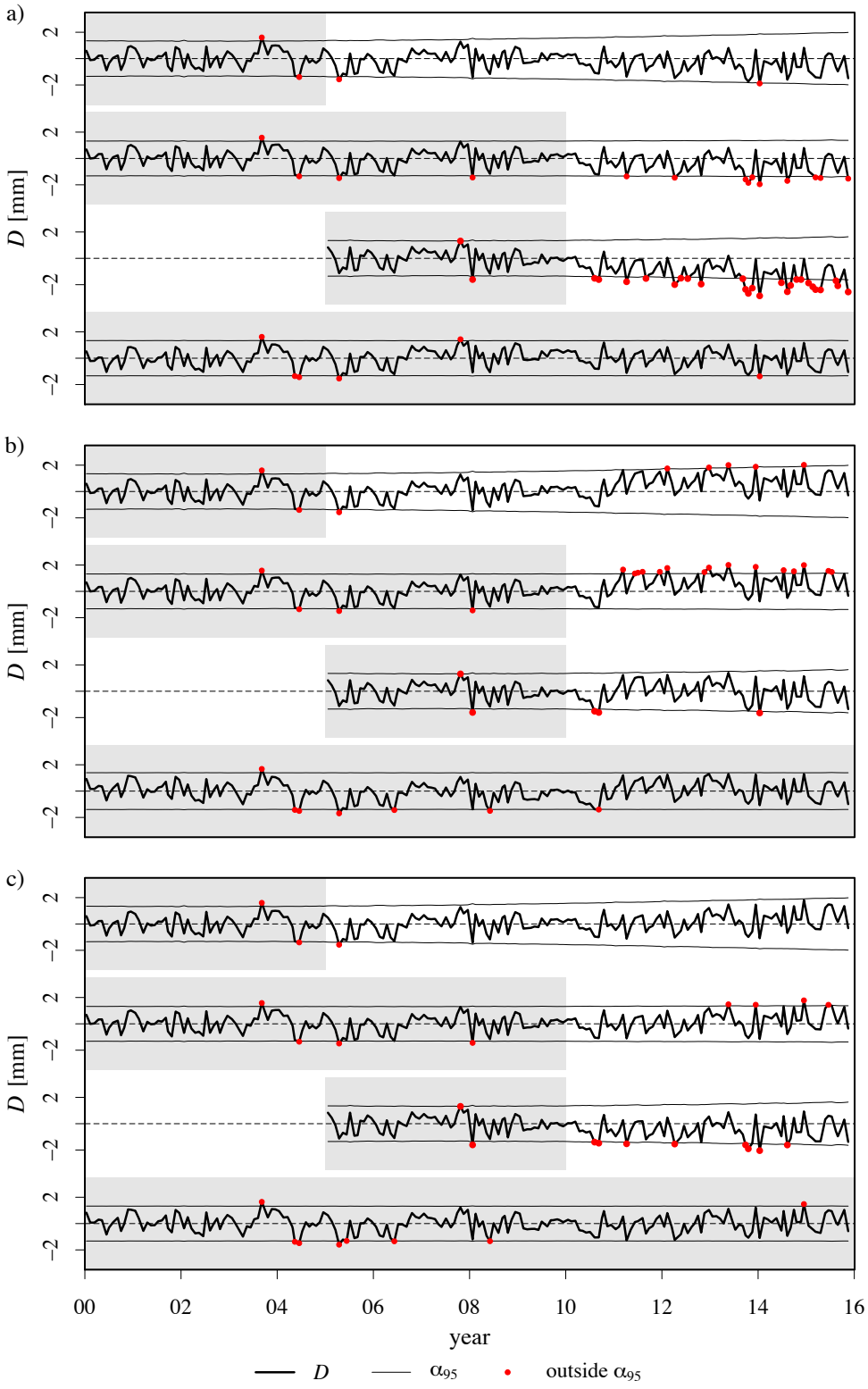

Fig. 4.3 Observed differences D of the hybrid model for different calibration periods indicated by the grey background. The differences that are larger than the estimated prediction band α_{95} are shown by red dots. a) original data; b) original data with added shift of 1.2 mm on the 1.1.2011 to the pendulum displacement; c) original data with added drift of 0.2 mm/a after 1.1.2010.

4.3.4 Analysis of adjusted behaviour indicator

The analysis of the adjusted behaviour indicator is an alternative to the observation-prediction comparison. The adjusted behaviour indicator M_{adj} of a fitted model can be written as

$$M_{adj} = M - \sum \beta_i h_i - \sum \beta_j T_j = \beta_0 + \beta_t t + e, \tag{4.4}$$

according to Section 2.5.5. In Eq. (4.4), M_{adj} are the measurements of a behaviour indicator M subtracted by the modelled influence of the water level $\sum \beta_i h_i$ and the influence of the temperature $\sum \beta_j T_j$. M_{adj} consists of a constant, the irreversible displacement and the model errors. As a consequence, an abnormal behaviour or a behaviour change can be recognised in M_{adj}. Nevertheless, the trend is hidden by the model errors. This means, the smaller the model errors are, the better a behaviour change is recognisable. Although the irreversible effects are not needed for the calculation of M_{adj}, they should be included in the regression model that is used to estimate the coefficients of the water level and the temperature. Otherwise, a potential abnormal behaviour may be caught by the reversible effects in the regression analysis and wrong coefficient estimates result (Amberg, 2009).

In Fig. 4.4, the adjusted behaviour indicators of the hybrid model are shown. For the calculation, the same fits as for the observation prediction comparison can be used. Instead of the differences D, the adjusted behaviour indicators were calculated. For the reason of comparison, the mean value of the 2000 - 2010 period was subtracted from each time series. Fig. 4.4a shows M_{adj} of the original data. Comparing the four graphs of the different calibration periods, the curve progression is nearly similar, even for the calibration periods 2000 - 2005 and 2005 - 2010 which do not overlap. In addition, M_{adj} is randomly distributed and all the four curves do not visually show a significant change in the behaviour.

Considering the adjusted behaviour indicators of the data with the added shift (Fig. 4.4b), it can be recognised that the curve progression is similar. Moreover, the artificially added shift is clearly visible, after 2011 the mean value of M_{adj} is shifted and only few values are smaller than 0. The drift that was added to the data (Fig. 4.4c) also can be recognised by looking at the adjusted behaviour indicators. The results of the HST and the HTT model are shown in Appendix A.6.2. The HTT model also clearly shows the added behaviour changes. For the HST model it is more difficult to detect the behaviour changes.

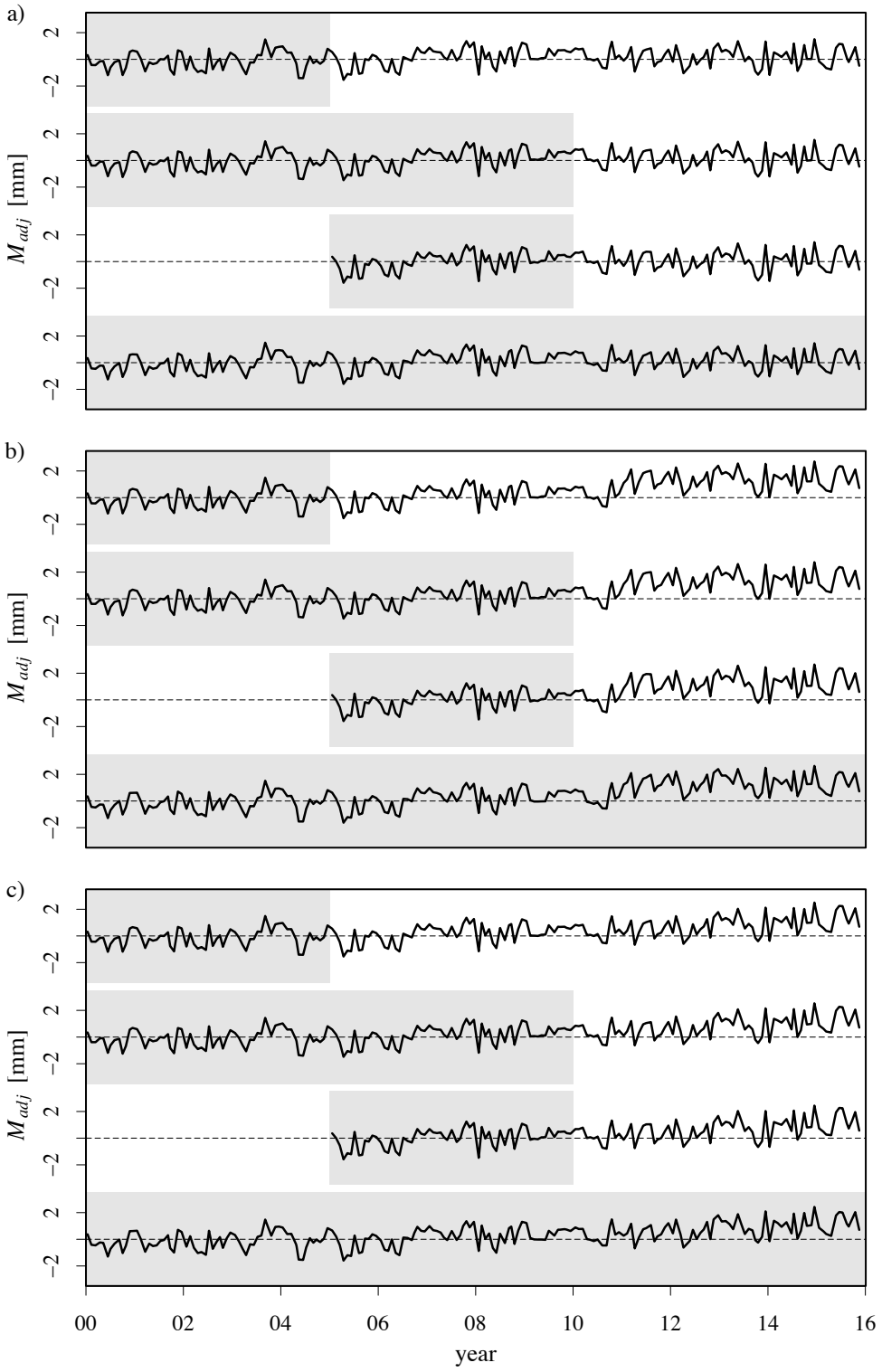

Fig. 4.4 Observed adjusted behaviour indicators M_{adj} of the hybrid model for different calibration periods indicated by the grey background. a) original data; b) original data with added shift of 1.2 mm (~$2 \cdot RSE$) on the 1.1.2011 to the pendulum displacement; c) original data with added drift of 0.2 mm/a after 1.1.2010.

4.3.5 Discussion

Regarding the example of the observation-prediction comparison, it is obvious that the results are not robust and the choice of the calibration period plays an important role. In addition, the artificial behaviour changes that were added to the data could not be identified in the estimated differences. This makes the analysis very difficult or even unreliable because it is not possible to state whether the behaviour is normal or not. The results are similar for all models of this study. This indicates that not the models but the methodology itself seems to have a conceptual weakness. Having a closer look on the regression coefficients of the hybrid model in Table 4.2, gives an indication about the origin of the difference between the different calibration periods. As expected for a hybrid model with physically-based shape functions, the coefficients β_h and β_T have values close to 1. For all calibration periods and data sets, the coefficients β_h and β_T are more or less equal. Their mean values vary within two standard errors. On the contrary, the coefficients for the irreversible displacement in the function of time β_t vary between 0.03 and 0.20. In reality, the irreversible displacement is an arbitrary function of the time t and not linear as assumed in the model. Regarding the calibration period from 2005 - 2010, the trend was estimated to be 0.20 mm/a whereas it is estimated to be 0.03 mm/a when using all data available. If the difference of 0.17 mm/a is predicted from 2010 - 2016, a difference of 1.02 mm results in 2016. This can be verified in Fig. 4.3a. As a consequence, the observation prediction comparison seems to fail if a non-constant irreversible displacement is present.

The behaviour analysis based on the adjusted behaviour indicator was successful. The progress of M_{adj} is the same for different calibration periods. Artificial behaviour changes are detected for all models of the study. Even the data set from 2000 - 2016, where the behaviour changes were inside the calibration data, can be used to identify the behaviour changes. Because there is no longer a prediction band available when using adjusted behaviour indicators, the conclusions have to be drawn based on a visual analysis of M_{adj}. Nevertheless, a quantitative tool to identify the behaviour changes would be useful. In the next section, a method based on MLR is presented. Furthermore, the results show that all models can be used to identify the behaviour change, although the HST model shows it less clearly. This issue is studied further in Section 4.5.2 where different temperature models are compared on a larger data basis.

Several of the dams analysed in this thesis show a non-constant irreversible displacement. Therefore, the use of the adjusted behaviour indicator instead of the observation-prediction comparison is highly recommended. In this thesis, all further analyses are based on the adjusted behaviour indicator.

4.4 Quantitative evaluation of adjusted behaviour indicators

4.4.1 Introduction

When using the adjusted behaviour indicator approach for the behaviour analysis, there is no prediction band that helps to detect a behaviour change. The evaluation may be done by a visual judgement as in the previous section. A running mean approach may also help to support the decision. However, this can be quite tricky, especially if there are small changes that are not obvious at first sight. Thus, three quantitative methods are proposed herein: (i) A potential abnormal behaviour, e.g. a drift or a change in the rate of the irreversible displacement, can be detected by MLR. The adjusted behaviour indicator can be used as response variable and the time as predictor variable. To detect the behaviour changes, classifier variables can be used. This approach is explained in Section 4.4.2. By the use of a hypothesis test, it can be tested how big and how significant a behaviour change at a certain date is. (ii) In Section 4.4.3, an extension of this algorithm is introduced. Instead of manually choosing the date where the hypothesis test is applied, the date of the most significant behaviour change is estimated automatically. (iii) Sometimes it is necessary to compare different models. In doing so, not only the goodness of fit but also the robustness of resulting models is of special interest. Thus, a coefficient of robustness based on the adjusted behaviour indicator was developed, as presented in Section 4.4.4.

4.4.2 Detect abnormal behaviour by MLR

A change in the behaviour can be found by application of MLR to the adjusted behaviour indicator. The base model includes the adjusted behaviour indicator M_{adj} as response variable and a constant β_0 plus a function of time that represents irreversible effects, as predictor variable. The function of time can be linear or exponential, for example. To test for the behaviour change, a kind of classifier variable δ_{BC} is introduced. The classifier variable contains the shape of the assumed behaviour change which is searched for. In Fig. 4.5, such shape functions for a shift, a drift and a change in the seasonal behaviour are shown. Obviously, any shape function can be used. An example of the model equation of such an MLR analysis is given by Eq. (4.5). As mentioned before, the function of time t and the shape of the behaviour change δ_{BC} can be chosen arbitrarily.

$$M_{adj} = \beta_0 + \beta_t\, t + \beta_{BC}\, \delta_{BC} \tag{4.5}$$

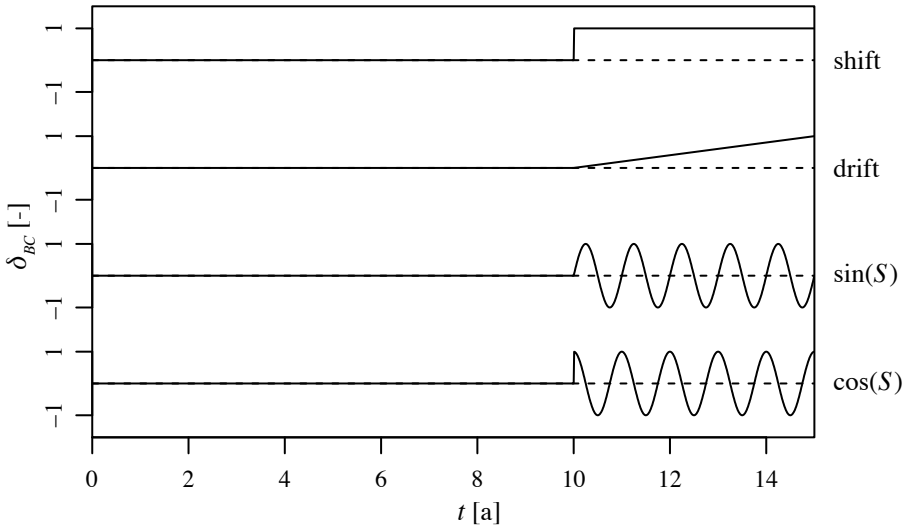

Fig. 4.5 Shape functions that can be used to search behaviour changes by MLR analysis.

After the MLR is carried out, the resulting regression coefficient β_{BC} is further analysed. Its value multiplied with the shape function leads to the estimate of the behaviour change. If the value of δ_{BC} was chosen to be dimensionless, the regression coefficient expresses the estimate of the behaviour change. Besides the value of the behaviour change, the statistical significance can be evaluated. This can be done by a hypothesis test (see Section 2.4.1.5). For a proper analysis, the autocorrelation of the residuals of the MLR model used to detect the behaviour change should be checked (see Section 2.4.3 for details).

4.4.3 Algorithm for automatic detection of behaviour changes

The detection of abnormal behaviour by an MLR analysis as described in the previous section is a valuable tool to support the analysis of the adjusted behaviour indicator. Unfortunately, the date of the behaviour change occurrence needs to be provided for this analysis. If the behaviour change is not identifiable by visual detection, a behaviour change will be difficult to find. Thus, an algorithm to automatically find a change in the behaviour was developed. Below, the pseudo-code of this algorithm is shown. For the loop for the search of behaviour changes, a maximum number of behaviour changes $n_{BC,max}$ that can be found and a cut-off p-value p_{cut} that is used for the hypothesis test needs to be provided. In addition, the type of the behaviour change which is searched for has to be provided. This can be a shift, a drift or a change in the seasonal pattern. The algorithm is very simple: at each date i of n measurement dates, a hypothesis test is performed to check for the behaviour change. The smallest and therefore most significant p-value is taken for the location of the behaviour change if $p < p_{cut}$. This procedure is repeated until $n_{BC} > n_{BC,max}$ or $p > p_{cut}$. In Section 6.4, the algorithm is applied to the case study of gravity dam G1.

```
define base model (e.g.  M_adj = β_0 + β_1 t)
choose type of behaviour change to search for
n_BC = 0
   while (n_BC > n_BC,max){
      for(i in 2:(n-1){
         create δ_BC,i variable
         add δ_BC,i to base model
         calculate p-value (significance of δ_BC,i in the model) and store it
      }
      search min p-value (date and type of behaviour change)
      if ( p > p_cut ){ stop
      } else{
         add δ_BC,i variable to base model
         n_BC = n_BC + 1
      }
   }
}
```

4.4.4 Coefficient of robustness

The robustness in the sense of calibration data dependency will be of special interest, if different models have to be compared. In doing so, models that lead to similar coefficient estimates for different calibration periods and consequently to a similar prediction are said to be robust (Montgomery *et al.*, 2012). Since it is proposed to do the behaviour analysis on the basis of adjusted behaviour indicator M_{adj}, a measure to compare M_{adj} for different calibration periods will be necessary.

For a number n_c of calibration periods, the adjusted behaviour indicator $M_{adj,i}$ shall be compared to a reference value $M_{adj,ref}$. The reference value $M_{adj,ref}$ represents the whole data set used for the analysis. The following proposed approach is similar to the coefficient of determination R^2. The variance of the difference $M_{adj,diff} = M_{adj,i} - M_{adj,ref}$ can be related to the variance of $M_{adj,ref}$:

$$r_{c,i} = 1 - \frac{\sum \left(M_{adj,diff} - \overline{M}_{adj,diff}\right)^2}{\sum \left(M_{adj,ref} - \overline{M}_{adj,ref}\right)^2} \tag{4.6}$$

It is suggested to choose the calibration periods similar to a cross-validation procedure but with $k = 3$ folds. A higher fold number leads to more robustness. The experience has shown that $k = 3$ works quite well. For a 15 years time series for example, a calibration set of 10 years is considered each. The robustness coefficient r_c is estimated as the mean value of all $r_{c,i}$:

$$r_c = \frac{1}{k} \sum r_{c,i} \tag{4.7}$$

A value of $r_c = 1$ implies a perfect agreement of the M_{adj} and a low r_c indicates a large fluctuation of the results; $r_c = 0.95$ for example, indicates that the variance of the difference between the M_{adj} is 5 % of the variance of $M_{adj,ref}$.

4.5 Displacement of concrete dams

In this section, the statistical models for the displacement of concrete dams that are described in Section 2.5.4.2 are evaluated. Since the different approaches for the influences of the water level, the temperature and the irreversible effects can be arbitrarily combined, they are evaluated separately in the Sections 4.5.1 - 4.5.3.

4.5.1 Approach to consider the effects of the water level

4.5.1.1 Introduction

A polynomial approach is most commonly used to approximate the effects caused by the water level. Alternatively, a hybrid or mixed approach can be used. Since they depend on the individual model that is used to calculate the displacement, they are not evaluated here. Besides the order of the polynomial function, the origins of the scaling can be chosen and a Chebyshev transformation may be applied. In this section, the influence of these options to the results is discussed on the basis of a case study. In addition, suggestions on the order of the polynomial are given.

4.5.1.2 Methodology

Data

As in Section 4.3, the results are presented for the case study of gravity dam G2. Typically, the reservoir is operated with a level above 252 m a.s.l. In 2004, it was lowered to the bottom of block no. 5 (Fig. A.21). Thus, four calibration periods (2000 - 2004 (1), 2000 - 2010 (2), 2005 - 2010 (3) and 2000 - 2016 (4)) were used for this investigation. Only the calibration periods (2) and (4) contain data of the reservoir lowering. This should allow for the evaluation of the extrapolation capability of the polynomial approach.

Comparison of water level approaches

Usually, polynomials of 3rd or 4th order are used as shape functions. To check, how the order of the polynomial influences the results and how it can be chosen correctly, polynomials up to the 7th order are analysed. Besides the order, different scalings are applied (for details see Section 2.5.4.4). The common approach is to scale the water level to 1 for a full reservoir and to 0 for an empty reservoir. Another approach is proposed by Weber (2002). He uses Chebyshev polynomials with a scaling between -1 for the lowest water level in the calibration period and 1 to the highest water level in the calibration period.

Temperature models

The temperature models as presented in Section 4.3 were used: A seasonal approach (HST, Eq. (4.1)), a direct temperature approach (HTT, Eq. (4.2)) and a physically-based model (mixed model). The mixed model consists of the physically-based temperature approach combined with the statistical approach for the effects of the water level and the irreversible displacement, that are considered by a linear function of the time t:

$$P(h,\delta_T,t) = \beta_0 + \sum \beta_i h^i + \beta_{i+1}\,\delta_T + \beta_{i+2}\,t \tag{4.8}$$

Evaluation procedures

The resulting influence functions for the effect of the water level are evaluated visually by plots. This is more concrete than the comparison of regression coefficients and goodness of fit criteria. The shape of the influence functions is compared between the different calibration periods and temperature models. In addition, polynomials of different order are compared. Especially the behaviour with regard to water levels not considered in the calibration period is of interest.

The determination of the polynomial order can be done by different quantitative analyses. Measures to assess the model such as the *RSE*, the *RMSPE*, the R^2_{adj} or a hypothesis test can be used (see Sections 2.4.1.4 and 2.4.1.5).

The drawback of the *RSE* is that it decreases by definition when adding variables. This can lead to overfitting. Thus, the splitting into a calibration and a test data set and calculation of the *RMSPE* seems more appropriate. Since this procedure is based on prediction, the test data set should not be longer than two or three years. Otherwise, the bias due to the prediction of the irreversible displacements as a function of time becomes too large (for details see Section 4.3). In addition, the water level in the test data set should not contain any extrapolations. Therefore, the cross-validation procedure cannot be used since it is based on predictions using the whole data set. Another method that prevents from

overfitting is calculating the R^2_{adj} that gives a penalty to models with many coefficients. Finally, there is the hypothesis test of single coefficients where the significance of a single variable of the model can be determined. In this case, the p-value of the highest order polynomial term in the model is determined. This approach works well, as long as there is no autocorrelation in the model residuals. For this analysis, the data from 2000 - 2010 were used for calibration and the data from 2010 - 2012 as test data set to calculate the $RMSPE$.

4.5.1.3 Results

Shape of the influence function

The two different scalings of the water level lead to exactly the same results concerning the shape of the influence functions, the coefficient estimates for the temperature and time approach and the goodness of fit criteria. The only differences are the regression coefficient estimates of the water level approach and the corresponding VIF values. Whereas the model with common polynomials and a scaling between 0 and 1 leads to VIF values up to 18'000, the model with Chebyshev polynomials has a maximum VIF value of 3.5. For the temperature approaches, the same VIF values resulted for both scalings.

The resulting influence functions for 3rd order polynomials and a scaling from 0 to 1 are shown in Fig. 4.6. For easier comparison, the functions are horizontally shifted so that the displacement at crest level is equal for all of them. In Fig. 4.6a - c, the functions are shown separately for the different temperature models. For the two data sets where no data with water level measurements below 252 m a.s.l. was in the calibration data set, extrapolations result. In most cases of extrapolation, physically meaningless results with a rising displacement for lowering the reservoir resulted. On the one hand, the calibration range, the influence functions look similar for the different calibration periods. On the other hand, a comparison of the different temperature models, as shown in Fig. 4.6d for calibration data (4), shows a difference. The shape of the functions is similar but the "stiffness" of the structure is estimated differently. Whereas the mixed temperature model leads to around 15 mm displacement for a complete reservoir filling, the HTT does only lead to 13.5 mm and the HST to 12.5 mm. This is a difference of 17%. In Fig. 4.7, the time series of the separated effects is shown for the different temperature models. The difference between the different temperature models can be recognised by the maximum and minimum displacement. In the next section, the performance of these temperature models is further investigated.

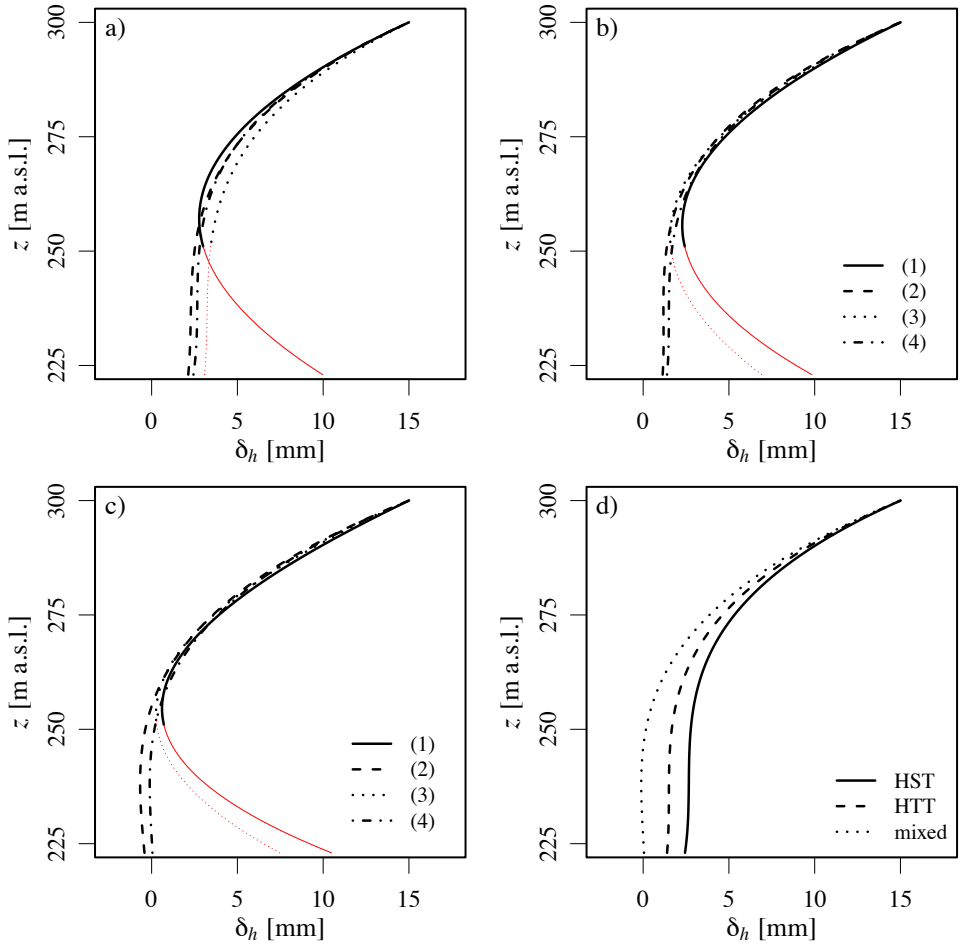

Fig. 4.6 Influence functions for the crest displacement in function of the water level: a) HST model; b) HTT model; c) mixed model; d) comparison of different temperature models for the calibration period (4). The calibrated part (thick black lines) is visually distinguished to extrapolation (thin red lines).

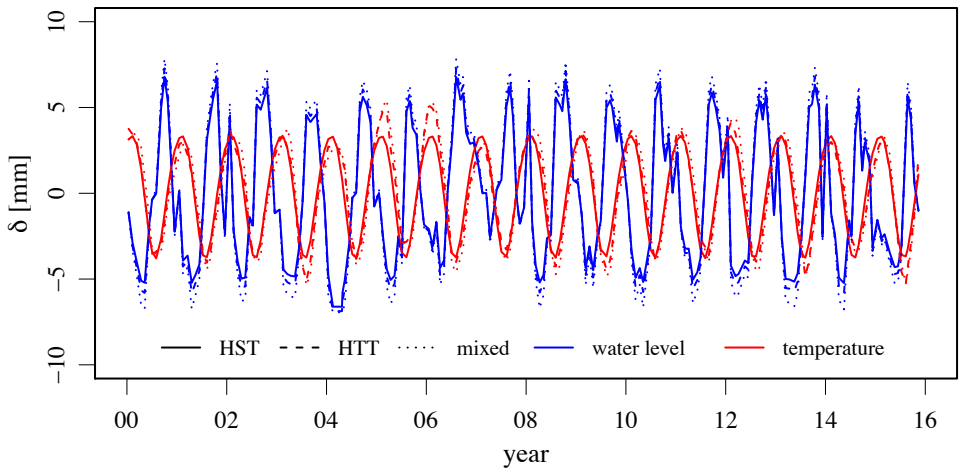

Fig. 4.7 Time series of separated effects for HST, HTT and mixed model based on calibration data 2000 - 2016.

Polynomial order

The resulting influence functions for different polynomial orders o_h are shown in Fig. 4.8a for the calibration period (1) and in Fig. 4.8b for the calibration period (2). Regarding the calibrated parts of the model, the influence functions, (black lines in Fig. 4.8a), do not differ much for orders greater than two. However, it is obvious that, the extrapolations (red lines in Fig. 4.8a) lead to physically meaningless results. From the qualitative point of view, a third order approach seems to work well. In Table 4.3, the *RSE*, the *RMSPE*, R^2_{adj}, and the p-values of the highest order polynomial term in the model are shown.

The *RSE* does not significantly decrease for orders greater than two. A similar pattern can be regarded for the *RMSPE*, where for orders greater than four the values slightly increases due to overfitting. In addition, the R^2_{adj} and the p-values again lead to the conclusion that a third order polynomial fits best.

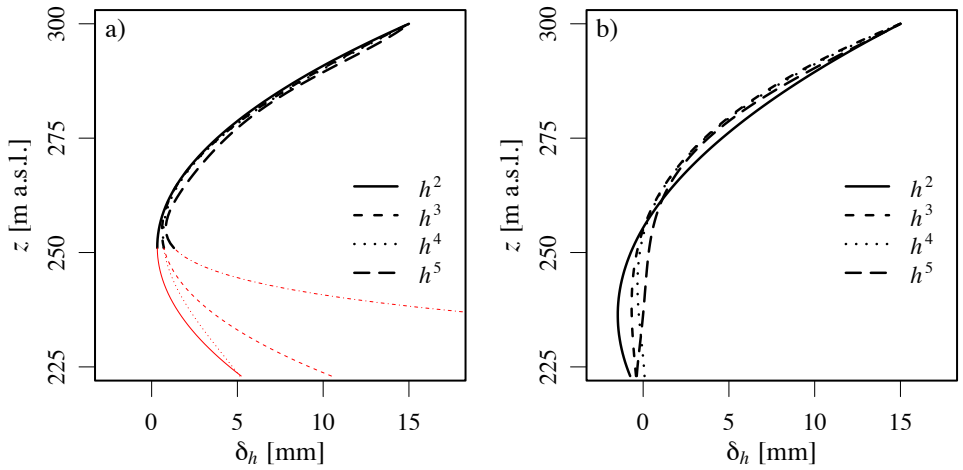

Fig. 4.8 Influence functions for water level for models with different polynomial orders: a) calibration period (1); b) calibration period (2). Calibration (thick black lines) is visually distinguished to extrapolation (thin red lines).

Table 4.3 Results of analysis for different polynomial orders o_h for calibration period (2): R^2_{adj} and p-values (*** p<0.001; ** p<0.01; * p<0.05; . p<0.1) of the polynomial term with the highest order h^n. The *RMSPE* was estimated with a 3-year test data set after the calibration period.

o_h [-]	*RSE* [mm]	*RMSPE* [mm]	R^2_{adj} [-]	$p(h^{o_h})$ [-]
1	2.28	1.84	0.656	***
2	0.78	0.68	0.966	***
3	0.59	0.61	0.977	***
4	0.59	0.61	0.977	
5	0.58	0.62	0.978	*
6	0.58	0.62	0.978	
7	0.58	0.62	0.978	

4.5.1.4 Discussion

On the one hand, the polynomial approach is straightforward to implement and gives good results concerning the goodness of fit. On the other hand, it is a black box approach and physically non-meaningful results may occur. Furthermore, the polynomial approach must not be used for extrapolations. There are different ways of determining the order of the polynomial. The most efficient way is a visual analysis in combination with analysing the *RSE*. Although the *RSE* does not prevent from overfitting, it allows for determining the polynomial order. In doing so, the order is chosen so that a higher order does only slightly improve the *RSE*. This can be compared to the one-standard-error rule explained in Section 2.4.1.7. The use of p-values is not recommended since then autocorrelation has to be analysed properly. This can be complicated and time-consuming (see Section 2.4.3).

For the gravity dam G2, a 3rd order polynomial leads to the best results. This also applies to gravity dam G1 and hollow gravity dam HG1. Furthermore, this corresponds to the analytical solution (Amberg, 2009).

4.5.2 Approaches for considering temperature effects

There are several models that can be used to represent the thermal effects of concrete dams (see Section 2.5.4.2). The aim of the investigation presented in this section is to evaluate and compare these models. Not only the goodness of fit and the prediction accuracy but also the ability to detect a change in the behaviour and the robustness of the models is evaluated.

4.5.2.1 Methodology

Data

Data of seven Swiss dams are used to have a good basis for the evaluation procedure. The selection criterion is a data set of around 15 years duration including temperature readings. A period of 10 years is used to calibrate the models, the rest is used for prediction. Furthermore, different dam types, three arch, two gravity, one arch-gravity and one hollow gravity dam are considered (Table 4.4). A description of the structures and the data sets can be found in Appendix A.5. For gravity dam G1, only a data set of 14 years is available. Nevertheless, this dam is used for the analysis with a 9-year calibration period and a 5-year prediction period. For some of the dams, more than 15 years data were available. To have comparable data sets, the data sets are cut to equal length (15 years). For arch dam A2, the data before the tunnelling works in the underground are taken.

Table 4.4 Dams used for the evaluation of temperature models and the chosen periods of the data sets.

	dam	data
1	G1	1999 - 2013
2	G2	2000 - 2015
3	A1	2000 - 2015
4	A2	1990 - 2005
5	A3	1999 - 2014
6	AG1	1999 - 2014
7	HG1	1999 - 2014

Temperature models

The most common and recent temperature models listed in Table 4.5 are evaluated. Only statistical models are considered since they can be applied in a straightforward way to several dams. A short description about the models can be found in Section 2.5.4.2. For the HSTT models, daily air temperature measurements of weather stations as close as possible to the dam site were used. These data are available from the data base of the Federal Office of Meteorology and Climatology MeteoSwiss (MeteoSwiss, 2017). For the HTT_{T_m,T_d} model, the mean core concrete temperature was used as reference temperature T_{ref}.

Table 4.5 Overview of evaluated temperature models.

	approach	used in
HST	$\beta_1 \sin(S) + \beta_2 \cos(S) + \beta_3 \sin(2S) + \beta_4 \cos(2S)$	Willm and Beaujoint (1967)
$\text{HSTT}_{Verbund}$	$\beta_1 \sin(S) + \beta_2 \cos(S) + \beta_3 \sin(2S) + \beta_4 \cos(2S) + \sum \beta_i \Delta T_i$	Widmann (1967), Breitenstein *et al.* (1985)
HSTT_{edf}	$\beta_1 \sin(S) + \beta_2 \cos(S) + \beta_3 \sin(2S) + \beta_4 \cos(2S) + \Delta T_R$	Penot *et al.* (2005)
HTT_{dir}	$\sum \beta_i T_i$	Swiss Committee on Dams (2003), Mata *et al.* (2013)
HTT_{T_m,T_d}	$\sum_{i=1}^{i=nLev} \left(\beta_{m,i}(T_m - T_{ref}) + \beta_{d,i} T_d\right)$	Léger and Leclerc (2007)
HTT_{PC}	$\sum \beta_i T_{PC,i}$	Mata *et al.* (2013)
$\text{HSTT}_{\Delta T_m,\Delta T_d}$	$\beta_1 \sin(S) + \beta_2 \cos(S) + \beta_3 \sin(2S) + \beta_4 \cos(2S) + \sum_{i=1}^{i=nLev} \left(\beta_{m,i}\Delta T_{m,i} + \beta_{d,i}\Delta T_{d,i}\right)$	Tatin *et al.* (2015)

The effects of the water level are represented by a polynomial approach up to fourth order. The most suitable order is determined separately for each dam. Nevertheless, the order was determined once for each dam and kept constant for the rest of the analysis. The irreversible effects are approximated by a linear function of time t for all dams.

Variable selection

For some of the temperature models, a subset of temperatures representing the thermal behaviour of the structure has to be chosen. In the case of the HTT_{dir} model, for example, many of the temperature measurements T_i are correlated. If two correlated temperature readings are taken into account in the model, multicollinearity occurs and unstable predictions may result. Here the approach of eliminating correlated variables is pursued. In doing so, best subset selection with the constraint $VIF < 10$ was performed (for details see Section 2.4.2).

Evaluation procedure

The model accuracy (goodness of fit) is evaluated by the RSE and the R^2. Whereas the RSE is a measure in the unit of the behaviour indicator, the R^2 is dimensionless and therefore suitable for comparing different dams. Besides the goodness of fit, the prediction accuracy and the robustness of the models are analysed. The prediction accuracy gives an indication about the quality of the prediction, while the robustness indicates how much the model output varies for a different calibration period. For instance, there can be accurate models that have a lot of variation when changing the calibration period. In contrast, there are models that are less precise but more robust. The prediction accuracy is evaluated based on $RMSPE_{CV}$ and R^2_{CV} estimated by cross-validation. To avoid a too large bias due to prediction of irreversible displacement, 10 folds were chosen. Furthermore, the data points where extrapolations of the water level occur, were not considered since they

can distort the results (see Section 4.5.1). The robustness of the model is evaluated by the robustness coefficients r_c (see Section 4.4.4) with $k = 3$ folds.

The most important question that should be answered by this study is whether the models allow for detecting a change in the structural behaviour or not. To examine this, behaviour changes in the form of drifts, shifts and changes in the seasonal pattern are added to the behaviour indicator in the five-year prediction period of the data. The magnitude of the behaviour changes was chosen to 50, 75, 100, 125 and 150 % of the *RSE* of each model. By this procedure, the relative size of the behaviour change compared to the *RSE* can be identified. The shifts were added at the beginning of the five-year prediction period. In the case of the drift, the magnitude increases linearly over the five-year prediction period. The seasonal pattern was added over the whole prediction period with an amplitude corresponding to the behaviour change.

To detect the artificial behaviour changes in the adjusted behaviour indicator M_{adj}, an MLR analysis based on a kind of classifier variable is used. This analysis is further explained in Section 4.4.2. Unfortunately, each dam is permanently affected to small behaviour changes and therefore only imperfect data are available. If the MLR analysis is applied to the original data, small behaviour changes might be found. To obtain unbiased results when searching for the artificial behaviour changes, these small behaviour changes had to be filtered out before the analysis. The filtering was performed by estimating the small behaviour changes by MLR and subtracting them from the original data. In Fig. 4.9, the original and modified (filtered) adjusted behaviour indicator M_{adj} are exemplarily shown for arch dam A1. It can be recognised that the modifications are small.

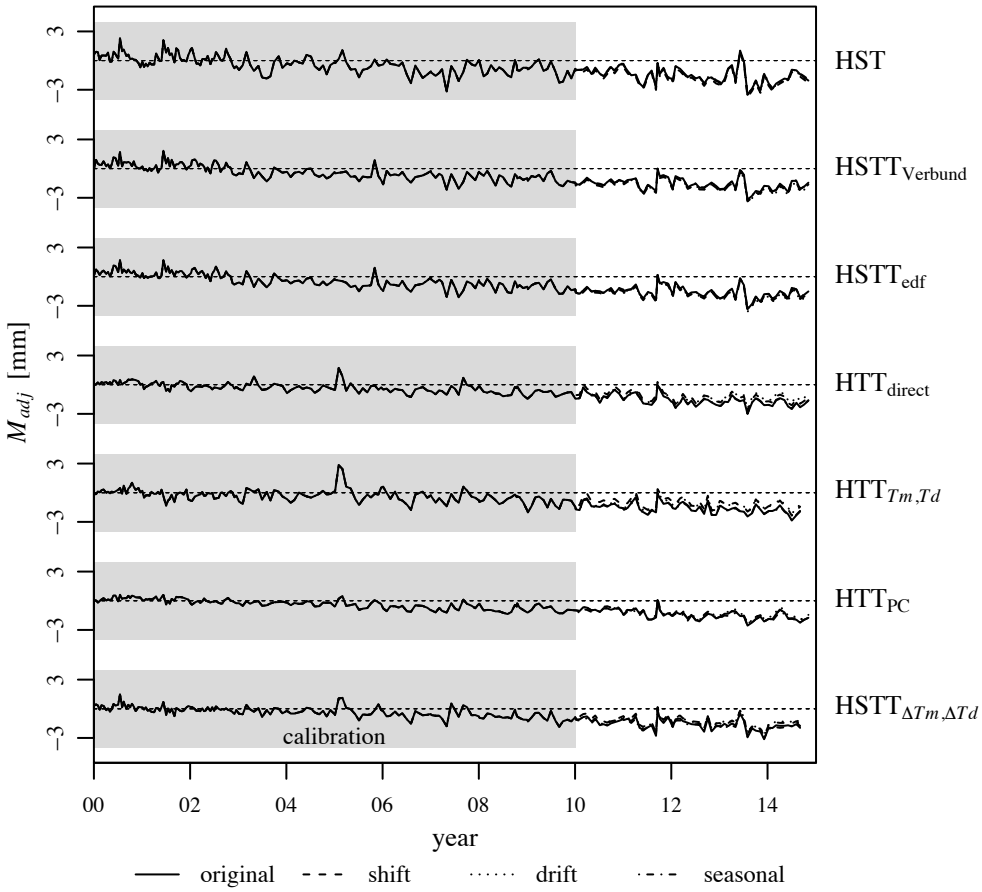

Fig. 4.9 M_{adj} of the different models for arch dam A1. In solid, the time series of the imperfect original data is shown. The other lines show the modified M_{adj} where the small behaviour changes were filtered out to obtain perfect data for the analysis. It can be recognised that the difference to the original data is marginal and the original shape of the time series is preserved.

4.5.2.2 Results

The results of the goodness of fit indicators *RSE* and R^2 and the prediction accuracy indicator $RMSPE_{CV}$ and R^2_{CV} are summarised in Table 4.6. The amount of the variance that can be described by the model (R^2) varies between 0.910 and 0.996. It can be recognised that the *RSE* varies between 0.29 mm and 2.16 mm and clearly depends on the structure and thus is not suitable for comparisons between different structures. Fig. 4.10a and 4.10b show values of R^2 grouped for dams and models. Overall, it can be stated that the dam-specific data lead to more variability than the choice of the model. A closer look shows that the $\text{HSTT}_{\Delta T_m,\Delta T_d}$ model belongs to the best performing models for all investigated dams. The HST model belongs to the poorest performing models. Nevertheless, it has still a good correlation. The performance of the HTT_{dir}, the HTT_{T_m,T_d} and the HTT_{PC} models is varying for the different dams. Generally, the chosen models perform better

for arch dams than for the gravity dams. However, the model of the arch gravity-dam performs worst.

To evaluate the prediction accuracy, the $RMSPE_{CV}$ and R^2_{CV} were estimated. The cross-validation prediction errors are generally larger than the calibration errors. Nevertheless, the pattern can be compared to the R^2. Again, the $\text{HSTT}_{\Delta T_m,\Delta T_d}$ performs best and the HST model worst (Fig. 4.10c and d). The model robustness (Fig. 4.10e and f) also mainly depends on the data and not on the model. In contrast to the goodness of fit and the prediction accuracy, the $\text{HSTT}_{\Delta T_m,\Delta T_d}$ model has no good performance concerning robustness. For some dams, it even was the least robust model.

The results of the hypothesis tests that were performed to find the artificial behaviour changes are shown in Table 4.7 in the form of p-values of different magnitude. In the case of a shift in the data, the results show that for all dams and models, shifts with a magnitude of $0.75 \cdot RSE$ can be found and stated as significant by the proposed MLR procedure. For some dams, magnitudes of $0.5 \cdot RSE$ can already be stated as significant. For the drifts, a similar pattern can be recognised. Drifts with $1 \cdot RSE$/5 a = $0.2 \cdot RSE$/a can be found by the procedure. The added seasonal pattern is detected for amplitudes > $1.25 \cdot RSE$ in most cases.

In Fig. 4.11, the adjusted behaviour indicators of the HST model of HG1 are shown for the added shifts, drifts and seasonal patterns. In Fig. 4.12, the same is provided for the $\text{HSTT}_{\Delta T_m,\Delta T_d}$ model of HG1. The HST model has an RSE of 0.82 mm. The RSE of the $\text{HSTT}_{\Delta T_m,\Delta T_d}$ is 0.38 mm, i.e. about half of the size of the RSE of the HST model. As a consequence, the added abnormal behaviour is half of the size for the $\text{HSTT}_{\Delta T_m,\Delta T_d}$ model. However, for both models, the shift, the drift and the seasonal pattern can be recognised by the MLR model. Visually, the abnormal behaviour of the HST model seems to be better recognisable.

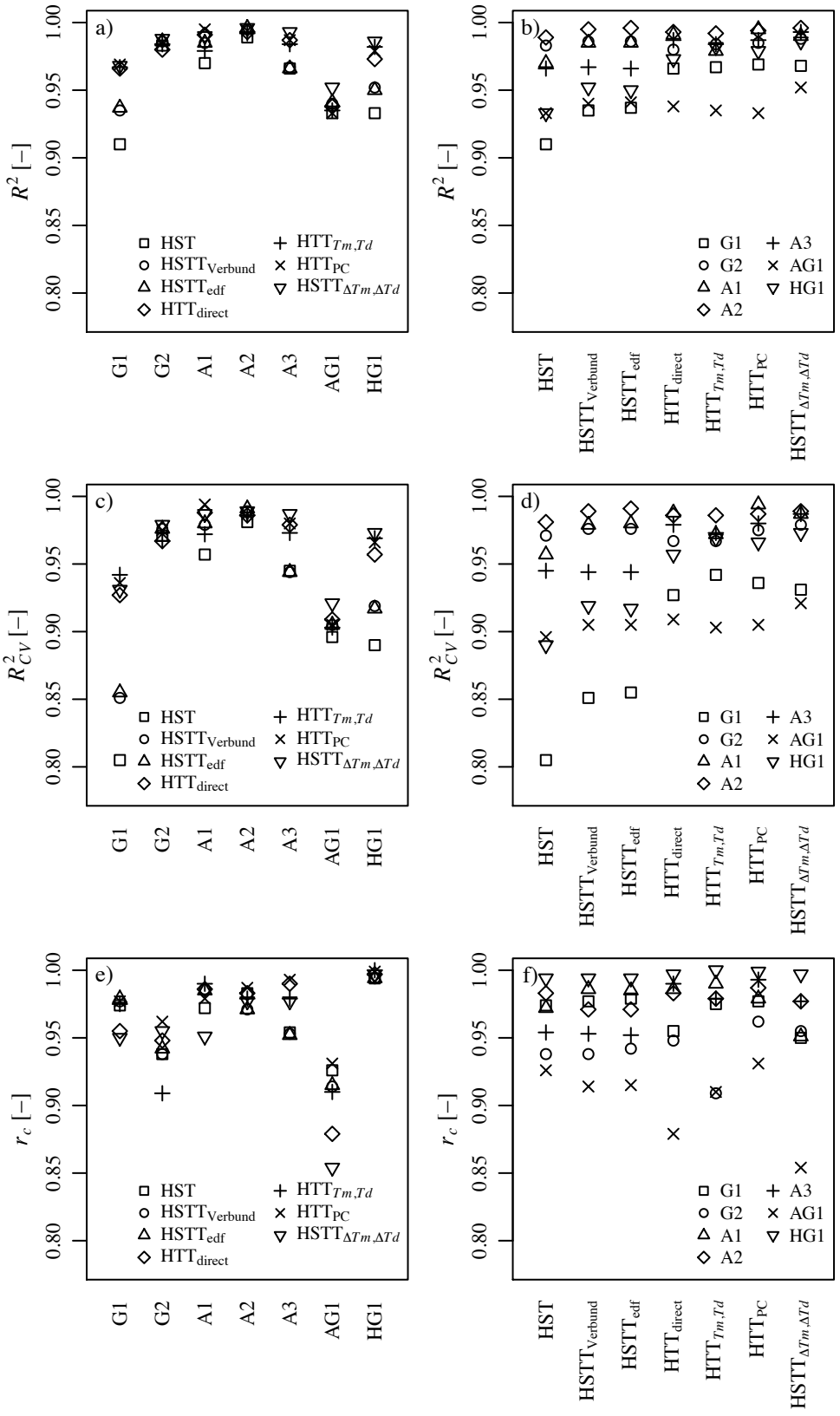

Fig. 4.10 Comparison of different temperature models for different dams: R^2 for a) different dams and b) for different models; R^2_{CV} for c) different dams and d) for different models; r_c for e) different dams and f) for different models.

Table 4.6 Goodness of fit (RSE and R^2), prediction accuracy ($RMSPE_{CV}$ and R^2_{CV}) and robustness coefficient r_c for different dams and temperature models.

dam	model	RSE [mm]	R^2 [-]	$RMSPE_{CV}$ [mm]	R^2_{CV} [-]	r_c [-]
G1	HST	0.80	0.910	0.86	0.805	0.974
	$HSTT_{Verbund}$	0.68	0.935	0.76	0.851	0.977
	$HSTT_{edf}$	0.67	0.937	0.75	0.855	0.979
	HTT_{dir}	0.49	0.966	0.53	0.927	0.955
	HTT_{T_m,T_d}	0.48	0.967	0.49	0.942	0.975
	HTT_{PC}	0.47	0.969	0.49	0.936	0.977
	$HSTT_{\Delta T_m,\Delta T_d}$	0.45	0.972	0.47	0.947	0.950
G2	HST	0.52	0.983	0.55	0.971	0.938
	$HSTT_{Verbund}$	0.48	0.986	0.51	0.976	0.938
	$HSTT_{edf}$	0.47	0.986	0.51	0.976	0.942
	HTT_{dir}	0.57	0.980	0.57	0.967	0.948
	HTT_{T_m,T_d}	0.51	0.984	0.56	0.967	0.909
	HTT_{PC}	0.49	0.985	0.51	0.975	0.962
	$HSTT_{\Delta T_m,\Delta T_d}$	0.44	0.988	0.44	0.979	0.955
A1	HST	0.69	0.970	0.75	0.957	0.977
	$HSTT_{Verbund}$	0.50	0.985	0.54	0.979	0.986
	$HSTT_{edf}$	0.49	0.985	0.52	0.980	0.985
	HTT_{dir}	0.38	0.991	0.38	0.988	0.986
	HTT_{T_m,T_d}	0.58	0.979	0.58	0.972	0.990
	HTT_{PC}	0.29	0.995	0.29	0.994	0.979
	$HSTT_{\Delta T_m,\Delta T_d}$	0.41	0.990	0.42	0.987	0.951
A2	HST	2.16	0.992	2.40	0.984	0.983
	$HSTT_{Verbund}$	1.44	0.996	1.64	0.991	0.971
	$HSTT_{edf}$	1.36	0.997	1.54	0.992	0.971
	HTT_{dir}	1.71	0.995	1.71	0.987	0.983
	HTT_{T_m,T_d}	1.68	0.995	1.88	0.989	0.979
	HTT_{PC}	1.59	0.996	1.64	0.989	0.987
	$HSTT_{\Delta T_m,\Delta T_d}$	1.60	0.996	1.76	0.990	0.977
A3	HST	1.76	0.965	1.92	0.945	0.954
	$HSTT_{Verbund}$	1.76	0.967	1.93	0.944	0.953
	$HSTT_{edf}$	1.77	0.966	1.93	0.944	0.952
	HTT_{dir}	1.11	0.987	1.19	0.979	0.990
	HTT_{T_m,T_d}	1.21	0.984	1.26	0.973	0.979
	HTT_{PC}	1.08	0.987	1.12	0.980	0.993
	$HSTT_{\Delta T_m,\Delta T_d}$	0.84	0.993	0.89	0.987	0.977
AG1	HST	1.52	0.933	1.65	0.896	0.926
	$HSTT_{Verbund}$	1.45	0.940	1.58	0.905	0.914
	$HSTT_{edf}$	1.44	0.941	1.58	0.905	0.915
	HTT_{dir}	1.47	0.938	1.56	0.909	0.879
	HTT_{T_m,T_d}	1.51	0.935	1.55	0.903	0.910
	HTT_{PC}	1.53	0.933	1.62	0.905	0.931
	$HSTT_{\Delta T_m,\Delta T_d}$	1.30	0.952	1.41	0.921	0.854
HG1	HST	0.82	0.933	0.86	0.890	0.994
	$HSTT_{Verbund}$	0.70	0.952	0.73	0.919	0.994
	$HSTT_{edf}$	0.71	0.95	0.74	0.917	0.994
	HTT_{dir}	0.51	0.973	0.53	0.957	0.997
	HTT_{T_m,T_d}	0.43	0.982	0.44	0.969	1.000
	HTT_{PC}	0.45	0.979	0.46	0.966	0.999
	$HSTT_{\Delta T_m,\Delta T_d}$	0.38	0.986	0.42	0.973	0.997

Table 4.7 Results of hypothesis test using MLR to find behaviour change for different magnitudes of abnormal behaviour (*** p<0.001; ** p<0.01; * p<0.05; . p<0.1).

		shift					drift					season				
dam	model	0.50	0.75	1.00	1.25	1.50	0.50	0.75	1.00	1.25	1.50	0.50	0.75	1.00	1.25	1.50
G1	HST	*	***	***	***	***		*	**	**	***			*	**	***
	$HSTT_{Verbund}$	*	***	***	***	***		*	**	***	***			*	**	***
	$HSTT_{edf}$	*	***	***	***	***		*	**	***	***			*	**	***
	HTT_{dir}	*	**	***	***	***		*	**	***	***			*	**	***
	HTT_{T_m,T_d}	*	**	***	***	***		*.	*	**	***			.	*	**
	HTT_{PC}	*	**	***	***	***		*	**	***	***			*	**	***
	$HSTT_{\Delta T_m,\Delta T_d}$	*	**	***	***	***		.	**	**	***			.	*	**
G2	HST	.	*	***	***	***	.	*	**	***	***				*	**
	$HSTT_{Verbund}$	.	*	***	***	***	.	*	**	***	***			.	*	**
	$HSTT_{edf}$	.	*	***	***	***	.	*	**	***	***				*	**
	HTT_{dir}	.	**	***	***	***	.	*	**	***	***			.	*	**
	HTT_{T_m,T_d}	.	**	***	***	***	.	*	**	***	***			.	*	**
	HTT_{PC}	.	**	***	***	***	.	*	**	***	***			.	*	**
	$HSTT_{\Delta T_m,\Delta T_d}$	.	*	***	***	***	.	*	**	***	***				*	**
A1	HST	.	**	***	***	***		.	*	**	***			.	*	**
	$HSTT_{Verbund}$	.	**	***	***	***		.	*	**	***			.	*	**
	$HSTT_{edf}$	.	**	***	***	***		.	*	**	***			.	*	**
	HTT_{dir}	.	**	***	***	***		.	*	**	***			.	*	**
	HTT_{T_m,T_d}	*	**	***	***	***		.	*	**	***			*	**	**
	HTT_{PC}	.	**	***	***	***		.	*	**	***			.	*	**
	$HSTT_{\Delta T_m,\Delta T_d}$	.	**	***	***	***		.	*	**	***			.	*	**
A2	HST	.	**	***	***	***		*	**	***	***			.	*	**
	$HSTT_{Verbund}$	.	**	***	***	***		*	**	***	***			.	*	**
	$HSTT_{edf}$	.	**	***	***	***		*	**	**	***			.	*	**
	HTT_{dir}	.	*	***	***	***		.	*	**	***			.	*	**
	HTT_{T_m,T_d}		*	**	***	***		.	*	**	***				.	*
	HTT_{PC}		*	**	***	***		.	*	**	***				*	**
	$HSTT_{\Delta T_m,\Delta T_d}$		*	**	***	***		.	*	**	***				.	*
A3	HST	.	**	***	***	***		.	*	**	***			.	*	**
	$HSTT_{Verbund}$	.	**	***	***	***		.	*	**	***			.	*	**
	$HSTT_{edf}$	.	**	***	***	***		.	*	**	***			.	*	**
	HTT_{dir}		*	**	***	***		.	*	**	**				.	*
	HTT_{T_m,T_d}	.	**	***	***	***		.	*	**	***				*	*
	HTT_{PC}	.	*	***	***	***		.	*	**	***				*	**
	$HSTT_{\Delta T_m,\Delta T_d}$		*	**	***	***		.	*	**	**				.	*
AG1	HST	**	***	***	***	***	.	**	***	***	***		.	**	***	***
	$HSTT_{Verbund}$	**	***	***	***	***	.	**	***	***	***		.	**	***	***
	$HSTT_{edf}$	**	***	***	***	***	.	**	***	***	***		.	**	***	***
	HTT_{dir}	*	***	***	***	***	.	*	**	***	***		.	*	***	***
	HTT_{T_m,T_d}	*	***	***	***	***	.	*	**	***	***		.	**	**	***
	HTT_{PC}	*	***	***	***	***	.	*	**	***	***		.	*	***	***
	$HSTT_{\Delta T_m,\Delta T_d}$	*	***	***	***	***	.	*	**	***	***		.	*	***	***
HG1	HST	.	**	***	***	***		.	*	**	***			.	*	**
	$HSTT_{Verbund}$	.	**	***	***	***		.	*	**	***				*	**
	$HSTT_{edf}$	.	**	***	***	***		.	*	**	***			.	*	**
	HTT_{dir}	.	*	**	***	***			*	**	***				*	*
	HTT_{T_m,T_d}	.	*	***	***	***		.	*	**	***				*	*
	HTT_{PC}	.	**	***	***	***		.	*	**	***			.	*	**
	$HSTT_{\Delta T_m,\Delta T_d}$	.	*	***	***	***		.	*	**	***				*	**

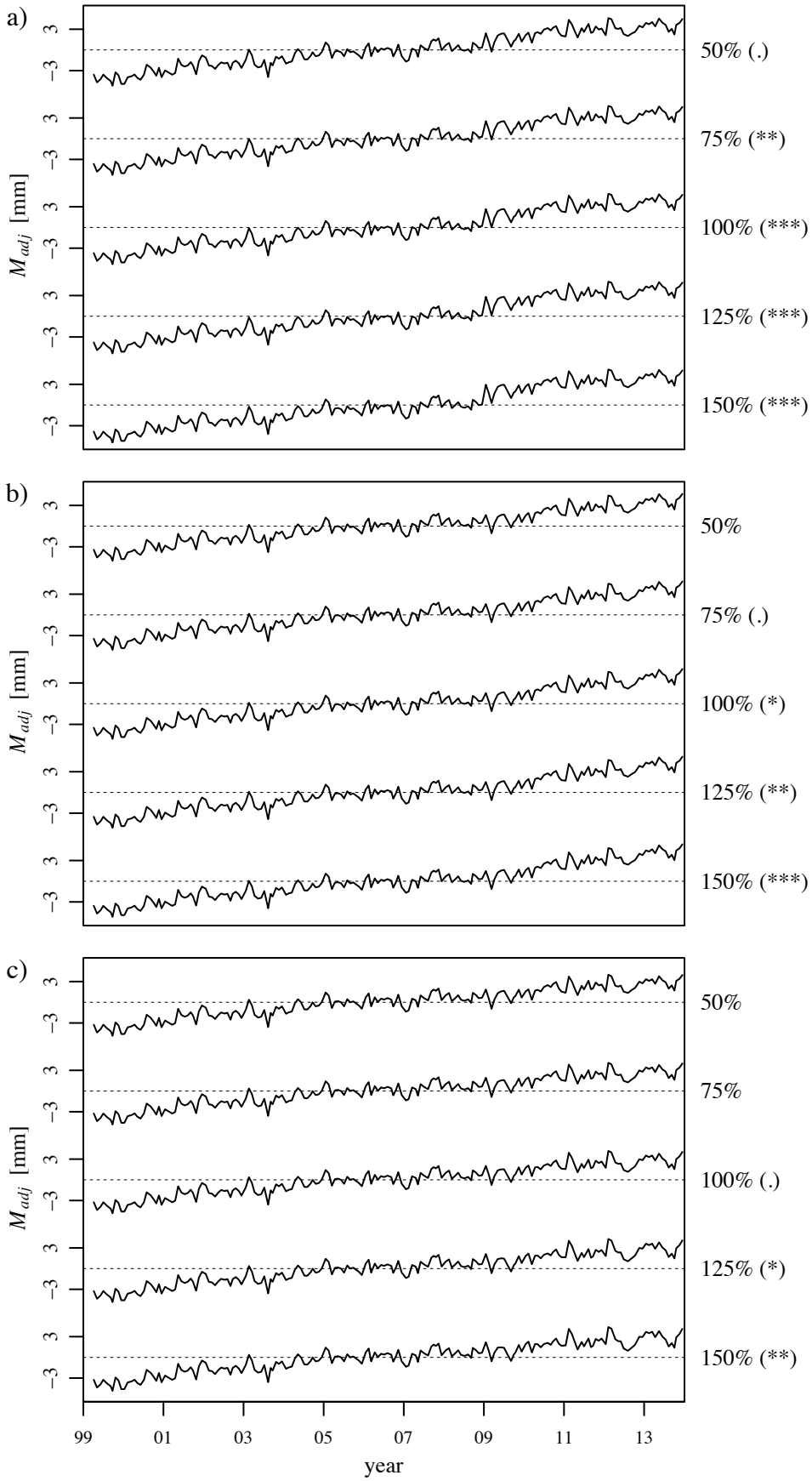

Fig. 4.11 Adjusted behaviour indicator M_{adj} of the HST model of HG1 for different magnitudes of added artificial abnormal behaviour: a) shift; b) drift; c) seasonal pattern. The original data already contain a strong drift (for data description see Appendix A.5.8).

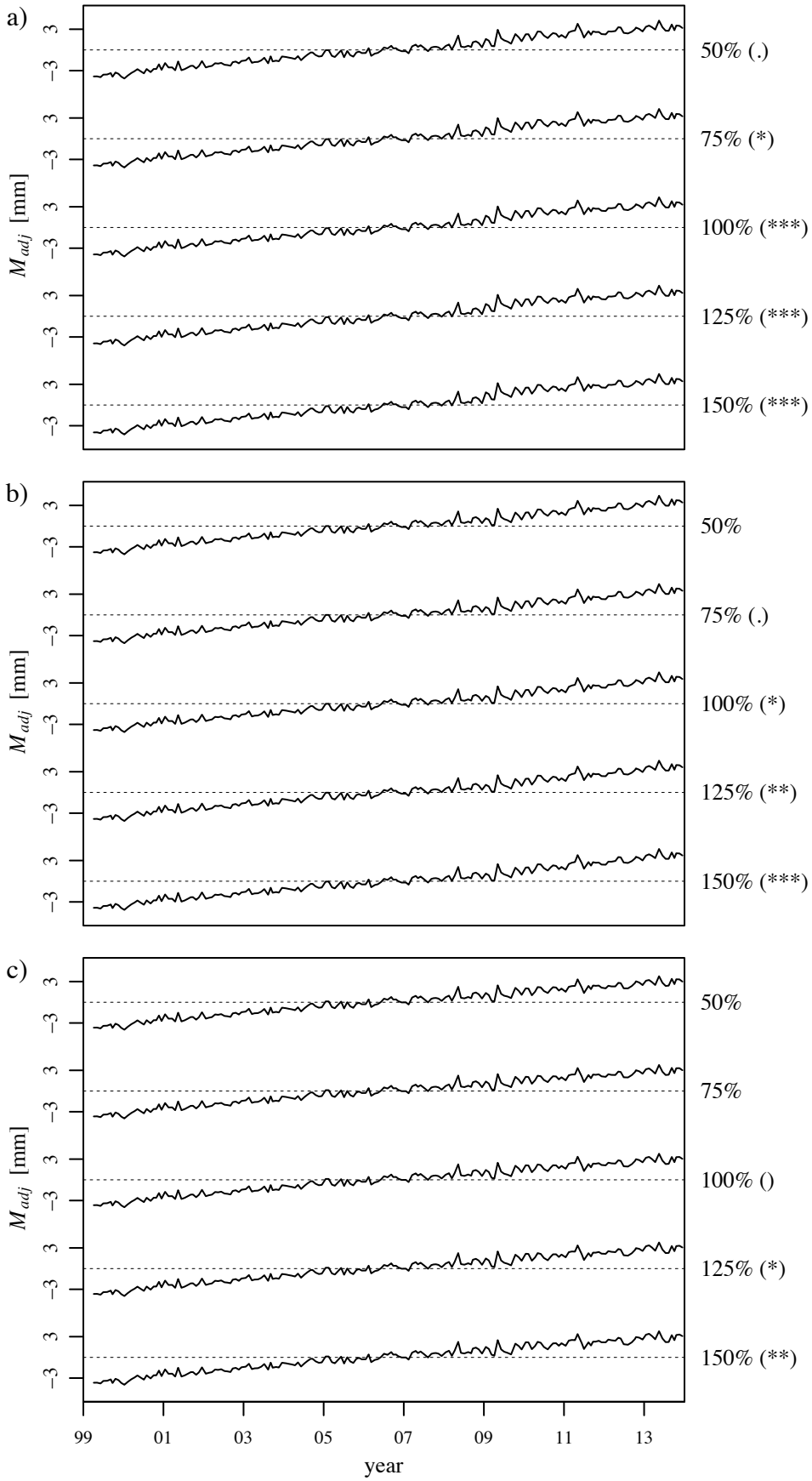

Fig. 4.12 Adjusted behaviour indicator M_{adj} of the $\text{HSTT}_{\Delta T_m, \Delta T_d}$ model of HG1 for different magnitudes of added artificial abnormal behaviour: a) shift; b) drift; c) seasonal pattern. The original data already contain a strong drift (for data description see Appendix A.5.8).

4.5.2.3 Thermometer failure

Another aspect that has to be considered when using temperature models is whether a model can still be used after a thermometer has failed. For instance, the HSTT model with delayed air temperature reading becomes unusable if the air temperature measurement fails. According to experience, the data of MeteoSwiss is very accurate and a malfunctioning of the infrastructure can be quickly eliminated. On the other hand, the thermometers that are installed in concrete dams (most of them were placed during concreting) cannot be replaced easily. Considering the HTT_{PC} model, all of the thermometers are used in the model. On the contrary, in the HTT_{dir} model only a selected number of thermometers are used. Therefore, it is less likely that exactly the thermometer that is used in the model fails. For the approaches based on the mean temperature and the temperature difference, all thermometers are used. The thermometers closest to the boundary are more important than the inner ones that are only used for the calibration of the thermal diffusivity. If one of the outermost thermometers fails, inverse thermal analysis may be an option. However, this depends on the location of the thermometers; if the thermometer is too far from the boundary, the high frequencies will be wiped out (see Section 3). In general, the issue of thermometer failure can be tackled by setting up a new model or estimating the values of the failed thermometer by a thermal analysis or simply by a statistical correlation.

4.5.2.4 Discussion

All models were successfully applied to find the artificial behaviour changes added to the data. The behaviour changes were detected by the use of MLR analysis (see Section 4.4.2). It is shown that the magnitude of a behaviour change that can be found by the MLR procedure is related to the *RSE* of the model. Generally, shifts with a magnitude of 0.75 *RSE* are identifiable. For example, in a model with an *RSE* of 1 mm, a shift of around 0.75 mm is identifiable and in a model with an *RSE* of 2 mm a shift of around 1.5 mm is identifiable. As a consequence, a model with a lower *RSE*, can identify smaller behaviour changes and may be preferred.

The performance of the models mainly depends on the data and not on the model itself. There was no outstanding model that can be suggested for general use. One of the good performing models was the HTT_{T_m,T_d}. Unfortunately, for some dams the robustness was weak. For some dams, even the simple HST model performed well. The extension by delayed air temperature measurement differences ($\mathrm{HSTT}_{Verbund}$ and HSTT_{edf}) improves the model in some cases. Overall, it is worth to compare different models for a dam to guarantee model quality. Models with a low *RSE* shall be chosen since they allow for an earlier detection of a potential behaviour change. In addition, the robustness of the models has to be checked as well.

4.5.3 Approach to consider irreversible effects

4.5.3.1 Introduction

The observation-prediction comparison procedure has to be used with caution, because irreversible displacements can hardly be predicted (see Section 4.3). Alternatively, the adjusted behaviour indicator $M_{adj} = \beta_0 + P_{ir} + e$ can be analysed. Nevertheless, a function of time $f(t)$ to model the irreversible displacements P_{ir} should be included in the model. This helps to avoid that the irreversible effects are partly assigned to the coefficients of the reversible effects.

Different shape function that can be used to consider the irreversible displacement can be found in the literature (see Section 2.5.4.2). Some of them contain several variables with a similar shape what may lead to multicollinearity. Because the time is the same for all variables considering irreversible displacement in function of time by definition, multicollinearity does not lead to stability problems as far as there is no extrapolation (for details see Section 2.4.2.1). The choice of the shape function can be checked visually by looking at partial residuals or by a partial F-test statistic that checks whether adding terms leads to a significant reduction of the sum of squared residuals SS_{Res}. Alternatively, a spline approach, as described in Fanelli *et al.* (2000), could be used. When using this flexible approach, overfitting must be prevented. To find the optimal degree of freedom of the spline, a cross-validation procedure can be used (James *et al.*, 2013).

4.5.3.2 Methodology

Considered models

A selection of shape functions to represent the irreversible effects from the literature (see Section 2.5.4.2) is taken for the analysis (Table 4.8). Besides these approaches, one model with no irreversible effects is considered. Some of the approaches need a nonlinear optimisation of the coefficients of the exponential function arguments. These coefficients were determined by nonlinear lest squares analysis in advance.

Table 4.8 Overview of shape functions to represent the irreversible effects for the case study.

	shape functions	used in
1	no irreversible effects considered	
2	$\beta_1 t$	Tatin *et al.* (2015)
3	$\beta_1 (1 - \exp(-\kappa t))$	Mata *et al.* (2013)
4	$\beta_1 t + \beta_2 \exp(-t)$	Léger and Leclerc (2007), Mata *et al.* (2013)
5	$\beta_1 t + \beta_2 t^2 + \beta_3 t^3 + \beta_4 t^4 + \beta_5 \exp(-t/c_1)$	Penot *et al.* (2005)
6	spline $s(t)$	Fanelli *et al.* (2000)

Selection of case study

The arch dam A2 was chosen for this analysis because it shows a nonlinear trend in the behaviour. The HTT_{PC} temperature model is chosen because it turned out to be the most robust in the temperature model evaluation (see Section 4.5.2). For the effects of the water level, a third order polynomial approach is used.

Evaluation procedure

As in the temperature model evaluation, the RSE and the R^2 are calculated as a measure for the goodness of fit. Furthermore, the prediction accuracy is evaluated by the cross-validation based $RMSPE_{CV}$ and R^2_{CV}. Furthermore, the robustness coefficient r_c is calculated.

4.5.3.3 Results

The results of the different approaches to represent the irreversible effects are summarised in Table 4.9. The non-linear approaches no. 3 - 6 lead to lower RSE than the linear approach no. 2 and the model without a function of time no. 1. The approach no. 5 is affected by overfitting. This can be seen in the very large $RMSPE_{CV}$ value. The adjusted behaviour indicator and the corresponding irreversible parts are shown in Fig. 4.13. The adjusted behaviour indicators are very similar for all reviewed approaches. Only the one without considering irreversible effects shows a slightly larger variation. This is due to the coefficient estimates that are different since no approach to represent irreversible effects was considered for calibration. This fact also can be confirmed by the robustness coefficient r_c that is lower than for all other models.

Table 4.9 Goodness of fit (RSE and R^2) and prediction accuracy ($RMSPE_{CV}$ and R^2_{CV}) for different shape functions representing the irreversible effects. Additionally, the robustness coefficient r_c is shown.

approach	RSE [mm]	R^2 [-]	$RMSPE_{CV}$ [mm]	R^2_{CV} [-]	r_c [-]
1	1.94	0.993	1.98	0.988	0.941
2	1.84	0.994	1.97	0.987	0.965
3	1.56	0.996	1.6	0.990	0.980
4	1.57	0.996	1.63	0.990	0.977
5	1.55	0.996	284’000	-	0.981
6	1.61	0.995	-	-	0.979

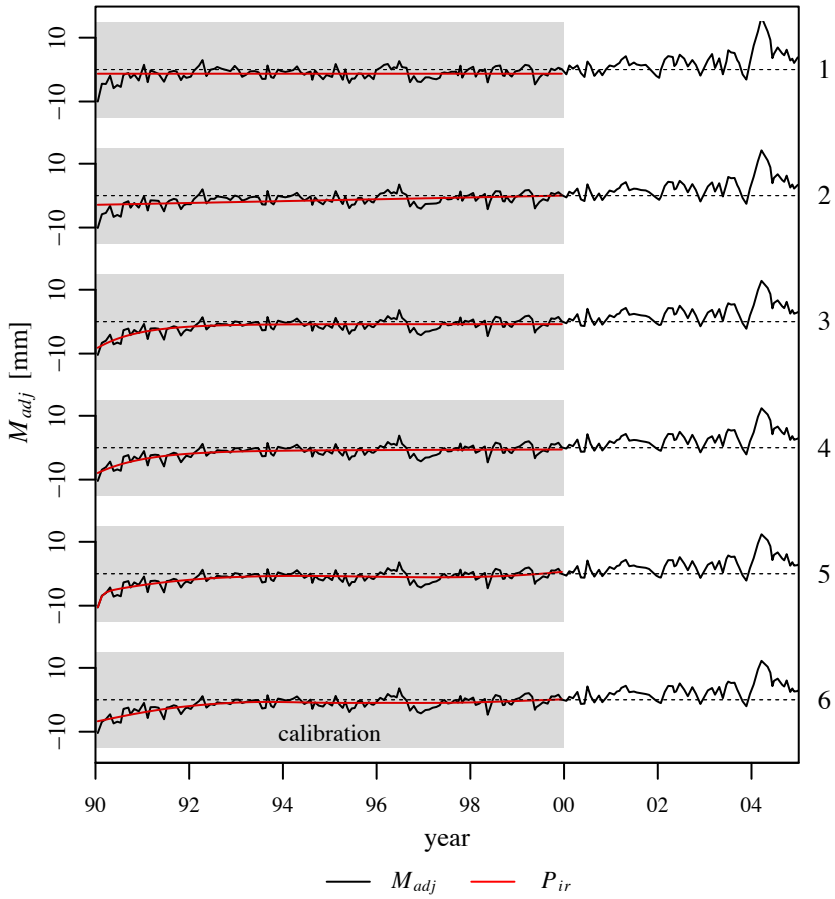

Fig. 4.13 Adjusted behaviour indicator of HTT_{PC} model of arch dam A2 for different approaches to consider the irreversible effects. The amount of the irreversible displacement P_{ir} is shown by the red line.

4.5.3.4 Discussion

When using the adjusted behaviour indicator approach, the main purpose of the approach to consider the irreversible effects is to avoid that they are partly assigned to reversible effects. Therefore, the chosen approach should be able to represent the trend of the irreversible displacement. In many cases, a linear function is a reasonable approach. For more complex cases, as for the arch dam A2, a nonlinear approach with an exponential function might fit better. In this case, a spline approach is an adequate tool. The engineer does not have to choose a certain shape but only evaluate the output of the analysis. The shape is estimated by the fitting procedure.

Unfortunately, there is no advantage of a smaller *RSE* achieved by the approach to represent the irreversible effects. This is because in behaviour analysis based on the adjusted behaviour indicator the residuals and the irreversible displacement are considered in one single term.

When using an approach with several terms, a correlation of them is likely and therefore multicollinearity may occur. Since no extrapolation is considered and the time t is the same in all functions, this multicollinearity can be tolerated. Nevertheless, strong overfitting as shown in the example of approach no. 5, should be avoided. This can be checked by a cross-validation procedure.

4.6 Drainage flow

Statistical models can also be applied to monitor drainage flow but it is less common than for monitoring of the displacements of concrete dams. A short overview of the models for this monitoring purpose is given in Section 2.5.4.3. One goal of this thesis is to evaluate the influence of the environmental conditions on drainage flow and the performance of the models. Thus, the drainage flow measurements of an embankment dam, a gravity dam and an arch dam were analysed with statistical models. The influences of the water level, a potential delay of the effect of the water level, and the precipitation were considered. Since no information about snow melt was available, a seasonal approach was used instead.

The results show that the water level has a major effect on the measured drainage flow. The delayed water level, the seasonal effects and the precipitation have only a minor contribution (Hauser, 2017). As for concrete dams, the effects of the water level can be described by a polynomial approach. However, the correlations were not as good as for concrete dam displacements (R^2 = 0.50 to 0.95).

Because the drainage flow mainly depends on the effect of the water level, its interpretation with MLR models is less common (Amberg, 2009). In the example shown in Section 2.4, also an SLR model with a polynomial approach leads to reasonable results. Such a model can easily be interpreted by a simple correlation plot. Thus, these models are not further evaluated in this thesis.

4.7 Multicollinearity

4.7.1 Introduction

There are different approaches how multicollinearity can be treated (see Section 2.4.2). The most common approach used in engineering practice is to remove correlated regressor variables (Amberg, 2009). This approach was applied for the evaluation of the temperature models in Section 4.5.2. In addition, ridge regression (RR) and principal component regression (PCR) are evaluated in this section.

4.7.2 Ridge regression

4.7.2.1 Methodology

Multicollinearity is mainly caused by correlated temperature readings. Thus, temperature models that are likely affected by this phenomenon are taken for the evaluation. These are the HTT_{dir} and the HTT_{T_m,T_d} models. Since RR shrinks the coefficients, all variables are taken into account in the model. The effects of the water level were considered by a polynomial function up to fourth order. The same orders as in Section 4.5.2 are used. The calculations are performed with the "glmnet" package of Friedman *et al.* (2010) which is available in the R environment (R Core Team, 2013). The shrinkage coefficient λ is estimated by cross-validation with $k = 10$. In doing so, extrapolations of the water level have to be removed, since they heavily disturb the analysis. If the extrapolations of the water level are not removed, very large λ values will result. This is because of multicollinearity between the different polynomial terms of the water level approach. As explained in Section 2.4.2, this multicollinearity can be tolerated.

As in Section 4.5.2, the *RSE* and the R^2 are used as a measure for the goodness of fit. The prediction accuracy is evaluated by the $RMSPE_{CV}$ and the R^2_{CV}. In addition, the robustness coefficient r_c is estimated. To evaluate if the RR models are able to detect behaviour changes, the same analysis as in Section 4.5.2 is performed. Furthermore, the same dams, data sets and calibration periods are used. This allows for comparison of the results.

4.7.2.2 Results

The hypothesis tests that were performed to find the artificial behaviour changes lead to the same results as in Section 4.4. The results of the coded p-values for the different magnitudes are shown in Appendix A.6.3. The magnitudes of the *RSE* at which the added behaviour changes are found are similar as in Section 4.5.2. As a consequence, the *RSE* of the MLR models and the RR models are comparable.

The results of the goodness of fit indicators *RSE* and R^2 and the prediction accuracy indicators $RMSPE_{CV}$ and R^2_{CV} are summarised in Table 4.10. In addition, the estimated robustness coefficient r_c and the shrinkage coefficients λ are provided. In Fig. 4.14, the R^2 and r_c values are shown separately for the different dams and models. In Fig. 4.14a, the R^2 of the RR models (black) and of the MLR models (red) are shown separately for the different dams. The R^2 values, and therefore also the *RSE* values, of the RR model are at least as good as for MLR models. However, the robustness coefficient of RR models is generally lower (Fig. 4.14b). For the HTT_{T_m,T_d} model of arch dam A2, it is lower than 0.4.

Table 4.10 Results of ridge regression analysis: Goodness of fit (*RSE* and R^2), prediction accuracy ($RMSPE_{CV}$) and robustness coefficient r_c for different dams and temperature models. Additionally, the estimated shrinkage coefficients λ are given.

dam	model	*RSE* [mm]	R^2 [-]	$RMSPE_{CV}$ [mm]	R^2_{CV} [-]	r_c [-]	λ [-]
G1	HTT_{dir}	0.45	0.974	0.48	0.941	0.926	0.0125
	HTT_{T_m,T_d}	0.45	0.972	0.46	0.950	0.918	0.00575
G2	HTT_{dir}	0.39	0.992	0.47	0.973	0.854	0.0025
	HTT_{T_m,T_d}	0.48	0.986	0.62	0.955	0.844	0.001
A1	HTT_{dir}	0.26	0.996	0.3	0.993	0.947	0.00775
	HTT_{T_m,T_d}	0.50	0.985	0.52	0.980	0.963	0.00275
A2	HTT_{dir}	1.80	0.995	2.40	0.980	0.775	0.075
	HTT_{T_m,T_d}	1.74	0.995	2.25	0.983	0.365	0.001
A3	HTT_{dir}	1.04	0.989	1.11	0.981	0.986	0.0425
	HTT_{T_m,T_d}	1.00	0.989	1.06	0.982	0.987	0.015
AG1	HTT_{dir}	1.48	0.939	1.76	0.881	0.811	0.0035
	HTT_{T_m,T_d}	1.47	0.939	1.60	0.897	0.843	0.001
HG1	HTT_{dir}	0.40	0.986	0.48	0.966	0.984	0.002
	HTT_{T_m,T_d}	0.40	0.985	0.44	0.972	0.995	0.00125

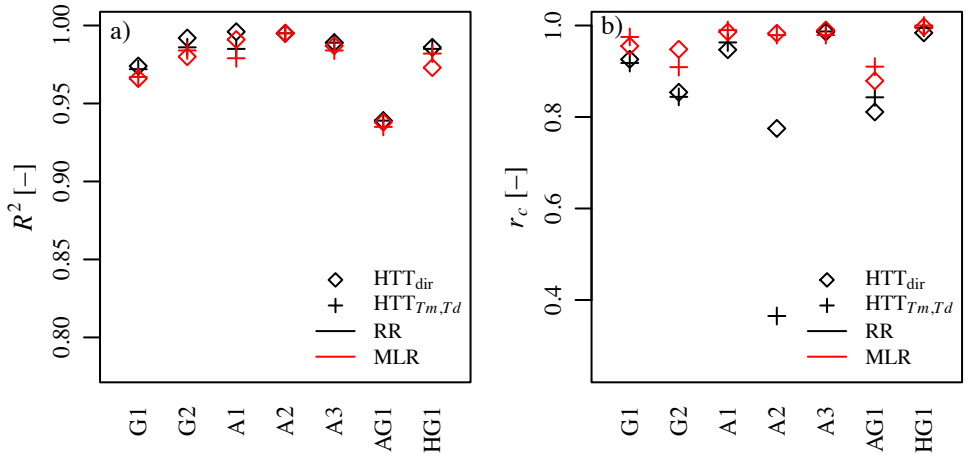

Fig. 4.14 Comparison of temperature models for different dams: a) coefficient of determination R^2; b) robustness coefficient r_c.

4.7.3 Principal component regression

4.7.3.1 Methodology

The same models as in the previous section are used for the evaluation of the principal component regression (see Section 4.7.2). After scaling the individual regressors by unit normal scaling, the principal components of all regressors are calculated. Then principal

component regression (PCR) is carried out by the "pls" package of Mevik and Wehrens (2007) which is available in the R environment (R Core Team, 2013). To determine the number of principal components n_{PC} that are taken into account in the model, a 10-fold cross-validation is performed. Data points with extrapolations of the water level are not considered since they may disturb the result. Then, the goodness of fit and prediction accuracy are estimated. In addition, the same analysis as in Section 4.5.2 is performed to check the capability of detecting behaviour changes. For the sake of comparison, the same calibration periods as for the temperature model evaluations are used.

4.7.3.2 Results

The results of the goodness of fit indicators RSE and R^2, the prediction accuracy indicator $RMSPE_{CV}$ and the robustness coefficient r_c are summarised in Table 4.11. Furthermore, the number of principal components n_{PC} is given. In Fig. 4.15, the R^2 and the r_c of the different models are compared. Because the current approach is similar to the HTT_{PC} model (see Section 4.5.2), which is a modification of the HTT_{dir} model, the results of the HTT_{PC} are shown as well. The R^2 of the PCR models are in a similar order as for the MLR models. However, the robustness of PCR models is smaller for most of the dams. For arch dam A2 it is only about 0.4. However, the HTT_{PC} model, which uses principal components of the temperatures but not of the other influences, is more robust than the PCR HTT_{dir} model. The results of the hypothesis tests that were performed to find the artificial behaviour changes are provided in Appendix A.4. As for RR models, the magnitudes at which the added behaviour changes were found are similar to the MLR models.

Table 4.11 Results of principal component analysis: Goodness of fit (*RSE* and R^2), prediction accuracy ($RMSPE_{CV}$) and robustness coefficient r_c for different dams and temperature models. Additionally, the number of principal components n_{PC} is given.

dam	model	*RSE* [mm]	R^2 [-]	$RMSPE_{CV}$ [mm]	r_c [-]	n_{PC} [-]
G1	HTT_{dir}	0.48	0.967	0.49	0.916	9
	HTT_{T_m,T_d}	0.54	0.960	0.48	0.799	5
G2	HTT_{dir}	0.41	0.990	0.49	0.865	14
	HTT_{T_m,T_d}	0.54	0.982	0.63	0.888	9
A1	HTT_{dir}	0.26	0.996	0.31	0.889	13
	HTT_{T_m,T_d}	0.52	0.984	0.51	0.962	6
A2	HTT_{dir}	1.62	0.995	2.39	0.401	25
	HTT_{T_m,T_d}	1.58	0.996	2.02	0.351	15
A3	HTT_{dir}	1.07	0.988	1.12	0.986	4
	HTT_{T_m,T_d}	1.01	0.989	1.08	0.981	8
AG1	HTT_{dir}	1.51	0.936	1.81	0.732	14
	HTT_{T_m,T_d}	1.51	0.935	1.64	0.862	8
HG1	HTT_{dir}	0.38	0.986	0.48	0.982	17
	HTT_{T_m,T_d}	0.39	0.985	0.44	0.995	11

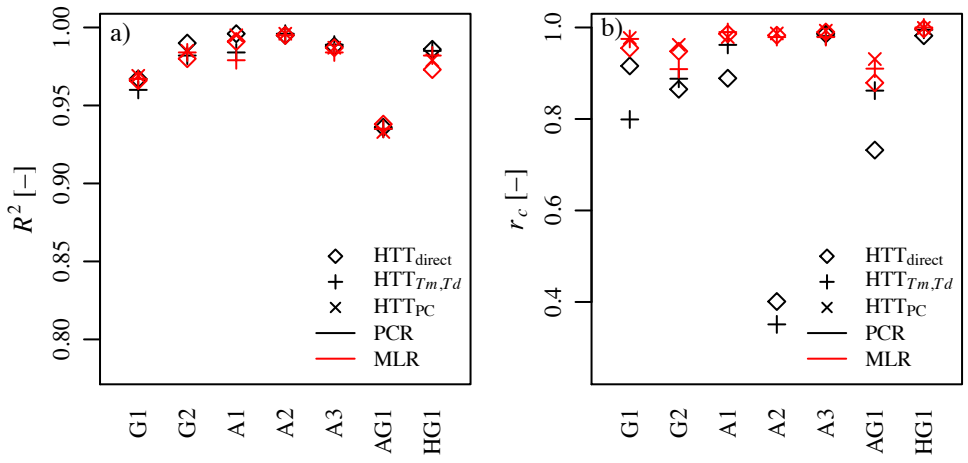

Fig. 4.15 Model comparison of principal component analysis for different dams: a) coefficient of determination R^2; b) robustness coefficient r_c (different axis scaling).

4.7.4 Discussion

Two methods for the treatment of multicollinearity have been evaluated: (i) ridge regression (RR) and (ii) principal component regression (PCR). The results of the two methods are very similar. The goodness of fit is at least as good as for MLR models. In some cases, it is even better. On the other hand, the robustness of the models is not as good as for MLR models for many dams. In both approaches, all temperature measurements

are included in the model. As a consequence, if one thermometer fails, the model will no longer be usable. Therefore, it is recommended to use the MLR models by excluding correlated variables, as it was performed in Section 4.5.2.

Furthermore, it is shown that the *RSE* magnitudes at which the added behaviour changes were found, are similar to those found by MLR analysis. Thus, the *RSE* can be used as a measure for comparison. Concerning RR, the order of magnitude of the shrinkage parameter λ is the same as in Weber (2002).

4.8 Autocorrelation

4.8.1 Introduction

Autocorrelation in the residuals of a regression model leads to correct coefficient estimates but the estimation of the standard errors is wrong. Unfortunately, many statistical test procedures are based on them (see Section 2.4.3). There are different methods to detect and treat autocorrelation. Visual detection based on the ACF- and the PACF-plot is explained in Appendix **??**. Here, two methods for the treatment of autocorrelation are evaluated. They lead to a correct estimation of the standard errors se(β) of the coefficients. These are the (i) thinning out of the data set and (ii) block bootstrap method. There are also the approaches of Cochrane-Orcutt and Prais-Winsten used by Weber (2002). However, experience has shown that these approaches may fail if a high autocorrelation is present (Schiefer, 2015). Therefore, they are not discussed herein. The content of this section mainly refers to Bühlmann *et al.* (2015).

4.8.2 Methodology

The analysis is carried out with the data set of arch dam A4, where daily readings for seven years are available. The data set and the dam are described in Appendix A.5.6. Due to the daily recording of the measurement data, the residuals are highly autocorrelated.

The HTT$_{Tm,Td}$ model given by Eq. (4.9) below is used in combination with a fourth order Chebyshev polynomial to represent the effects of the water level. This avoids the presence of multicollinearity. In addition, a time-delayed reversible deformation h_v (viscous elastic deformation of the structure) that is influenced by the water level is taken into account (Perner and Obernhuber, 2009). Including the delayed part leads to a more accurate model with less autocorrelation of the residuals. The temperatures were pre-processed to mean temperatures T_m and linear temperature differences T_d by thermal analysis. Due to the multicollinearity, the first principal components of T_m and T_d are entered in the model. The irreversible displacements are considered by a linear function.

$$P(h,T,t) = \beta_0 + \beta_1 h + \beta_2 h^2 + \beta_3 h^3 + \beta_4 h^4 + \beta_5 h_v + \beta_6 T_{m,I} + \beta_7 T_{d,I} + \beta_8 t \quad (4.9)$$

First of all, the original data set with daily measurements is used. In a second step, the data set with daily measurement data is thinned out considering intervals of 7, 14 and 28 days in order to reduce autocorrelation. For the data sets with 28 day intervals, two different start dates are chosen (1.1.1992 and 14.1.1992). The new data sets can be seen as data sets with larger measurement intervals. For all these models, the coefficient estimates and the corresponding standard errors are calculated. In terms of a hypothesis test, the standard errors are used to calculate the p-values. In addition, goodness of fit indicators are estimated.

Finally, the block bootstrap (BBS) method is applied. Blocks with a size of 40 d, which corresponds to the period where correlation of the daily measurement data was detected, are sampled 1000 times. This leads to 1000 slightly different data sets based on the same data. For each data set, an MLR is performed. Out of these 1000 regression coefficients β_i, the mean value and the corresponding p-values are calculated.

4.8.3 Results

The autocorrelation of the model residuals based on the different data sets of the original and the thinned-out data is shown by the ACF- and PACF-plots in Fig. (4.16). The spike of lag 1 in the PACF-plot can be seen as a rough estimate of the coefficient ρ_1 of a first order autoregressive model AR(1) $e_t = \rho_1 e_{t-1} + \varepsilon$ (Dettling, 2014). For daily data, ρ_1 is close to 1, which corresponds to high autocorrelation. For the weekly and bi-weekly time-lags, the autocorrelation is still present. For the time series with 28 d intervals, the autocorrelation is no longer present.

The values of the regression coefficients β_i and the corresponding p-values are displayed in Table 4.12. The regression coefficients β_i do not differ much for the different time-intervals and the BBS method but the p-values do. For the 1 d, 7 d and 14 d data, the hypothesis test of the individual coefficients leads to significance for all tested variables. However, for the two 28 d data sets and the BBS method, the fourth order term of the water level and the linear irreversible displacement are not significant. The BBS method is able to estimate correct standard errors of the coefficients even though all data are used for calibration. This leads to more accurate models than by removing data since more data is used to estimate the coefficients. This can be seen by comparing the model accuracy parameters in Table 4.13. Furthermore, the two different data sets with time-lags of 28 d lead to different results.

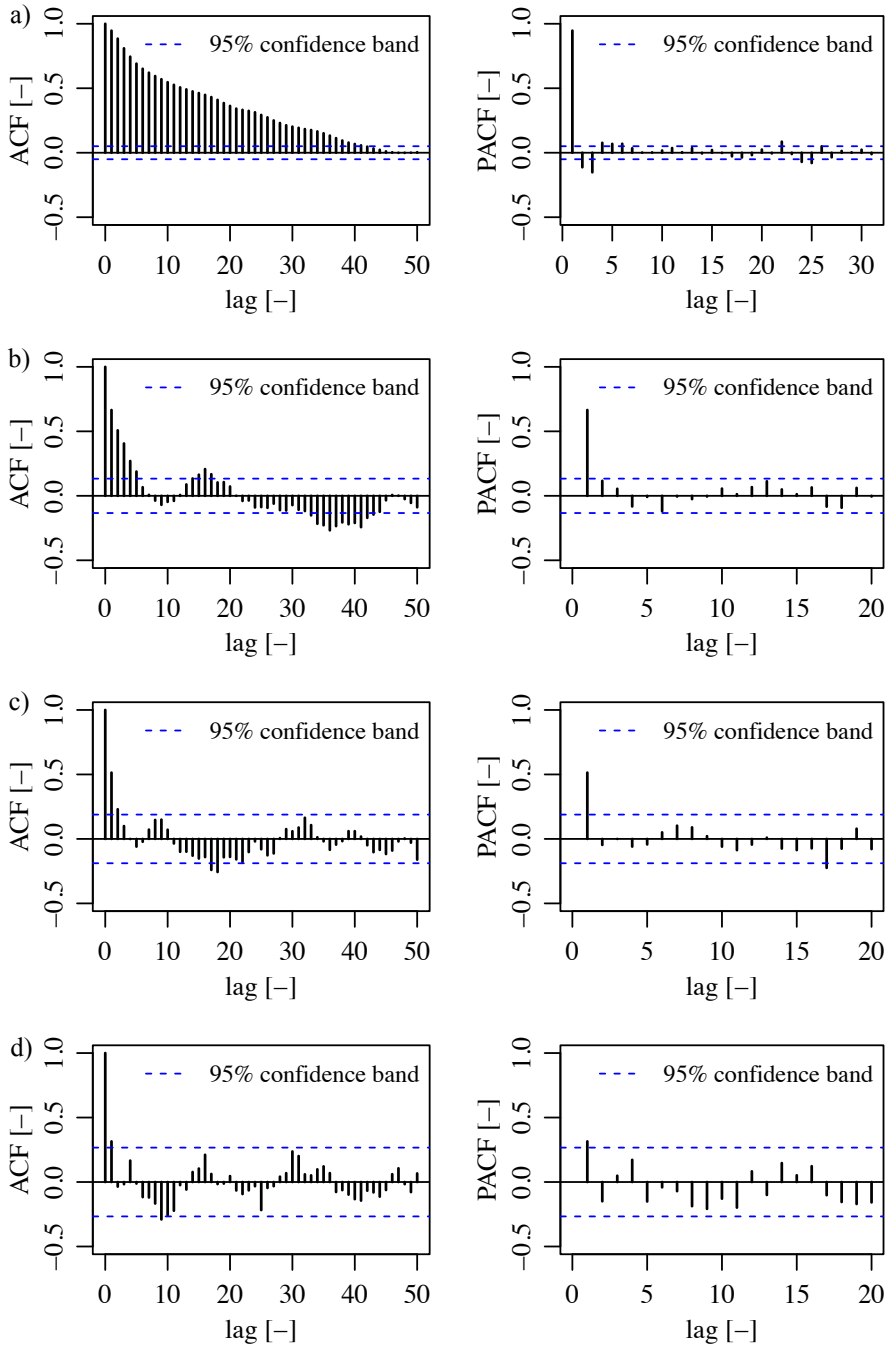

Fig. 4.16 ACF- (left) and PACF-plots (right) for residuals based on different data sets: a) original data with daily measurements; thinned out data with b) 7 d time-lag c) 14 d time-lag and d) 28 d time-lag.

Table 4.12 Values of regression coefficients and p-values (*** p<0.001; ** p<0.01; * p<0.05; . p<0.1) resulting from the different models.

		1 d	7 d	14 d	28 d (I)	28 d (II)	BBS
β_0	value	61.43	61.40	61.31	60.20	60.25	61.30
	p	***	***	***	***	***	***
β_h	value	24.08	23.72	23.30	22.81	21.36	23.94
	p	***	***	***	***	***	***
β_{h^2}	value	7.21	7.08	6.87	6.60	5.81	7.08
	p	***	***	***	***	***	***
β_{h^3}	value	1.37	1.30	1.28	1.29	0.96	1.42
	p	***	**	***	***	**	***
β_{h^4}	value	0.46	0.49	0.48	0.52	0.37	0.44
	p	***	***	*	.		.
$\beta_{h,v}$	value	0.29	0.29	0.32	0.32	0.33	0.30
	p	***	***	***	***	***	***
$\beta_{Tm,I}$	value	-3.92	-3.95	-3.94	-4.06	-3.87	-3.89
	p	***	***	***	***	***	***
$\beta_{Td,I}$	value	-0.48	-0.50	-0.46	-0.43	-0.51	-0.45
	p	***	***	***	***	***	***
t	value	0.32	0.32	0.37	0.29	0.46	0.35
	p	***	**	*		.	

Table 4.13 Model accuracy indicators of the different models.

	1 d	7 d	14 d	28 d (I)	28 d (II)	BBS
R^2_{adj} [-]	0.991	0.991	0.991	0.991	0.988	0.991
RSE [mm]	1.50	1.46	1.61	1.56	1.94	1.52
R^2_{pred} [-]	0.982	0.982	0.979	0.984	0.971	0.981
$RMSPE$ [mm]	1.75	1.90	2.13	1.73	2.95	1.86

4.8.4 Discussion

The example based on daily measurement data presented above nicely shows the effect of autocorrelated residuals on the standard errors of the coefficients. Both methods, thinning out the data and BBS, enabled to calculate correct coefficient estimates and therefore can be used to perform proper hypothesis tests. Since the BBS model is based on more data, it is more accurate and more robust for prediction. The difficulty lies in the choice of the block length. For this case study, the block length was selected as long as the period where correlation of the daily measurement data has been detected. It is not clear if the boot strap approach worked well for the present case by coincidence. Therefore, a sensitivity analysis is recommended.

If the variable selection is done based on the p-values, autocorrelation must be treated if present. Instead of variable selection by p-values, the cross-validation test error can be used as a decision basis. Autocorrelation has not to be treated when using the cross-validation approach even when autocorrelated residuals are present because the coefficients are always correct. Variable selection by p-values is one possible application of hypothesis tests. Another application for hypothesis tests is to search for abnormal behaviour changes based on MLR models (see Section 4.5). Thus, autocorrelation should be check when applying such MLR models to search for behaviour changes.

For all investigated dams, except arch dam A4, the measurement data are recorded bi-weekly or monthly. This leads to models without or with only low autocorrelation. Thus, large measurement intervals are an advantage with respect to autocorrelation.

4.9 Summary

Two concepts which can be used to analyse the behaviour of dams were evaluated. The application of the observation-prediction comparison can lead to misinterpretation of the behaviour. The results are not robust and heavily depend on the calibration period. However, the concept of the adjusted behaviour indicator leads to robust results that do not depend on the chosen calibration period. Thus, the latter concept is recommended for application.

Unfortunately, no prediction band is available when using the adjusted behaviour indicator approach. To support the detection of behaviour changes, an algorithm based on MLR was developed. The algorithm can be seen as a useful tool for engineering practice. Nevertheless, engineering judgement is most important, i.e. it is not recommended to use such an algorithm for an automatic alert system. To evaluate the robustness of the resulting adjusted behaviour indicator, the robustness coefficient r_c was introduced. It expresses the variability of M_{adj} for different calibration periods.

Furthermore, the approaches to consider the effects of the water level, the temperature and the irreversible displacements of concrete dams were evaluated separately. The polynomial approach to consider the effects of the water level works well as long as there is no extrapolation. In considered cases with extrapolation, physically meaningless results were obtained. Thus, extrapolation is not recommended. The polynomial order can be determined by the *RSE* of the model. It can be increased until the *RSE* does no longer decrease significantly. Usually, a polynomial of third or fourth order leads to satisfying results. Polynomials that are scaled between the bottom and the top level and Chebyshev polynomials result in exactly the same shape functions. The advantage of Chebyshev polynomials is that they help to identify multicollinearity between the effects of the water level and the temperature.

The evaluation of the temperature models has shown that their performance mainly depends on the data, and the dam, respectively, and less on the model. All of the models were able to detect behaviour changes that were artificially added to the original data. The magnitude of abnormal behaviour changes that can be detected depends on the *RSE* of the model. Thus, the *RSE* can be used as a measure to compare different models. As soon as several temperature measurements are taken into account in a model, multicollinearity occurs. Two procedures to consider multicollinearity, i.e. ridge regression and principal component regression, were evaluated. However, the goodness of fit and the prediction performance could not be improved when applying them. These models are less robust than the MLR models. Thus, the application of these procedures is not recommended but the model building with the constraint $VIF < 10$ is suggested instead.

When using the adjusted behaviour indicator as a basis for the behaviour analysis, the irreversible effects contained in the model have the function to reduce the error in the reversible effects. When estimating the coefficients, a linear or an exponential function usually lead to satisfying results.

Because the displacement of the dam and environmental conditions are recorded at certain intervals, autocorrelated errors are expected in the analysis. The degree of the autocorrelation depends on the chosen measurement interval. Nevertheless, as long as only the coefficient estimates but not the prediction interval or the p-values are of interest, present autocorrelation does not distort the results and a treatment is not necessary. If the variable selection is done with the cross-validation approach and the adjusted behaviour indicator is used instead of the observation-prediction comparison, autocorrelation does not have to be treated. As soon as a hypothesis test based on the p-values is performed, however, autocorrelation should be checked and treated if present. The block bootstrap method is the suggested tool to apply. The application of the Prais-Winsten algorithm does not lead to meaningful results for a high degree of autocorrelation and is therefore not recommended.

The application of statistical models to drainage flow as behaviour indicator has shown that the relation is mainly described by the water level. This can be considered by an SLR model with a polynomial approach for the water level.

5 New approaches for dam behaviour analysis

5.1 Introduction

In this chapter, approaches that are new in the application of dam behaviour analysis are presented. They are applied to the same case studies as used for the model evaluation in Chapter 4. This allows for comparison with the established procedures. At first, a beam model that can be used to calculate the deformation of gravity dams is introduced. In the scope of the application of the hybrid model, the gain of a multi-objective calibration where the displacement on several levels is fitted simultaneously is shown. In addition, an arch-cantilever beam model for arch dams is presented. This model can be applied to create hybrid shape functions for the effects of the water level and the temperature. Moreover, the potential of general additive models is shown by two case studies. Instead of a linear relation they allow for nonlinear approaches in the form of smoothed spline functions. Thus, no assumption about the shape of the relation has to be provided in advance.

5.2 Beam model for gravity dams

5.2.1 Introduction

The purpose of this model is to have a simple structural model that can be used to create physically-based shape functions for statistical dam behaviour analysis models. This approximation leads to mixed or hybrid models for gravity and also hollow gravity dams. Due to the fact that there is no analytical solution of the elastic slab equation for the situation with a water level not equal to the crest level, a beam model is considered. In this model, the gravity dam is modelled as a cantilever beam with elastic foundation, similar to Rescher (1965) or Léger and Seydou (2009). This approach only approximates the deformation of a gravity dam but it is very simple to implement. The displacements in lake-valley direction are used as behaviour indicator. In addition, this model can be used to calculate rotations that can be used for comparison with inclinometer measurements.

After the description of the model and its implementation, the influence of the discretisation and the individual influence of the model constants is discussed. Then, the model is applied to create hybrid models for the gravity dams G1 and G2 and the hollow gravity dam HG1. The results are compared to the models evaluated in Chapter 4. Furthermore, multi-objective calibration where the displacement is matched on several measurement levels simultaneously by using the same material properties is performed.

5.2.2 Model description

A typical vertical section of a gravity dam and the acting loads that are considered in the model is given in Fig. 5.1a. The loads are the water pressure $p_w(z)$ resulting from the water level h, the mean temperature $T_m(z)$ and the temperature difference $T_d(z)$. These temperatures have to be estimated in a thermal pre-processing as presented in Chapter 3. The geometrical information that needs to be provided are the abutment level z_a, the crest level z_{cr}, the varying thickness $t_c(z)$ and the y-coordinate of the upstream surface $y_{usf}(z)$. By the definition of $t_c(z)$ and $y_{usf}(z)$, the y-coordinate of the downstream surface $y_{dsf}(z)$ is implicitly defined. In addition, the Young's modulus E_c, the Poisson's ratio ν_c, the spring constants k_V and k_M and the thermal expansion coefficient α_T must be provided. The spring constants k_V and k_M depend on the material properties of the rock foundation and can be estimated by the Vogt's method (see Section 2.2.2.4).

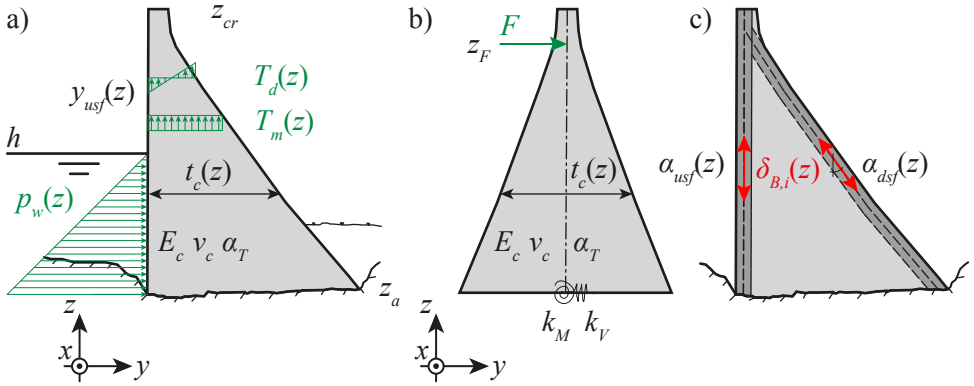

Fig. 5.1 a) Vertical section of a gravity dam with acting loads; b) beam model for the calculation of the displacement due to the water level and the temperature difference T_d; c) tripod beam model to calculate the displacement due to a change in the mean temperature T_m.

To keep the static system as simple as possible, the beam is modelled with a vertical axis instead with an inclined axis (Fig. 5.1b). Models with an inclined axis are not straightforward to implement because not only a shear force but also a normal force components have to be included. Thus, it was decided to implement the simpler form and keeping in mind that it is about 10 - 15 % weaker than a more complex model with an inclined axis. This can be compensated by using a Young's modulus E_c that is slightly larger. A vertical axis is also used in Rescher (1965).

Due to the static determinacy, the deformation can be calculated directly by applying the work theorem Eq. (2.17). In doing so, a unit load F in the direction and on the level z_F of the deformation of interest is applied (see Fig. 5.1b). From Eq. (2.17) it follows that the deformation due to a water level h can be calculated by

$$\delta_h = \int_{z_a}^{z_F} \frac{V_{y,i} V_{y,j}}{G A_{v,y}} + \frac{M_{x,i} M_{x,j}}{E I_x} + \frac{R_{V,i} R_{V,j}}{k_V} + \frac{R_{M,i} R_{M,j}}{k_M} \mathrm{d}z, \tag{5.1}$$

where $V_{y,i}$ and $M_{x,i}$ are the stress resultants due to the unit load F, $V_{y,j}$ and $M_{x,j}$ due to the water level h. $R_{V,i}$ and $R_{M,i}$ are the reactions due to the unit load, and $R_{V,j}$ and $R_{M,j}$ due to h. The same static system can be used to calculate the deformation due to a linear temperature difference $T_d(z)$ by the work theorem:

$$\delta_{Td} = \alpha_T \int_{z_a}^{z_F} M_{x,i} \frac{T_d(z)}{t_c(z)} \mathrm{d}z. \tag{5.2}$$

The displacement δ_{Td} depends linearly on the thermal expansion coefficient α_T. The static system in Fig. 5.1b cannot be used to calculate the deformation due to a difference in the mean temperature T_m. The use of a model with inclined axis and the displacement in horizontal direction estimated by the horizontal component of the beam extension would lead to an underestimation of the displacement. Thus, a model similar to the one described in Kolly and Joos (1995) was used (Fig. 5.1c). In this model, the gravity dam is considered to consist of two beams, one upstream and one downstream, that build a tripod. Since this static system is statically determinate, the stiffness and therefore the thickness of the tripod is not relevant. The displacement of the upstream beam in y-direction $\delta_{B,us,y}$ is obtained by

$$\delta_{B,us,y} = \alpha_T \int_{z_a}^{z_{cr}} \frac{T_m(z)}{\tan(\alpha_{usf})} \mathrm{d}z, \tag{5.3}$$

and of the downstream beam $\delta_{B,ds,y}$ by

$$\delta_{B,ds,y} = \alpha_T \int_{z_a}^{z_{cr}} \frac{T_m(z)}{\tan(\alpha_{dsf})} \mathrm{d}z. \tag{5.4}$$

To get the total displacement at the level z_F, the sum of the upstream and the downstream beam displacement is multiplied by the relative coordinate $z_F/(z_{cr} - z_a)$:

$$\delta_{Tm} = \frac{\alpha_T \, z_F}{z_{cr} - z_a} \int_{z_a}^{z_{cr}} \frac{T_m(z)}{\tan(\alpha_{usf}) + \tan(\alpha_{dsf})} \mathrm{d}z. \tag{5.5}$$

5.2.3 Implementation

For a convenient use, the beam model was implemented in the form of an R package. R is a functional programming language that allows object-oriented programming (R Core Team, 2013). The model is set up by specification of the gravity dam and the loads. In addition, different methods to calculate the deformation were implemented. The R package "RUnit" was used as test framework (König *et al.*, 2015). Different test cases were created to guarantee that a modification of the code does not lead to unwanted changes and errors. The calculation of stress resultants and displacements was compared to the results of the commercial statics tool STATIK-6 (Cubus AG, 2014b).

The calculation of the deformation is based on influence functions. This means that the deformation for a certain level z_F is calculated by Eq. (5.1) and (5.2) for a unit shear force $V_{y,j} = 1$, a unit bending moment $M_{x,j} = 1$ and unit reaction forces $R_{V,j} = 1$ and $R_{M,j} = 1$. Furthermore, the material properties can be set to 1 for the integration. As a consequence, the integration has to be performed only once for different load cases and different material properties. Due to the superposition law, the deformations of the individual components (bending, shear, elastic foundation) can be added after the integration. This makes the calculation of the deformation very efficient. This is of advantage when performing nonlinear optimisations, as treated in Section 5.3. The numerical integration of Eq. (5.1) and (5.2) is done with a midpoint Riemann sum with constant element length dz. Since the temperature information is not measured continuously over the height but only at certain levels, it must be interpolated. This is done by a linear interpolation between the different levels and a constant extrapolation as described in Schnitter (1969) or Bremen and Bianchi (2000) (see Fig. 5.12b).

The workflow is straightforward and is summarised as follows:

1. `Provide geometry data and material parameters`
2. `Create influence functions for certain locations and deformation directions (integration)`
3. `Interpolate and extrapolate temperature measurements`
4. `Multiply influence functions with measured loads (`h`,` T_m`,` T_d`) and material properties`
5. `Sum up individual deformations to the total deformation for each date`

5.2.4 Influence of spatial discretisation

For the integration of Eq. (5.1) to (5.5), a spatial discretisation with element lengths dz has to be chosen. To get an idea of the required element length, the relative error to a

reference solution is studied for the case study of gravity dam G2. The displacement at crest level is analysed for different element lengths. The loads were assumed to a full reservoir level and a constant mean temperature T_m = 1 °C as well as a constant temperature difference T_d = 1 °C over the height. The reference solution was estimated with an element length of d$z = 0.001$ m. The element length was varied between 0.01 m and 5 m. The estimated relative errors are very small (Fig. 5.2). For an element length of 5 m, an error of 0.005 mm was observed for the effect of the water level and 0.0025 mm for a change of 1 °C in the difference temperature. Thus, a yearly temperature variation of 20 °C corresponds to 0.5 mm. This is in the order of the measurement tolerance. To be on the safe side, an element length of dz = 2 m was considered for the applications.

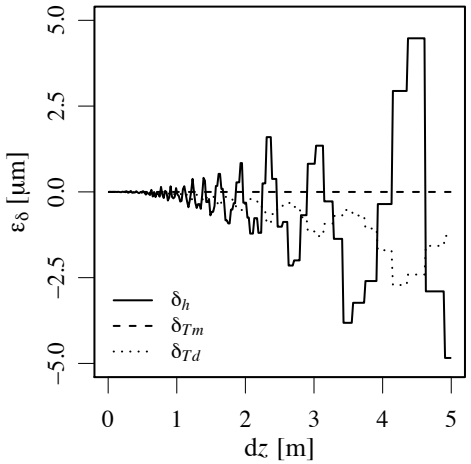

Fig. 5.2 Relative error ε_δ for a varying element length dz for the displacement at crest level of gravity dam G2.

5.2.5 Comparison to commercial deep beam calculation software

The results of the beam model as mentioned above, were compared to the solution of the commercial software CEDRUS-6 that has a deep beam module (Cubus AG, 2014a). As for the study of the influence of the discretisation, case study G2 is used. Here, the maximum element length is chosen to 1 m and the boundary condition at the foundation is set rigid. the element length of 1 m ws resulting from a sensitivity analysis. Because the foundation does not affect the thermal deformation in a statically determinate system, this assumption is justified. The comparison is done for the load cases of the water level of 262 and 301 m a.s.l. and the thermal loads T_m and T_d at 223, 250, 272 and 296 m a.s.l. The displacement was calculated at the crest level (301 m a.s.l.) and the medium level (262 m a.s.l.). The resulting displacements are shown in Table 5.1. The difference between the displacements calculated by the beam model (δ_{beam}) and the deep beam model (δ_{CED}) are small for the load case of the water level. The beam model is around 3 to 13% softer. This can be compensated by the Young's modulus. For the load case of the temperature

difference T_d, the agreement is good but the beam model leads to slightly smaller displacements. The maximal difference is 0.05 mm/°C. For the mean temperature T_m, except for the bottom level, the agreement is acceptable at most of the levels. At the bottom level, the variation of the mean temperature is small and thus the total errors of the calculate total displacement are not large.

Table 5.1 Comparison of the calculated displacements of the beam model (δ_{beam}) and the commercial deep beam software CEDRUS-6 (δ_{CED}). The displacements are calculated at the medium level (262 m a.s.l.) and the crest level (301 m a.s.l.). The load of the water level was considered on these two levels. The thermal loads are chosen to be 1 °C.

	z_F	h		T_m				T_d			
	level	262	301	223	250	272	296	223	250	272	296
δ_{beam} [mm]	301	0.45	8.93	-0.10	-0.18	-0.15	-0.06	-0.15	-0.35	-0.35	-0.20
	262	0.32	3.23	-0.05	-0.09	-0.07	-0.03	-0.08	-0.08	0	0
δ_{CED} [mm]	301	0.40	8.62	-0.01	-0.12	-0.15	-0.07	-0.20	-0.40	-0.40	-0.22
	262	0.29	2.93	-0.02	-0.12	-0.02	0.00	-0.09	-0.11	-0.01	0.00

5.2.6 Influence of individual parameters

The individual influence of the material and spring constants on the displacement δ at crest level is shown in Fig. 5.3. Again, the example of gravity dam G2 is used. While one parameter is varied, the others are kept constant. The constants are E_c = 30 GPa, ν_c = 0.2, $\log_{10}(k_V)$ = 10.5, $\log_{10}(k_M)$ = 13.25 and $\alpha_T = 10^{-5}$ 1/K. In Fig. 5.3a - d, the influence of a varying water level h on the displacement is visualised. The shape of the influence functions due to the variation of E_c, k_V and k_M is similar. Whereas a varying Young's modulus of concrete E_c leads to changes in the upper part of the dam, changes in the spring constant lead to slight variations in the lower part. Due to the similar shape, collinearity is expected when fitting these parameters individually. The Poisson's ratio of concrete does not significantly influence the results. In Fig. 5.3e - f, the influence functions of T_m and T_d for a temperature variation of 1°C is shown for different thermal expansion coefficients α_T. On the other hand, due to the surface inclination of the dam, the influence of mean temperature is higher at the bottom. On the other hand, the influence on the temperature difference is dominated by two concurrent influences. One is the inverse value of the thickness $1/t_c(z)$, which rapidly changes near the top level and the other the bending moment $M_{x,i}(z)$ which rises linearly from the top to the bottom.

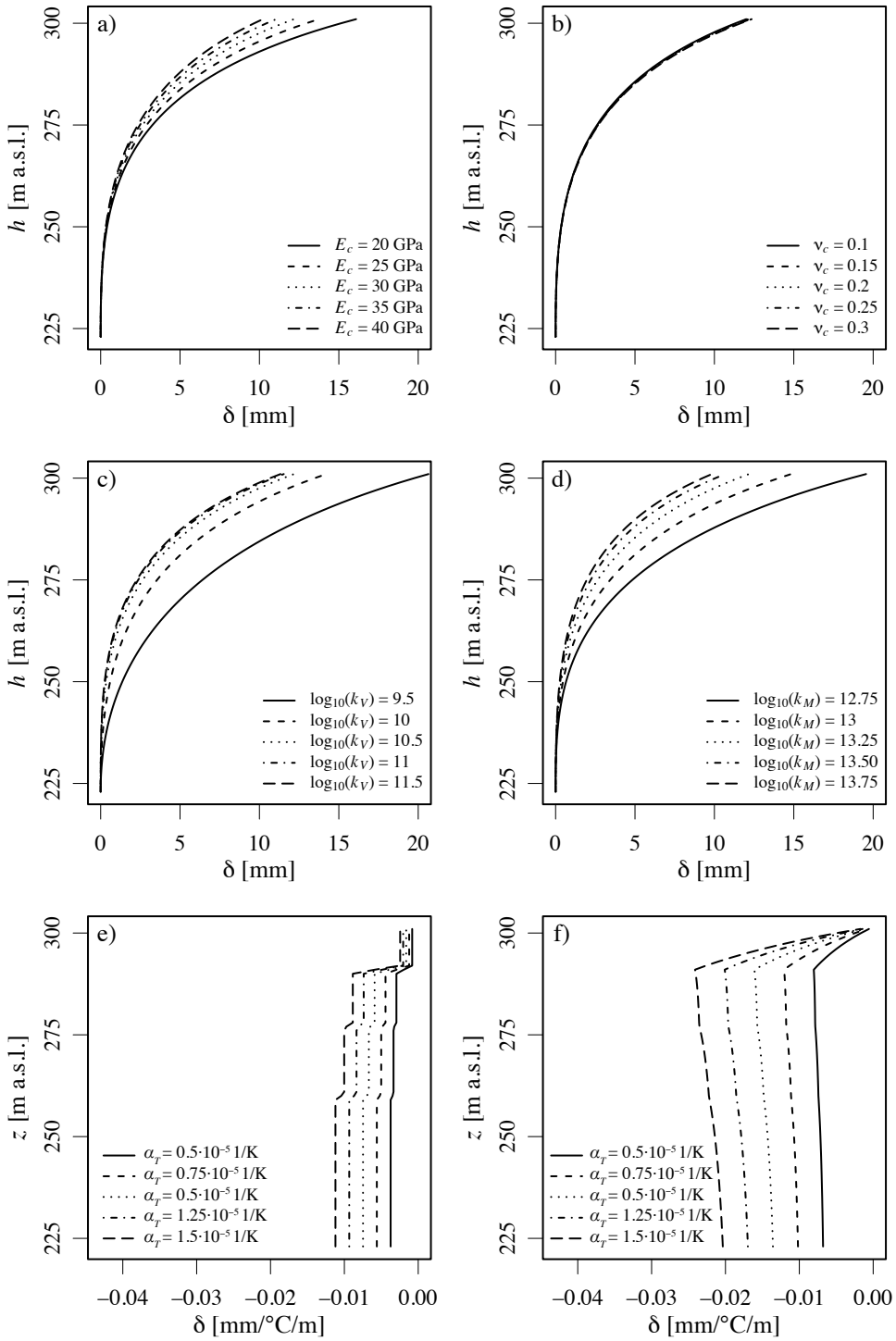

Fig. 5.3 Influence functions with varying parameters for the displacement at crest level of gravity dam G2; a) varying Young's modulus E_c and b) Poisson's ratio ν_c of concrete; c) spring constants of shear force k_V and d) of bending moment k_M; influence of thermal expansion coefficient of concrete α_T on e) the mean temperature T_m and f) the temperature difference T_d.

5.2.7 Input data for hybrid MLR model

5.2.7.1 Introduction

The output of the beam model described in Section 5.2.2 is used as input data for a hybrid DBA model. The model was applied to the two gravity dams G1 and G2 and the hollow gravity dam HG1.

5.2.7.2 Material properties

The output was generated for two different parameter sets: (i) with parameter values from material tests or values from literature and (ii) with material parameters that were estimated by a nonlinear calibration. In the nonlinear calibration, the material parameters are adjusted individually so that the calculated displacements agree with the measured displacement as well as possible. Different methods have been applied to perform nonlinear calibration but not all of them converged. The best convergence was reached with the Markov Chain Monte Carlo method that is based on Bayesian inference where prior knowledge about the material properties can be brought into the model. The material parameters are obtained by walking through the parameter space by using the DE-MCMC algorithm described in Section 2.4.5.3. Its implementation is presented in Section 5.3. The goal of using two parameter sets is to evaluate how the choice of the material parameter influences the goodness of fit of the hybrid models.

In Tables 5.2, the material parameters for the three analysed dams are shown. The Young's modulus of rock E_r is a more intuitive number than a spring constant. Thus, the spring constants are transformed into a corresponding Young's modulus using the Poisson's ratio of rock and the equations of Vogt (see Section 2.2.2.4).

Table 5.2 Material parameters used as input data for the beam model. Two parameter sets were used for each dam: (i) uncalibrated set and (ii) set with MCMC calibrated parameters.

dam	calibration	E_c [GPa]	ν_c [-]	$E_{r,kV}$ [GPa]	$E_{r,kM}$ [GPa]	ν_r [-]	α_T [1/K]
G1	no	30	0.2	50	50	0.2	10^{-5}
	yes	31.2	0.2	46.8	34	0.2	$0.95 \cdot 10^{-5}$
G2	no	26	0.2	50	50	0.21	$0.9 \cdot 10^{-5}$
	yes	25.46	0.2	22.82	13.08	0.21	$1.26 \cdot 10^{-5}$
HG1	no	30	0.2	30	30	0.2	10^{-5}
	yes	32.1	0.2	50.8	37.6	0.2	$0.55 \cdot 10^{-5}$

5.2.7.3 Methodology

To compare the results of the new hybrid model to the approaches from the literature, the same data as in Section 4.5.2 were used. In addition, the goodness of fit is also evaluated by the *RSE* and the R^2, the prediction accuracy by the $RMSPE_{CV}$ and the R^2_{CV} and the

robustness by r_c. The hybrid model (Eq. (5.6)) was completed by a linear function considering the irreversible effects. The capability to find abnormal behaviour was evaluated by the same procedure as in Section 4.5.2.

$$P(\delta_h, \delta_T, t) = \beta_0 + \beta_1 \delta_h + \beta_2 \delta_T + \beta_3 t \tag{5.6}$$

5.2.7.4 Results

The results of the hybrid models are given in Table 5.3. There is no noticeable difference in the goodness of fit, the prediction accuracy and the robustness when comparing the models with uncalibrated and calibrated material parameters. However, the resulting regression coefficients β_1 and β_2 are different. For the models with calibrated material parameters, they are almost 1, as expected in a physically-based model. On the other hand, the prediction accuracy of the models based on uncalibrated material parameters is as good as for the models with calibrated parameters. On the other hand, for inference it might be useful to use calibrated parameters since the regression coefficients gain a physical meaning.

The model is very robust. For all dams, r_c was estimated to 0.995 or more. Compared to the models from the literature evaluated in Chapter 4, this is better. The robustness can also be seen in the VIF values that are estimated between 1.13 and 1.67, which is very low. The comparison of the RSE shows that for gravity dam G1 the beam model is as good as the best performing statistical model. On the other hand, for gravity dam G2 the beam model is the worst performing model regarding goodness of fit. Nevertheless, the RSE is only 0.2 mm higher than for the best statistical model. For the HG1, the RSE of the beam model is an average value compared to the statistical models of HG1.

Table 5.3 Evaluation of hybrid model for gravity dams: goodness of fit (RSE and R^2), prediction accuracy ($RMSPE_{CV}$ and R^2_{CV}) and robustness coefficient r_c for different dams and temperature models. Additionally, the maximal VIF_{max} is provided for each model

dam	calibration	RSE [mm]	R^2 [-]	$RMSPE_{CV}$ [mm]	R^2_{CV} [-]	r_c [-]	VIF_{max}[-]
G1	no	0.46	0.969	0.45	0.953	0.995	1.14
	yes	0.46	0.969	0.45	0.954	0.995	1.14
G2	no	0.66	0.971	0.68	0.958	0.995	1.67
	yes	0.62	0.975	0.62	0.965	0.997	1.66
HG1	no	0.53	0.972	0.53	0.958	0.999	1.13
	yes	0.52	0.972	0.53	0.958	0.999	1.13

5.2.7.5 Linear assumption

The validity of the linear assumption of an MLR model can be checked by a partial residuals plot of a corresponding hybrid model. In Fig. 5.4, the partial residuals plot of the hybrid model of gravity dam G1 is shown. The linear assumption is satisfied very well. This can be verified by the smoothed relationship (solid green line, LOESS $\alpha = 0.3$) that well expresses the linear one (dashed red line).

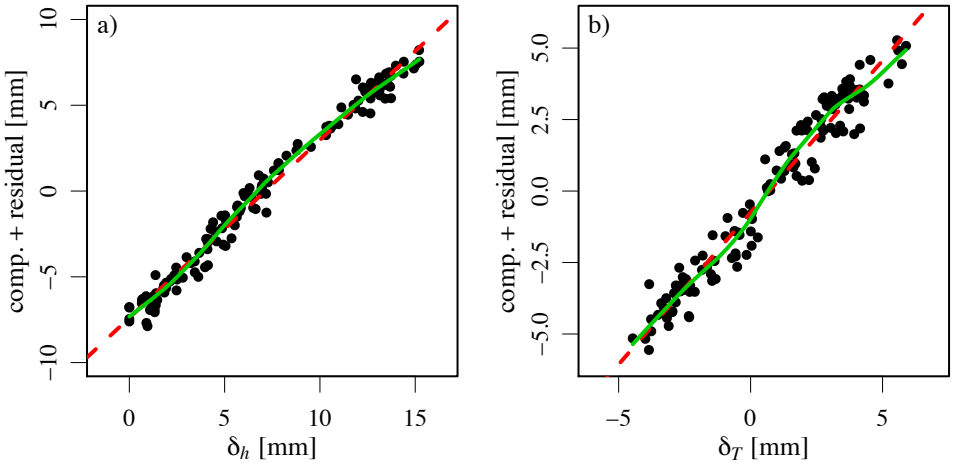

Fig. 5.4 Partial residuals plot for hybrid model of gravity dam G1; a) effect of the water level; b) temperature effects.

5.2.7.6 Discussion

The hybrid model for gravity dams works quite well for the investigated case studies. Furthermore, it was successfully applied to a hollow gravity dam. Although it is not the most accurate model, it is very robust. Due to the thermal pre-processing and multiplication by influence functions based on the geometry of the dam, there is no multicollinearity between the different thermometer measurements. Moreover, there is also no multicollinearity between the effect of the water level and the effect of temperature. If the model parameters are calibrated in advance, the regression coefficients can be used for a physically-based inference. The physical transformation leads to variables that satisfy the linear assumption of an MLR model very well.

5.3 Multi-objective calibration

5.3.1 Introduction

Dam behaviour models are commonly set up and calibrated to fit the displacement at one level. If several levels are analysed, different sets of parameters will be estimated. However, the beam model for gravity dams described in the previous section can be used to calculate the displacement at several levels. This allows for a multi-objective calibration

of the material parameters where the measured displacement is simultaneously matched with the model output at several levels. Unfortunately, common MLR analysis is not suitable for such a calibration. Thus, different optimisation algorithms that can be used for multi-objective calibration were applied and evaluated. These are different algorithms provided by the R function "optim", such as the L-BFGS-B method of Byrd *et al.* (1995) that allows for box constraints and the Markov Chain Monte Carlo method (MCMC). The best results were obtained with the MCMC method. The other algorithms suffered from finding local minima or even did not converge. Thus, the implementation of the MCMC framework based on Bayesian inference is described in this section. The advantage of a Bayesian approach is that prior knowledge about the parameters can be brought into the model. Since the model parameters are physically-based, engineering knowledge or results from material tests can be used.

5.3.2 Implementation

In the following, the implementation of the DE-MCMC algorithm of Braak (2006) (see Section 2.4.5) is implemented for the gravity dam beam model is described. It is shown how the spring constants are determined, how the prior information is chosen, how the likelihood function is considered, how the sampling is done and how the most probable parameter values are obtained.

5.3.2.1 Spring constants

Instead of the spring constants, the Young's modulus of rock E_r is sampled. In a second step, the corresponding spring constants are determined by the equations of Vogt (see Section 2.2.2.4). This is more intuitive from an engineering point of view. Two different moduli $E_{r,i}$ for the spring constant due to a shear force k_V and due to a bending moment k_M are considered. The use of a single Young's modulus was too restrictive, leading to larger model errors.

5.3.2.2 Prior information

The prior information about the physical parameters $\theta = (E_c, E_{r,kV}, E_{r,kM}, \alpha_T)$ can be provided in the form of an arbitrary distribution. In most cases, this is either a normal distribution with a mean value and a standard error or a uniform distribution with a lower and an upper limit. The parameter values are provided by engineering knowledge or by laboratory tests if available. The more precise the available information, the narrower the prior distribution can be chosen.

5.3.2.3 Likelihood function

In the MCMC algorithm, the likelihood function $\mathscr{L}(y = M|\theta)$ of observing the data M having the parameters θ has to be defined. This was done based on the residuals $e =$

$M - P$ which are the difference between the measurements and the model output. In a typical DBA model, the irreversible effects should be included in the calibration in addition to the effect of the water level and the temperature that can be represented by the beam model. Excluding the irreversible effects may leads to wrong estimation of the reversible effects (Amberg, 2009). The sampling of the parameters of irreversible effects in the MCMC procedure is an option. Because this may minimise a potential abnormal behaviour, the parameter estimates might be misleading. Thus, the following two-step procedure is proposed:

1. Evaluation of the model at a number of chosen levels n_{lev} with the sampled parameters θ and calculation of the adjusted behaviour indicators at those levels $M_{adj,lev} = M_{lev} - \delta_{h,lev} - \delta_{T,lev}$.
2. Use of a spline approach to separate the irreversible effects $\delta_{t,lev}$ and the residuals e that can be used as basis for the likelihood function at each level.

The residuals correspond to the noise of the model that has to be minimised. The separation of the irreversible effects and the residuals was done by using a GAM model (see Section 5.5 for details). In Fig. 5.5a and b, histograms of the residuals resulting from the two different parameter sets θ_1 and θ_2 are shown exemplarily. It can be recognised that the parameter set θ_2 leads to smaller residuals. Applying a kernel density estimation leads to the probability density functions (PDF) shown in Fig. 5.5c and d. The likelihood $e = 0$ can be obtained from the PDF. For the two parameter sets, this is shown by the vertical red line in Fig. 5.5c and d. $\mathscr{L}(y = M|\theta_1)$ is around 0.2, while $\mathscr{L}(y = M|\theta_2)$ is around 0.6.

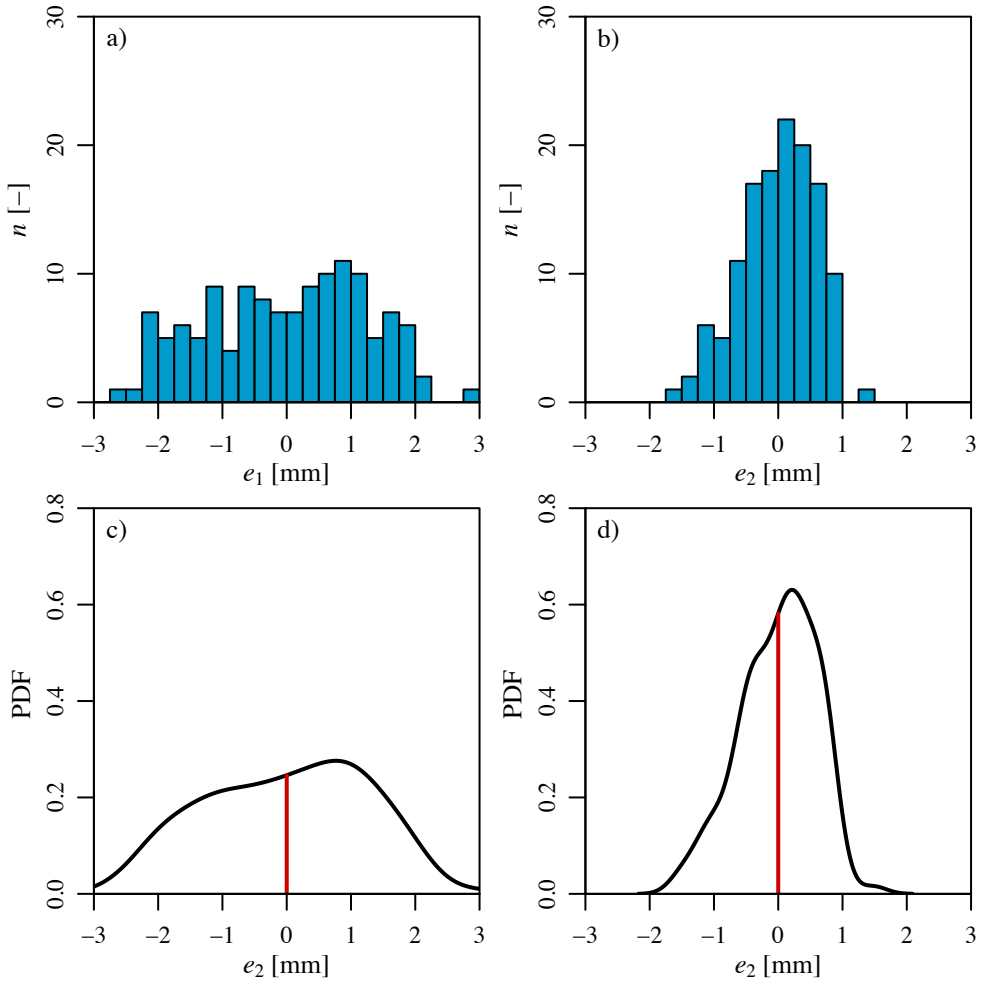

Fig. 5.5 Histogram of residuals from the two different parameter sets a) θ_1 and b) θ_2; c) and d) corresponding probability density functions.

The goal of the multi-objective calibration is to reduce the residuals on all levels simultaneously. Thus, the sum of the likelihood $e = 0$ of all levels is maximised. By this procedure, the different levels are implicitly treated with the same weights.

5.3.2.4 Sampling procedure

The sampling of the parameters is performed by the DE-MCMC algorithm of Braak (2006) described in Section 2.4.5. By using 16 parallel chains the calibration usually converges within 500 to 2000 evaluations. For a gravity dam with calibration on five levels, the calculation of one step with 16 chain needs around one second; a calculation with 4000 steps therefore requires around one hour.

5.3.2.5 Most probable parameter values

From the Sampling procedure, the distributions of the individual parameters result. The most probable parameter values can be determined by the joint probability distribution obtained by a multidimensional kernel density estimation. This was performed by the

"ks" package of Duong (2007) which is available in R. To reach a faster convergence, an adaptive refinement of the parameter space was used.

5.3.3 Application to case studies

5.3.3.1 Introduction

The multi-objective calibration with the MCMC method is applied to the case studies of the gravity dams G1 and G2 and the hollow gravity dam HG1. The goodness of fit and the robustness of the results is estimated for the same calibrations periods as used in the evaluation of the statistical models and the hybrid model. This allows for a comparison of the results. Furthermore, the results of the MCMC models are used as a basis for a hybrid model.

5.3.3.2 Methodology

The parameters θ are chosen to be the Young's moduli of concrete and rock that are used to determine the two spring constants and the thermal expansion coefficient. Due to the fact that the Poisson's ratios have a minor effect to the results (see Section 5.2.6), they are assumed to be constant, with $\nu = 0.2$. The MCMC simulations are performed with 16 parallel chains and 10'000 iteration steps each. A temperature of $T_{MH} = 0.02$ is used, which leads to reasonable acceptance rates.

For gravity dam G2, the operator provided data of material tests of the concrete. For gravity dam G1 and HG1, no such information was available. Thus, the Young's moduli of concrete and rock were both set to $E = 30$ GPa. The thermal expansion coefficient α_T was set to 10^{-5} 1/K. In Table 5.4, the prior information used for this analysis is summarised. For the cases were no material tests are available, wider standard deviations of the parameters are assumed. Since there is more uncertainty in the Young's modulus of rock E_r, a wider distribution is assumed.

Table 5.4 Prior information of material parameters used for multi-objective calibration (mean values with standard deviations in brackets).

dam	E_c [GPa]	$E_{r,kV}$ [GPa]	$E_{r,kM}$ [GPa]	$\alpha_T \cdot 10^5$ [1/K]
G1	30 (±10)	30 (±30)	30 (±30)	1 (±0.5)
G2	26 (±5)	30 (±30)	30 (±30)	0.9 (±0.5)
G3	30 (±10)	30 (±30)	30 (±30)	1 (±0.5)

The calibration data are the same as in Section 4.5.2 which allows for comparison of the results. After calibration, the adjusted behaviour indicator M_{adj} is estimated. However, due to the fact that M_{adj} also contains the irreversible component, they cannot be directly compared to the results of the MLR analysis, where a linear function of the time was

considered for calibration. Nevertheless, the linear function reduces the *RSE*. Thus, an MLR model $M_{adj} = \beta_0 + \beta_1 t$ is used to calculate residuals that can be used for comparison. Based on these residuals, the *RSE* and the R^2 are estimated. The robustness of the method shall be estimated with respect to the estimated material parameters. Thus, different parameter sets with $k = 3$ are estimated by MCMC to calculate the robustness coefficient r_c.

To show how appropriate the global material properties are for fitting the measurement data on the different levels, the output was used to create locally calibrated hybrid MLR models $M_{adj} = \beta_0 + \beta_h \delta_h + \beta_T \delta_T + \beta_t t$ for each level. The coefficient estimates indicate how good the model fits on the individual levels. For coefficient estimates close to 1, it can be assumed that the material properties fit well. In addition, the goodness of fit comparison with the multi-objective calibrated MCMC model indicates whether further calibration might be useful.

5.3.3.3 Results

The resulting parameters of the nonlinear calibration using MCMC are summarised in Table 5.5. In addition, the goodness of fit for the displacement at crest level was determined. Compared to the hybrid model, the multi-objective calibrated MCMC model is almost as good. The robustness is slightly worse for G1 and G2 and about the same for HG1, compared to Table 5.3. Generally, the results are in good agreement when using different calibration periods.

In Fig. 5.6, the prior and the posterior distributions and the correlation between the different parameters are shown for gravity dam G2. Since the prior distribution of the Young's moduli of the rock was chosen very broad, it is almost not recognisable. Nevertheless, all the parameters converged. $E_{r,kM}$ was estimated to be significantly lower than for $E_{r,kV}$. As expected from the analysis in Section 5.2.6, a negative correlation between E_c and $E_{r,kM}$ is explored.

To evaluate the model performance, the output of the multi-objective calibrated beam model was used to create hybrid models for the different levels. In Table 5.6, the goodness of fit of the multi-objective calibrated MCMC-model and the locally calibrated hybrid models are shown. The MCMC-calibration leads to a generally high goodness of fit ($R^2 > 0.90$) for all levels except the two lowermost levels of gravity dam G1 and hollow gravity dam HG1. The hybrid models show a slightly better goodness of fit. The main improvement of using hybrid models is on the lower levels where the *RSE* are already small. This is highlighted by the coefficient estimates β_h and β_T that are close to 1.

Table 5.5 Posterior information about material parameters resulting from nonlinear calibration using MCMC. Additionally, the goodness of fit parameters were estimated based on residuals by using an MLR model $M_{adj} = \beta_0 + \beta_1 t$.

dam	E_c [GPa]	$E_{r,kV}$ [GPa]	$E_{r,kM}$ [GPa]	$\alpha_T \cdot 10^5$ [1/K]	RSE [mm]	R^2 [-]	r_c [-]
G1	31.21	46.81	34.00	0.948	0.49	0.964	0.939
G2	24.26	22.82	13.08	1.26	0.68	0.970	0.969
HG1	32.13	50.78	37.65	0.55	0.58	0.965	0.995

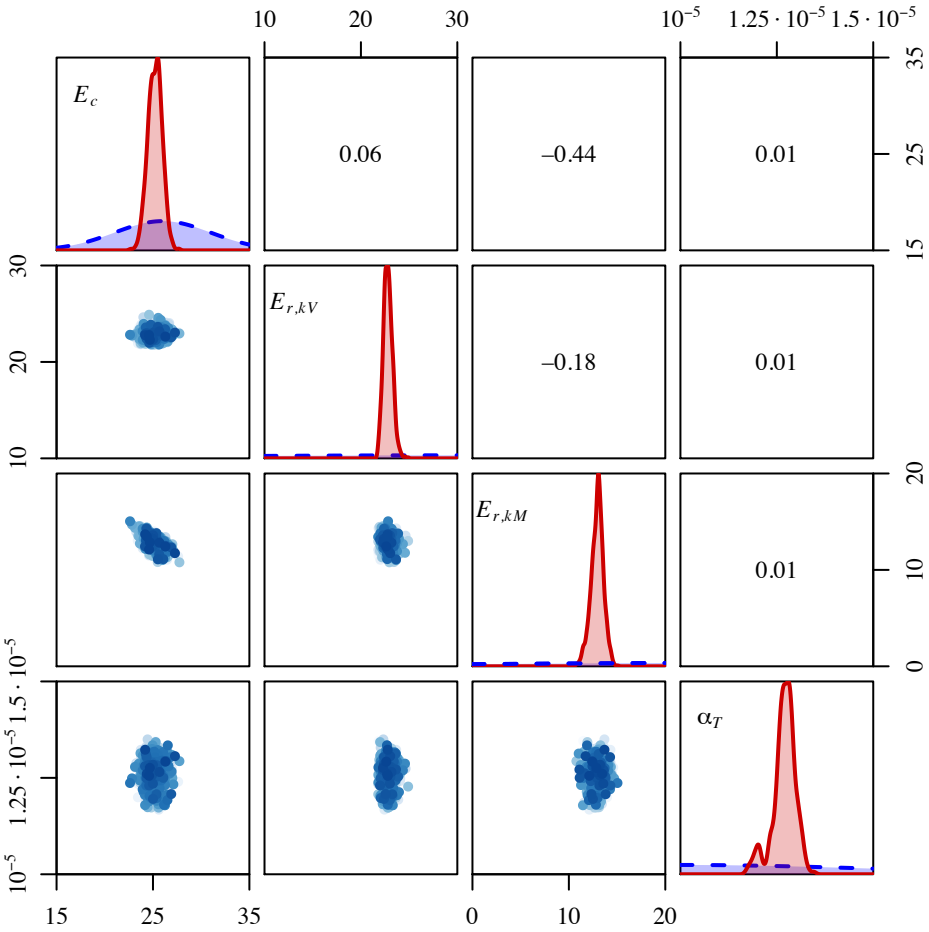

Fig. 5.6 Result of the MCMC analysis of gravity dam G2. The dashed blue lines correspond to the prior distribution and the solid red lines to the posterior distribution of the parameters θ. The blue points show the correlation between the individual parameters. In addition, the correlation coefficient is given on the top right part.

Table 5.6 Goodness of fit of the multi-objective calibrated MCMC model and the locally calibrated hybrid MLR models. In addition, the estimated regression coefficients β_h and β_T of the hybrid models are given.

dam	level	multi-objective calibrated MCMC		locally calibrated hybrid MLR			
		RSE [mm]	R^2 [-]	β_h [-]	β_T [-]	*RSE* [-]	R^2 [-]
G1	301	0.49	0.964	1.11	0.94	0.46	0.969
	288	0.34	0.946	1.01	1.06	0.34	0.948
	270	0.21	0.916	0.95	1.10	0.21	0.921
	249	0.15	0.775	0.80	1.13	0.13	0.835
	238	0.12	0.33	0.86	0.79	0.07	0.759
G2	289	0.68	0.970	1.08	1.03	0.62	0.975
	277	0.48	0.976	1.04	1.05	0.47	0.978
	250	0.30	0.968	0.97	1.31	0.25	0.978
	223	0.16	0.935	0.97	0	0.16	0.935
HG1	302	0.58	0.965	0.92	1.06	0.512	0.972
	289	0.36	0.966	0.90	1.00	0.32	0.972
	279	0.37	0.574	0.66	0.50	0.18	0.905
	223	0.16	-0.114	0.48	0.43	0.07	0.782

5.3.4 Discussion

The multi-objective calibration was successfully applied to two gravity- and one hollow gravity dams. The convergence of the MCMC-algorithm was good and, leading to robust results. This was shown by the use of different calibration periods ($k = 3$ folds) resulting in robustness coefficients of $r_c \geq 0.94$. The goodness of fit has been elevated for several levels. Only for the levels close to the bottom deviations occur, because the beam model is limited to 1D-processes. Since the measured displacements are generally small at these levels, a proper behaviour analysis is however possible. The use of the output data for hybrid models only slightly improves the goodness of fit. Moreover, the excellence of having a model that can describe the displacement with only four parameters is lost when creating hybrid models. Nevertheless, the coefficient magnitudes of hybrid models can be a good control instrument to check the performance of the multi-objective calibration. If they are close to 1, the physical assumption is verified.

5.4 Arch-cantilever-model for arch dams

5.4.1 Introduction

Similar to the beam model for gravity dams, a structural model can be used to create physical influence functions for arch dams. For the latter, FE-models are popular but also elaborate to set up. Alternatively, a simplified beam model in the form of an arch

cantilever model can be used. The goal of this work was to develop a general applicable model that can be used for different structures. FE-models have to be set up individually for each structure. Thus, an arch cantilever model was developed and implemented. After the description of the model, the discretisation and the shape of the influence functions is discussed. Afterwards, the model is applied in a case study to the arch dams A1 and A2.

5.4.2 Model description

5.4.2.1 Definition of geometry

The geometry of the arch dam is described by the shape of n arches on different levels and m cantilevers that are defined by the shape of the arches and additional parameters. A three-dimensional coordinate system with the y-axis in the direction of the arch dam axis is introduced (Fig. 5.7).

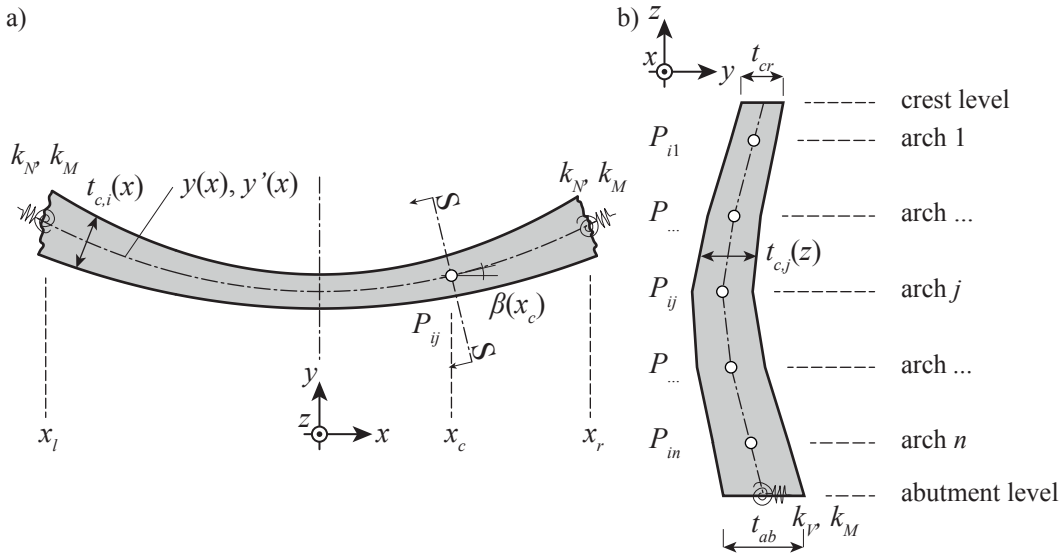

Fig. 5.7 a) Geometry of an arch; b) geometry of a cantilever at section $S-S$.

The axis of the arches is defined by a function $y(x)$ (Fig. 5.7a). This function must be continuous but it can consist of three-centre curves that do not need to have the same derivative $y'(x)$ at the intersection point. Therefore, the derivative function of the axis $y'(x)$ must be provided as well. In addition, the thickness of the arches can be defined by an arbitrary function $t_{c,i}(x)$. The arch height $h_{a,j}$ is assumed to be constant over the length of each arch. The numbering of the arches was selected from the top arch 1 to the bottom arch n (Fig. 5.8).

The shape of the cantilevers is given by a cross section S-S through the arches (Fig. 5.7a). The direction of the cross section at the cantilever location x_c is assumed to be orthogonal to the slope $\beta(x_c)$ of the top arch at location x_c. The cross section defines a polygonal line from the intersection point P_{i1} of arch 1 to the intersection point P_{in} of arch n. This

polygonal line is completed with a line segment connecting arch 1 and the crest level and another one connecting arch n and the abutment level. The inclinations of the boundary segments are assumed to be the same as for their neighbouring segments. The thickness of the cantilever beams $t_{c,i}(z)$ is linearly interpolated between the thickness of the arches at the intersection points. Additionally, the thickness at the crest level t_{cr} and at the abutment level t_a must be provided. The width $B_{c,i}$ of the cantilevers is supposed to be constant.

The arches and the cantilevers form a grillage, also called arch-cantilever-model, which can be used as an approximate static model for an arch dam. In Fig. 5.8 it is visualised how the geometry of an arch dam can be discretised into a grillage model with n arches and m cantilevers.

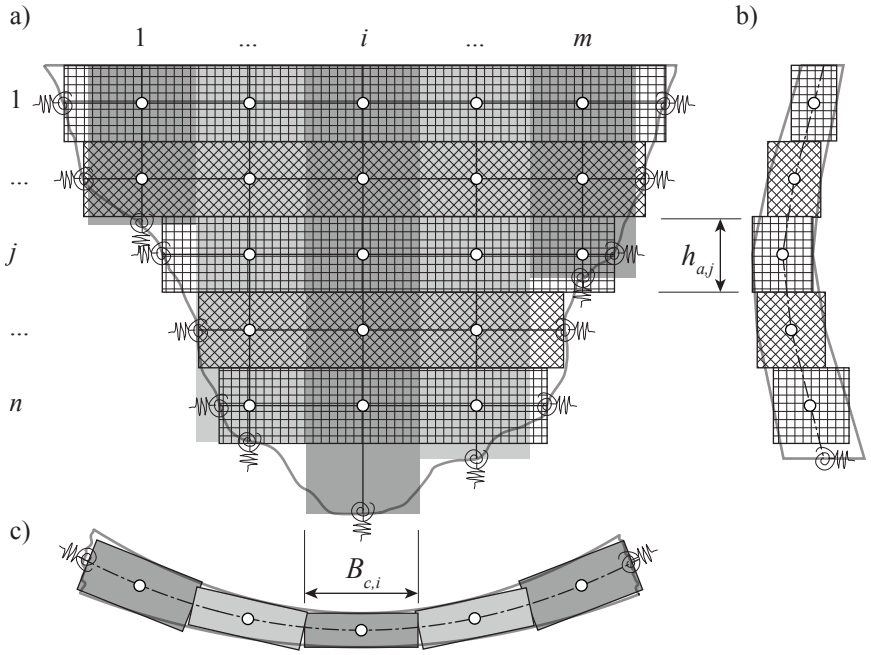

Fig. 5.8 Discretisation of an arch dam in n arches and m cantilevers; a) frontal view; b) cross section; c) plan view.

5.4.2.2 Supports

The supports of the model are assumed to be elastic in some directions. For the arches, elastic supports for the resulting normal force and the bending moment around the z-axis are considered. Since they are of minor importance, the other supports are modelled as being fixed. An estimate for the elastic constants can be obtained by the equations of Vogt (see Section 2.2.2.4). For the cantilevers, the elastic deformation due to a shear force in y-direction and a bending moment around the local x-axis is considered.

5.4.2.3 Statics

The linear elastic calculation of a grillage is done by distributing the load (e.g. water load) to the arches and cantilevers so that the compatibility condition at the intersection

points is satisfied. There are six compatibility conditions in total, three displacements (d_x, d_y, d_z) and three rotations (r_x, r_y, r_z). From an application point of view, only some of them are satisfied (Schleiss and Pougatsch, 2011). The higher the number of satisfied compatibility conditions, the higher the accuracy and the calculation time. For a grillage with $n_c = 20$ intersection points (as in Fig. 5.8), the number of displacements that need to be calculated is $(20 \cdot 1)^2 = 400$ for one compatibility condition and $(20 \cdot 6)^2 = 14'400$ for all six conditions. Consequently, the number of integrations increases with n_c^2. In the following, the calculation method of the deformation of the arches and the cantilevers is presented. Additionally, it is shown how the load distribution on the grillage can be calculated by the compatibility condition.

Arches

For a three-dimensional arch, there are six support loads at each arch abutment (Fig. 5.9a). Therefore, the degree of statically indeterminacy is $r = 6$. Thus, the force method is applied (see Section 2.2.3.2) to calculate the displacement of the arches. To have a statically determinate system, the six supporting loads at the right abutment are removed and replaced by the redundant variables X_1 to X_6 (Fig. 5.9b).

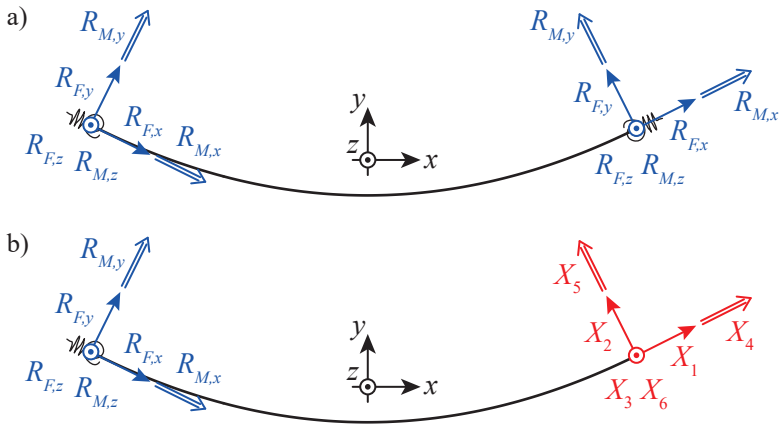

Fig. 5.9 Static system of arches; a) statically indeterminate system with 12 support forces; b) statically determinate system with six support forces and six redundant variables X_1 to X_6 for the application of the force method.

The considered loads are shown in Fig. 5.10. The water pressure p_w is supposed to be orthogonal to the arch axis. The thermal loads due to the mean temperature T_m and the temperature difference T_d are assumed to be constant along the arch axis. In addition to these loads, point loads F in all six directions can be considered.

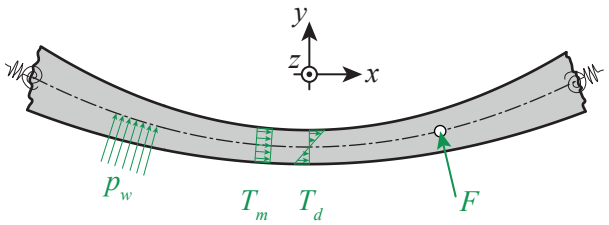

Fig. 5.10 Loads acting on arch: water pressure p_w, mean temperature T_m, temperature difference T_d and point load F.

To calculate the deformation due to a load F at a certain location, the force method can be applied. In doing so, the support forces and the stress resultants due to the redundant variables and the load F have to be calculated with the statically determinate system. For calculation, the functions of the stress resultants due to all six redundant variables and the loads described above are presented in Appendix A.1.2. With the use of these stress resultants, the displacement matrix Δ_{ij} of the redundant variables and the vector of deformations δ_{i0} due to the considered load can be calculated. This is done by the use of the work theorem (Eq. (2.17)). Then, Eq.(2.18) can be applied to calculate the redundant variables. The deformation is calculated by applying the work theorem again and using a virtual force $X_j = 1$ at the position and in the direction of the deformation of interest.

Cantilevers

Because the cantilevers are statically determinate, the stress resultants can be derived by the equilibrium condition. This has to be done for point loads in all six directions (see Fig. 5.11). The functions for other load cases do not need to be known because the load is given to the arches in the arch-cantilever-model. With the obtained stress resultants and the use of the work theorem (Eq. (2.17)), the displacement can be calculated.

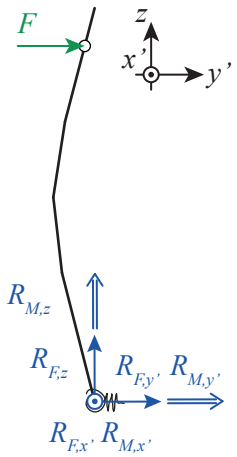

Fig. 5.11 Static system of cantilevers.

Grillage

The arches and cantilevers that are described above can be used to describe a grillage as a simplified static system of an arch dam. The procedure is described in Section 2.2.3.3. The unit loads are introduced at the intersection points P_{ij}. Then the deformations of the arches and the cantilevers due to the unit loads are calculated and stored in the grillage matrix Δ_G. With the use of the inverse Δ_G^{-1}, the load distribution for different load cases can be estimated using the inversion of Eq. (2.20).

5.4.3 Implementation

As for the beam model for gravity dams, the arch-cantilever model was also implemented in the form of an R package (R Core Team, 2013). The model is set up by specification of the arches, the cantilevers, the arch dam and the different types of forces. To minimise the errors in the code, the results were compared to the commercial frame statics software STATIK-6 (Cubus AG, 2014b). A good agreement is obtained except for the calculation of the rotations, where STATIK-6 uses a simplified approach.

The calculation of the deformation consists of two steps. First, influence functions for the different load cases are generated. In the second step, the influence functions are used to calculate the deformation by the principle of superposition which is a common procedure in linear elastic statics.

The influence functions can be created for the deformation at a certain location in a certain direction. In dam behaviour analysis, this is commonly the displacement in radial direction at crest level which is measured by a pendulum. Here, the load (water pressure and temperature) is given to the arches. Therefore, an influence function for every load case and every arch has to be determined. In other words, the influence functions contain the information of how much the deformation changes when the arch is loaded by 1 N/m^2 of water pressure or 1 °C change of the mean temperature T_m or the temperature difference T_d.

In the second step, the measurement values and the influence functions are used to calculate the deformation. Since the thermal information is not available on every arch level, it must be interpolated. This is done by the method presented in Schnitter (1969) or Bremen and Bianchi (2000) (Fig. 5.12).

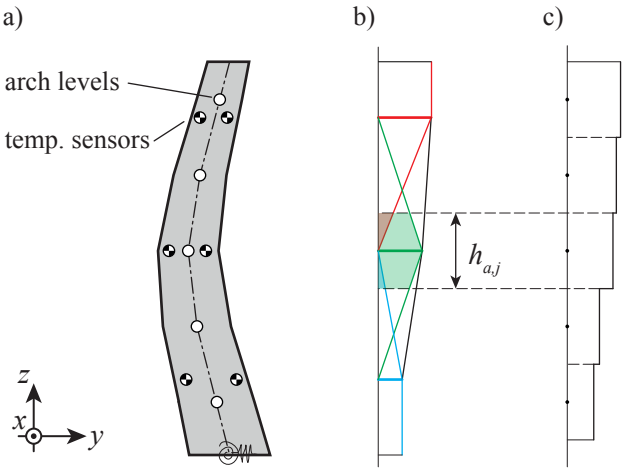

Fig. 5.12 Interpolation of the temperature at different arch levels a) cross-section with arch levels that are different from temperature sensor levels b) linear interpolation of temperature information between the different sensor levels c) constant temperature for the different arches (adapted from Bremen and Bianchi (2000)).

The numerical integration is done with a Riemann middle sum. The arch-cantilever-model is discretised by choosing a number of arches and cantilevers. The arches and the cantilevers are divided in elements $\mathrm{d}l_{i,j}$ of same size between different intersection points (Fig. 5.13). Thus, the element length may vary over the arches and the cantilevers. The influence of the discretisation is discussed in Section 5.4.5. Ideally, the width of the cantilevers is about the height of the arches.

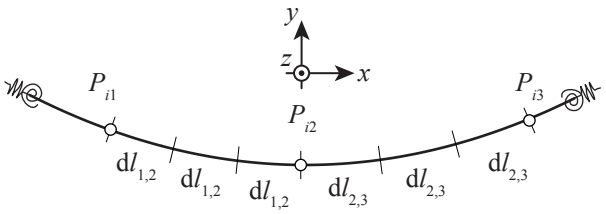

Fig. 5.13 Discretisation in elements $\mathrm{d}l_{i,j}$. Since the element boundaries are set to the intersection nodes $P_{i,j}$, the elements can have different sizes over the arches or cantilevers.

The workflow can be summarised by the following steps:

1. `Choose a number of arches`
2. `Determine number of cantilevers that` $B_c \sim (1 \div 2)\, h_{a,j}$
3. `Define geometrical functions for arches (`$y(x)$`,` $y'(x)$ `and` $t_c(x)$`)`
4. `Set up arch-cantilever model`
5. `Create influences functions for certain locations and directions (integr.)`
6. `Interpolate and extrapolate temperature measurements`
7. `Multiply influence functions with measured loads and material properties`

8. `Sum up the individual deformations to the total deformation`

5.4.4 Influence functions of arch dams A1 and A2

In Fig. 5.14, influence functions for the radial deformation at the crest level in the central sections of the arch dams A1 and A2 are shown. The influence of the two different geometries is visible when comparing the two dams. The arch dam A1 ($L_{cr}/H = 1.2$) reacts stiffer to a change in the water level nearby the crest level than arch dam A2 ($L_{cr}/H = 3.1$). For the mean temperature T_m with regard to arch dam A1, especially the temperature in the upper part of the dam influences the displacement. For the arch dam A2 a linear increase of the influence from the bottom to the top level is observed. In addition, the influence of the temperature difference T_d is more than one order of magnitude smaller than the one of T_m for both dams. This displacement depends mainly on the stiffness of the elastic abutment. For a fixed abutment, no deformation but only residual stresses occur. Furthermore, the direction of the deformation due to T_d depends on the dam geometry. For arch dam A1, a positive temperature difference leads to a positive displacement whereas for arch dam A2 a negative displacement results.

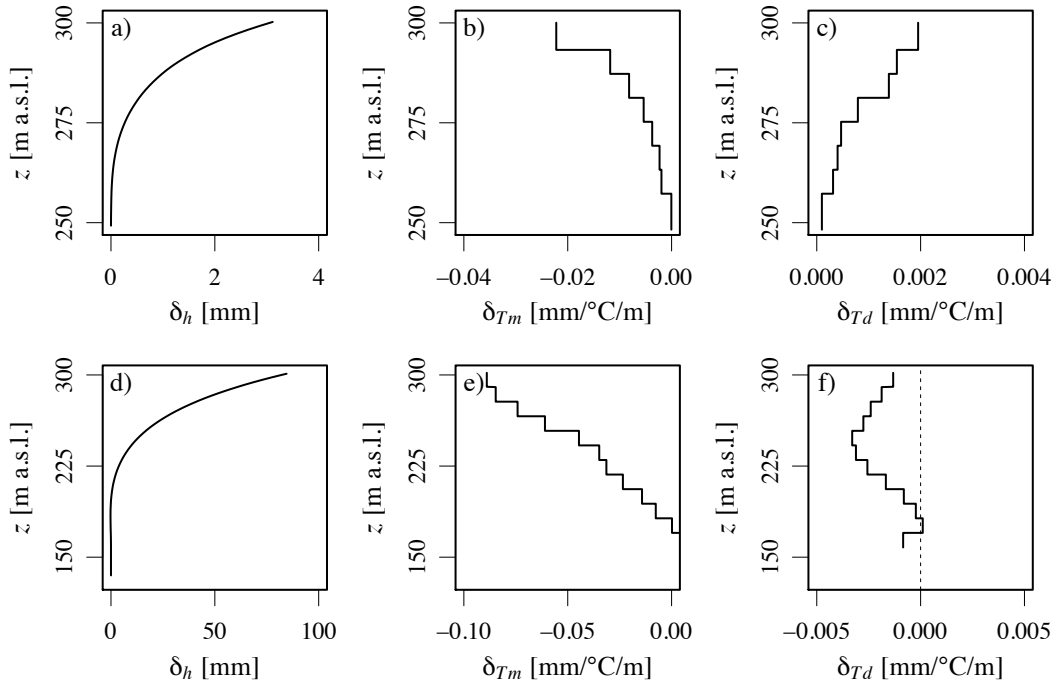

Fig. 5.14 Influence functions for the deformation in radial direction at crest level in the central section: a) δ_h; b) δ_{Tm} and c) δ_{Td} for arch dam A1; d) δ_h; e) δ_{Tm} and f) δ_{Td} for arch dam A2.

As for the gravity dams, the influence of varying material properties is analysed. In Fig. 5.15, the influence functions for the varying material parameters are presented for

the displacement at crest level in radial direction for arch dam A1. They are shown separately for the displacements due to the water level δ_h (left), the mean temperature δ_{Tm} (middle) and the temperature difference δ_{Td} (right). A change in the Young's modulus of concrete E_c (Fig. 5.15a), leads to variation of δ_h and δ_{Td}. As for the gravity dams, the Poisson's ratio of concrete ν_c does not significantly influence the result (Fig. 5.15b). In Fig.5.15c - f, the Young's modulus of rock E_r, which defines the spring constants at the abutments, is varied. A varying spring constant k_N of the arches has a large influence on δ_h and a moderate influence on the two temperature loads, whereas, the spring constant k_M of the arches only influences δ_{Td}. For the case of the arch dam A1 that is located in a narrow valley, the spring constants of the cantilevers do not influence the displacement at crest level. The thermal expansion coefficient of concrete α_T linearly influences the displacement due to the two temperatures but not due to the water level. Hence, the temperature displacement is mainly influenced by α_T and slightly by the spring constant due to the normal force at the arch abutments. The effects of the water level are mainly influenced by the Young's modulus of concrete and the spring constant due to the normal force at the arch abutments.

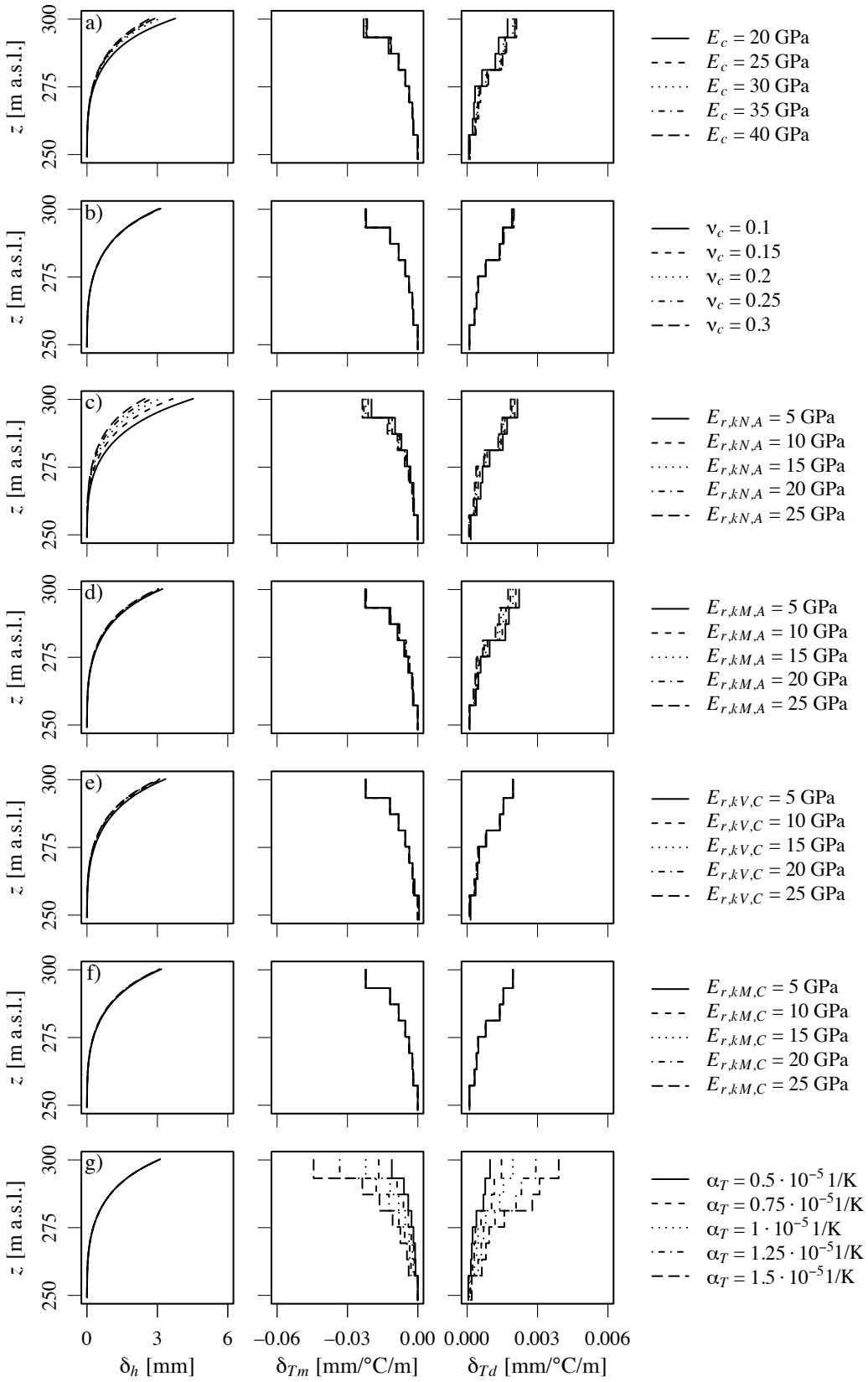

Fig. 5.15 Influence functions for radial displacement at crest level in central section of arch dam A1; a) varying E_c; b) ν_c; c) - f) varying spring constants due to varying E_r; g) varying α_T.

5.4.5 Role of discretisation

The arch-cantilever-model consists of a discrete number of arches and cantilevers. The number of arches may be limited to a few levels where a mathematical formulation of the arch axis $y(x)$ is available. Since the geometry of the cantilevers is defined by the arches, there is no limitation in the number of cantilevers except the computational resources. In Fig. 5.16, the influence of the discretisation is shown for the two dam sites A1 and A2. The coarse model of arch dam A1 consists of 5 arches and 5 cantilevers and the fine model of 8 arches and 9 cantilevers. For arch dam A2 there are 5 arches and 11 cantilevers for the coarse model and 12 arches and 22 cantilevers for the fine model. For both arch dams, the finer model is stiffer. Moreover, for arch dam A2 the influence of the mean temperature on the top arches is slightly larger for the fine model. Moreover, the influence of the temperature difference may heavily depend on the discretisation. This might be influenced by the stiffness nearby the abutment that depends on the discretisation. The discretisation affects the stiffnesses near the boundary. Resulting from a sensitivity analysis regarding the maximal element length $\mathrm{d}l_{max}$ there are no significant changes in the result for a range $0.5\ \mathrm{m} \leq \mathrm{d}l_{max} \leq 5\ \mathrm{m}$. For further analysis, $\mathrm{d}l_{max} = 2\ \mathrm{m}$, which is on the safe side, was chosen.

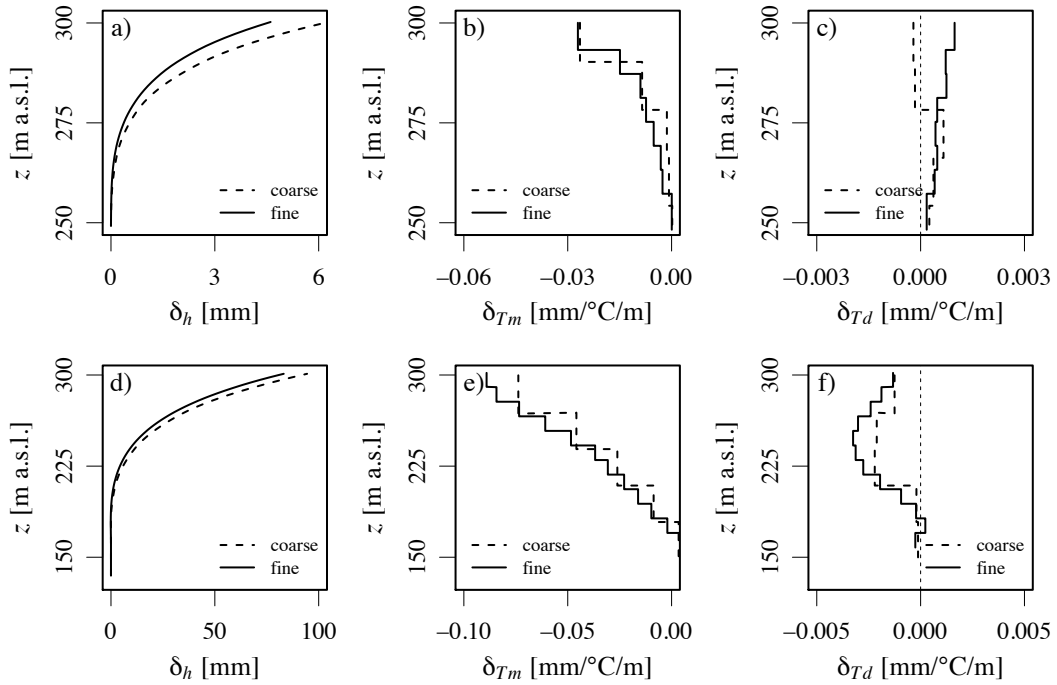

Fig. 5.16 Influence functions for the deformation in radial direction at crest level in the main section for a coarse (dashed line) and a fine (solid line) discretisation: a) δ_h; b) δ_{Tm} and c) δ_{Td} for arch dam A1; d) δ_h; e) δ_{Tm} and f) δ_{Td} for arch dam A2.

5.4.6 Compatibility conditions

In a next step, the influence of the number of satisfied compatibility conditions is analysed for arch dam A2. In doing so, (i) all six compatibility conditions (δ_x, δ_y, δ_z, r_x, r_y, r_z), (ii) only the displacements (δ_x, δ_y, δ_z) and (iii) only the displacement in radial direction (δ_y) are considered. The resulting influence functions are shown in Fig. 5.17. For a rising water level between 175 and 225 m a.s.l. the radial deformation at crest level is negative for both one and three compatibility conditions whereas it is almost zero when considering all six compatibility conditions. Regarding the temperature deformation, considering all compatibility conditions leads to smaller displacements, especially for the temperature difference T_d.

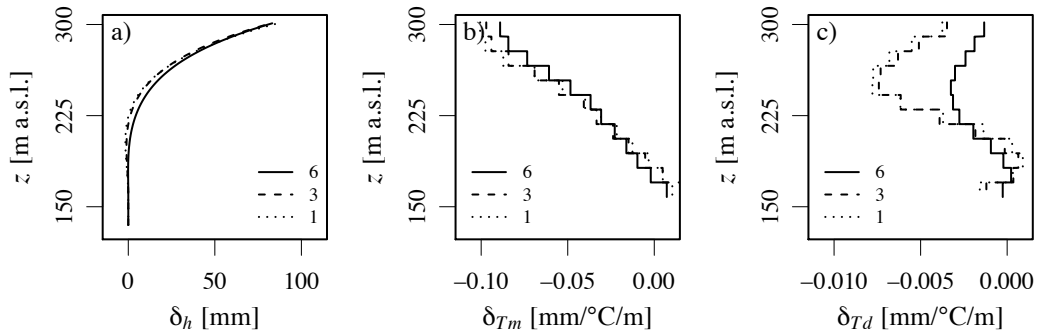

Fig. 5.17 Influence functions for radial displacement at crest level in main section of arch dam A2 for a different number of considered compatibility conditions; a) δ_h; b) δ_{Tm} and c) δ_{Td}.

5.4.7 Input data for hybrid MLR model

5.4.7.1 Introduction

For the case studies of the arch dams A1 and A2, the output of the arch-cantilever-model described in Section 5.4.2 is used as input data for a hybrid DBA model. The results are compared to the models from the literature. The hybrid models are evaluated by the same procedure as described in Section 5.2.7.3.

In addition, an arch-cantilever-model was set up for arch dam A3. Unfortunately, there is no mathematical description of the arch axes available. Thus, the geometry had to be interpolated from provided drawings. The resulting model did not result in a linear relationship as for the arch dams A1 and A2 and the approximate description of the geometry did not lead to useful results. Thus, this model is no longer used here. A possible reason might be that the available 1:1000 drawings were not precise enough.

5.4.7.2 Material properties

As for the evaluation of the beam models for gravity dams, the output is generated with two different parameter sets: (i) with parameter obtained by material tests or known values

from literature and (ii) and with material parameters estimated by single-objective MCMC calibration where the displacement at crest level in the central section was calibrated. The material parameters for the analysed arch dams are shown in Table 5.7. Instead of the spring constant the Young's modulus of rock E_r is provided because it is a more intuitive number. For its estimation, the Poisson's ratio of rock and the equations of Vogt (see Section 2.2.2.4) are used. The spring constants are assumed to be different for the arches and the cantilevers.

Table 5.7 Material parameters used as input data for the arch-cantilever models. Two parameter sets are used for each dam: (i) uncalibrated and (ii) nonlinear calibrated with single-objective MCMC.

dam	calib.	E_c [GPa]	$E_{r,kN,A}$ [GPa]	$E_{r,kM,A}$ [GPa]	$E_{r,kV,C}$ [GPa]	$E_{r,kM,C}$ [GPa]	α_T [1/K]
A1	no	27	11	11	11	11	10^{-5}
	yes	34.18	45.3	20.8	62.8	26.2	$1.38 \cdot 10^{-5}$
A2	no	28	15	15	15	15	10^{-5}
	yes	30.6	39.2	17.7	12.2	16.8	$1.46 \cdot 10^{-5}$

5.4.7.3 Results

The results of the model evaluation are shown in Table 5.8. As for gravity dams, there is not a large difference in the goodness of fit, the prediction accuracy and the robustness when comparing the models with uncalibrated and calibrated material parameters. As expected, the regression coefficients of the calibrated model are close to one.

The robustness coefficient r_c is around 0.99 for both models, indicateing very robust models. Compared to the statistical models evaluated in Chapter 4, this is slightly better. The maximal VIF values of the models (VIF_{max}) are very low and indicate no multicollinearity. The goodness of fit of the hybrid model is not as good as for the statistical models for both arch dams. For arch dam A1 the RSE is 0.19 mm and for arch dam A2 2.23 mm higher, respectively.

Table 5.8 Evaluation of hybrid model for arch dams A1 and A2: goodness of fit (RSE and R^2), prediction accuracy ($RMSPE_{CV}$ and R^2_{CV}) and robustness coefficient r_c. Additionally, the maximal VIF is provided.

dam	calib.	RSE [mm]	R^2 [-]	$RMSPE_{CV}$ [mm]	R^2_{CV} [-]	r_c [-]	VIF_{max}[-]
A1	no	0.60	0.978	0.59	0.971	0.993	1.09
	yes	0.60	0.977	0.59	0.971	0.993	1.09
A2	no	3.67	0.975	3.28	0.975	0.998	1.81
	yes	3.76	0.974	3.35	0.974	0.998	1.81

5.4.7.4 Linear assumption

The assumption of a linear relationship between the residuals and the corresponding displacement is checked by a partial residuals plot of the hybrid models of the arch dams A1 and A2 (Fig. 5.18). Generally, the linear assumption is satisfied well. This can be verified by the smoothing (solid green line, LOESS with $\alpha = 0.3$) that well expresses the linear relationship (dashed red line). Regarding arch dam A2, the linear relationship deviates for low displacements δ_h. The origin of this deviation lies in the change of the structural behaviour for low reservoir levels. The arching effect is no longer active since the joints between the blocks are open.

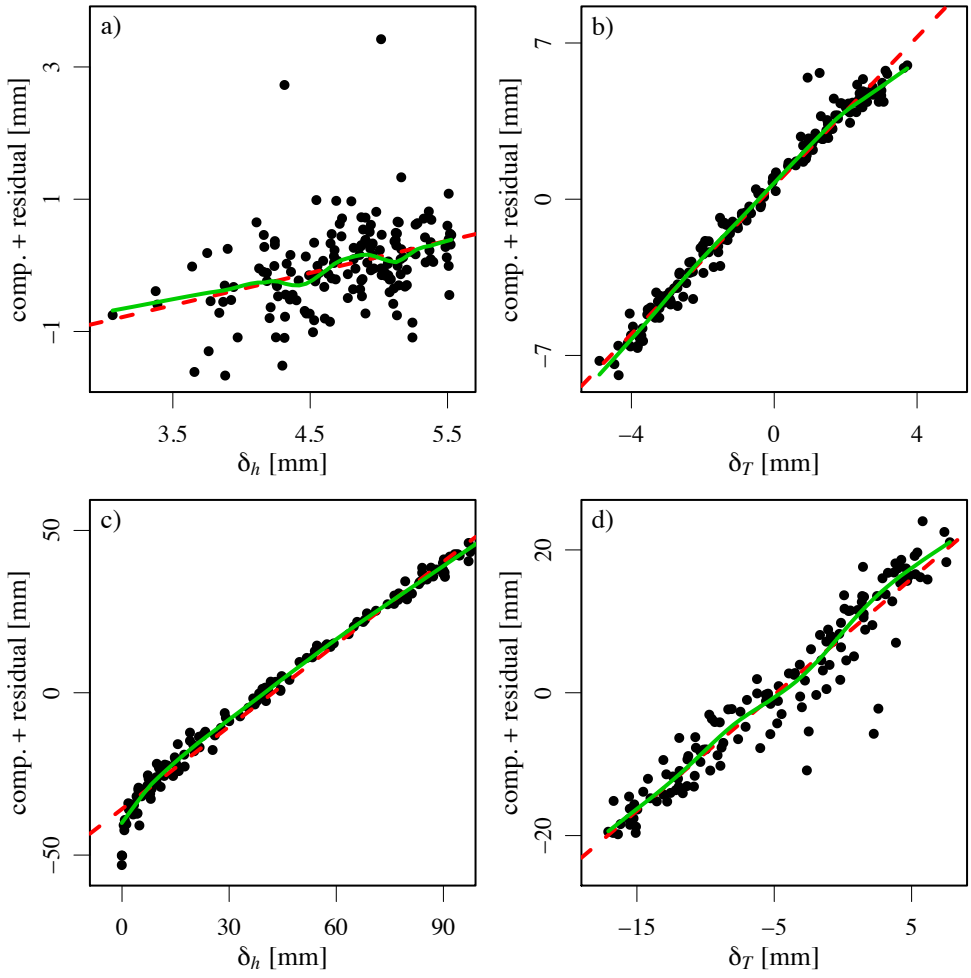

Fig. 5.18 Partial residuals plot for hybrid arch dam models; A1: effect off a) water level and b) temperature; A2: effect of c) water level and d) temperature.

5.4.7.5 Discussion

As for the hybrid model for gravity dams, the two material parameter sets (calibrated and uncalibrated) lead to the same goodness of fit and prediction accuracy but different regression coefficients. The analysis of the influence functions (Section 5.4.4) has shown

that the influence of the water level is mainly dominated by the Young's modulus of concrete E_c and the spring constant in normal direction of the arches. The displacement due to the temperature distribution in turn is mainly influenced by the thermal expansion coefficient α_T and moderately by the spring constant in normal direction of the arches. As a consequence, a change in the regression coefficient for the effects of the water level mainly results in a change of E_c and k_N, while a change in the regression coefficient of the temperature results in a change of α_T.

The nonlinear calibration of the arch-cantilever-model with the MCMC method is time-consuming and convergence cannot always be reached. Fortunately, this can be avoided without any drawbacks when using the output data of the arch-cantilever model as input data of a hybrid model.

The goodness of fit of the hybrid models is not as good as for the statistical models from the literature applied in Section 4.5.2. For arch dam A1, the *RSE* is about 0.2 mm lower, which is not much. However, for arch dam A2 the difference in the *RSE* is around 2.2 mm, which is twice as large as for the statistical models. The main part of this difference is due to the polynomial of third order used in the statistical models. If a mixed model with a polynomial third order for the effects of the water level and the output of the arch-cantilever model for the temperature effects is used, the *RSE* will decrease to 2.17 mm. This is still around 0.5 mm higher than for the statistical models. Nevertheless, the mixed and the hybrid model are more robust than the statistical models and multicollinearity does no longer occur. Thus, its application might be reasonable despite of a higher *RSE*. In Section 5.5, a mixed GAM model is presented.

5.4.8 Multi-objective calibration

As for the gravity dams, multi-objective calibration with the Markov Chain Monte Carlo method of the arch-cantilever model is performed. In doing so, different objectives were combined: (i) the radial displacement on several levels of a single pendulum, (ii) the radial and tangential displacement on several levels of a single pendulum, (iii) the radial displacement on several levels of all pendulums and (iv) the radial and tangential displacement on several levels of all pendulums. Especially for the simultaneous calibration of several pendulums, the convergence was bad. The reason for this can be found in the results of the single pendulum calibrations where the convergence was generally good. For different pendulums, different material properties and especially spring constants at the abutments result. This indicates that the stiffness of the foundation is different on different locations and it is not possible to use global values for such complex static systems as arch dams. Moreover, the calculation time of a multi objective calibration of an arch dam takes around two days. This seems not acceptable for practical applications. Therefore, the multi-objective calibration of the arch-cantilever-model is not recommended.

5.5 Generalized Additive Models

5.5.1 Introduction

When applying MLR for dam behaviour analysis models, the acting influence parameters are known but the shape of the relationship between these and their effects may not. Thus, variable selection procedures to determine the order of the polynomial function to represent the effects of the water level, the order of a seasonal function or the type of the function to represent irreversible effects are required. This can be overcome by Generalized Additive Models (GAM) that describe the relation between the predictor variables and the response by smoothed spline functions (for details see Section 2.4.4).

The potential of GAM models is exemplified by the displacement at crest level in the central section of arch dam A2. The hybrid model that was used to model the displacement at crest level in radial direction has shown deviations from the linear relationship for low reservoir levels where the joints between the blocks are open. Furthermore, the irreversible displacement shows a nonlinear trend. Since the shape of these relations is not known in advance, GAM models are a suitable approach to tackle this problem.

5.5.2 Methodology

For the purpose of comparison, the same data as for the models evaluated in Chapter 4 were used. Since the effects of the temperature show a linear progress in the MLR models, they are considered by linear functions. Furthermore, two temperature models were used: (i) a mixed model with the output of the beam model:

$$P(h,\delta_T,t) = \beta_0 + s(h) + \beta_1\,\delta_T + s(t), \tag{5.7}$$

and (ii) the $\mathrm{HTT}_{\Delta T m \Delta T d}$ model as representative of the statistical models:

$$\begin{aligned} P(h,T,t) = {} & \beta_0 + s(h) + \beta_1\,\sin(S) + \beta_2\,\cos(S) + \beta_3\,\sin(2S) + \\ & + \beta_4\,\Delta T_{m,1929} + \beta_5\,\Delta T_{d,1929} + \beta_6\,\Delta T_{d,1911} + \beta_7\,\Delta T_{d,1881} \\ & + s(t). \end{aligned} \tag{5.8}$$

In Eq. (5.8) the subscripts of the temperatures indicate the measurement levels.

5.5.3 Results

The resulting shape functions to represent the effects of the water level h of the two GAM models and of the hybrid MLR model from Section 5.4.7 are shown in Fig. 5.19. The

shape functions of the arch-cantilever-model and the GAM models diverge below 210 m a.s.l. This is the level where the joint opening was observed in an FE-analysis by the operator. Thus, the GAM model seems to be appropriate to find the change in the structural behaviour due to joint opening and closing.

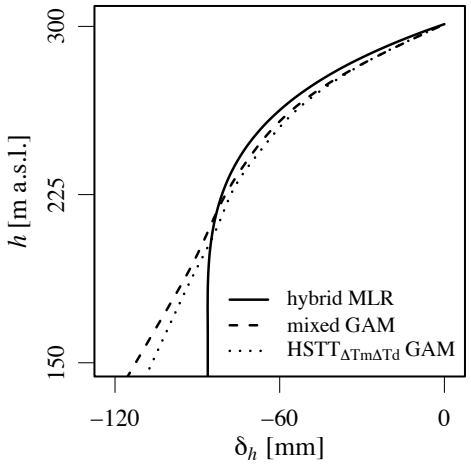

Fig. 5.19 Resulting shape functions for the influence of the water level h for the hybrid MLR, the mixed GAM and the HSTT$_{\Delta Tm\Delta Td}$ GAM models of arch dam A2.

In Table 5.9, the goodness of fit estimators, the prediction accuracy and the robustness coefficients of the two GAM models are given. The goodness of fit measured by the *RSE* of the mixed model is about 0.5 mm larger than for the statistical models evaluated in Chapter 4. Nevertheless, the R^2 of 0.992 is quite high, meaning that 99.2% of the pendulum variance is explained by the model. The *RSE* of the HTT$_{\Delta Tm\Delta Td}$ model is 1.56 mm, which is slightly better than the MLR model (see Table 4.6). However, the prediction accuracy and the robustness are slightly lower than for the MLR model.

Table 5.9 Evaluation of GAM models for arch dam A2: goodness of fit (*RSE* and R^2), prediction accuracy ($RMSPE_{CV}$ and R^2_{CV}) and robustness coefficient r_c

model	*RSE* [mm]	R^2 [-]	$RMSPE_{CV}$ [mm]	R^2_{CV} [-]	r_c [-]
mixed	2.23	0.992	2.47	0.985	0.983
HTT$_{\Delta Tm\Delta Td}$	1.56	0.996	2.00	0.986	0.965

5.5.4 Discussion

The use of GAM allows to consider nonlinear relations, as exemplarily shown for the effects of the water level of arch dam A2. The goodness of fit and the robustness of the GAM models can be compared to the MLR models. Unfortunately, the relationship modelled by splines is fully statistical, not physically-based. Besides the use as a model for prediction, GAM are a nice tool for inference. The application of GAM is fast and leads to a result that shows the shape of the relationships, what may help to detect nonlinearities.

5.6 Range of calibration data

5.6.1 Introduction

The state-of-the-art procedure in dam behaviour analysis is the observation-prediction comparison (e.g. Swiss Committee on Dams, 2003), where one part of the data is used for calibration and the other for prediction. The evaluation of the behaviour is based on the prediction errors for a corresponding prediction interval. In Section 4.3 it is shown that this can result in misleading interpretation. The adjusted behaviour indicator M_{adj} allows for more meaningful analysis. The robustness of the resulting M_{adj} can be expressed by the newly introduced robustness coefficient r_c that was greater than 0.94 for the investigated case studies. This means that the M_{adj} do not vary much for different calibration periods. As a consequence, all data can be used for model calibration; instead of a predicted behaviour the adjusted behaviour indicator is analysed. This can be seen as a paradigm shift from a statistical prediction problem to an inference problem where the separated effects are analysed. In doing so, mainly the irreversible effects that are the basis for the behaviour evaluation are of interest.

5.6.2 Case study

This new concept is shown for the case study of the radial displacement at crest level in the main section of arch dam A2. The data between 1986, 10 years after the first impounding, and 2016 are used for the analysis. Due to the construction works for a new pumped storage power plant that started in 2009 the operation conditions changed. The reservoir has been lowered each spring since 2009. The concept is applied to the same models as evaluated in Section 4.5.2, the hybrid model based on the arch-cantilever model and the mixed GAM model that is also based on the arch-cantilever-model. To show the robustness of the results, r_c is estimated with $k = 3$ folds for all of the models. In addition, the adjusted behaviour indicator M_{adj} is estimated for all three folds, (Fig. 5.20). A difference between the different folds is hardly recognisable what is approved by the large robustness coefficients r_c.

Regarding the hybrid model, a high deviation can be recognised after 2009 when operation conditions changed, i.e. the frequent reservoir lowering during the construction phase of the new power plant. As explained in Section 5.4.7, regarding the effects of the water level the hybrid model is not valid for low reservoir levels due to the change in the structural behaviour (joint opening). Nevertheless, the analysis has shown that the resulting M_{adj} are congruent for both the data after 2009 included and excluded in the calibration data. This underlines the robustness of this approach.

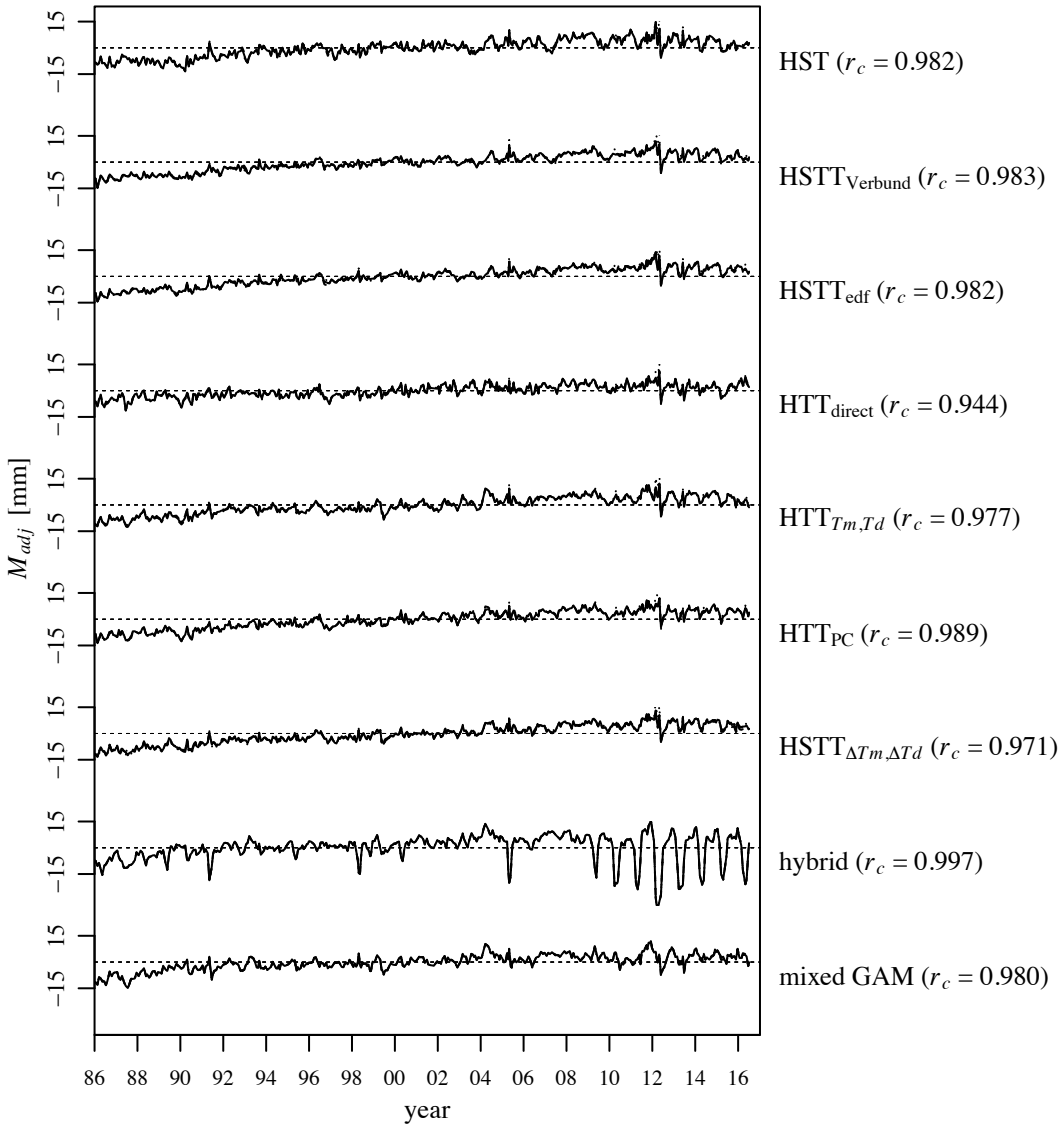

Fig. 5.20 Adjusted behaviour indicator M_{adj} for the displacement in radial direction at crest level in central section of arch dam A2 for different models. To show the robustness of the models, M_{adj} were estimated for different calibration periods (k = 3 folds) and for a reference period with all data from 1986 - 2016. The four different M_{adj} are all shown in the plot but a difference is almost not recognisable due to the high robustness (therefore a legend is not provided).

5.6.3 Discussion

The concept of using all data to calibrate the model was applied to arch dam A2. Although the operation conditions changed in 2009, the model results are very robust. The advantage of using all data is that no longer extrapolations, e.g. for lowering the water level or unusual temperature conditions, are present. In addition, the more data are available for the coefficient estimation, the more accurate they are. Nevertheless, the robustness of the model should always be verified by calculating r_c.

5.7 Summary

The physically-based beam models lead to robust hybrid models that do not suffer from multicollinearity. For arch dams, the output of the arch-cantilever-model can be used to produce shape functions that can be statistically adjusted. For a good model, a correct mathematical description of the arch geometry should be available. By the use of partial residuals plots it can be checked, if the linear relationship between the model output and the response is violated. The material parameters, which are mainly the Young's moduli of concrete and rock, the corresponding Poisson's ratios and the thermal expansion coefficient of concrete, can be taken from laboratory tests or literature. For the spring constants at the abutments the method of Vogt, described in USBR (1938), can be used. The regression coefficient of the effects of the water level represent a correction of the Young's modulus of concrete and the spring constant in normal direction at the arch abutments. The coefficient for the temperature displacement represents mainly a correction of the thermal expansion coefficient of concrete. This is confirmed by Schnitter (1969).

The beam model for gravity dams can also be used to produce shape functions for hybrid models. In addition, the beam model allows for a multi-objective calibration of the material parameters where the measured displacement is simultaneously matched with the model output on several levels. The calibration can be performed by using the Markov Chain Monte Carlo (MCMC) algorithm that is based on Bayesian inference. This allows to consider prior knowledge about the material parameters. MCMC does not only result in the most probable parameter set but also provides their distribution and correlations. When performing multi-objective calibration, only one set of physically meaningful parameters is calibrated for one block of a gravity dam. Based on three case studies, it can be said that the correlation is good on several levels. This leads to simple models that allow for comprehensible inference by engineering judgement. Moreover, due to the simultaneous analyses of the displacement at different levels, a potential abnormal behaviour can be detected and correctly located. This is demonstrated by a case study in Section 6.4.

The analysis has shown that the models are very robust concerning the use of different calibration periods. Based on the knowledge of the model robustness, a new concept is introduced: Instead of using a data set for calibration and prediction, the use of all available data for the model fitting is proposed. This avoids extrapolations and leads to more precise coefficient estimates. This kind of analysis can be seen as an inference problem where the different effects are evaluated and separated. The behaviour analysis is done in a next step based on the adjusted behaviour indicator.

The relation between the influence parameters and the effects may be nonlinear. This cannot be represented by an MLR model. In such situations, GAM are a valuable tool to identify and model such relations.

6 Proposed workflow and applications

6.1 Introduction

Based on the experience and the findings gained in the previous chapters, a workflow for dam behaviour analysis is proposed. The workflow is summarised as a flow chart (Fig. 6.1). Based on this flow chart, two case studies are treated. One is the analysis of arch dam A2 and the other of gravity dam G1.

6.2 Proposed workflow

In Fig. 6.1, the flow chart of the proposed workflow to perform dam behaviour analysis for the monitoring of the displacements of concrete dams is shown. In the following sections, more details about the individual steps are given.

6.2.1 Pre-processing

6.2.1.1 Preliminary data analysis

Before a regression model is set up, it is highly recommended to do a visual analysis of the data. These are (i) time series plots of the behaviour indicators and the environmental conditions and (ii) correlation plots, e.g. between the measured displacement and the water level. This gives an idea of the basic behaviour and outliers in the data may be found. In a next step, outlier analysis based on history and correlation plots can be done according to Lombardi (1992).

6.2.1.2 Temperature pre-processing

A thermal analysis can be carried out if concrete temperature measurements are available. For a proper analysis, the thermometers should be located on different levels distributed over the dam height. Ideally, two thermometers are placed nearby the upstream and downstream surfaces at each level and one or more in the centre of the dam. With such a configuration, the thermal conductivity can be calibrated. If only two measurements are available, the thermal conductivity can be taken from a neighbouring level or from the literature. If there is only one thermometer at a level, or the outermost thermometers are too far from the boundary (> 2.5 - 2.75 m), thermal analysis based on heat conduction is not possible. The details and the proposed workflow can be found in Chapter 3.

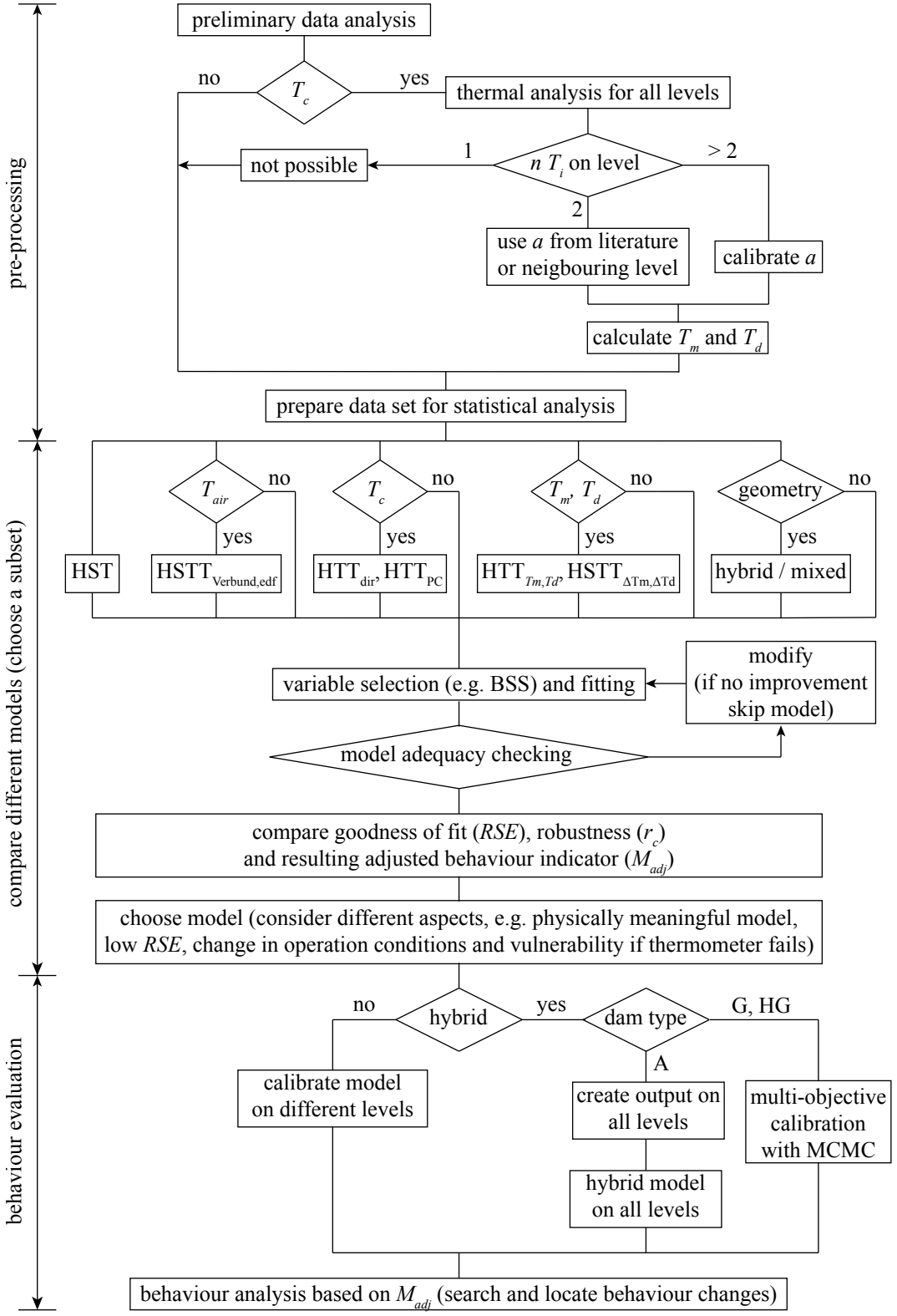

Fig. 6.1 Flow chart of the workflow for dam behaviour analysis for the monitoring of the displacements of concrete dams.

6.2.1.3 Prepare data set for statistical analysis

When heat conduction analysis is possible, the calculated mean temperature and the temperature difference can be added to the data set. Obvious outliers should be removed from the data. Basically, the readings are considered as individual data points that may have individual measurement intervals. Thus, missing data and outliers do not have to be replaced by interpolated values for model calibration. Interpolation is only recommended, if a model that is based on delayed effects (e.g. creep in Perner and Obernhuber (2009)), is used. Furthermore, it may be useful to interpolate missing values for the behaviour analysis that is performed after calibration. The goal is to have a proper data set without any outliers and missing values that can be used for calibration.

6.2.2 Compare different models

In Chapter 4, different models have been evaluated. It could be shown that the performance of the models mainly depends on the structure and the corresponding data set and less on the individual models. Therefore, it is recommended to compare the results of different models, especially if no geometry data is available to set up a hybrid or mixed model or where the physical models have a bad performance.

First of all, the variables for the chosen models have to be selected. This refers mainly to the temperature approach since for the effect of the water level either the polynomial approach or the output of a physical model is taken. The selection can be done by a best subset selection with a cross-validation procedure for example. With the constraint of $VIF < 10$, multicollinearity can be avoided. The resulting models should be checked for adequacy. This means to check the linear assumption by a partial residuals plot, the presence of multicollinearity (also between the water level and the temperature) and whether the estimated shape functions make sense.

Then, the different models can be compared with regard to the goodness of fit, the robustness and the resulting adjusted behaviour indicator. Based on this, the appropriate model for the behaviour analysis can be chosen.

6.2.3 Behaviour analysis

The behaviour analysis is supposed to be done based on the adjusted behaviour indicator. The MLR procedure proposed in Section 4.4.2 and the corresponding algorithm described in Section 4.4.3 help to identify changes in the behaviour. The latter can be shifts in the data, changes in the drift or changes in the seasonal behaviour. Analysing the behaviour at different locations of the dam may help to locate and identify abnormal behaviour.

6.3 Case study of arch dam A2

6.3.1 Introduction

The case study of arch dam A2 is complex due to the construction works for the new pumped storage power plant that started in 2009. This led to different operation conditions, mainly the lowering of the reservoir every spring time, that is noticeable in the measurement data. The main goal of this behaviour analysis is to verify if the construction works lead to irreversible displacements.

6.3.2 Pre-processing

6.3.2.1 Preliminary data analysis

In Appendix A.7.1, the displacements in radial and tangential direction are shown for the pendulum lines PII, PIII and PV. The largest displacements are measured at the top levels in the central section (PIII) in radial direction. The two topmost levels have nearly the same displacement. The change in the operation condition in 2009 is clearly visible. In radial direction of pendulum PII, a trend towards the upstream direction can be identified. In tangential direction, higher amplitudes are recognised after 2009. In addition, a slight trend is recognisable in tangential direction of PIII. The data of the water level h and the temperature $T_{299,5}$, which is 0.50 m away from the downstream boundary, are shown in Appendix A.5.4. The water level clearly shows the change in the operation mode after the start of the construction works.

In Fig. 6.2, the correlation between the measured displacement and the water level h is shown for the radial directions at crest level of PII and PIII. For both pendulums, the effects of the temperature show a hysteresis. In addition, a difference between the different periods is identifiable. Especially for PII, the trend into negative direction during the recent years is visible. For PIII, there is no difference between the periods 2000 - 2008 and 2008 - 2016. In addition, the plausibility check according to Lombardi (1992) can be performed for all temperature measurements. In Fig. 6.3, it is exemplarily shown for the temperature measurements $T_{1,203}$. To highlight unusual temperatures for the corresponding season, a second order seasonal function was fitted to the data. In addition, a 95% prediction interval was created. The effect of the reservoir lowering on the concrete temperature at the upstream surface is clearly visible. For example, the concrete temperature $T_{1,203}$ is significantly below the 95% prediction interval in February 2012 and 2013. Furthermore, the analysis of the time series indicated that the thermometers $T_{4,251}$ and $T_{4,203}$ might be damaged. Thus, they will not be used for thermal analysis. Moreover, the time series of $T_{1,251}$ ends in December 2013 because the thermometer failed afterwards.

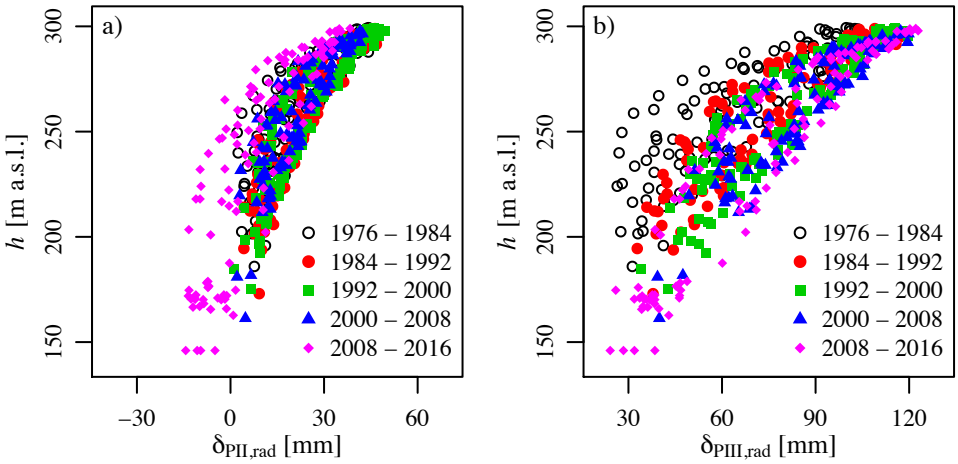

Fig. 6.2 Correlation between radial displacement at crest level and the water level h for pendulums a) PII and b) PIII. The measurement period is split in five periods of equivalent length indicated by different symbols.

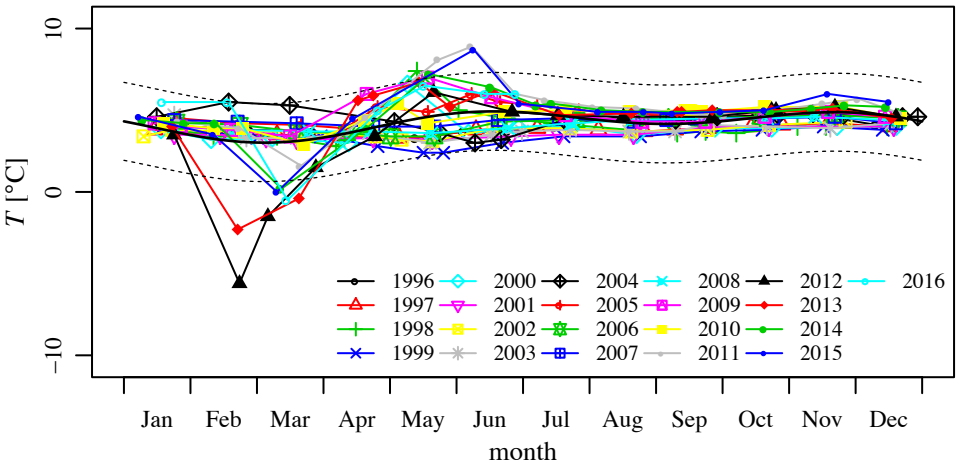

Fig. 6.3 Plausibility check according to Lombardi (1992). The temperature measurements $T_{1,203}$ are plotted on the same axis for every year. To highlight unusual temperatures for the corresponding season, a second order seasonal function was fitted to the data (solid black line). In addition, the 95% prediction interval is shown (dashed black line).

6.3.2.2 Temperature pre-processing

Since temperature data at five levels are available, a thermal analysis is performed. The data can be used to calibrate the thermal diffusivity a since there are more than two thermometers on each level. The calibration can be done by following the procedure described in Section 3.2. The resulting diffusivities and the difference between the measured and the calculated inner temperatures in the form of the *RMSE* are given in Table 6.1. In addition, the number of inner thermometers n_i to calibrate a, the slab length L and the duration of the estimated initial phase t_I is given. The data before 1986 were not used to calibrate the

thermal diffusivity since these temperatures might be influenced by hydration heat. The comparison of the measurements and calculated temperatures used for the calibration of the thermal diffusivity may help to detect any discrepancies in the data. For instance, if $T_{4,203}$, which was identified to be damaged in the preliminary data analysis, was used for calibration, a difference becomes visible.

Table 6.1 Calibrated thermal diffusivity a for different levels. In addition, the *RMSE* of the calibration, the number of thermometers available for the calibration n_i, the slab length L and the estimated duration of the initial phase t_I are given.

level [m a.s.l.]	a [m^2/d]	*RMSE* [°C]	n_i [-]	L [m]	t_I [a]
299	0.278	1.48	3	9.80	2
281	0.135	1.36	3	14.29	4
251	0.100	0.96	3	17.63	4
203	0.122	0.35	4	21.19	4
158	0.168	0.51	4	28.80	4

Due to the failure of the boundary thermometer $T_{1,251}$ after 2013, the calculation of the mean temperature T_m and the temperature difference T_d is performed in two steps. Firstly, the data before 2013 are used to calibrate a and to calculate T_m and T_d for this period. Secondly, the whole data are used to calculate T_m and T_d with $T_{2,251}$ as upstream boundary condition. The temperatures used for the further analysis are composed from the first (before 2013) and the second (after 2013) calculation. This procedure was chosen, because the calculation of T_m and T_d is more accurate the closer the thermometers lie next to the boundary. Thus, more accurate results before 2013 were gained by this two-step procedure. The resulting mean temperatures T_m and temperature differences T_d are shown in Fig. 6.4 for all levels. The amplitude of the resulting mean temperatures decreases with elevation and vice-versa for the temperature differences. Especially at 251 m a.s.l., the temperature seems to be influenced by the new operation conditions that are present due to the construction works.

6.3.2.3 Preparation of data set for statistical analysis

There are a couple of dates for which no pendulum readings are available. These data points are removed from the data set. Since delayed effects are not considered, this will not influence the result. All data points are treated as individual samples in the MLR analysis. The pre-processed mean temperatures and temperature differences are added to the data set.

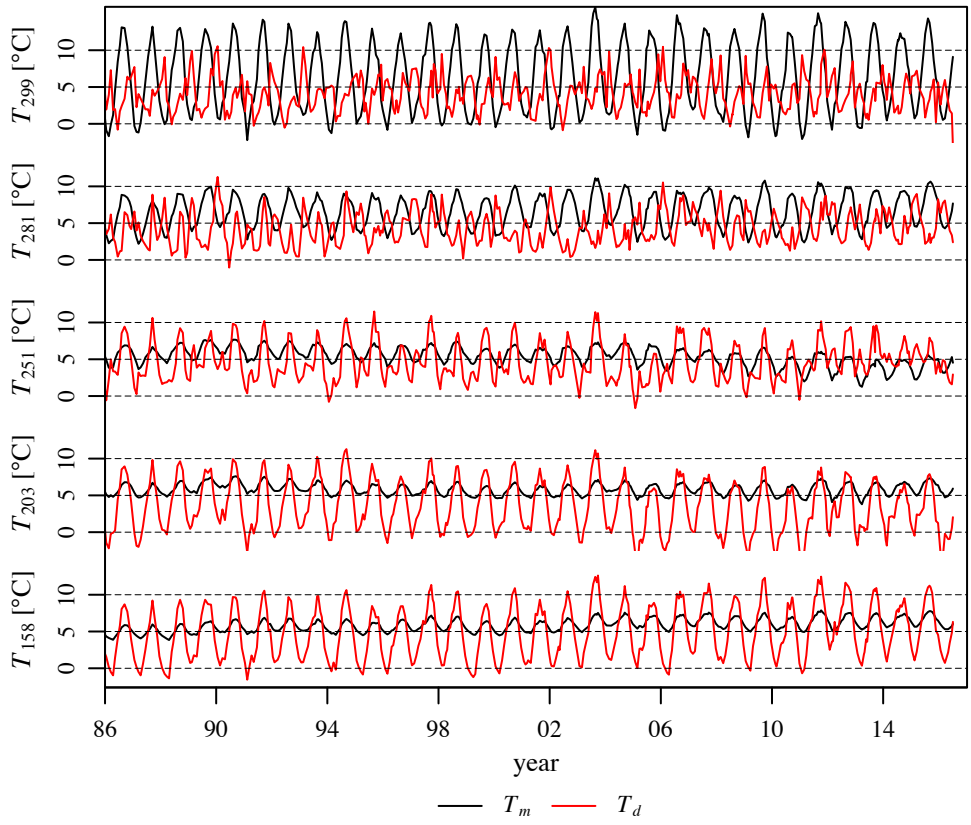

Fig. 6.4 Mean temperatures T_m and temperature differences T_d estimated by heat conduction analysis.

6.3.3 Comparison of different models

In a first step, the performance of different DBA models is analysed. This is done based on the displacement in radial direction at the crest level of pendulum PIII. The basic requirement to set up a DBA model for displacement monitoring are measurements of the water level h and the displacement itself. If no temperature measurements are available, an HST model can be set up. Since there are air temperature measurements available in the region of arch dam A2, an $HSTT_{Verbund}$ or an $HSTT_{edf}$ model can be set up as well. Due to the available concrete temperature measurements, HTT_{dir} and HTT_{PC} models are also possible. Furthermore, the pre-processed mean and difference temperature can be used to crate $\mathrm{HTT}_{Tm,Td}$ or $\mathrm{HSTT}_{\Delta Tm,\Delta Td}$ models. Finally, due to the description of the geometry provided by the operator, an arch-cantilever model can be set up and used as hybrid or mixed model. In the following, all these models are set up and compared.

The variables of the individual models are selected by the best subset selection procedure based on a cross-validation with $k = 10$ folds. To avoid serious multicollinearity, the temperatures are selected with the constraint $VIF_{max} \leq 10$. The resulting models are checked for adequacy. This is done by checking the linear assumptions by a partial residuals plot and by checking the VIF values for the presence of multicollinearity. For the detection

of multicollinearity between the water level and the temperature, Chebyshev polynomials are used to represent the effects of the water level in the statistical models. The data between 1986 and 2016 are used to calibrate the model. The data of the first 10 years are not used, since it may be affected by hydration heat. The robustness of the model is checked by the robustness coefficient r_c.

In Table 6.2, the goodness of fit indicators *RSE* and R^2, the maximal VIF values and the coefficient of robustness r_c are summarised. In addition, a plot of the resulting adjusted behaviour indicator M_{adj} is shown in Fig. 6.5. The trend is highlighted by a LOESS smoother with a span of $\alpha = 0.1$ (3 years). The progression is similar for all models. The span of the *RSE* is about 2.4 to 3.6 mm. All of the models containing a seasonal function have maximal VIF values of around 10, i.e. collinearity between the seasonal function and the water level is detected. Furthermore, since the model is not used for prediction purposes but for inference, this does not play a role. Although the effects of the water level and the temperature cannot be separated properly due to this multicollinearity, they correctly describe the total reversible displacement that is used to calculate the adjusted behaviour indicator. This multicollinearity between the water level and the temperature is not present in models that do not contain a seasonal function. Unfortunately, the coefficient estimates of the HTT_{T_m,T_d} and the $\text{HSTT}_{\Delta T_m,\Delta T_d}$ models do not correspond with the expected physical behaviour. The HTT_{PC} model performs quite well but inference is not easy since data of all thermometers are contained in the principal components. The simplest model is the hybrid model that only has a constant, one parameter for the effects of the water level, one for the effects of the temperature and a linear function to represent the irreversible displacement. There is nearly no multicollinearity between the different variables. Since this model is based on physics, inference by engineering knowledge is easier. Although the *RSE* is higher than for the other models, the hybrid model has the best performance among the evaluated models and thus is taken for the behaviour analysis.

Table 6.2 Goodness of fit (*RSE* and R^2), maximal VIF and robustness coefficient r_c for the different models.

model	*RSE* [mm]	R^2 [-]	VIF_{max} [-]	r_c [-]
HST	3.06	0.984	9.76	0.982
$\text{HSTT}_{Verbund}$	2.59	0.988	10.41	0.982
HSTT_{edf}	2.36	0.990	10.42	0.982
HTT_{dir}	2.84	0.986	3.07	0.988
HTT_{T_m,T_d}	2.84	0.986	5.74	0.978
HTT_{PC}	2.46	0.990	4.42	0.989
$\text{HSTT}_{\Delta T_m,\Delta T_d}$	2.45	0.990	9.88	0.968
hybrid	3.55	0.970	1.80	0.997

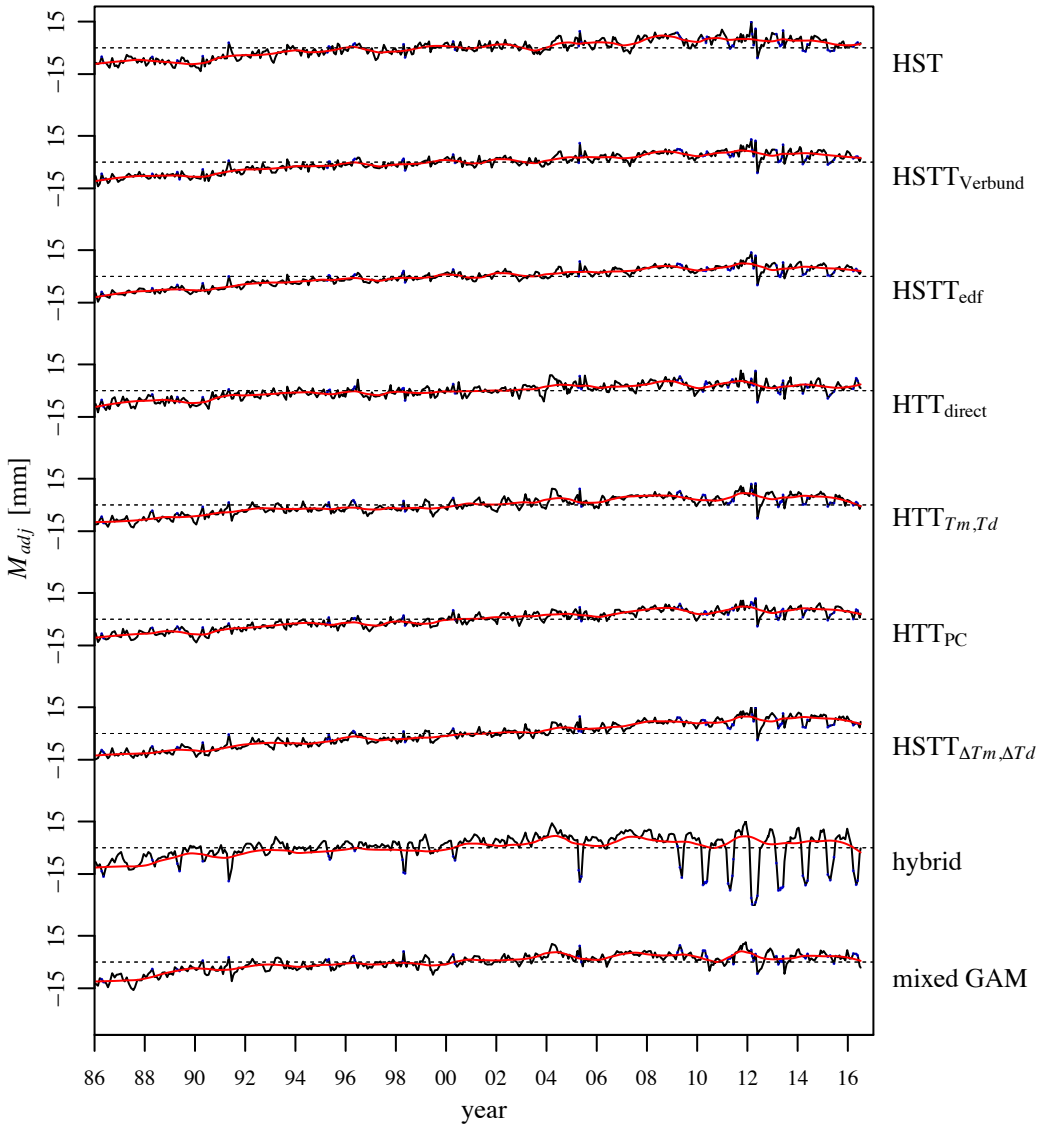

Fig. 6.5 Resulting adjusted behaviour indicator M_{adj} (black). For a better recognition of the trend, a LOESS smoother with a span of $\alpha = 0.1$ (3 years) is shown (red).

6.3.4 Behaviour analysis

The output of the hybrid model is created for all pendulum measurements shown in Appendix A.7.1. This output is used to fit a hybrid model for each measured displacement, resulting in 14 models in tangential and 14 models in radial direction of the dam. In Appendix A.7.2 the calculated displacements are shown separately for the water level and the temperature. Since the temperature displacement is almost zero at some locations, it can be skipped when setting up the hybrid model. The coefficient estimates of the hybrid models are an indicator for the model accuracy. Moreover, there are models that do not lead to physically meaningful coefficients, e.g. for the tangential displacement of PIII. Because the variation of these displacement is small, the behaviour analysis will be done

based on the raw displacement measurements. In Table 6.3, the estimated coefficients and the goodness of fit indicators are given.

Table 6.3 Goodness of fit (*RSE* and R^2), coefficient estimates β_i and robustness coefficients r_c for the different hybrid models. In addition, the detected drift for the period after 2008 is given.

model			*RSE* [mm]	R^2 [-]	β_h [-]	β_T [-]	r_c [-]	drift [mm/a]
PII	rad	299	3.25	0.934	1.48	1.24	0.998	-1.17
		275	2.55	0.960	1.55	1.68	0.998	-1.00
		254	1.82	0.977	1.57	2.22	0.998	-0.77
		233	1.63	0.982	1.43	2.81	0.997	-0.51
		191	-	-	-	-	-	-0.69
	tan	299	1.48	0.928	0.68	-	0.998	-
		275	1.22	0.928	0.66	-	0.999	-
		254	0.93	0.916	0.55	-	0.999	-
		233	0.95	0.918	0.70	-	0.998	-
		191	-	-	-	-	-	-
PIII	rad	299	3.06	0.978	0.83	1.56	0.997	-0.17
		275	3.12	0.978	0.87	1.76	0.995	-0.37
		233	2.68	0.981	0.91	2.08	0.997	-0.73
		191	1.82	0.979	0.92	2.37	0.996	-0.38
		149	1.39	0.901	1.01	-	0.998	-
	tan	299	-	-	-	-	-	-0.36
		275	-	-	-	-	-	-0.27
		233	-	-	-	-	-	-0.28
		191	-	-	-	-	-	-0.13
		149	-	-	-	-	-	-0.10
PV	rad	299	1.02	0.939	0.65	1.51	0.995	-0.50
		275	0.90	0.963	0.80	1.87	0.995	-0.30
		233	1.18	0.929	0.97	-	0.997	-
		191	-	-	-	-	-	-
	tan	299	1.32	0.936	0.75	-	0.999	-
		275	1.33	0.921	0.94	-	0.999	-
		233	0.85	0.916	0.90	-	0.998	-
		191	-	-	-	-	-	-

Based on these 28 hybrid models, the adjusted behaviour indicators are calculated and used as a basis for the behaviour analysis. In contrast to the calibration of the models, where the first 10 years of the measurement data of the dam lifetime were not used, all data are used when calculating M_{adj}. This leads to a complete picture of the dam for the whole

lifetime. The MLR procedure described in Section 4.4.2 is used to search for behaviour changes around 2008, when the construction works started. The estimated drifts are given in Table 6.3. In Figs. 6.6 - 6.8, the resulting M_{adj} and the behaviour changes found by the MLR procedure are shown. For a better recognition of the behaviour changes, the scaling of the y-axis is different for each pendulum. Pendulum PII shows a drift in upstream radial direction but no drift in tangential direction. Pendulum PIII also shows a slight drift in radial upstream direction after 2008. Compared to PII, the drift of PIII is smaller. In addition, there is a slight drift in tangential direction towards the left abutment. Finally, PV shows a drift in radial upstream direction but not in tangential direction.

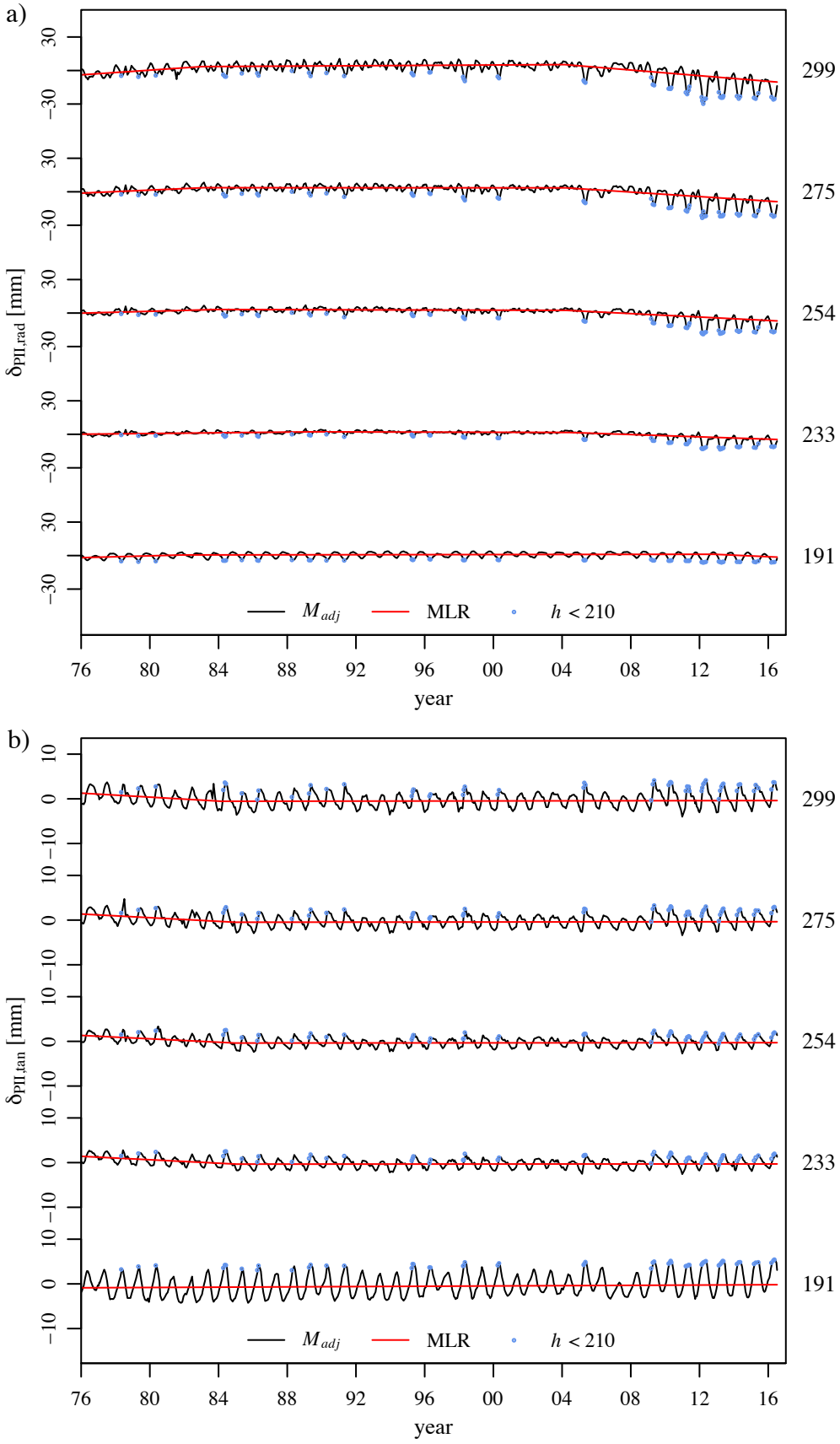

Fig. 6.6 Behaviour analysis for PII: a) radial and b) tangential displacement. The data points where the water level was below 210 m a.s.l. (and open joints) are marked by blue dots. The change in the trend starts around 2009.

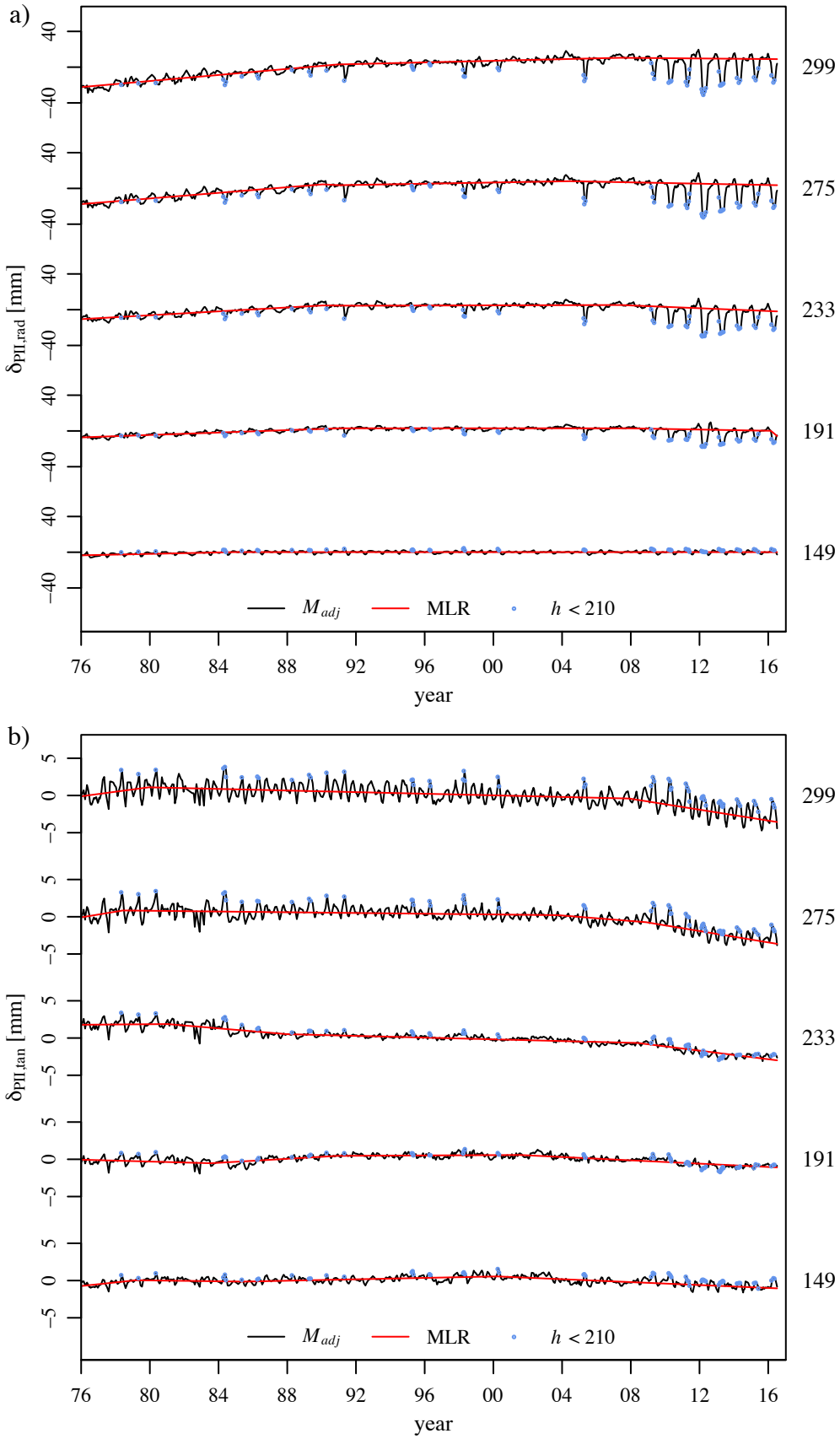

Fig. 6.7 Behaviour analysis for PIII: a) radial and b) tangential displacement. The data points where the water level was below 210 m a.s.l. (and open joints) are marked by blue dots. The radial and tangential displacement are affected by a very small trend as well. Both start around 2009.

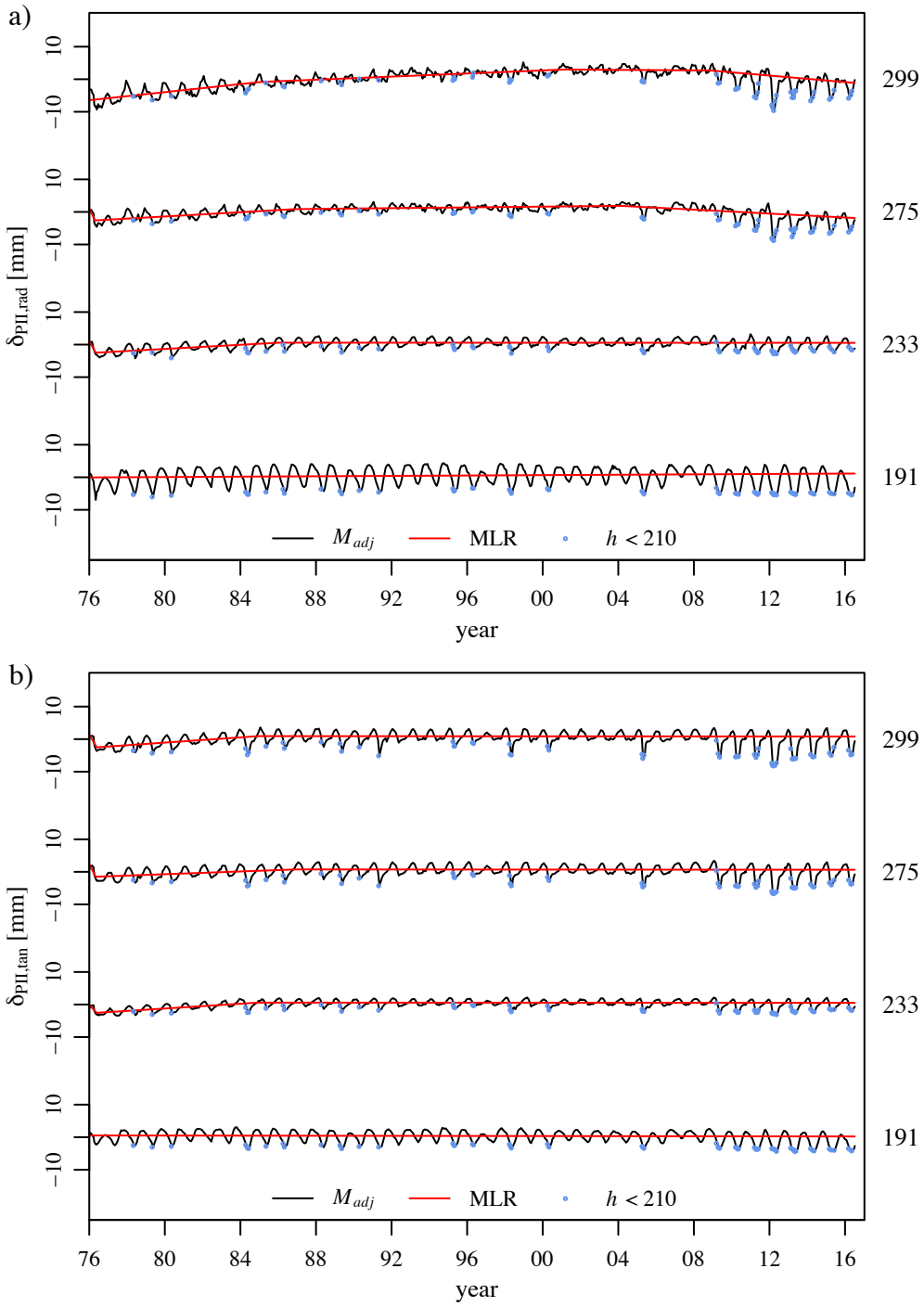

Fig. 6.8 Behaviour analysis for PV: a) radial and b) tangential displacement. The data points where the water level was below 210 m a.s.l. (and open joints) are marked by blue dots. The radial and tangential displacement are affected by a very small trend as well. Both start around 2009.

The analysis shows that a trend in upstream direction starts for all pendulums around 2009. In addition, pendulum PIII shows a trend in tangential direction. The arch-cantilever model could be used to detect and quantify these behaviour changes. Some of the behaviour changes were already recognisable in the raw measurement data. But the trend in

radial direction of PIII was hidden due to the fluctuation of the effects of the water level and the temperature. In these situations, a DBA model in combination with the analysis of the adjusted behaviour indicator helps to identify trends. The effects on the stress state in the dam body and on dam safety must be analysed by deterministic models. With the help of these, displacement limits for the irreversible displacements can be formulated and checked by the DBA model in the future.

6.4 Case study of gravity dam G1

6.4.1 Introduction

The case study of gravity dam G1 shows the potential of a multi-objective calibration of the beam model for gravity dams. Before multi-objective calibration is done, the pre-processing of the data and the comparison of different models is performed. These steps are not shown here, since they are similar as presented in the case study of arch dam A2. As for arch dam A2, all available data are used to calibrate the model.

6.4.2 Calibration

As in Section 5.3.3, the Young's moduli of concrete and rock are sampled and the Poisson's ratios are assumed to be constant with $\nu = 0.2$. From the sampled Young's modulus of rock E_r, the spring constants k_V and k_M are estimated with the Vogt's method. The ratio b/a of an equivalent foundation area was estimated to be 10. To consider independent spring constants, two Young's moduli E_r are sampled, one for k_V and one for k_M. 16 parallel chains with 10'000 iteration steps are chosen for the MCMC algorithm. In addition, a temperature of $T_{MH} = 0.02$ was used, which lead to reasonable acceptance rates. The likelihood function for the multi-objective calibration for the five levels is

$$\mathscr{L}(y|\theta) = \mathscr{L}(M_{301}|\theta)\,\mathscr{L}(M_{288}|\theta)\,\mathscr{L}(M_{270}|\theta)\,\mathscr{L}(M_{249}|\theta)\,\mathscr{L}(M_{238}|\theta), \quad (6.1)$$

and the prior information is considered by

$$\pi(\theta) = \pi(E_c)\,\pi(E_{r,kV})\,\pi(E_{r,kM})\,\pi(\alpha_T). \quad (6.2)$$

These equations are optimised by the MCMC algorithm as described in Section 2.4.5.3.

6.4.3 Convergence

The convergence is checked by the *PSRF* according to Brooks *et al.* (2011). In Fig. 6.9, the *PSRF* is given for the different parameters. Convergence ($PSRF < 1.1$) is reached very

fast. Since there are enough iteration steps, the burn-in period was set to iteration steps 1 - 2'500 which means that 7'500 samples are left for further analysis. The acceptance rates of the individual chains are between 0.27 and 0.29, which is close to the target value of 0.25 proposed by Gelman *et al.* (1996).

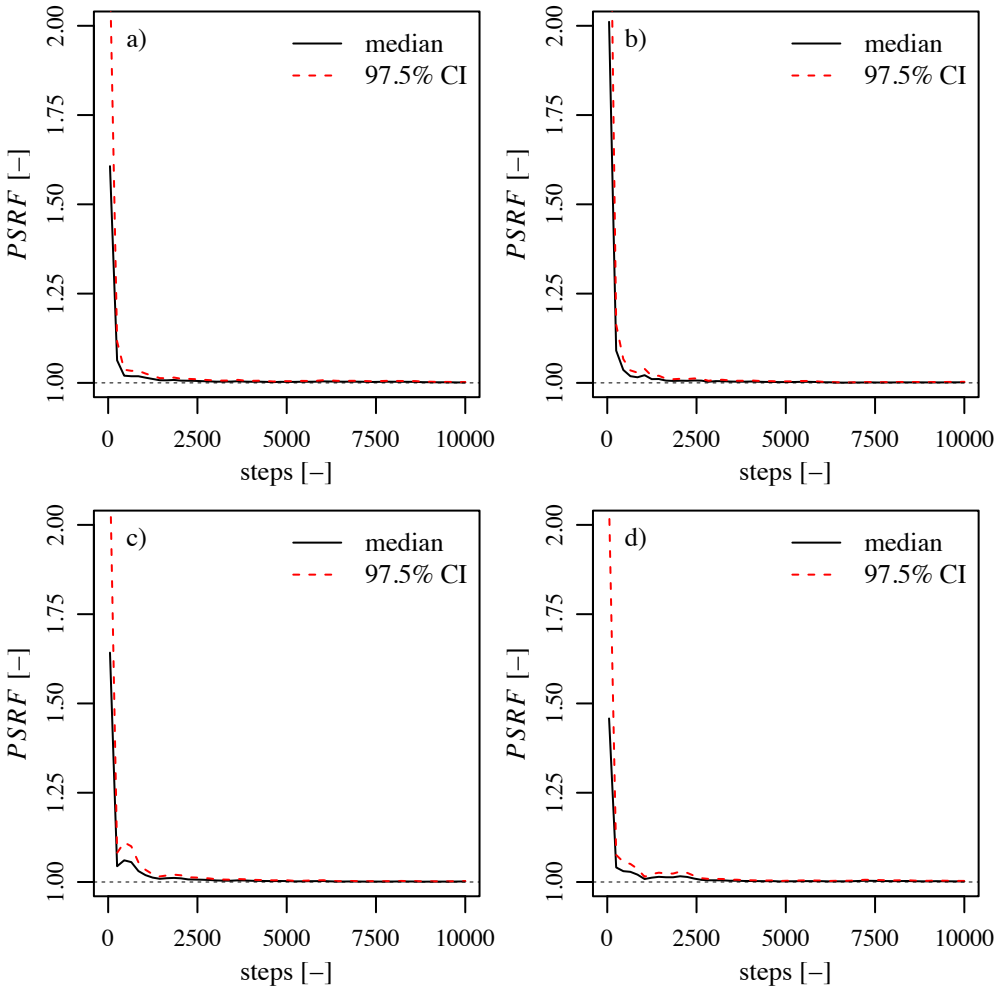

Fig. 6.9 *PSRF* according to Brooks *et al.* (2011); Young's moduli of a) concrete E_c b) rock due to shear force $E_{r,kV}$; c) rock due to bending moment $E_{r,kM}$; d) thermal expansion coefficient of concrete α_T.

6.4.4 Autocorrelation

In Fig. 6.10, the ACF-plots are shown for the individual chains of the different parameters. The correlation structure of the sampling decreases in the first 40 lags. Thus, the sampled data set is thinned out and only every 40^{th} sampling parameter set θ is taken to have independent samples. This results in 187 independent parameter sets that can be used to determine the joint probability distribution.

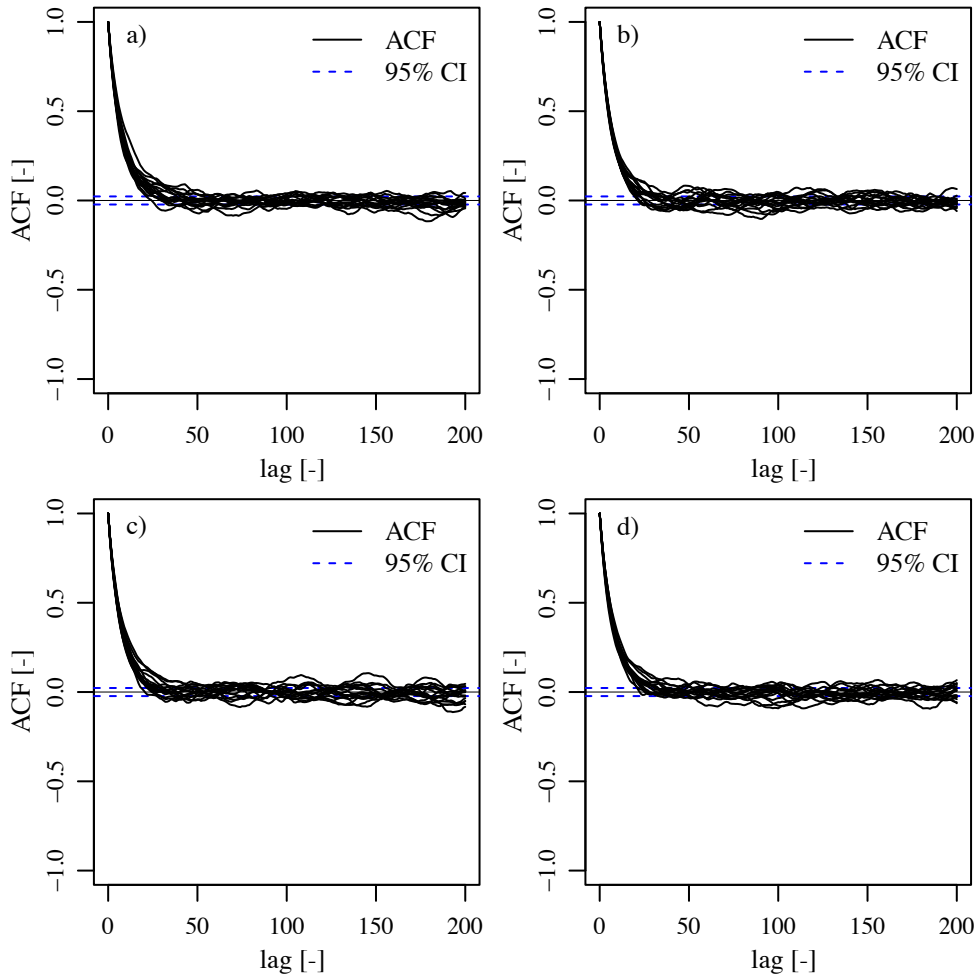

Fig. 6.10 ACF functions for the individual chains; Young's moduli of a) concrete E_c b) rock due to shear force $E_{r,kV}$; c) rock due to bending moment $E_{r,kM}$; d) thermal expansion coefficient of concrete α_T.

6.4.5 Resulting parameters

In Fig. 6.11, the prior distributions (blue dashed lines) and the posterior distributions (red solid lines) are given for the different parameters. Altough the prior distributions were chosen very broad, especially for the Young's modulus of rock and the thermal expansion coefficient, the parameters converge well. The distribution of E_c is smaller than those of $E_{r,i}$. This means that there is more uncertainty in the elastic abutment than in the concrete properties. In addition, a slight negative correlation of $r = -0.38$ between E_c and $E_{r,kM}$ was detected. Based on the MCMC samples, the joint probability function can be determined, leading to E_c = 30.2 GPa, $E_{r,kV}$ = 48.8 GPa, $E_{r,kM}$ = 34.0 GPa. and $\alpha_T = 0.91 \cdot 10^{-5}$ 1/K.

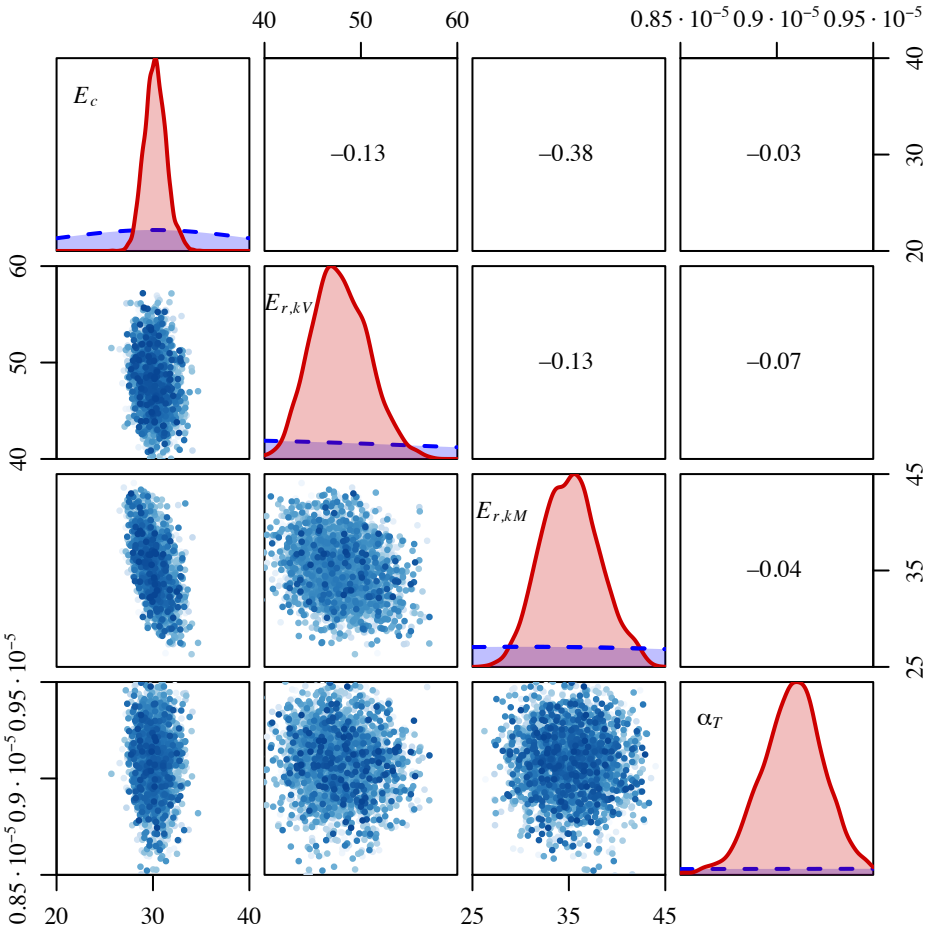

Fig. 6.11 Result of the MCMC calibration. The dashed blue lines correspond to the prior distribution and the solid red lines to the posterior distribution of the parameters θ. The blue points show the correlation between them. In addition, the correlation coefficient is given in the upper right part.

6.4.6 Robustness

Since all data are used for the model calibration, the robustness coefficient r_c is evaluated with $k = 3$ folds. Due to the multi-objective calibration, this is done for all levels. The results of this analysis are shown in Table 6.4. The parameter estimation with the MCMC algorithm leads to robust results on all levels. Hence, the model is suitable for a simultaneous behaviour analysis on several levels.

Table 6.4 Robustness coefficient r_c of the MCMC algorithm for different levels.

level [m a.s.l.]	301	288	270	249	238
r_c	0.947	0.943	0.955	0.992	0.980

6.4.7 Behaviour analysis

Based on the parameters resulting from Section 6.4.5, the displacement due to the effect of the water level and the temperature is calculated for each level. Subsequently, the adjusted behaviour indicator M_{adj} is estimated. They are shown in Fig. 6.12 for all levels. A shift in the data is clearly visible on the mid-levels. In addition, a drift at crest level occurs.

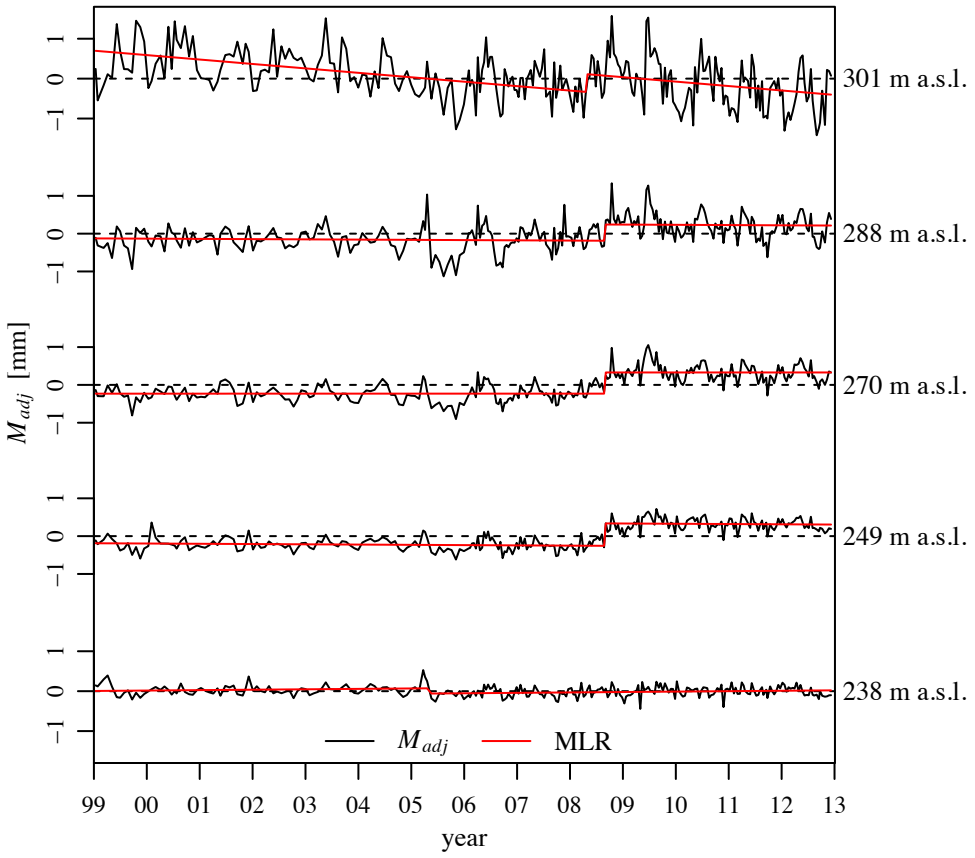

Fig. 6.12 Adjusted behaviour indicators resulting from the output of the multi-objective calibrated beam model (black). In addition, the results of the MLR algorithm to search behaviour changes are shown (red). On all levels except the bottom, a shift of around 0.5 mm is detected in summer 2008.

In a next step, the algorithm described in Section 4.4.3 was used to search for behaviour changes in the form of shifts. In Table 6.5, the results of the MLR analysis are shown. The algorithm detected a shift of around 0.5 mm at crest level in 2008. This shift was not obvious and not visually recognisable. The size of the shift corresponds to the estimated shift of the mid-level, which is also around 0.5 mm. Furthermore, there is no shift on the bottom level in 2008. This leads to the conclusion that there might have been a damage of the measurement equipment of the direct pendulum at 238 m a.s.l. in 2008. The operator confirmed that there were maintenance works in the pendulum shaft at that time.

Table 6.5 Results from MLR algorithm to search for behaviour changes.

level [m a.s.l.]	drift [mm/a]	shift [mm]	shift date
301	-0.11	0.45	16.4.2008
288	-0.01	0.43	21.8.2008
270	0	0.56	21.8.2008
249	0	0.60	21.8.2008
238	0.01	-0.13	18.4.2005

6.4.8 Summary

This case study exemplarily shows the potential of using a beam model in combination with multi-objective calibration based on Bayesian inference. Only one set of physically meaningful parameters is calibrated for one block of a gravity dam. This leads to simple models that allow for comprehensible inference by engineering judgement. Moreover, due to the simultaneous analyses of the displacement on different levels, a potentially abnormal behaviour can be detected and correctly located.

7 Conclusions and outlook

7.1 Conclusions

In the scope of this thesis, existing models for analysing the behaviour of concrete dams were systematically evaluated. Based on the gained findings, new approaches and models were developed. One of the main problems stated by engineers who apply dam behaviour analysis models is that the models are not robust in terms of using different calibration periods. This makes the set-up and the interpretation of the models very difficult. The main reason for a lack of model robustness was assumed to be the approach to represent temperature effects. Usually, a large set of correlated measurements is available and a subset has to be chosen.

There are two concepts to assess the behaviour of dams: (i) the observation-prediction comparison, which is commonly used in Switzerland and (ii) the concept of the adjusted behaviour indicator. A systematic analysis has shown that the robustness of the results mainly depends on the choice of the concept but not on the temperature approach.

The behaviour analysis by the observation-prediction comparison is based on prediction. A model is calibrated within a chosen calibration period and used to predict the displacement based on environmental conditions measured in the prediction period. Then the predicted displacements are compared to the corresponding measured displacements. In doing so, not only the effects of the water level and the temperature but also the irreversible effects must be predicted. However, experience has shown that in most of the cases the progress of the irreversible effects cannot be described by a simple mathematical function. As a consequence, predicting irreversible displacements likely leads to deviations from the observed behaviour and the observation-prediction comparison indicates an abnormal behaviour. Moreover, the estimation of the irreversible effects may heavily depend on the calibration period, which results in different and therefore not robust results.

In the concept of the adjusted behaviour indicator, the only purpose of the function to represent the irreversible effects in the model is to reduce the error in the coefficients of the reversible effects. If a trend is present in the measured displacement and no approach to represent irreversible effect is used in the model, the estimates of the reversible effects might be disturbed. After the estimation of the coefficients of the water level and the temperature, the reversible effects are subtracted from the measured displacement. The resulting adjusted behaviour indicator contains the irreversible displacement overlaid with the model errors. To quantify the robustness of the adjusted behaviour indicators estimated for different calibration periods, a robustness coefficient r_c is introduced. It expresses the variability between the results for two different calibration periods compared to the total variability. For most of the models analysed in this thesis, an $r_c > 0.9$ was

determined. This implies that the analysis based on the adjusted behaviour indicator is very robust.

Another origin of instabilities is multicollinearity between the different predictor variables. This can be between different temperature variables themselves or between the temperature and the water level if the reservoir is operated as seasonal storage. If multicollinearity is present, the model does not allow to calculate correct estimates and instabilities occur when predicting situations for environmental conditions not used for calibration. The presence of multicollinearity can be easily detected by the variance influence factor VIF. If multicollinearity is present, variables can either be omitted or special statistical methods can be used. Ridge regression and principal component regression were analysed in this thesis. Both of them did not allow to create more accurate and robust results. Thus, it is recommended to remove variables until $VIF < 10$ is reached.

The most effective way to reduce multicollinearity is the use of physically-based hybrid models that contain only few predictor variables. Two such models were developed and evaluated in this thesis. The goal was to have simple models that can be applied in a straightforward way. Thus, beam models that describe the structure of the dam in a simplified way were used. These were (i) a beam model to approximate the deformation of gravity and hollow gravity dams and (ii) an arch-cantilever model for the approximation of the deformation of arch dams. In beam models, the deformation due to the influence of the water level and the temperature are approximated by means of statics. Consequently, the influence of the individual temperatures and the effect of the water level is defined by the geometry and no variable selection has to be done. The resulting displacements can be used as input data for hybrid models. A change in the coefficient of the water level mainly corresponds to a different Young's modulus of concrete and a change in the coefficient of the temperature corresponds to a different thermal expansion coefficient. The beam models were applied to different dams. The results were very robust ($r_c \approx 0.99$) and no multicollinearity was observed for all investigated dams.

Regarding gravity dams, the beam model was used for a multi-objective calibration, where the measured displacements are simultaneously matched with the model output at several levels. The calibration was performed by using Bayesian inference where prior information about the material parameters can be considered. The Markov Chain Monte Carlo method (MCMC) was used as optimisation algorithm. Since only one set of physically meaningful parameters is calibrated for one block of a gravity dam, simple models that allow for comprehensible inference by engineering judgement result. Moreover, due to the simultaneous analyses of the displacement on different levels, a potentially abnormal behaviour can be detected and correctly located. The multi-objective calibration was also applied to the arch-cantilever model. Unfortunately, due to the global assumption of stiffness and the spring constants, the convergence was not good.

To create beam models, the temperature values which are physically relevant for the displacements have to be known. These are the mean temperature and the linear temperature difference between the upstream and the downstream dam faces. They can be obtained by heat conduction analysis. Unfortunately, the measurement sensors are located inside the dam a certain distance away from the dam face. It was shown that if this region where no temperature information is available is not considered in the heat conduction analysis, a phase shift and an amplitude damping of the mean temperature and the temperature difference occurs. Whereas a change in the amplitude can be compensated by the regression coefficient, the phase shift cannot. Thus, inverse heat conduction analysis is required. Since this is a mathematically ill-conditioned problem, a stabilisation procedure is required. The application of the latter by mollifier functions is successful as long as temperature measurements near the surface are available to determine the stabilisation parameters. Since this is not the general case, a new stabilisation procedure was developed. The idea behind the new approach is to limit the amplification of the recorded measurement noise when estimating the mean temperature and the temperature difference.

The current procedure of dam behaviour analysis is to split the data set into two parts: One part is used for model calibration (including validation) and the other for prediction. The behaviour analysis is usually done based on the prediction part. Because the results are very robust for the approach of adjusted behaviour indicators, all data can be used for model calibration. The only exception are the first ten years or so of the lifetime of a dam, since hydration heat and the change of concrete properties may distort the results. Using all available data for calibration can be seen as a paradigm shift from a statistical prediction to an inference problem. Inference means that the different effects on a system are related to the response of the system and are analysed. In the scope of dam behaviour analysis, the effects of the water level and the temperature are estimated and the therefrom derived irreversible effects are analysed. There are several advantages when using all data for the model calibration:

- There are no longer extrapolations since all data are used for calibration. This refers to unusual water levels and temperatures in colder or warmer periods.
- Multicollinearity mainly causes problems in prediction. For inference problems, the different effects cannot be separated properly but the estimation of their sum is still valid. If there is multicollinearity between the water level and the temperature for instance, they might not be separated properly but the estimated adjusted behaviour indicators are still correct.
- More calibration data lead to more accurate coefficient estimates.

Thus, it is recommended to use all available data for the model calibration.

7.2 Summary of main results

The main results of this thesis can be summarised as follows:

- The robustness of the results depends mainly on the choice of the concept to assess the dam behaviour.
- The adjusted behaviour indicator (ABI) approach leads to robust results; this has been proven by a systematic analysis on several models and dams.
- Since the results of the ABI are exceedingly robust, it is recommended to use all available data for model calibration.
- Using all data for calibration can be seen as a paradigm shift from a statistical prediction to an inference problem.
- Multicollinearity shall be omitted if a model is used for prediction purposes or if the separation of the effects is of interest.
- A straightforward way to reduce multicollinearity is to remove variables until $VIF < 10$ is reached.
- Multicollinearity disappears by the use of physically-based hybrid models.

7.3 Outlook

The results of this thesis show that the application of the concept of adjusted behaviour indicators leads to robust models. For practical application this concept shall be preferred to the well established observation-prediction comparison.

The investigations made within this thesis show that physically-based models are robust and allow for a relatively easy interpretation of the results based on engineering judgement. Thus, future developments should go further into this direction. Here, the behaviour analysis based on the adjusted behaviour indicator was done statistically. This problem could also be tackled with shape functions for irreversible behaviour estimated by a structural model. These may be the consideration of imposed valley deformations in certain directions, the volume expansion of concrete to represent AAR at certain levels or the change of the Young's moduli, and so on.

The beam model for gravity dams leads to good results, especially on the upper part of the dams. To have a better agreement on the lower part where deep-beam action is expected, a parametrised deep-beam FE-model could be set up and implemented. This as well could be used for multi-objective calibration based on Bayesian inference. Further, the use of the arch-cantilever-model works fine to create shape functions for hybrid models but for a global optimisation it is too simple. Thus, a 3D-FE-model could be set up and used for multi-objective calibration for arch dams.

Bibliography

Amberg, F. (2003). Thermal analysis of a RCC Dam during construction. *Proc. 7th ICOLD Benchmark Workshop on Numerical Analysis of Dams*. Bucarest, Romania: 1–17.

Amberg, F. (2009). Interpretative models for concrete dam displacements. *Proc. 23rd ICOLD Congress. International Commission on Large Dams (ICOLD)*, Brasilia, Brasil. Q.91, R.209: 1–20.

Amberg, F. (2011). Performance of Dams affected by Expanding Concrete. *Proc. 79th annual meeting of ICOLD, Lucerne, Switzerland, Dams and Reservoirs under Changing Challenges*, A. J. Schleiss; R. M. Boes (eds.). *CRC Press*, Boca Raton, USA: 115–122.

Amberg, F. (2015). Reaction alcali-granulat pour les barrages Suisse. STK Workshop 2015, Berne, Switzerland [in French].

Baehr, H. D.; Stephan, K. (2008). Wärme- und Stoffübertragung ('Heat and mass transfer'). *Springer*, Berlin Heidelberg, Germany. `http://dx.doi.org/10.1007/978-3-642-36558-4` [in German].

Bathe, K.-J. (1996). Finite Element Procedures. ISBN 0-13-301458-4. *Prentice-Hall*, Upper Saddle River, USA.

Becker, T. W.; Kaus, B. J. P. (2014). Numerical Modeling of Earth Systems — An introduction to computational methods with focus on solid Earth applications of continuum mechanics. *Lecture Notes*, University of Southern California [unpublished].

Bianchi, M.; Bremen, R. (2000). Health monitoring of arch dams, recent developments. *Proc. 6th International Workshop on Material Properties and Design, Present and future of health monitoring. Bauhaus-University*, Weimar, Germany.

Biedermann, R. (1997). Safety concept for dams: Development of the Swiss concept since 1980. *Wasser, Energie, Luft*, 89(3/4): 55–63.

Boes, R. M. (2015a). Wasserbau I ('Hydraulic Engineering I'). *Lecture Notes*, ETH Zurich [unpublished, in German].

Boes, R. M. (2015b). Wasserbau II ('Hydraulic Engineering II'). *Lecture Notes*, ETH Zurich [unpublished, in German].

Bofang, Z. (2014). Thermal Stresses and Temperature Control of Mass Concrete. ISBN 9780124077232. *Butterworth-Heinemann*, Oxford, UK.

Bonaldi, P.; Fanelli, M.; Giuseppetti, G. (1977). Displacement forecasting for concrete dams. *Water Power & Dam Construction*, 29(9): 42–50.

Bosshard, E. (1949). Beiträge zur Theorie und Berechnung der Bogenstaumauern ('Contributions to the theory and calculation of arch dams'). *PhD Thesis*, ETH Zürich, Zürich,

Switzerland. http://dx.doi.org/dx.doi.org/10.3929/ethz-a-000103453.

Bossoney, C. (1985). Comparison des observation avec le comportement prévu a l'aide de modèles analytique et statistique ('Comparison of observations to predictions of analytical and statistical models'). *Proc. 15th ICOLD Congress. International Commission on Large Dams (ICOLD)*, Lausanne, Switzerland. Q.56, R.12: 85–89 [in French].

Bossoney, C.; Balissat, M. (2005). Uncertainty about origin of permanent deformations on existing concrete dams. *Proc. 73rd annual meeting of ICOLD*. Tehran, Iran: 1–10.

Braak, C. J. F. T. (2006). A Markov Chain Monte Carlo version of the genetic algorithm Differential Evolution: easy Bayesian computing for real parameter spaces. *Statistics and Computing*, 16(3): 239–249. http://dx.doi.org/10.1007/s11222-006-8769-1.

Breitenstein, F.; Köhler, W.; Widmann, R. (1985). Safety control of the dams of the Glockner-Kaprun hydro-electric development. *Proc. 15th ICOLD Congress. International Commission on Large Dams (ICOLD)*, Lausanne, Switzerland. Q.56, R.59: 1121–1134.

Bremen, R. (2005). Oberflächensetzungen als Folge von Tunnelbauten in grosser Tiefe ('Surface settlements due to deep tunneling'). *Proc. Swiss Tunnel Congress 2005. Swiss Tunneling Society*, Lucerne, Switzerland [in German].

Bremen, R.; Bianchi, M. (2000). Möglichkeiten und Grenzen deterministischer Modelle zur Überwachung von Verformungen an Betonsperren ('Potential and limits of deterministic models for the deformation monitoring of concrete dams'). *Proc. Betrieb und Überwachung wasserbaulicher Anlagen*, G. Heigerth (ed.). *TU Graz*, Graz [in German].

Brooks, S.; Gelman, A.; Jones, G. L.; Meng, X.-L. (2011). Handbook of Markov Chain Monte Carlo. ISBN 9781420079418. *Chapman and Hall/CRC*, Boca Raton, USA.

Brooks, S. P.; Gelman, A. (1998). General Methods for Monitoring Convergence of Iterative Simulations. *Journal of Computational and Graphical Statistics*, 7(4): 434–455. http://dx.doi.org/10.1080/10618600.1998.10474787.

Bundesamt für Energie (2015). Richtlinie über die Sicherheit der Stauanlagen ('Swiss dam safety guidelines'), Version 2.0. Richtlinie des BFE [in German].

BWG (2002). Sicherheit der Stauanlagen, Basisdokumentation zu Überwachung und Unterhalt ('Safety of dams, basic document for monitoring and maintenance'), Version 1.0. Bundesamt für Wasser und Geologie, Biel, Switzerland [in German].

Byrd, R. H.; Lu, P.; Nocedal, J.; Zhu, C. (1995). A Limited Memory Algorithm for Bound Constrained Optimization. *SIAM Journal on Scientific Computing*, 16(5): 1190–1208. http://dx.doi.org/10.1137/0916069.

Bühlmann, M.; Vetsch, D. F.; Boes, R. M. (2015). Influence of measuring intervals on goodness of fit of dam behaviour analysis models. *Proc. 13th ICOLD Benchmark Workshop on the Numerical Analysis of Dams*, R. M. Gunn; M. Balissat; P. Manso; L. Mouvet; A. J. Schleiss (eds.). Lausanne, Switzerland: 317–325.

Carslaw, H. S.; Jaeger, J. C. (1986). Conduction Of Heat in Solids. ISBN 9780198533689. *Oxford*, London, UK.

Çengel, Y. A.; Ghajar, A. J. (2015). Heat and Mass Transfer — Fundamentals & Applications. ISBN 978-0-07-339818-1. 5. edn. *McGraw-Hill*, New York, USA.

Conte, S. D.; de Boor, C. (1980). Elementary Numerical Analysis — An Algorithmic Approach. ISBN 0-07-012447-7. *McGraw-Hill*, New York, USA.

Copen, M. D.; Lindholm, E. A.; Tarbox, G. S. (1977). Chap. Design of Concrete Dams: 385–499. In: A. R. Golzé (ed.) Handbook of Dam Engineering. *Van Nostrand Reinhold Company*, New York, USA.

Cryer, J. D.; Chan, K.-S. (2008). Time Series Analysis — With Applications in R. ISBN 9780387759586. *Springer*, New York, USA.

Cubus AG (2014a). CEDRUS-6, Handbuch ('CEDRUS-6, user manual') [in German].

Cubus AG (2014b). STATIK-6, Handbuch ('STATIK-6, user manual') [in German].

Dallmann, R. (2009). Baustatik 2, Berechnung statisch unbestimmter Tragwerke ('Statics 2, Calculation of statically indeterminate systems'). 2 edn. *Carl Hanser*, München. `http://dx.doi.org/10.3139/9783446421585` [in German].

De Sortis, A.; Paoliani, P. (2007). Statistical analysis and structural identification in concrete dam monitoring. *Engineering Structures*, 29(1): 110–120. `http://dx.doi.org/10.1016/j.engstruct.2006.04.022`.

Dettling, M. (2014). Applied Time Series Analysis. *Lecture Notes*, ETH Zurich, Switzerland.

Dettling, M. (2015). Applied Statistical Regression. *Lecture Notes*, ETH Zurich, Switzerland.

Duong, T. (2007). ks: Kernel Density Estimation and Kernel Discriminant Analysis for Multivariate Data in R. *Journal of Statistical Software*, 21(7): 1–16. `http://dx.doi.org/10.18637/jss.v021.i07`.

Fanelli, M.; Giuseppetti, G.; Mazza, F. (2000). Analysis of the phenomenon of time drift in the observation data of dam behavior. *Proc. 20th ICOLD Congress. International Commission on Large Dams (ICOLD)*, Beijing, China. Q.78, R.67: 1083–1098.

Friedman, J.; Hastie, T.; Tibshirani, R. (2010). Regularization Paths for Generalized Linear Models via Coordinate Descent. *Journal of Statistical Software*, 33(1): 1–22.

http://www.jstatsoft.org/v33/i01/.

Gelman, A.; Roberts, G. O.; Gilks, W. R. (1996). Efficient Metropolis Jumping Rules. *Proc. Bayesian Statistics 5: Proceedings of the Fifth Valencia International Meeting*, J. M. Bernardo; J. O. Berger; A. P. Dawid; A. F. M. Smith (eds.). Oxford University Press, Oxford, UK: 599–607. ISBN 9780198523567.

Gerber, M.; Bühlmann, M.; Vetsch, D. (2015). DamBASE — Software Application. ETH Zurich.

Gonçalves, S.; White, H. (2005). Bootstrap standard error estimates for linear regression. *Journal of the American Statistical Association*, 100(471): 970–979. http://www.jstor.org/stable/27590627.

Hastie, T.; Tibshirani, R.; Friedman, J. (2009). The Elements of Statistical Learning — Data Mining, Inference, and Prediction. *Springer*, New York, USA. http://www.springer.com/de/book/9780387848570.

Hauser, F. R. (2017). Statistische Überwachung von Drainagewassermenge, Auftriebsdruck und Porenwasserdruck an Talsperren ('Statistical monitoring of drainage flow, uplift pressure and pore pressures on dams'). *Master Thesis*, ETH Zurich, Switzerland [unpublished, in German].

Herzog, M. (1988a). Die Baugrundverformung bei Gewölbestaumauern ('Building deformation of arch dams'). *Bautechnik*, 65(11): 376–380 [in German].

Herzog, M. (1988b). Die jährliche Kronenbewegung von Gewölbestaumauern ('Yearly crest deformation of arch dams'). *Bautechnik*, 65(3): 73–79 [in German].

Holcim Schweiz AG (2008). Betonpraxis —- Der Weg zum dauerhaften Beton ('practical experience of concrete'), 5. edn. [in German].

Huggenberger AG (2016). Measuring devices. http://www.huggenberger.com/en/measuring-devices-for.html. Accessed: 2016-04-24.

ICOLD (2013). Guidelines for use of numerical models in dam engineering. *ICOLD Bulletin 155*. International Commission on Large Dams (ICOLD).

James, G.; Witten, D.; Hastie, T.; Tibshirani, R. (2013). An Introduction to statistical learning — with applications in R. *Springer*, New York, USA. http://www.springer.com/de/book/9781461471370.

Johansson, S. (1997). Seepage Monitoring in Embankment Dams. *PhD Thesis*, Royal Institute of Technology, Stockholm, Sweden.

Kobelt, A.; Pougatsch, H.; Salzgeber, H.; Aeschbach, M.; Ziegler, H.-J.; Lombardi, G.; Schneider, T. R.; Amber, W.; Egger, K. (2004). AlpTransit und Sicherheit der Talsperren — Erkenntnisse im Lötschberggebiet ('AlpTransit and dam safety — findings in the

Lötschberg area'). *Wasser Energie Luft*, 96(11/12): 285–298 [in German].

Kolly, J.-C.; Joos, B. (1995). D'un model simple de determination des deformations d'un barrage-poids sous l'influence de la temperature ('A simple model for the determination of the temperature influence of a gravity dam'). *Proc. Research and Development in the Fiels of Dams*. Crans-Montana, Switzerland [in French].

König, T.; Jünemann, K.; Burger, M. (2015). RUnit — a unit test framework for R. `https://cran.r-project.org/web/packages/RUnit/vignettes/RUnit.pdf` [Accessed: 17/01/2016].

Lang, H.-J.; Huder, J.; Amann, P.; Puzrin, A. M. (2011). Bodenmechanik und Grundbau — Das Verhalten von Böden und Fels und die wichtigsten grundbaulichen Konzepte ('Soil Mechanics and Geotechnics — Behaviour of Rock and Soil and Basic Geotechnical Conceps'). *Springer-Verlag*, Berlin, Germany. `http://www.springer.com/de/book/9783642146862` [in German].

Leclerc, M.; Léger, P. (2004). TADAM — Thermal analysis of cocrete Dams — Software Application. Polytechnique Montreal, Canada.

Léger, P; Cote, P; Tinawi, R (1996). Finite element analysis of concrete swelling due to alkali-aggregate reactions in dams. *COMPUTERS & STRUCTURES*, 60(4): 601–611. `http://dx.doi.org/10.1016/0045-7949(95)00440-8`.

Léger, P.; Leclerc, M. (2007). Hydrostatic, Temperature, Time-Displacement Model for Concrete Dams. *Journal of Engineering Mechanics (ASCE)*, 133(3): 267–277. `http://dx.doi.org/10.1061/(ASCE)0733-9399(2007)133:3(267)`.

Léger, P.; Seydou, S. (2009). Seasonal Thermal Displacements of Gravity Dams Located in Northern Regions. *Journal of Performance of Constructed Facilities*, 23(3): 166–174. `http://dx.doi.org/10.1061/(ASCE)0887-3828(2009)23:3(166)`.

Léger, P.; Venturelli, J.; Bhattcharjee, S. S. (1993). Seasonal temperature and stress distributions in concrete gravity dams. Part 1: modelling. *Canadian Journal of Civil Engineering*, 20(6): 999–1017. `http://dx.doi.org/10.1139/l93-131`.

Liu, J.; Wang, G.; Chen, Y. (2008). Research and application of GA neural network model on dam displacement forecasting. *Proc. Earth and Space 2008*: 1–9. `http://dx.doi.org/10.1061/40988(323)69`.

Lombardi, G. (1992). L'informatique dans l'auscultations des barrages ('Information technology for structural monitoring of dams'). *Wasser, Energie, Luft*, 84(1/2): 2–8 [in French].

Lombardi, G.; Amberg, F.; Darbre, G. R. (2008). Algorithm for the prediction of functional delays in the behaviour of concrete dams. *Hydropwer & Dams*, 15(3): 111–116.

Marcello, C.; Spagnoletti, S. (1960). Sul comportamento della diga a gravità alleggerita ad elementi cavi tipo Marcello — il comportamento teorico ('On the structural behaviour of hollow buttresses gravity dams — Theoretical behaviour'). *L'Energia elettrica*, 37(10) [in Italian].

Marti, P. (2013). Theory of Structures — Fundamentals, Framed Structures, Plates and Shells. ISBN 978-3-433-02991-6. *Ernst & Sohn*, Berlin, Germany.

Mata, J. (2011). Interpretation of concrete dam behaviour with artificial neural network and multiple linear regression models. *Engineering Structures*, 33(3): 903–910. `http://dx.doi.org/10.1016/j.engstruct.2010.12.011`.

Mata, J.; Tavares de Castro, A.; Sá da Costa, J. (2013). Constructing statistical models for arch dam deformation. *Structural Control and Health Monitoring*, 21(3): 423–437. `http://dx.doi.org/10.1002/stc.1575`.

MeteoSwiss (2017). IDAweb — Datenportal für Lehre und Forschung ('IDAweb — data portal for education and science'). `https://gate.meteoswiss.ch/idaweb/` [in German].

Mevik, B.-H.; Wehrens, R. (2007). The pls Package: Principal Component and Partial Least Squares Regression in R. *Journal of Statistical Software*, 18(2): 1–23. `http://dx.doi.org/10.18637/jss.v018.i02`.

Mirzabozorg, H.; Hariri-Ardebili, M. A.; Shirkhan, M.; Seyed-Kolbadi, S. M. (2014). Mathematical Modeling and Numerical Analysis of Thermal Distribution in Arch Dams considering Solar Radiation Effect. *The Scientific World Journal*, 2014: 1–15. `http://dx.doi.org/10.1155/2014/597393`.

Montgomery, D. C.; Peck, E. A.; Vining, G. G. (2012). Introduction to Linear Regression Analysis. ISBN 978-0-470-54281-1. 5. edn. *John Wiley and Sons*, Hoboken, USA.

Moran, M. J.; Shapiro, H. N. (2010). Fundamentals of Engineering Thermodynamics — SI Version. ISBN 978-0-470-54019-0. 6. edn. *John Wiley & Sons*, Hoboken, USA.

Obernhuber, P.; Perner, F. (2005). Displacements in concrete dams caused by temperature variation. *Hydropower & Dams*, 12(5): 80–86.

Özisik, M. N.; Orlande, H. R. B. (2000). Inverse Heat Transfer — Fundamentals and Applications. ISBN 978-1560328384. *Taylor & Francis*, New York, USA.

Palumbo, P.; Piroddi, L.; Lancini, S.; Lozza, F. (2001). NARX modelling of radial crest displacements of the Schlegeis arch dam. *Proc. 6^{th} ICOLD Benchmark Workshop on Numerical Analysis of Dams*. Salzburg, Austria: 1–9.

Penot, I.; Daumas, B.; Fabre, J.-P. (2005). Monitoring behaviour. *International Water Power & Dam Construction*, 57(12): 24–27.

Perner, F.; Obernhuber, P. (2009). Analyse der Verformungen von Gewölbemauern ('Displacement analysis of arch dams'). *Österreichische Wasser- und Abfallwirtschaft*, 61(9-10): 138–143. http://dx.doi.org/10.1007/s00506-009-0118-0 [in German].

Pichler, W. (2009). Langzeitverhalten von Talsperrenbeton ('Long term behaviour of dam concrete'). *Österreichische Wasser- und Abfallwirtschaft*, 61(9-10): 133–137. http://dx.doi.org/10.1007/s00506-009-0120-6 [in German].

Piroddi, L.; Spinelli, W. (2003). Long-Range Nonlinear Prediction: A Case Study. *Proc. of the* 42nd *IEEE Conference on Decision and Control*. Maui, USA.

Poulikakos, D. (2011). Thermodynamik II — Teil II ('Thermodynamics II — part II'). *Lecture Notes*, ETH Zurich, Switzerland [in German].

Ranković, V.; Grujović, N.; Divac, D.; Milivojević, N. (2014). Development of support vector regression identification model for prediction of dam structural behaviour. *Structural Safety*, 48: 33–39. http://dx.doi.org/10.1016/j.strusafe.2014.02.004.

Raynaud, M.; Beck, J. V. (1988). Methodology for Comparison of Inverse Heat Conduction Methods. *Journal of Heat Transfer*, 110(1): 30–37. http://dx.doi.org/10.1115/1.3250468.

Raynaud, M.; Bransier, J. (1986). A new finite-difference method for the nonlinear inverse heat conduction problem. *Numerical Heat Transfer*, 9(1): 27–42. http://dx.doi.org/10.1080/10407788608913463.

R Core Team (2013). R: A language and environment for statistical computing. R Foundation for Statistical Computing, Vienna, Austria. ISBN 3-900051-07-0, URL http://www.R-project.org/.

Rescher, O. J. (1965). Talsperrenstatik — Berechnung und Bemessung von Gewichtsstaumauern ('Statics of dams — calculation of gravity dams'). *Springer-Verlag*, Berlin, Germany. http://www.springer.com/de/book/9783540033899 [in German].

Robert, C. P.; Casella, G. (2010). Introducing Monte Carlo Methods with R. *Springer*, New York, USA. http://www.springer.com/de/book/9781441915757.

Rocha, M.; Serafim, J.L.; Da Silveira, A.F. (1958). A method of quantitative interpretation of the results obtained in the observation of dams. *Proc.* 6th *ICOLD Congress. International Commission on Large Dams (ICOLD)*, New York, USA. Q.21, R.36: 371–396.

Salazar, F.; Toledo, M. A.; Oñate, E.; Morán, R. (2015). An empirical comparison of machine learning techniques for dam behaviour modelling. *Structural Safety*, 56(2015): 9–17. http://dx.doi.org/10.1016/j.strusafe.2015.05.001.

Santillán, D.; Salete, E.; Toledo, M. Á. (2015). A new 1D analytical model for computing the thermal field of concrete dams due to the environmental actions. *Ap-*

plied Thermal Engineering, 85(2015): 160–171. http://dx.doi.org/10.1016/j.applthermaleng.2015.04.023.

Santillán, D.; Salete, E.; Vicente, D. J.; Toledo, M. Á. (2014). Treatment of Solar Radiation by Spatial and Temporal Discretization for Modeling the Thermal Response of Arch Dams. *Journal of Engineering Mechanics*, 140(11): 1–18. http://dx.doi.org/10.1061/(ASCE)EM.1943-7889.0000801.

Saouma, V. (2014). Numerical Modeling of AAR. ISBN 9780415636971. *Taylor & Francis*, London, UK.

Saouma, V.; Hansen, E.; Rajagopalan, B. (2001). Statistical and 3D Nonlinear Finite Element Analysis of Schlegeis Dam. *Proc. 6th ICOLD Benchmark Workshop on Numerical Analysis of Dams*. Salzburg, Austria.

Saouma, V.; Perotti, L.; Shimpo, T. (2007). Stress Analysis of Concrete Structures Subjected to Alkali-Aggregate Reactions. *ACI Structural Journal*, 104(5): 532–541.

Schackow, A.; Effting, C.; Gomes, I. R.; Patruni, I. Z.; Vicenzi, F.; Kramel, C. (2016). Temperature variation in concrete samples due to cement hydration. *Applied Thermal Engineering*, 103: 1362–1369. 0141-0296. http://dx.doi.org/10.1016/j.applthermaleng.2016.05.048.

Schiefer, F. (2015). Verhalten von Talsperren ('Dam behaviour'). *Master Thesis*, ETH Zurich, Switzerland [unpublished, in German].

Schleiss, A. J.; Pougatsch, H. (2011). Les barrages — Du projet à la mise en service ('Dams -from the projekt to maintenance'). ISBN 978-2-88074-831-9. *PPUR*, Lausanne [in French].

Schnitter, N. (1969). Die sofortige Überprüfung von Staumauerdeformationen ('The immediate control of dam displacements'). *Schweizerische Bauzeitung*, 87(49): 961–963. http://dx.doi.org/10.5169/seals-70824 [in German].

Serra, C.; Batista, A. L.; Tavares de Castro, A. (2012). Creep of Dam Concrete Evaluated from Laboratory and in Situ Tests. *Strain, An International Journal for Experimental Mechanics*, 48(3): 241–245. http://dx.doi.org/10.1111/j.1475-1305.2011.00818.x.

Simon, A.; Royer, M.; Mauris, F.; Fabre, J. P. (2013). Analysis and interpretation of dam measurements using artificial neural networks. *Proc. 9th ICOLD European Club Symposium. Il Comitato Nazionale Italiano per le Grandi Dighe (ITCOLD)*, Venezia, Italy.

Stahel, W. A. (2008). Statistische Datenanalyse — Eine Einführung für Naturwissenschaftler ('Statistical data analysis — an Introduction for natural scientists'). *Vieweg + Teubner*', Wiesbaden, Germany. http://www.springer.com/us/book/

9783322999306.

Storn, Rainer; Price, Kenneth (1997). Differential Evolution - A Simple and Efficient Heuristic for global Optimization over Continuous Spaces. *Journal of Global Optimization*, 11(4): 341–359. http://dx.doi.org/10.1023/A:1008202821328.

Strom-online (2018). http://www.strom-online.ch/talsperren_infos.html [Accessed: 09/01/2018].

Stucky, A.; Derron, M.-H. (1957). Problèmes thermiques posés par la construction des barrages-réservoirs ('thermal probles in dam construction'). *Publication No. 38*, EPF Lausanne, Switzerland [in French].

Su, H.; Chen, Z.; Wen, Z. (2016). Performance improvement method of support vector machine-based model monitoring dam safety. *Structural Control and Health Monitoring*, 23(3): 252–266. http://dx.doi.org/10.1002/stc.1767.

Swiss Committee on Dams (2003). Methods of analysis for the prediction and the verification of dam behaviour. *Wasser Energie Luft*, 95(3/4): 73–110.

Taler, J.; Duda, P. (2006). Solving Direct and Inverse Heat Conduction Problems. *Springer*, Berlin, Germany. http://www.springer.com/de/book/9783540334705.

Tannehill, J. C.; Anderson, D. A.; Pletcher, R. H. (1997). Computional Fluid Mehanics and Heat Transfer. ISBN 9781591690375. 2 edn. *Taylor & Francis*, Washington, USA.

Tatin, M. (2014). Comportement thermique des barrages en béton: Amélioration des modèles d'analyses physico-statistiques des mesures de déplacements (Thermal bebehaviour of concrete dams: Improvement of hybrid models for monitoring displacements'. *PhD Thesis*, Universitè de Grenoble, France [in French].

Tatin, M.; Briffaut, M.; Dufour, F.; Simon, A.; Fabre, J.P. (2013a). Thermal displacements of concrete dams: finite element and statistical modelling. *Proc. 9th ICOLD European Club Symposium. Il Comitato Nazionale Italiano per le Grandi Dighe (ITCOLD)*, Venezia, Italy.

Tatin, M.; Briffaut, M.; Dufour, F.; Simon, A.; Fabre, J. P. (2015). Thermal displacements of concrete dams: Accounting for water temperature in statistical models. *Engineering Structures*, 91: 26–39. http://dx.doi.org/10.1016/j.engstruct.2015.01.047.

Tatin, M.; Briffaut, M.; Dufour, F.; Simon, A.; Fabre, J. P.; Rousset, B. (2013b). Thermal deformation of concrete dams: justification, clarification and improvement of statistical analysis. *Proc. 17th biennial conference of the British Dam Society, Dams: Engineering in a social and environmental context*, Andrew Pepper (ed.). Leeds, UK.

Timoshenko, S.; Goodier, J. N. (1970). Theory of Elasticity. ISBN 0-07-085805-5. *McGraw-Hill*, New York, USA.

USBR (1938). Boulder Canyon project — final reports — part V — technical investigation — Bulletin 1 — trial load method of analyzing arch dams. United States, Department of the Interiour, Bureau of Reclamation (USBR), Denver, USA.

van Ravenzwaaij, D.; Cassey, P.; Brown, S. D. (2016). A simple introduction to Markov Chain Monte-Carlo sampling. *Psychonomic Bulletin & Review*: 1–12. 1531-5320. http://dx.doi.org/10.3758/s13423-016-1015-8.

Weber, B. (2002). Vorhersage des Verhaltens von Talsperren mit Hilfe des Soll-Ist-Vergleichs — Statistischer Teil ('Prediction of dam behaviour with observation-prediction comparison — statistical part') [in German].

Weber, B. (2004). DamReg — Software Application. Swiss Federal Office of Energy, Switzerland.

Weber, B.; Perner, F.; Obernhuber, P. (2010). Displacements of Concrete Dams Determined from Recorded Temperatures. *Proc. of the* 8^{th} *ICOLD European Club Symposium: dam safety - sustainability in a changing environment*. *Austrian National Committee on Large Dams (ATCOLD)*, Graz, Austria: 623–628.

Werkle, H. (2008). Finite Elemente in der Baustatik — Statik und Dynamik der Stab- und Flächentragwerke ('Finite eleelement in statics — statics and dynamics of framed structures and plates'). 3. edn. *Vieweg*, Wiesbaden, Germany. http://www.springer.com/de/book/9783528288822 [in German].

Widmann, R. (1967). Evaluation of deformation measurements performed at concrete dams. *Proc.* 9^{th} *ICOLD Congress*. *International Commission on Large Dams (ICOLD)*, Istanbul, Turkey. Q.34, R.38: 671–676.

Willm, G.; Beaujoint, N. (1967). Les méthodes de surveillance des barrages au service de la production hydraulique d'Electricité de France — Problèmes anciens et solutions nouvelles ('Surveillance methods of dams of EDF — Old problems and new solutions')'. *Proc.* 9^{th} *ICOLD Congress*. *International Commission on Large Dams (ICOLD)*, Istanbul, Turkey. Q.34, R.30: 529–550.

Wilson, E. L.; Habibullah, A. (2003). SAP2000 structural analysis — user's manual. Computers and Structures Inc., Berkeley, California.

Wood, S. N. (2004). Stable and Efficient Multiple Smoothing Parameter Estimation for Generalized Additive Models. *Journal of the American Statistical Association*, 99(467): 673–686. http://dx.doi.org/10.1198/016214504000000980.

Wood, S. N. (2006). Generalized Additive Models: An Introduction with R. ISBN 9781584884743. *Chapman and Hall/CRC*, Boca Raton, USA.

Nomenclature

Abbreviations

1D	one-dimensional
3D	three-dimensional
A	arch dam
AAR	alkali aggregate reaction
ACF	autocorrelation function
AG	arch-gravity dam
ANN	artificial neural network
AR	auto regressive model
BBS	block bootstrap
DBA	dam behaviour analysis
DHCA	direct heat conduction analysis
FE	finite element
FFT	fast Fourier transformation
FSL	full supply level
G	gravity dam
GAM	generalized additive models
HCE	heat conduction equation
HG	hollow gravity dam
HST	hydrostatic seasonal time
HSTT	hydrostatic seasonal temperature time
HTT	hydrostatic temperature time
IHCA	inverse heat conduction analysis
IHCP	inverse heat conduction problem
LOESS	locally weighted scatterplot smoothing
MCMC	Markov chain Monte Carlo
MLR	multiple linear regression
ODE	ordinary differential equation
OLS	ordinary least squares
OPC	observation-prediction comparison
PACF	partial autocorrelation function
PCR	principal component regression

PDE	partial differential equation
PDF	probability density function
RR	ridge regression
SLR	simple linear regression

Greek Symbols

α	inclination of the upstream and downstream surfaces of a gravity dam	[-]
α	significance level in hypothesis tests	[-]
α_T	thermal expansion coefficient	[1/K]
β	regression coefficient	[-]
χ	curvature	[-]
Δh_i	delayed water level	[m]
ΔT_a	difference to average annual temperature curve	[°C]
ΔT_d	difference to average annual temperature difference	[°C]
ΔT_m	difference to average annual mean temperature	[°C]
ΔT_R	thermal correction for HSTT-model	
Δ	Laplace operator	
δ	deformatin (displacement, rotation)	[m]
Δ_G	matrix of compatibility conditions of a grillage	
δ_{i0}	deformation at location of removed supports	
Δ_{ij}	deformation matrix due to the redundant variables X_i	
ε	error	
ε	normal strain	[-]
γ	regularisatiuon parameter for mollifier function	[-]
γ_w	unit weight of water	[N/m^3]
γ_{de}	parameters to scale jump with in DE-algorithm	[-]
$\hat{\beta}$	estimate of regression coefficient	[-]
$\hat{\sigma}^2$	estimated variance	
λ	ridge estimator	[-]
λ	thermal conductivity	[W/(m K)]
∇	nabla operator	
ν	Poisson's ratio	[-]
ω	angular frequency	[1/s] or [1/d] or [1/a]
ϕ	angle	[-]

ϕ	argument of complex number, phase shift	
π	distribution	
π_k	partial auto correlation coefficient of lag k	
ρ	density	[kg/m^3]
ρ_k	autocorrelation coefficient of lag k	
σ^2	variance	
τ_i	constants of annual temperature curve	[-]
θ	parameters used in MCMC analysis	

Roman Symbols

$\bar{x}$	mean value of predictor variable	
$\bar{y}$	mean value of response variable	
$\dot{Q}$	heat flux	[W]
$\dot{q}$	specific heat flux	[W/m^2]
$\dot{Q}_s$	heat source term	[W]
$\dot{q}_s$	specific heat source term	[W/m^3]
$\hat{T}$	temperature in the frequency domain	[°C]
$\hat{y}$	estimated value of predictor variable	
F_o	Fourier number	[-]
$\mathbf{A}$	matrix of finite difference scheme	
$\mathbf{H}$	hat matrix $\mathbf{X}(\mathbf{X}'\mathbf{X})^{-1}\mathbf{X}'y$	
$\mathbf{I}$	unity matrix	[-]
$\mathbf{X}$	model matrix	
A	area	[m^2]
A	constant	[-]
a	rectangle height of approximated foundation surface	[m]
a	thermal diffusivity	[m^2/s]
A_v	shear area	[m^2]
B	constant	[-]
b	rectangle width of approximated foundation surface	[m]
B_b	beam width	[m]
B_c	cantilever width	[m]
BC	behaviour change	[-]
C	constant	[-]

C	diagonal elements of the matrix $(\mathbf{X}'\mathbf{X})^{-1}$	
c	specific heat capacity	[J/(kg K)]
D	difference between observation M and the prediction P	
d_1	distance to boundary of left thermometer	[m]
d_2	distance to boundary of right thermometer	[m]
D_i	Cook's distance	[-]
d_i	standardised residual	[-]
E	Young's modulus	[N/m^2]
E	energy	[J]
e	residuals	
F	load	[N]
f	function	
$f_{k,M}$	factor to determine spring constant due to bending moment	[-]
$f_{k,N}$	factor to determine spring constant due to normal force	[-]
$f_{k,V}$	factor to determine spring constant due to shear force	[-]
G	shear modulus	[Pa]
G	transfer function for heat conduction analysis	
H	dam height	[m]
H	hydrostatic effects in dam behaviour analysis models	
h	water level	[m] or [-]
H_0	null hypothesis	
h_a	arch height	[m]
h_b	beam height	[m]
h_{ii}	diagonal elements of hat matrix $\mathbf{H}$	
I	moment of inertia	[m^4]
i	imaginary unit	[-]
j	current location	[-]
j	number of day in the year starting on the 1$^{\text{st}}$ of January	
j_x	number of elements in spatial discretisation	[-]
k	auxiliary quantity for heat conduction analysis	[1/m]
k	lag in auto regressive (AR) models	[-]
k	number of folds used for cross-validation and robustness coefficient	[-]
k_M	spring constant for bending moment	[Nm]

k_N	spring constant for normal force	[N/m]
k_V	spring constant for shear force	[N/m]
L	length of 1D-section	[m]
l	distance between two thermometers	[m]
L_{cr}	crest length	[m]
M	bending moment	[Nm]
M	model	
m	number of cantilevers in arch-cantilever model	[-]
m_γ	mollifier function for inverse heat conduction analysis	[-]
M_{adj}	adjusted behaviour indicator	
Mod_{th}	threshold value for frequency amplification	[-]
$MS_{res,p}$	mean squared residuals of prediction	
MS_{res}	mean squared residuals	
N	normal force	[N]
N	number of iteration steps in MCMC analysis	[-]
n	current time step	[-]
n	number of arches in arch-cantilever model	[-]
n	number of observations	[-]
n	order	[-]
n_t	number of time steps	[-]
$n_{BC,max}$	maximum number of behaviour changes to search for	[-]
n_{BC}	number of found behaviour changes	[-]
n_i	number of thermometers used for the calibration of a	[-]
n_l	number of levels	[-]
n_{PC}	number of thermometers used for thermal model in statistical analysis	[-]
n_p	number of observations used for prediction	[-]
n_T	number of thermometers used for thermal model in statistical analysis	[-]
o_h	polynomial order of water level approach	[-]
P	intersection point	
P	number of chains in MCMC analysis	[-]
P	predicted values of dam behaviour analysis model	
p	p-value used for hypothesis tests	[-]
p	number of regression coefficients in a model	[-]

p_{cut}	cut-off p-value for hypothesis test	[-]
P_{ir}	irreversible displacements	
P_{rev}	reversible displacements	
p_w	water pressure	[Pa]
$PSRF$	potential scale reduction factor	[-]
q	number of regression coefficients added to a model	[-]
Q_{tot}	total drainage flow at the bottom of the dam	[m^3/s]
R	rainfall and snowmelt effects in dam behaviour analysis models	
R	supporting force	[N] or [Nm]
r	absolute value of complex number, amplitude of harmonic	
$R^2_{pred,CV}$	cross-validation prediction coefficient of determination	[-]
R^2_{pred}	prediction coefficient of determination	[-]
R^2	coefficient of determination	[-]
r_i	studentised residual	[-]
R^2_{adj}	adjusted coefficient of determination	[-]
r_c	coefficient of robustness	[-]
R^2_{pred}	prediction coefficient of determination	[-]
r_{Td}	ratio between the temperature difference in the total region and in the direct region	
r_{Tm}	ratio between the mean temperature in the total region and in the direct region	
$RMSE$	root mean squared error	
$RMSPE$	root mean squared prediction error	
$RMSPE_{CV}$	cross-validation test error	
RSE	residual standard error	
S	season	
S	seasonal effects in dam behaviour analysis models	
SS_{res}	residual sum of squares	
SS_t	total sum of squares	
T	temperature	[°C]
T	temperature effects or irreversible effects in function of time in dam behaviour analysis models	
T	torsional moment	[Nm]
t	t-test statistic	[-]
t	time	[a] or [d] or [s]

T_b	boundary temperature	[°C]
T_d	linear temperature difference in 1D-section	[°C]
T_h	period of a harmonic	[s] or [d] or [a]
T_m	mean temperature in 1D-section	[°C]
T_n	nonlinear temperature part in 1D-section	[°C]
T_{ref}	temperature at the grouting of the joints or the long term average temperature	
T_{air}	air temperature	[°C]
t_a	dam thickness at the abutment	[m]
t_c	thickness of concrete dam	[m]
t_I	duration of the initial phase	[a]
T_{mh}	temperature used for Metropolis-Hastings algorithm	[-]
v_{ts}	propagation velocity of thermal signal	[m/s]
VIF	variance inflation factor	[-]
VIF_{max}	maximal VIF in a model	[-]
X	virtual load	[-]
x	coordinate	
x	independent variable, predictor variable, regressor	
y	coordinate	
y	dependent variable, response variable	
z	complex number	
z	coordinate	
z_a	abutment level	[m a.s.l.]
z_{cr}	crest level	[m a.s.l.]
dl	element length	[m]

Subscripts

dsf	downstream surface
ref	reference
usf	upstream surface
a	abutment
b	boundary
BC	behaviour change
bw	backward
c	concrete

cal	calibration	
cr	crest, crest level	
cr	crest	
CV	cross-validation	
d	difference (between lake and valley)	
d	difference	
$diff$	difference	
fw	forward	
j	grid point	
l	left	
lev	level	
ll	lower limit	
M	bending moment	[Nm]
m	mean	
m	mean	
N	normal force	[N]
p	prediction	
r	right	
r	rock	
r	rock	
s	source	
st	stabilised	
t	time	
ul	upper limit	
V	shear force	[N]

A Appendix

A.1 Statics

A.1.1 Curves for Vogt's formula

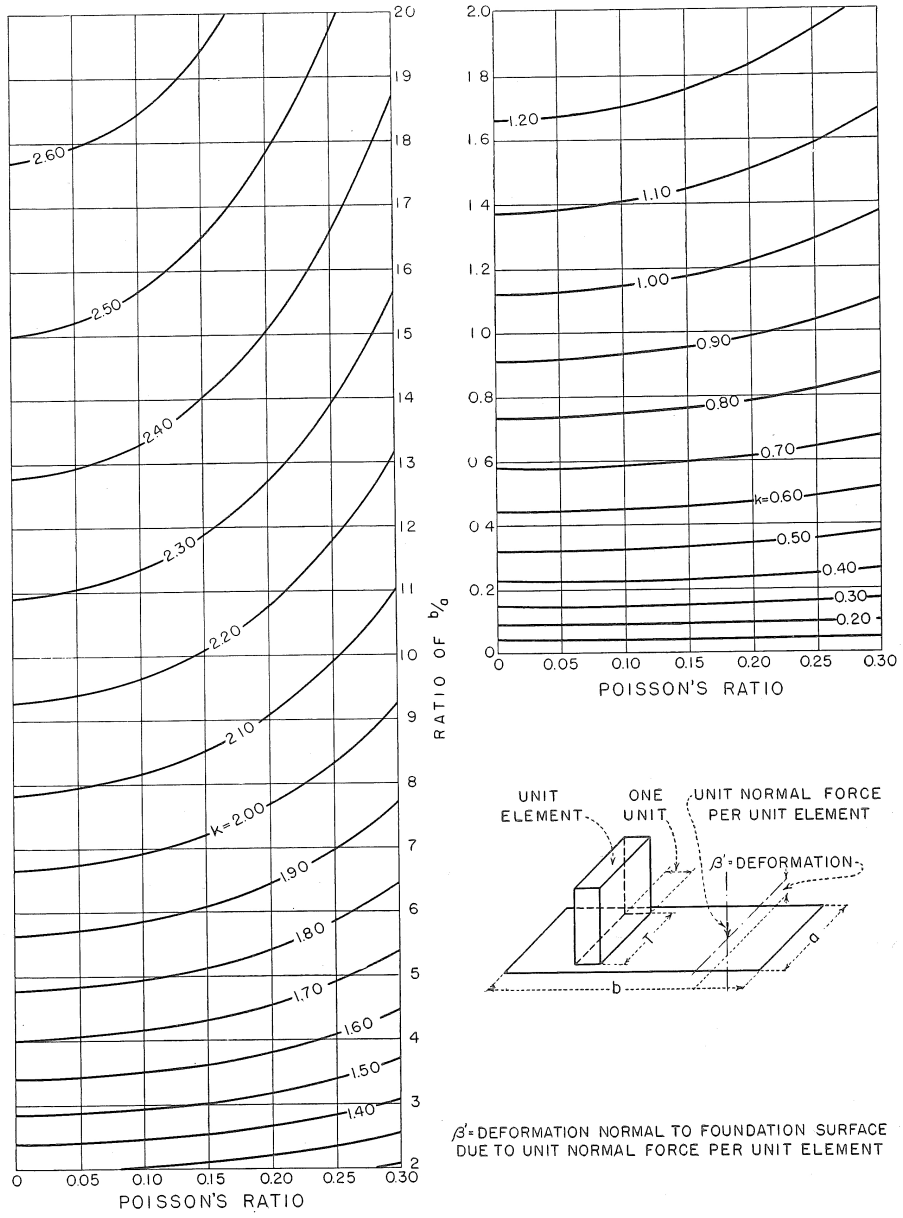

Fig. A.1 Factors $f_{k,N}$ to estimate the spring constant of a rock foundation due to a normal load N (USBR, 1938).

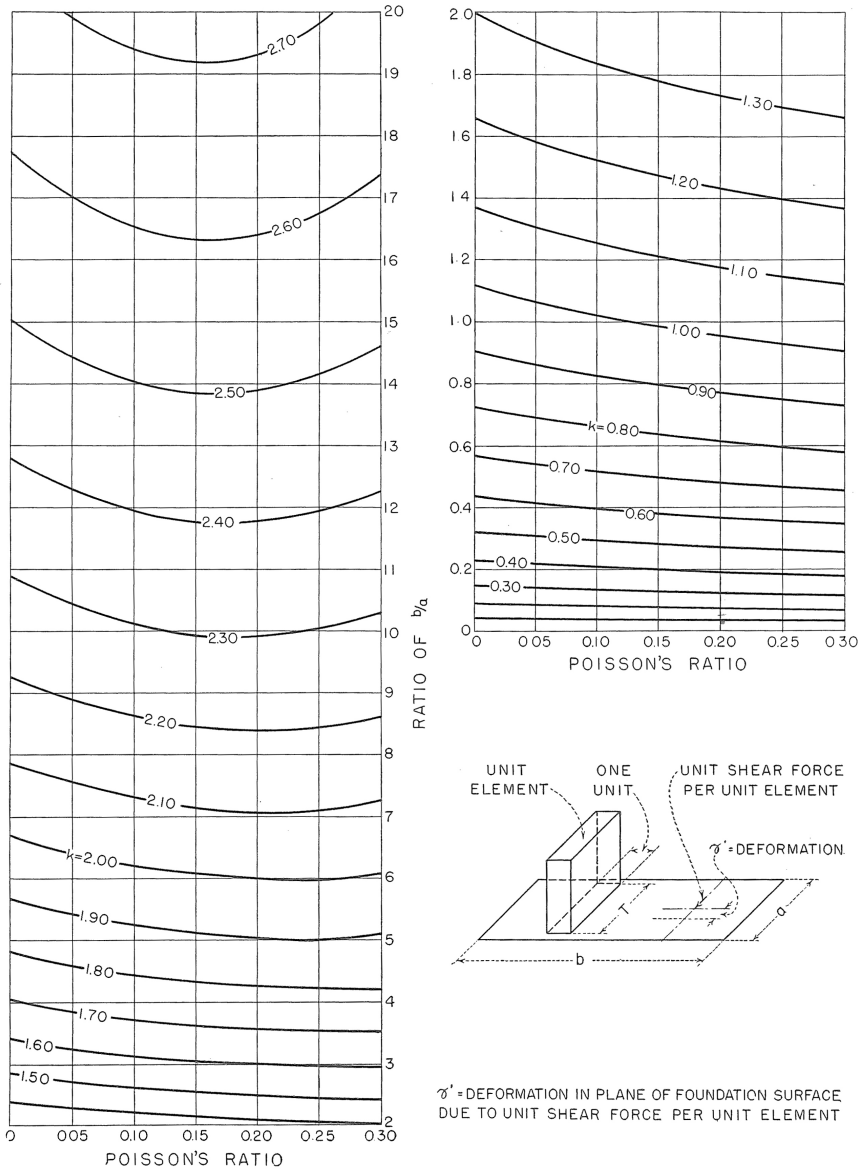

Fig. A.2 Factors $f_{k,V}$ to estimate the spring constant of a rock foundation due to a shear force V (USBR, 1938).

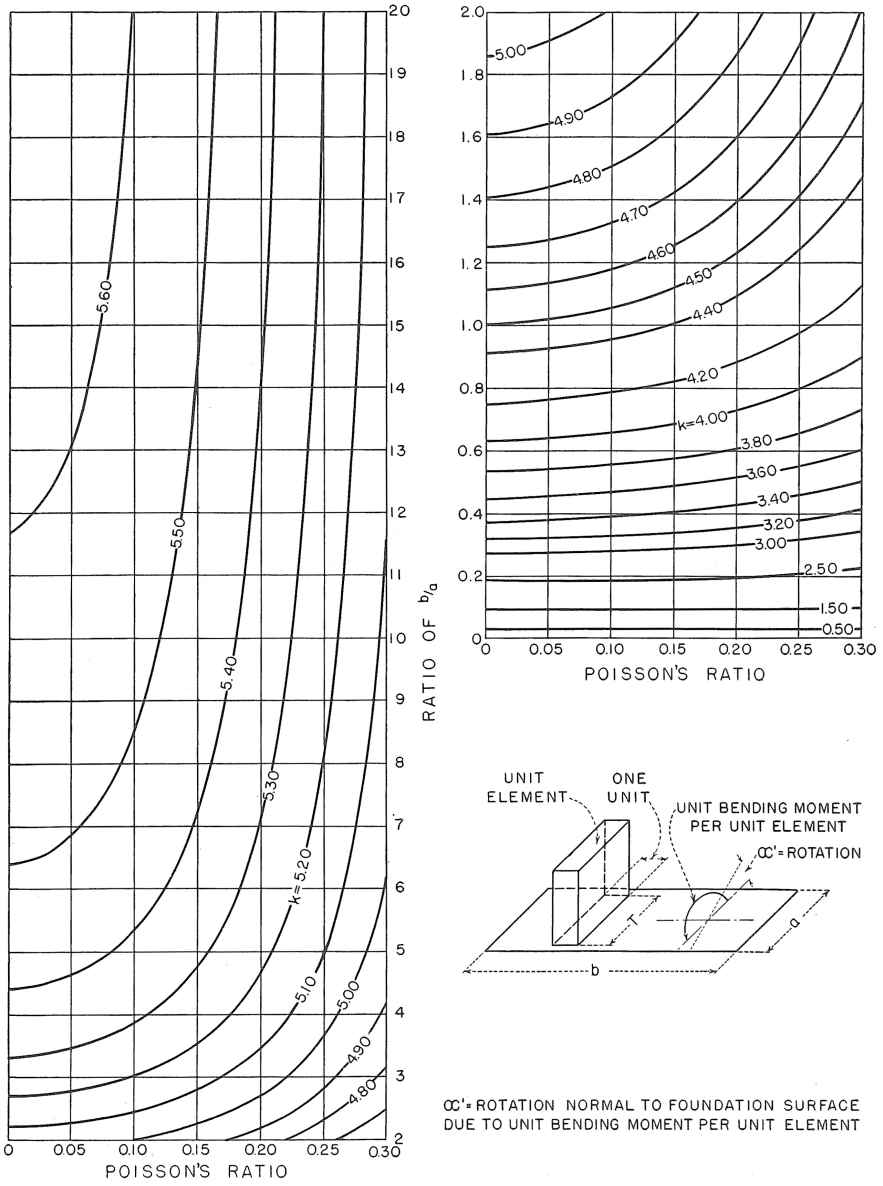

Fig. A.3 Factors $f_{k,M}$ to estimate the spring constant of a rock foundation due to a bending moment M (USBR, 1938).

A.1.2 Stress resultants on arch

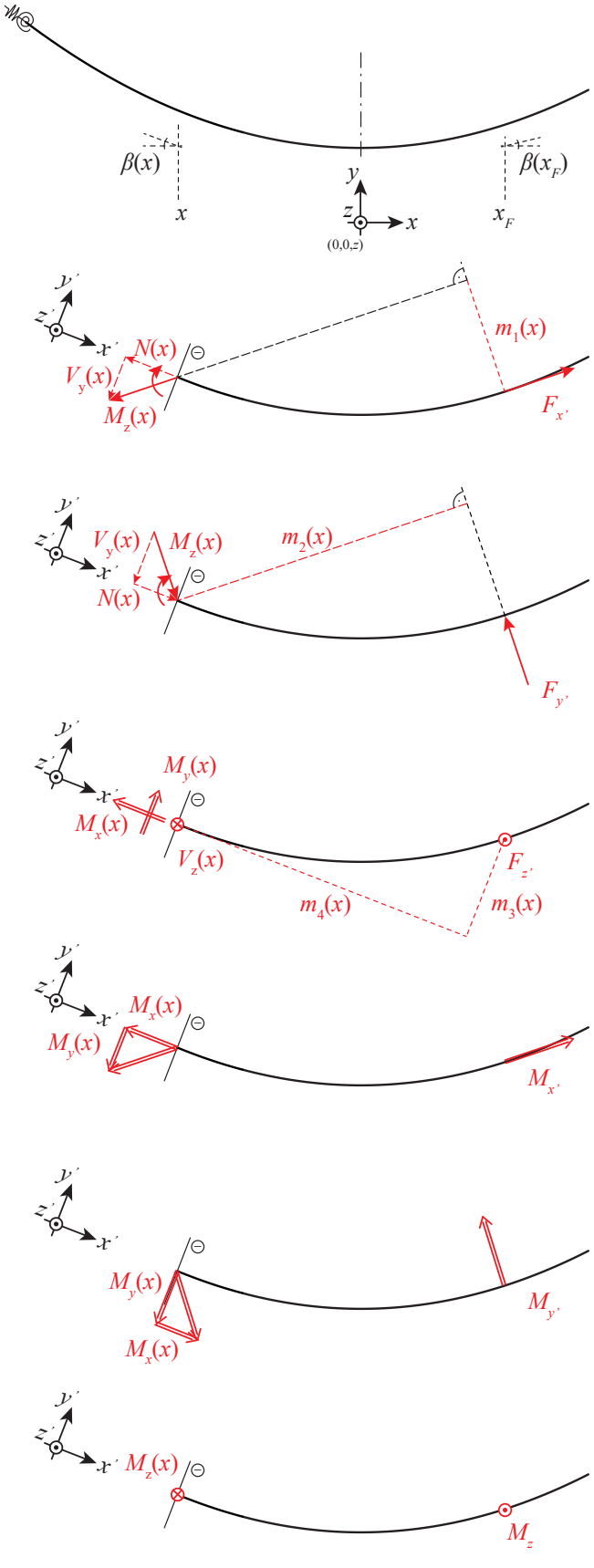

$N(x) = \cos(\beta(x_F) - \beta(x))\, F_{x'}$
$V_y(x) = \sin(\beta(x_F) - \beta(x))\, F_{x'}$
$V_z(x) = 0$
$M_x(x) = 0$
$M_y(x) = 0$
$M_z(x) = m_1(x)\, F_{x'}$

$N(x) = -\sin(\beta(x_F) - \beta(x))\, F_{y'}$
$V_y(x) = \cos(\beta(x_F) - \beta(x))\, F_{y'}$
$V_z(x) = 0$
$M_x(x) = 0$
$M_y(x) = 0$
$M_z(x) = m_2(x)\, F_{y'}$

$N(x) = 0$
$V_y(x) = 0$
$V_z(x) = -F_z$
$M_x(x) = m_3(x)\, F_{z'}$
$M_y(x) = -m_4(x)\, F_{z'}$
$M_z(x) = 0$

$N(x) = 0$
$V_y(x) = 0$
$V_z(x) = 0$
$M_x(x) = \cos(\beta(x_F) - \beta(x))\, M_{x'}$
$M_y(x) = \sin(\beta(x_F) - \beta(x))\, M_{x'}$
$M_z(x) = 0$

$N(x) = 0$
$V_y(x) = 0$
$V_z(x) = 0$
$M_x(x) = \sin(\beta(x_F) - \beta(x))\, M_{y'}$
$M_y(x) = \cos(\beta(x_F) - \beta(x))\, M_{y'}$
$M_z(x) = 0$

$N(x) = 0$
$V_y(x) = 0$
$V_z(x) = 0$
$M_x(x) = 0$
$M_y(x) = 0$
$M_z(x) = M_z$

Fig. A.4 Functions of stress resultants on arch due to point loads

A.2 Heat transfer analysis

A.2.1 Finite difference solution for heat conduction analysis

A.2.1.1 Direct heat conduction

The content of the current section is mainly based on Becker and Kaus (2014) and Çengel and Ghajar (2015), other sources are cited as common.

Introduction

The method of finite differences approximates the derivatives of a PDE by a discretisation of the governing variables. This approximation can be derived by a Taylor expansion. Suppose the continuous and differentiable function $f(x)$ in Fig. A.5. The function can be discretised by dividing into small elements of length Δx. A Taylor series expansion around point x in forward direction for $f(x+\Delta x)$ can be written as

$$f(x+\Delta x) = f(x) + \frac{\partial f(x)}{\partial x}\Delta x + \frac{\partial^2 f(x)}{\partial x^2}\frac{\Delta x^2}{2!} + \ldots + \frac{\partial^n f(x)}{\partial x^n}\frac{\Delta x^n}{n!} + \mathscr{O}(\Delta x^{n+1}), \quad \text{(A.1)}$$

where $\mathscr{O}(\Delta x^{n+1})$ means that the full solution also would include terms with order $> n+1$ that are neglected here. $\mathscr{O}$ is called truncation error; if Δx decreases also the error decreases. Rearranging Eq.(A.1) leads to the first derivative of the function $f(x)$:

$$\frac{\partial f(x)}{\partial x} = \frac{f(x+\Delta x) - f(x)}{\Delta x} - \frac{\partial^2 f(x)}{\partial x^2}\frac{\Delta x}{2!} - \ldots - \frac{\partial^n f(x)}{\partial x^n}\frac{\Delta x^{n-1}}{n!} + \mathscr{O}(\Delta x^{n+1}) \quad \text{(A.2)}$$

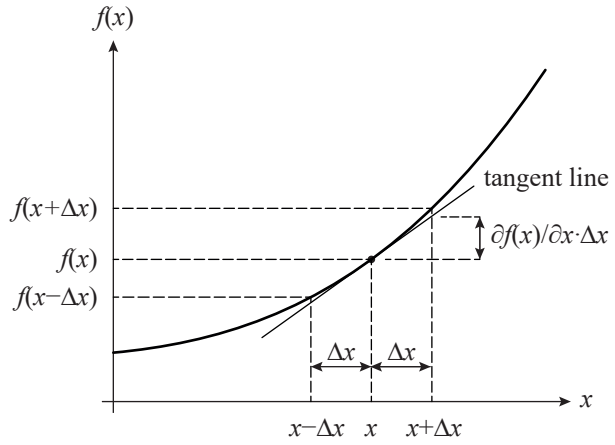

Fig. A.5 First derivative of function $f(x)$ at point x (adapted from Çengel and Ghajar, 2015).

If all terms with an order > 1 are neglected, the first derivative can be written as

$$\frac{\partial f(x)}{\partial x} = \frac{f(x+\Delta x) - f(x)}{\Delta x} + \mathscr{O}(\Delta x) \tag{A.3}$$

Eq.(A.3) is a first order estimation of the first forward derivative and it can also be written in the following short form

$$f'_{fw} = \frac{f_{j+1} - f_j}{\Delta x} + \mathscr{O}(\Delta x) \tag{A.4}$$

The Taylor series can also be developed backwards for $f(x-\Delta x)$ as well. This leads to the first order estimation of the first backward derivative:

$$f'_{bw} = \frac{f_j - f_{j-1}}{\Delta x} + \mathscr{O}(\Delta x) \tag{A.5}$$

The second order accurate central (j is in the centre of $j+1$ and $j-1$) second derivative can be found as follows

$$f''_c = \frac{f'_{j+1/2} - f'_{j-1/2}}{\Delta x} = \frac{\frac{f_{j+1} - f_j}{\Delta x} - \frac{f_j - f_{j-1}}{\Delta x}}{\Delta x} = \frac{f_{j+1} - 2f_j + f_{j-1}}{\Delta x} + \mathscr{O}(\Delta x^2) \tag{A.6}$$

Explicit scheme for the 1D transient HCE

The 1D transient HCE Eq.(2.34) can be discretised in the same manner as described above. Since with the time t and the direction x two governing variables are present, a grid is used for the discretisation (Fig. A.6). The time is divided into n_t regular time steps Δt and the direction in j_x elements with length Δx. The current time step is represented by n and the location by j. The derivative of the temperature respecting to the time $\partial T/\partial t$ can be replaced by the forward finite difference approximation

$$\frac{\partial T}{\partial t} = \frac{T_j^{n+1} - T_j^n}{\Delta t} \tag{A.7}$$

where T_j^n is the temperature at location j at the current time step and T_j^{n+1} at the new time step. The second derivative of the temperature respecting to the direction $\partial^2 T/\partial x^2$ can be replaced by the central finite difference approximation

$$\frac{\partial^2 T}{\partial x^2} = \frac{T_{j+1}^n - 2T_j^n + T_{j-1}^n}{\Delta x^2} \tag{A.8}$$

with T_{j-1}^n, T_j^n and T_{j+1}^n at the time steps n and the locations $j-1$, j, $j+1$. The 1D transient HCE can now be expressed as

$$\frac{T_j^{n+1} - T_j^n}{\Delta t} = a \frac{T_{j+1}^n - 2T_j^n + T_{j-1}^n}{\Delta x^2} \tag{A.9}$$

Since all temperatures at the time step n are known and T_j^{n+1} is the only unknown in Eq.(A.9), it can be explicitly calculated by

$$T_j^{n+1} = T_j^n + \mathsf{F}_o \left(T_{j+1}^n - 2T_j^n + T_{j-1}^n \right) \tag{A.10}$$

where F_o is the Fourier number, which is dimensionless:

$$\mathsf{F}_o = \frac{a\Delta t}{\Delta x^2} \tag{A.11}$$

Since T_j^{n+1} can be calculated explicitly from three temperatures of the current time step n, this scheme is called an explicit finite difference scheme (Fig. A.7a). It is first order accurate in time and second order accurate in space (Becker and Kaus, 2014).

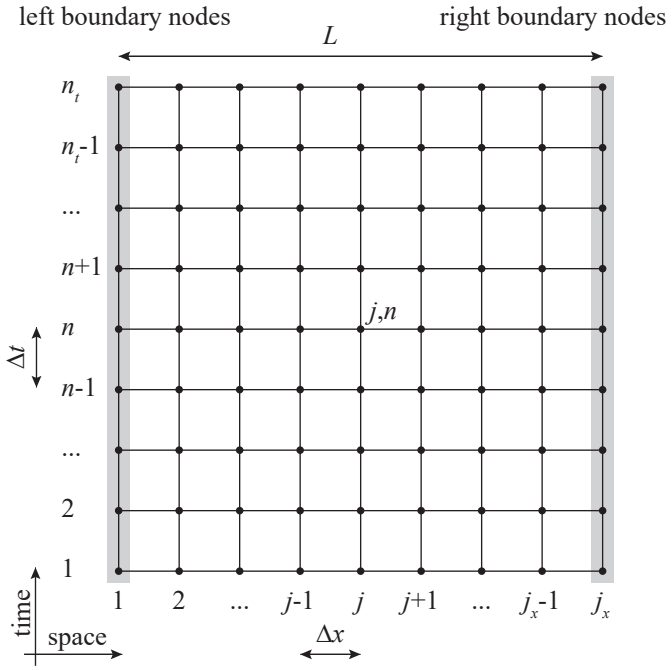

Fig. A.6 Grid for finite difference discretisation of the 1D transient HCE (adapted from Becker and Kaus, 2014).

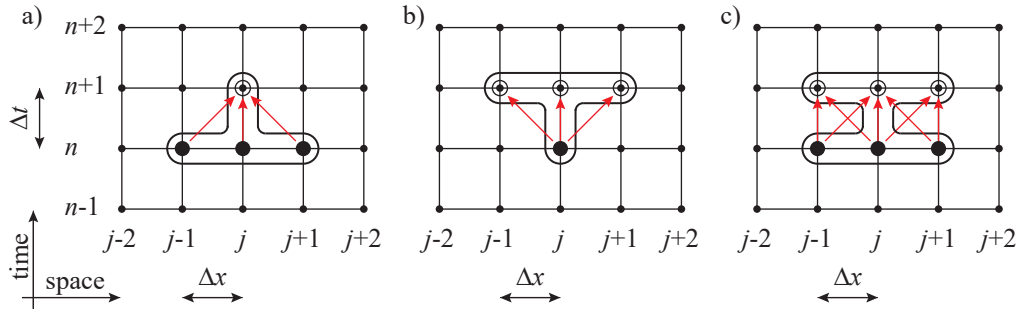

Fig. A.7 Finite difference schemes: a) explicit, b) fully implicit c) Crank-Nicolson (adapted from Becker and Kaus, 2014).

Stability analysis for explicit scheme

The stability of Eq.(A.10) can be shown by the following example. Consider three nodes with the temperatures $T_{j-1}^n = T_{j+1}^n = 50°C$ and $T_j^n = 80°C$ on the time step n. At the next time step, it is expected that temperature T_j^{n+1} is between 50°C and 80°C. With regard to Eq.(A.10), this is satisfied if $\mathsf{F}_o \leq 0.5$. For $\mathsf{F}_o > 0.5$, the result becomes physically impossible and violates the second law of thermodynamics. Thus, the solution of the explicit finite difference scheme of the heat conduction equation is only conditionally stable for $\mathsf{F}_o = a\Delta t/\Delta x^2 \leq 0.5$. This means that the maximal possible time step is given by the spatial discretisation or vice versa (Çengel and Ghajar, 2015).

Implicit scheme

The stability problems of the explicit scheme can be overcome by using a conditionally stable implicit finite difference scheme. In an implicit scheme, the spatial derivative is partially determined at the next time step. The simplest form is the fully implicit scheme, where the derivative is evaluated completely at the new time step (Fig. A.7b). By using a forward approximation for the derivative $\partial T/\partial t$, the fully implicit finite difference approximation of the heat 1D transient HCE is

$$\frac{T_j^{n+1} - T_j^n}{\Delta t} = a\frac{T_{j+1}^{n+1} - 2T_j^{n+1} + T_{j-1}^{n+1}}{\Delta x^2} \tag{A.12}$$

Using the dimensionless Fourier number F_o and rearranging that the unknown parameters are on the left side and the known ones on the right side leads to

$$\mathsf{F}_o T_{j+1}^{n+1} - (1+2\mathsf{F}_o) T_j^{n+1} + \mathsf{F}_o T_{j-1}^{n+1} = -T_j^n \tag{A.13}$$

Eq.(A.13) contains three unknown and only one known temperature, therefore it cannot be solved explicitly. If Eq.(A.13) is formulated for all locations $j = 2$ to $j = (j_x - 1)$, the following system of linear equations can be formulated:

$$(\mathsf{F}_o\mathbf{A}-\mathbf{I})\,\overrightarrow{T}^{n+1} = -\overrightarrow{T}^{n} \tag{A.14}$$

$$\mathbf{A} = \begin{bmatrix} 1 & 0 & 0 & 0 & 0 & 0 & 0 \\ 1 & -2 & 1 & 0 & 0 & 0 & 0 \\ \dots & \dots & \dots & \dots & \dots & \dots & \dots \\ 0 & 0 & 1 & -2 & 1 & 0 & 0 \\ \dots & \dots & \dots & \dots & \dots & \dots & \dots \\ 0 & 0 & 0 & 0 & 1 & -2 & 1 \\ 0 & 0 & 0 & 0 & 0 & 0 & 1 \end{bmatrix} \tag{A.15}$$

where $\mathbf{I}$ is the unity matrix, $\mathbf{A}$ the matrix of the finite difference approximation of the central spatial derivative, $\overrightarrow{T}^{n+1}$ the vector of temperatures at the next time step and $\overrightarrow{T}^{n}$ the vector of the temperatures at the current time step. The temperatures at the next time step are obtained by the calculation of the inverse of the matrix $\mathsf{F}_o\mathbf{A}-\mathbf{I}$ and multiplying it with the temperatures at the current time step (Eq.(A.16)). This means that the inverse $(\mathsf{F}_o\mathbf{A}-\mathbf{I})^{-1}$ needs to be calculated only one time.

$$\overrightarrow{T}^{n+1} = -\left(\mathsf{F}_\mathbf{o}\mathbf{A}-\mathbf{I}\right)^{-1}\overrightarrow{T}^{n} \tag{A.16}$$

Since the matrix $\mathsf{F}_o\mathbf{A}-\mathbf{I}$ is a tridiagonal band matrix, the fastest way to calculate its inverse is the Thomas algorithm that is well described in Conte and de Boor (1980). As the explicit scheme, the implicit scheme is first order accurate in time and second order accurate in space. However, no stability criteria need to be satisfied since it is unconditionally stable. This does not mean that this scheme is accurate for large time steps (Becker and Kaus, 2014). Using a too large discretisation leads to inaccurate solutions for fast changing temperature phenomenons. Thus, it is recommended to check the convergence of the solution by a grid refinement.

Crank-Nicolson scheme

If the spatial derivative is taken at the current and the next time step, the so-called Crank-Nicolson scheme results:

$$\frac{T_j^{n+1}-T_j^n}{\Delta t} = \frac{a}{2\Delta x^2}\left(T_{j+1}^n - 2T_j^n + T_{j-1}^n + T_{j+1}^{n+1} - 2T_j^{n+1} + T_{j-1}^{n+1}\right) \tag{A.17}$$

Rearranging Eq.(A.17) leads to

$$\left(\frac{\mathsf{F}_o}{2}\mathbf{A}-\mathbf{I}\right)\overrightarrow{T}^{n+1} = -\left(\frac{\mathsf{F}_o}{2}\mathbf{A}+\mathbf{I}\right)\overrightarrow{T}^{n} \tag{A.18}$$

The temperatures at the next time step can be obtained by

$$\overrightarrow{T}^{n+1} = -\left(\frac{\mathsf{F_o}}{2}\mathbf{A}-\mathbf{I}\right)^{-1}\left(\frac{\mathsf{F}_o}{2}\mathbf{A}+\mathbf{I}\right)\overrightarrow{T}^{n} \tag{A.19}$$

The computational cost for the Crank-Nicolson scheme is nearby the same as for the fully implicit scheme, the inverse of $\mathsf{F}_o/2\,\mathbf{A}-\mathbf{I}$ needs to be calculated once and multiplied with $\mathsf{F}_o/2\,\mathbf{A}-\mathbf{I}$. The advantage lies in the fact that the Crank-Nicolson scheme is second order accurate in both time and space.

Convergence check

The solution converges for small time steps $\Delta t \to 0$ and element lengths $\Delta x \to 0$. The error contains the round off error and the truncation error (Çengel and Ghajar, 2015). The discretisation that is needed for an error that is small enough, depends also on the gradient of the thermal signals that are processed. Therefore, no general statement about a discretisation can be given.

Boundary conditions

Since Eq.(A.10), Eq.(A.12) and Eq.(A.17) are not applicable on the boundary nodes, another relation is needed to implement the boundary conditions. Usually it is specified problem-dependent by the energy balance equation. In Çengel and Ghajar (2015) solutions for different boundary conditions are described (heat flux, convection, radiation and combinations of it). For the case of known boundary temperatures $T(t,0)$ and $T(t,L)$ (measurements), they can be inserted directly into the finite difference grid.

Initial condition

To solve Eq.(A.10), (A.16) and (A.19), the temperature distribution on the first time step must be known. A common way is to assume a constant temperature and to cut the initial part of the calculation since it needs to converge. To achieve a faster convergence, the initial temperature along the cross section can be given as near as possible to the finial reference temperature (Léger *et al.*, 1993). For this, the measurement values of inner thermometers could be used.

A.2.1.2 Inverse heat conduction

Raynaud and Bransier (1986) developed a stabilised finite difference scheme to solve the inverse heat conduction problem (IHCP). They propose to calculate the interior temperature field between x_1 and x_2 by a Crank-Nicolson scheme first. In a second stage, the IHCP is solved by the scheme presented in Fig.(A.8a). The temperature T_{j-1}^{n+1} is calculated by the arithmetic mean of two estimators $\tilde{T}_{j-1}^{n+1}$ and $\tilde{\tilde{T}}_{j-1}^{n+1}$ that are based on two energy balance equations.

$$T_{j-1}^{n+1} = \frac{\tilde{T}_j^{n+1} + \tilde{\tilde{T}}_j^{n+1}}{2} \tag{A.20}$$

$$\tilde{T}_{j-1}^{n+1} = \frac{1+\mathsf{F}_o}{\mathsf{F}_o} T_j^{n+2} + \frac{\mathsf{F}_o - 1}{\mathsf{F}_o} T_j^{n+1} + T_{j+1}^{n+2} \tag{A.21}$$

$$\tilde{\tilde{T}}_{j-1}^{n+1} = \frac{1+\mathsf{F}_o}{\mathsf{F}_o} T_j^{n+1} + \frac{\mathsf{F}_o - 1}{\mathsf{F}_o} T_j^{n} + T_{j+1}^{n} \tag{A.22}$$

Because of the use of temperatures that are in the past and in the future of the regarded time step $n+1$, this scheme is stabilised. A spatial grid refinement (Δ_x smaller) leads to the consideration of more temperature information (Fig. A.8b). In view of that fact, the finer the spatial step, the smoother the estimated boundary temperature and the less the sensitivity to measurement errors (Raynaud and Beck, 1988). However, a too smooth boundary temperature cuts some thermal waves one may be interested in. Therefore, a trade-off, which is case dependent, has to be found. In contrary to direct problems the explicit finite difference method is more stable, since they better allow for the delay in temperature changes (Taler and Duda, 2006).

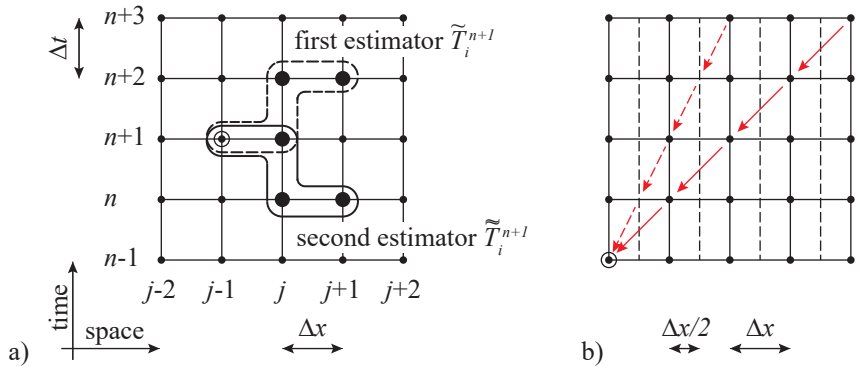

Fig. A.8 a) Finite difference scheme for inverse heat conduction problem (adapted from Raynaud and Bransier, 1986) b) the influence of the spatial discretisation to the information flow.

A.2.2 General considerations in the frequency domain

A.2.2.1 Signal propagation velocity

Deriving the phase shift ϕ (Eq. (2.44)) to the direction x leads to a change of the phase shift in space:

$$\frac{d\phi}{dx} = \sqrt{\frac{\omega}{2a}} \tag{A.23}$$

Setting the angular velocity $\omega = d\phi/dt$ into Eq. (A.23) leads to the propagation velocity v_{ts} of the thermal signal:

$$v_{ts} = \frac{dx}{dt} = \sqrt{2a\,\omega} \tag{A.24}$$

Eq. (A.24) shows that the propagation velocity of the thermal signal rises with the square root of the product of $a\,\omega$. Since the thermal diffusivity of concrete does not vary much, it mainly depends on the angular frequency ω. Higher frequencies lead to a faster propagation velocity v_{ts}. Calculated values of v_{ts} for a range of frequencies and thermal diffusivities are given in Table A.1.

Table A.1 Propagation velocity v_{ts} of thermal signal in [m/d] for different frequencies ω and thermal diffusivities a

	$a = 0.10$ m^2/d	$a = 0.15$ m^2/d	$a = 0.20$ m^2/d
$\omega = 1 \cdot 2\pi/\text{a}$	0.0587	0.0718	0.0830
$\omega = 12 \cdot 2\pi/\text{a}$	0.203	0.249	0.287
$\omega = 52 \cdot 2\pi/\text{a}$	0.423	0.518	0.598
$\omega = 365 \cdot 2\pi/\text{a}$	1.12	1.37	1.59

A.2.2.2 Amplitude decay

Let us consider a semi-infinite space (Fig. A.9). Because of the diffusive nature of heat conduction, the amplitude of a signal decays with increasing depth x. Higher frequencies are damped within shorter distance x than lower ones (Fig. A.9). The influence of the thermal diffusivity increases with decreasing frequency. For yearly frequencies, 15 - 20 m away from the boundary, only 1% of the frequency measured at the boundary is recognisable. For a yearly amplitude of 20°C, this expresses to 0.2°C, what is in the order of magnitude of the measurement accuracy. Thus, the yearly thermal variation cannot be measured in dams with a thickness L greater than 20 - 30 m. In addition, daily frequencies are recognisable until 1 m and weekly ones until around 2.7 m inside the concrete. Table A.2 shows within which distances x the amplitude decays to 10, 5 and 1% of its original value at the boundary for $a = 0.15$ m^2/d.

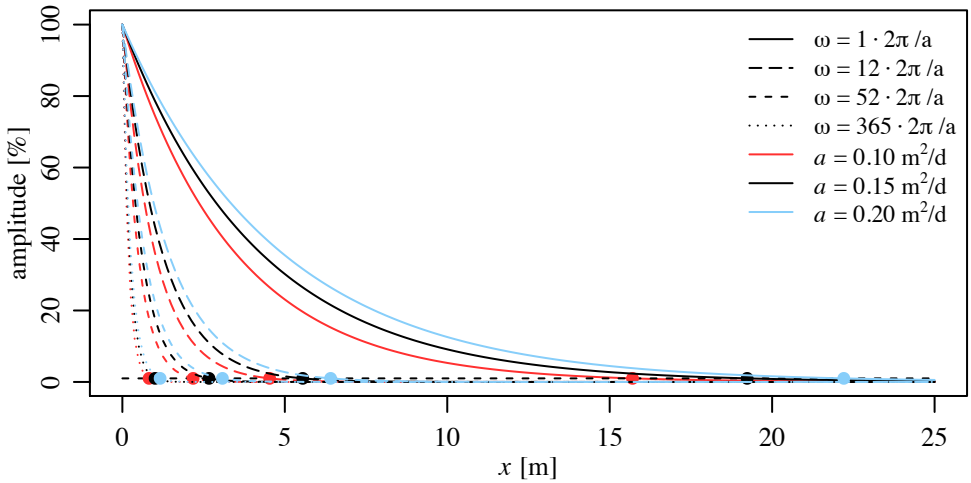

Fig. A.9 Amplitude decay of thermal signals in function of distance to the boundary x for different frequencies ω and thermal diffusivities a

Table A.2 Amplitude decay for thermal signals to values of 10, 5 and 1% of their original values for different frequencies ω and $a = 0.15$ m^2/d.

	10%	5%	1%
$\omega = 1 \cdot 2\pi/\text{a}$	9.62	12.51	19.23
$\omega = 12 \cdot 2\pi/\text{a}$	2.78	3.61	5.55
$\omega = 52 \cdot 2\pi/\text{a}$	1.33	1.73	2.67
$\omega = 365 \cdot 2\pi/\text{a}$	0.50	0.65	1.01

A.3 Statistics

A.3.1 Model adequacy checking in MLR

A.3.1.1 Scaling the residuals

The residuals can be standardised by the residual standard error *RSE*:

$$d_i = \frac{e_i}{RSE}, \quad i = 1,2,\ldots,n \tag{A.25}$$

This so called standardised residuals d have zero mean and approximately unit variance. Thus, large standardised residuals ($d_i > 3$) indicate potential outliers. There are also the so called studentised residuals that account for the correct standard deviation of the residuals by using the properties of the hat matrix $\mathbf{H}$ (for details see Montgomery *et al.*, 2012).

$$r_i = \frac{e_i}{RSE\sqrt{1-h_{ii}}} \quad i = 1,2,\ldots,n \tag{A.26}$$

where h_{ii} are the diagonal element of the hat matrix $\mathbf{H} = \mathbf{X}(\mathbf{X}'\mathbf{X})^{-1}\mathbf{X}'y$. The studentised residuals have unite variance $\mathrm{Var}(r_i) = 1$. For large datasets, standardised and studentised residuals are equivalent.

A.3.1.2 Tukey-Anscombe-plot

A plot of the residuals against the fitted values, called Tukey-Anscombe-plot, is useful to detect if (i) the expected value of the residuals is zero ($E(\varepsilon_i) = 0$), (ii) the variance is constant and (iii) if there are nonlinear effects that are not considered in the model. The residuals can be used in scaled or unscaled form. Fig. A.10 shows typical patterns for Tukey-Anscombe-plots. In a), the expected value of the residuals $E(\varepsilon_i)$ does not systematically deviate from 0 and the variance is constant along the fitted values $\hat{y}$. In b) and in c), $E(\varepsilon_i)$ is constant but the variance is not constant. In d), $E(\varepsilon_i) \neq 0$ due to a nonlinear pattern (Montgomery *et al.*, 2012).

In the case of deviations, the model must be adjusted since it contains systematic errors and some general assumptions of the least squares are violated. This can be done by a transformation of the predictor- or the response variables. In the case on nonlinearities, adding more predictor variables, e.g. higher order terms might be helpful (Dettling, 2015; Montgomery *et al.*, 2012).

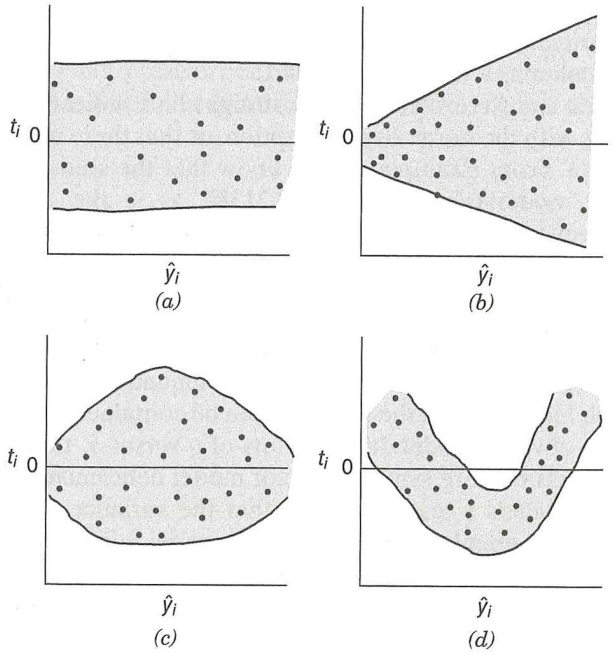

Fig. A.10 Patterns for Tukey-Anscombe-plots a) satisfactory; b) funnel, not constant variance; c) double bow, not constant variance; d) nonlinear (Montgomery *et al.*, 2012).

In Fig. A.11, the Tukey-Anscombe-plots for the standardised residuals of SLR and MLR drainage flow example are shown. According to Dettling (2015), a deviation of $E(\varepsilon_i) = 0$ can be checked by adding LOESS a smoother to the plot. To check if a deviation is systematically or not, Dettling (2015) suggests to a resampling approach. The fitted values are kept as they are but assigned to new residuals r_i^*. This is done by sampling with replacement of the residuals r_i. Afterwards a LOESS smoother is applied as well and added to the plot. By doing this several times, e.g. 100, it gets visible in which range a random deviation of the smoother can be accepted. This means, if the red line of the smoother of the original data lies outside of the range of the smoother of the resampling approach, a systematic deviation seems to be present. Regarding the SLR example (Fig. A.11a), there is a clear systematic deviation visible. For low- and high drainage flows, the residuals are too low and for medium drainage flows they are too large. In the MLR model (Fig. A.11b) seems to be a slight systematic deviation for the largest drainage flows.

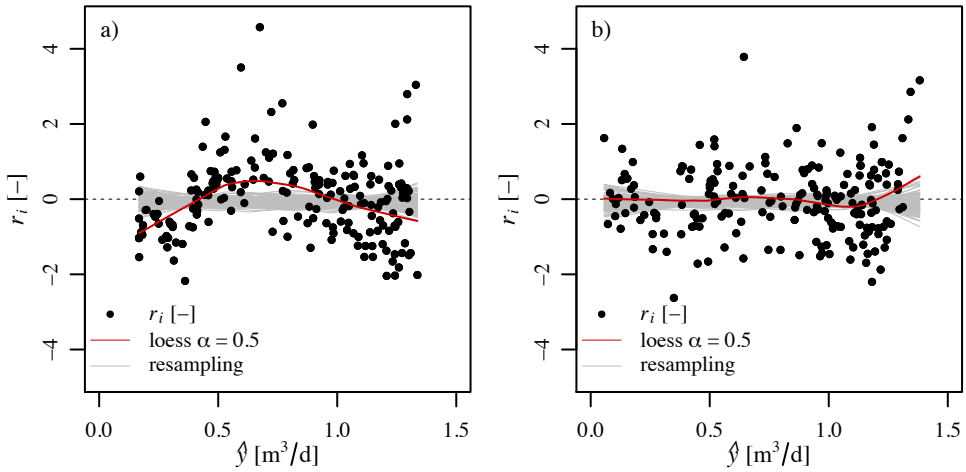

Fig. A.11 Tukey-Anscombe-plots for the drainage flow example a) SLR model; b) MLR model.

A.3.1.3 Partial residuals plot

A partial residuals plot can be used to study if the relationship of individual predictors variables x_j to the response is specified correctly (Montgomery *et al.*, 2012). A direct plot of x_j to the response can be deceiving since in an MLR model all other regressor variables have an effect to the response as well. Thus, a plot which shows the relation between x_j and y if the other variables are present is needed (Dettling, 2015).

A partial residuals plot is created by plotting the residuals of the regression model of all variables except x_j to the response versus the residuals of a regression model of all other variables to x_j. A linear relationship results if x_j enters the model linearly. On the other hand, if a nonlinear relationship results, a variable transformation might be needed (Montgomery *et al.*, 2012). Thus, this plot is similar in interpretation as a Tukey-Anscombe-plot. More details about partial residuals plots can be found in Montgomery *et al.* (2012).

A.3.1.4 Scale-location-plot

The scale-location-plot is similar to the Tukey-Anscombe-plot, but it is a bit simpler to detect non-constant variance (Dettling, 2015). The square root of the absolute values of the residuals $\sqrt{|r_i|}$ are plotted versus the fitted values $\hat{y}$. Due to the absolute values, a dependency of the residual magnitude to the fitted values can be detected easier. Consequently, for the case of a constant variance, a horizontal line is expected. To detect systematic deviations, the same resampling approach as for the Tukey-Anscombe-plot can be used.

Fig. A.12 shows the scale-location plot for the drainage flow examples. The SLR model (Fig. A.11a) as also the MLR model (Fig. A.11b) show a more or less constant variance except for the largest drainage flows.

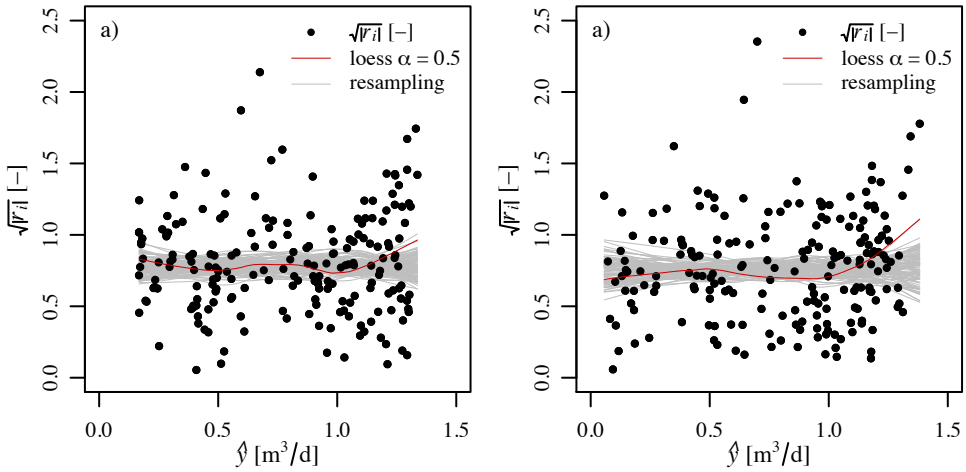

Fig. A.12 Scale-location-plots for the drainage flow example a) SLR model; b) MLR model.

A.3.1.5 Normal probability plot

With the normal probability plot (also quantile-quantile plot or Q-Q-plot), the assumption of the normal (Gaussian) distribution of the residuals can be checked. The normal probability plot is made by plotting the ordered studentised residuals (sample quantiles) versus the theoretical quantiles of the standard normal distribution. Fig. A.13 shows different patterns for Q-Q-plots. In a), the points lie on a straight line and therefore the sample quantiles represent the theoretical quantiles of the normal distribution well. In b), the Q-Q plots indicates a light tailed distribution and in c) a heavy-tailed distribution is recognisable. The patterns in Fig. A.13d) and Fig. A.13e) represent distributions with positive and negative skew.

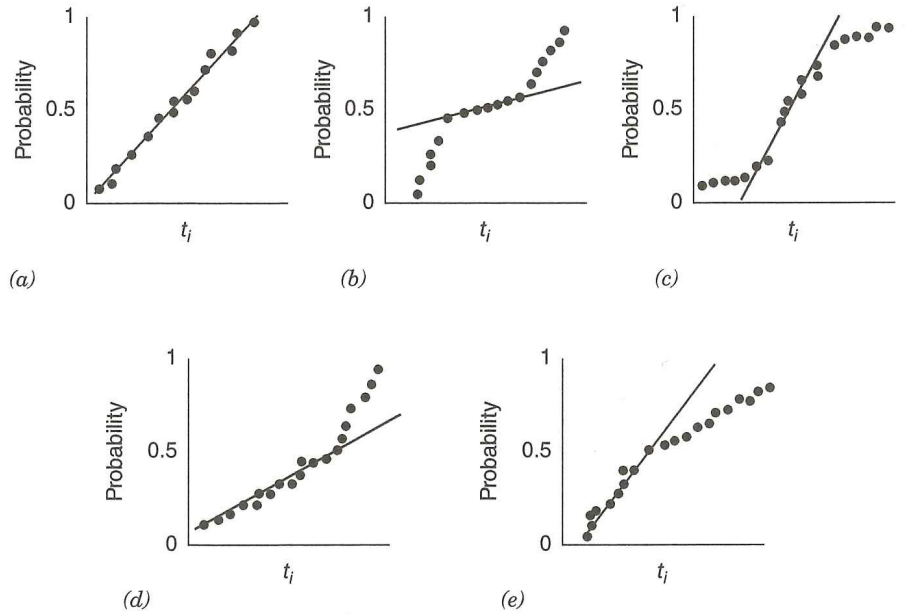

Fig. A.13 Patterns for Normal-probability-plots (Q-Q-plots) a) ideal; b) light tailed; c) heavy-tailed; d) positive skew; e) negative skew (Montgomery *et al.*, 2012).

The assumption of a normal distribution is the basis for the hypothesis tests (see section 2.4.1.5). In addition, the least squares estimator is insufficient under non-Gaussian distributions, especially for skewed distributions where systematic errors result. Short- and heavy tailed distribution cause less problems as long as they are symmetrically distributed. The problem of heavy tailed distributions is that they often cause outliers that influence the coefficients too much. In this case, other estimators, such as robust regression can be considered (Dettling, 2015; Montgomery *et al.*, 2012).

In Fig. A.14a), the Q-Q-plot for the SLR drainage flow example is given. As a help to define to which extend random deviations can be expected, the same resampling approach as for the Tukey-Anscombe-plot was applied. The distribution seems to be slightly positive skewed since more data points than usual are between the 3rd and the 4th sample quantile. Fig. A.14b) shows the distribution of the studentised residuals (grey bars) and the sample quantiles for the normal distribution (red line). This plot also visualises the deviation of the normal distribution and helps to understand the idea behind the Q-Q-plot. For the MLR example (Fig. A.14c)), the skew is weaker, what can also be verified in Fig. A.14d).

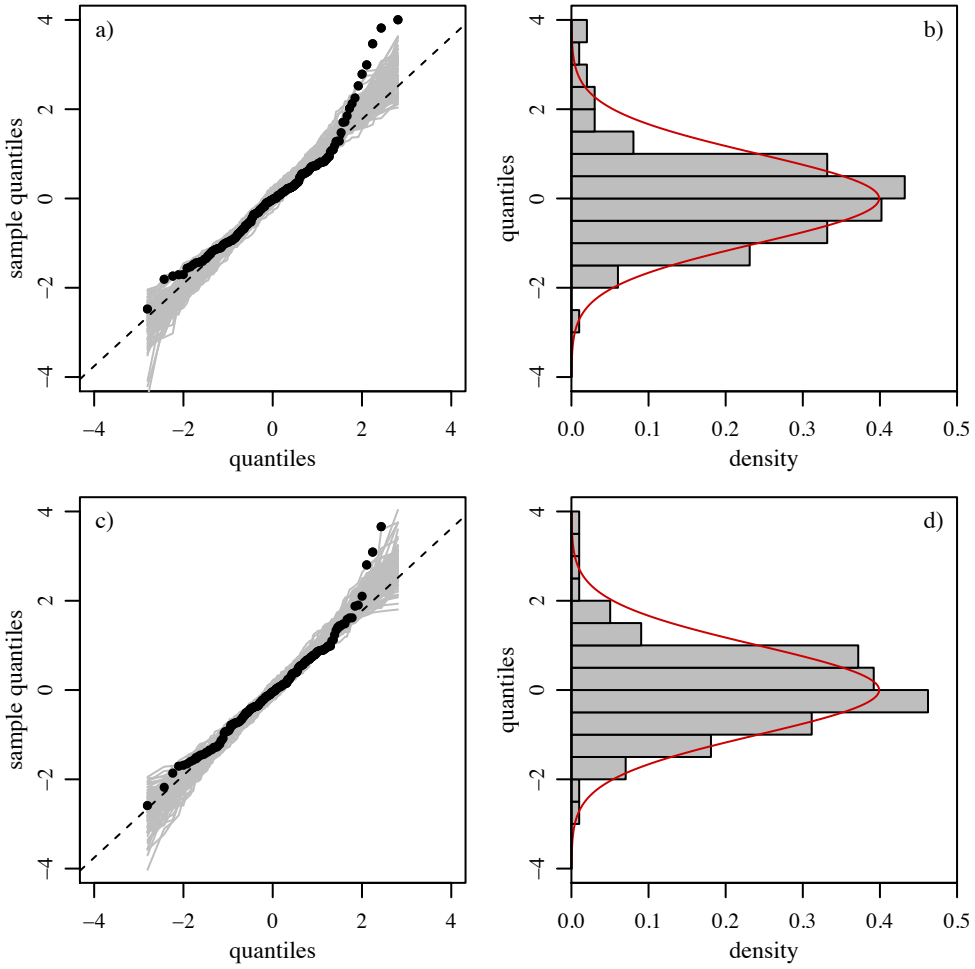

Fig. A.14 a) Q-Q-plot and b) density distribution plot for the SLR drainage flow example; c) Q-Q-plot and d) density distribution plot for the MLR drainage flow example.

A.3.1.6 Cooks's distance

To show the influence of single data points, three virtual data points (A, B, C) were added the scatterplot of the SLR example in Fig. A.15. The centroid of the original data ($\bar{x}$,$\bar{y}$) is marked with a grey dashed line. Point A has an x-value that is sufficiently larger than all the other points on the x-axis. Such points are called leverage points. Since the point lies on the straight-line of the fitted equation, it does not influence the result. On the other hand, point B influences the result since it deviates significantly from the straight-line relationship of the other points. The fitted model point B included results in the straight-line relationship that is shown by the green dashed line. Such points are called influential leverage points. Furthermore, point C also significantly differs from the straight line relationship but is has not much influence to the results since it is close to the centroid and has no leverage.

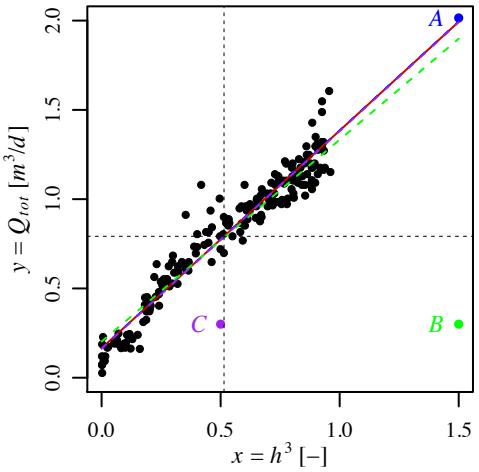

Fig. A.15 Scatterplot of SLR drainage flow example. Three points (A, B, C) were added to show the influence of single data points to the regression model.

The influence of a single data point to the regression model depends on the distance to the centroid $\bar{x}$, the its residual e_i and the number of observations n. The more observations that are available, the less is the influence of one single point. With the Cook's distance, the influence of a single data point to the regression model can be measured. It sets the influence of leverage in relation to the standardised residuals and the number of coefficients in the model:

$$D_i = \frac{h_{ii}}{1-h_{ii}} \frac{d_i^2}{p} \quad i = 1,2,\ldots,n \tag{A.27}$$

Measurement points with $D_i > 0.5 \div 1.0$ are influential points and should be treated further (Dettling, 2015; Montgomery *et al.*, 2012). This means the model might be changed by a transformation or that there are outliers that need a special treatment as e.g. robust regression (for details see Montgomery *et al.* (2012)). The points added to the SLR example have a Cook's distance of $D_A = 0$, $D_B = 3.6$, $D_C = 0.06$.

A.3.2 Visual detection of autocorrelation

The visual detection is straightforward but needs some experience. The values ρ of the ACF for k lags back are defined by

$$\rho_k = \frac{\mathrm{Cov}(e_t, e_{t-k})}{\sqrt{\mathrm{Var}(e_t)\,\mathrm{Var}(e_{t-k})}} \tag{A.28}$$

This is a dimensionless measure for the correlation between two lags. The perfect correlation is expressed by 1, 0 indicates that there is no correlation and -1 indicates a perfect negative correlation. In Fig. A.16a the ACF-plot for the drainage flow MLR example is

given. In ACF-plots, it is common to plot lag 0, which is always 1 (correlation by itself). The plot shows an exponentially decaying pattern, which is typically for autoregressive (AR) models (Dettling, 2014). The values are $\rho_1 = 0.42$ and $\rho_2 = 0.23$. The dashed line shows a 95% confidence band. Values outside this band indicate autocorrelation. With the ACF-plot, it can be seen that the errors are correlated two lags back in the regarded example.

It must be kept in mind that the residuals which depend on the residuals 1 lag back also depend on the residuals two lags back since the residuals one lag back depend on them. This can be explained by the theoretical autocorrelation function (for details see Cryer and Chan (2008)). To measure the direct influence on the residuals two lags back, the partial autocorrelation can be calculated by

$$\pi_k = \mathrm{Cor}(e_t, e_{t-k}) \tag{A.29}$$

For the MLR example, the PACF is shown in Fig. A.16b. It is recognisable that the influence of the correlation goes one lag back. With $\pi_1 = 0.42$ it follows that the error of the current time step depends on the last error. This can be expressed with an AR(1) model that writes as

$$e_t = 0.42\, e_{t-1} + E_t, \tag{A.30}$$

where the residuals at time t contains depends to 42% on the residuals of the last time step $t-1$ and a random ternmE_t. The theory behind these models is well described in Cryer and Chan (2008) and Dettling (2014). Here, the focus lies on detecting such correlations. This can be done visually by looking at the ACF- and PACF-plot. If the spikes in the plot are outside the 95% confidence band a correlation is present. It should be remembered that in a 95% confidence band, 5% of the values are expected to be outside of it. As a comparison, in Fig. A.17, the ACF- and PACF-plot are shown for uncorrelated data.

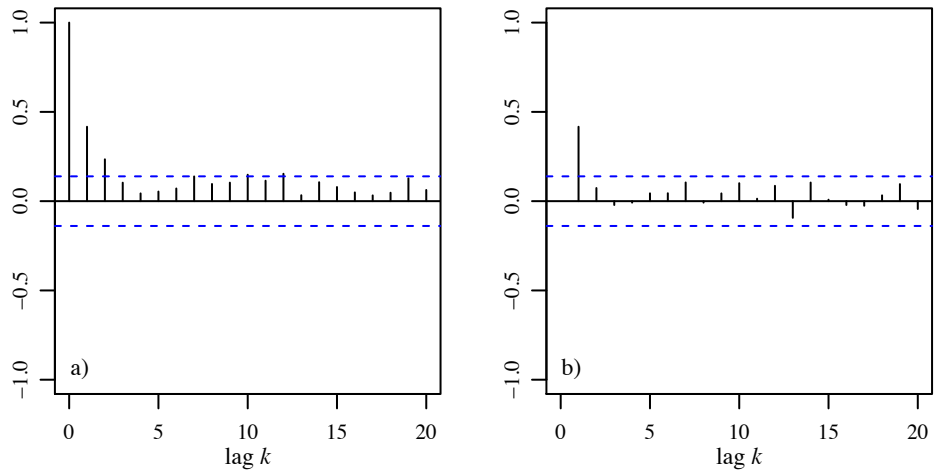

Fig. A.16 a) ACF-plot and b) PACF-plot for MLR example.

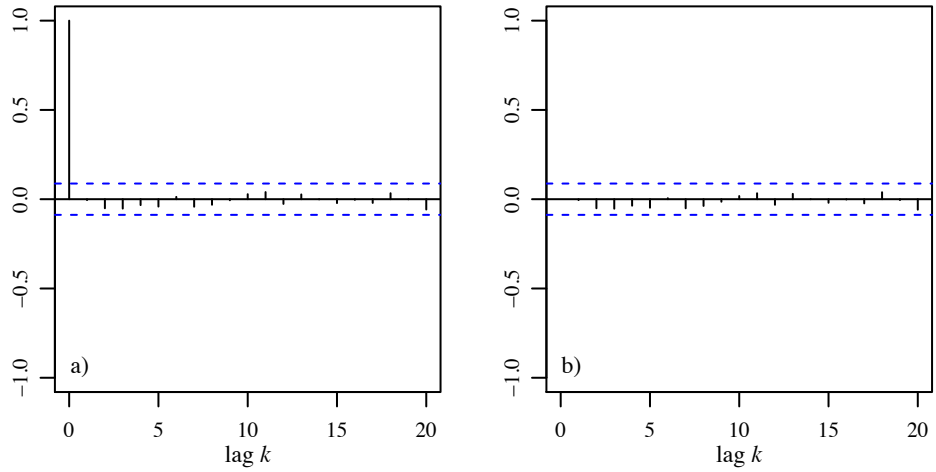

Fig. A.17 a) ACF-plot and b) PACF-plot as it is expected for uncorrelated data.

Further, autocorrelation can also be detected by formal tests. There is the Durbin-Watson test, which allows to detect first order (AR(1)) autocorrelation. This test is well described in Montgomery *et al.* (2012). In addition, there is also the Ljung-Box test, which is described in Cryer and Chan (2008). This test allows to detect autocorrelation up to a certain order k.

A.4 Dam behaviour analysis models

In the following, in addition to Section 2.5.4.2, more dam behaviour analysis models for monitoring the displacement of concrete dams are given.

One of the first publications in the field of dam behaviour analysis comes from Rocha *et al.* (1958). The developed model allows to predict the crest displacement as the sum of a function of the influence of the hydrostatic pressure δ_h, the mean temperature T_m and the temperature difference T_d on different levels:

$$P(h,T) = \delta_h + \sum \beta_i T_{m,i} + \sum \beta_j T_{d,j} \tag{A.31}$$

To solve Eq. (A.31), a two-step procedure was suggested: In the first step, Eq. (A.31) was applied to different temperature conditions measured for the same water level. The influence coefficients β and therefore the influence of the temperature was determined for one level only. In the second step, Eq. (A.31) was used to determine the function δ_h by using different water levels. In the presented case study, 11 equations were used to determine the effect of the temperature and 4 equations for the effect of the water level. The idea behind this model was the same as for common regression models, but the proposed solution procedure was different.

Another hybrid model was developed by Bonaldi *et al.* (1977). In this model, the displacement is considered to be a sum of the influences of the water level, the temperature and the time, whereas the first two are considered hybrid and the last statistically. The deterministic displacement of the water level can be calculated by

$$\delta_h \quad = \quad \delta_{h,0} + \frac{R}{R_i}(\delta_{h,i} - \delta_{h,0}), \tag{A.32}$$

where $\delta_{h,0}$ is the displacement for a rigid foundation ($R = 0$), $\delta_{h,i}$ the displacement for an elastic foundation with a ratio $R = E_c/E_r$ between the elastic modulus for concrete E_c and for rock E_r and R_i is the ratio for an arbitrary chosen stiffness for the calculation of $\delta_{h,i}$. The displacement for another ratio R can be calculated by a linear interpolation (Swiss Committee on Dams, 2003). In the model equation, the ratio R/R_i is replaced by a regression coefficient and fitted. If only a rigid foundation is considered, the second term of Eq. (A.32) can be neglected. The deterministic displacement of the temperature δ_T Eq. (A.33) was suggested to be a sum of measured temperatures and the time derivative of smoothed temperatures, multiplied by influence coefficients. Bonaldi *et al.* (1977) suggested to derive the influence functions by the use of a FE-analysis under the use of an assumed thermal expansion $\alpha_{c,0}$.

$$\delta_T = \sum \left(b_i T_i + c_i \frac{\mathrm{d}T_{i,s}}{\mathrm{d}t} \right) \tag{A.33}$$

The irreversible displacement was considered to determine as a sum of exponential functions:

$$\delta_t = \sum d_i \exp(m_i(t - t_0)) \tag{A.34}$$

where d_i, m_i and t_0 are adjustable constants. The sum of the described influences leads to Eq. (A.35). This equation is linear, except for the coefficients, d_i, m_i and t_0. Thus, Bonaldi *et al.* (1977) advised to use an initial assumption for these constants. As in the model of Schnitter (1969), β_1, β_2 and β_3 correspond to a correction of physical properties.

$$P(h,T,t) = \beta_0 + \beta_1\, \delta_{w,0}(h) + \beta_2(\delta_{w,i}(h) - \delta_{w,0}(h)) + \beta_3\, \delta_T + \beta_4\, \delta_t \tag{A.35}$$

Breitenstein *et al.* (1985) published a slightly modified form of Eq. (2.97) of Widmann (1967). The main difference is the shape of Eq. (A.36) for the irreversible effects. In addition, they suggest using periods of different length for thin and thick dams to consider the delayed effects. The irreversible effects depend on three adjustable constants c_1, c_2 and c_3 that can be optimised outside the common MLR procedure.

$$\begin{aligned} P(h,S,T,t) = {} & \beta_0 + \beta_1\, h + \beta_2\, h^2 + \beta_3\, h^3 + \beta_4\, \Delta h_t \\ & + \beta_5\, \sin(S) + \beta_6\, \cos(S) + \beta_7\, \sin(2S) + \beta_8\, \cos(2S) \\ & + \beta_9\, \Delta T_{t,i} + \beta_{10}\, \Delta T_{t,j} + \beta_{11}\, \Delta T_{t,k} \\ & + \beta_{12}\, t + \beta_{13}\, (\ln(1 + t/c_1))^{1/c_2} + \beta_{14}\, (1 - \exp(-t/c_3)) \end{aligned} \tag{A.36}$$

Bossoney (1985) proposed to consider the derivative of the water level h respecting the time t to consider the delayed influence of the water level.

Fanelli *et al.* (2000) propose the idea to use cubic spline functions to represent the irreversible behaviour. They present the idea but do not apply it on a case study. In addition, they propose to show the drift in the phase plane, which is an illustrative graphical tool to analyse drifts.

For the special case of hollow buttress gravity dams, De Sortis and Paoliani (2007) developed a hybrid model. Dimensionless influence functions were created by the use of a FE-model. The influence function of the water level was compared to the analytical solution of Marcello and Spagnoletti (1960). De Sortis and Paoliani (2007) use the air temperature and the water temperature as boundary conditions for their thermal analysis. Hence, no inner temperature measurements are needed when applying this model.

The same approach for T_m and T_d was used in Léger and Seydou (2009). Instead of a statistical model equation, Léger and Seydou (2009) used a hybrid model based on a deterministic beam model (Fig. A.18) for gravity dams. The structure was divided in 11 beams with different inertia and the model was implemented in the software *SAP2000 (Wilson and Habibullah, 2003).*

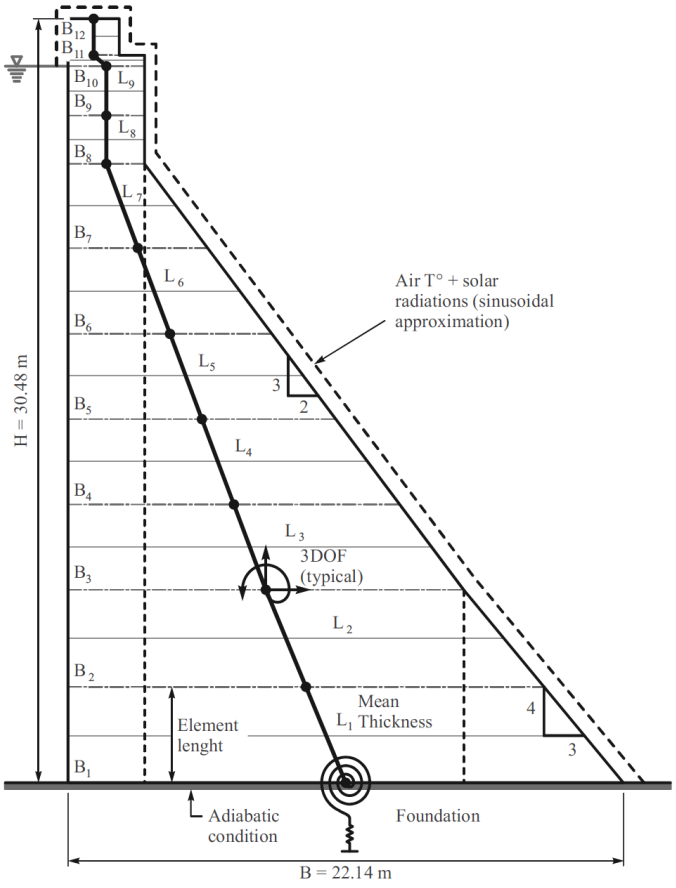

Fig. A.18 Deterministic beam model of gravity dam. The dam was divided in 11 sections of different thicknesses (Léger and Seydou, 2009).

Perner and Obernhuber (2009) present a hybrid model for arch dams where they use the approach of Obernhuber and Perner (2005) and Weber *et al.* (2010) to calculate T_m and T_d. They assume that the displacement is the sum of the reversible instantaneous hydrostatic deformation $\delta_{w,i}$, the deferred hydrostatic deformation $\delta_{w,d}$, the reversible temperature deformation δ_T and the irreversible displacement due to the time δ_t:

$$P(h,T,t) = \beta_0 + \beta_1\,\delta_{h,i} + \beta_2\delta_{h,d} + \beta_3\,\delta_T + \beta_4\,\delta_t \tag{A.37}$$

For the reversible instantaneous hydrostatic deformation $\delta_{w,i}$, the results of a FE-model were taken and approximated with a polynomial function 7^{th} order. The deferred hydrostatic deformation $\delta_{w,d}$ was considered by the following convolution integral based on the creep function $\phi(t) = \phi_\infty(1-\exp(-\eta\,t))$:

$$\delta_{h,d} = \eta\,\phi_\infty \int_0^t \exp(-\eta(t-\tau))\delta_{h,i}(\tau)\mathrm{d}\tau, \tag{A.38}$$

where τ is the control variable, η is a constant that is set to 0.01 on the basis of laboratory tests and ϕ_∞ is the creep number that can be determined by the regression analysis. Due to the fact that $\delta_{h,i}$ is part of Eq. (A.38), the whole procedure is iterative. To calculate the influence of the temperature, a thermal analysis with the approach of Obernhuber and Perner (2005) and also Weber *et al.* (2010), which is described in Section 2.3.4.2, needs to be done first. Then, they calculate the displacement on the basis of the thermo-elastic reciprocal theorem (see Section 2.2.2.3). With the assumption that T_m and T_d do not vary along the arches, the displacement at crest level due to temperature can be calculated as follows:

$$\delta_T = \int_0^H M(z)\,T_m(z,t)\,\mathrm{d}z + \int_0^H D(z)\,T_d(z,t)\,\mathrm{d}z \tag{A.39}$$

The over the level z varying influence functions $M(z)$ and $D(z)$ are determined by a FE-analysis. The irreversible displacement δ_t is considered by Eq. (A.40). The constant κ, what is defining the bending of the function, was defined to $1/3448/d^{-1}$ in pre-studies.

$$\delta_t = 1-\exp(-\kappa t) \tag{A.40}$$

A.5 Reference dams for investigation

A.5.1 Gravity dam G1

The gravity dam G1 was built in the 1960s and features a height of 68 m in the central block (Fig. A.19). The downstream surface has an average inclination of 1:0.75 and the north-east oriented upstream surface is vertical. To save concrete, hollows were placed inside the dam. Since they are small, the dam is treated as a common gravity dam in this thesis. The reservoir is used as a regulating reservoir for pumped storage operation. Data of the displacement, the water level and several temperature measurements from 1999 until 2012 were provided by the operator. The readings were taken manually once a month until 2006, since then they are taken bi-weekly. A pendulum and an inverted pendulum is used to measure the displacement on five levels. In addition, 18 concrete temperatures and three water temperatures are measured on three different levels (Fig. A.19).

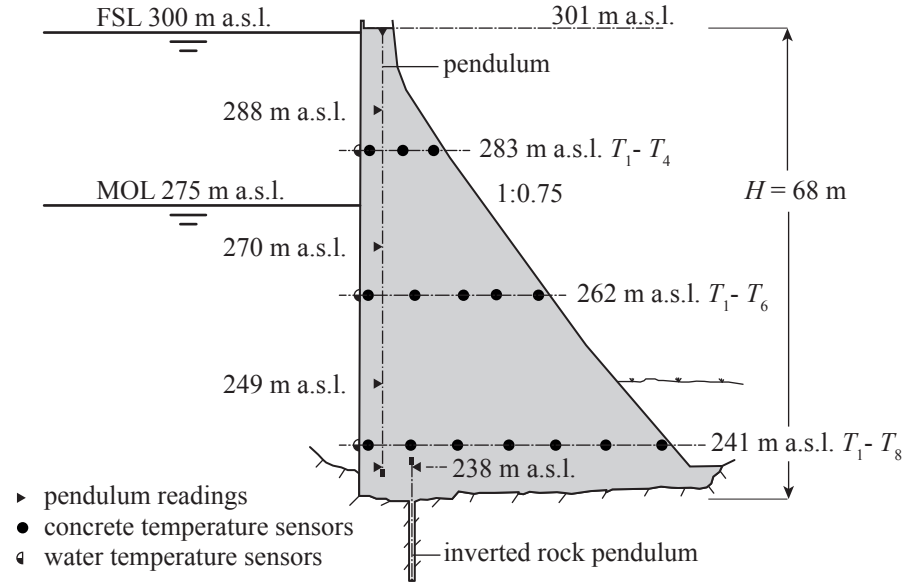

Fig. A.19 Cross section of gravity dam G1 in the main section.

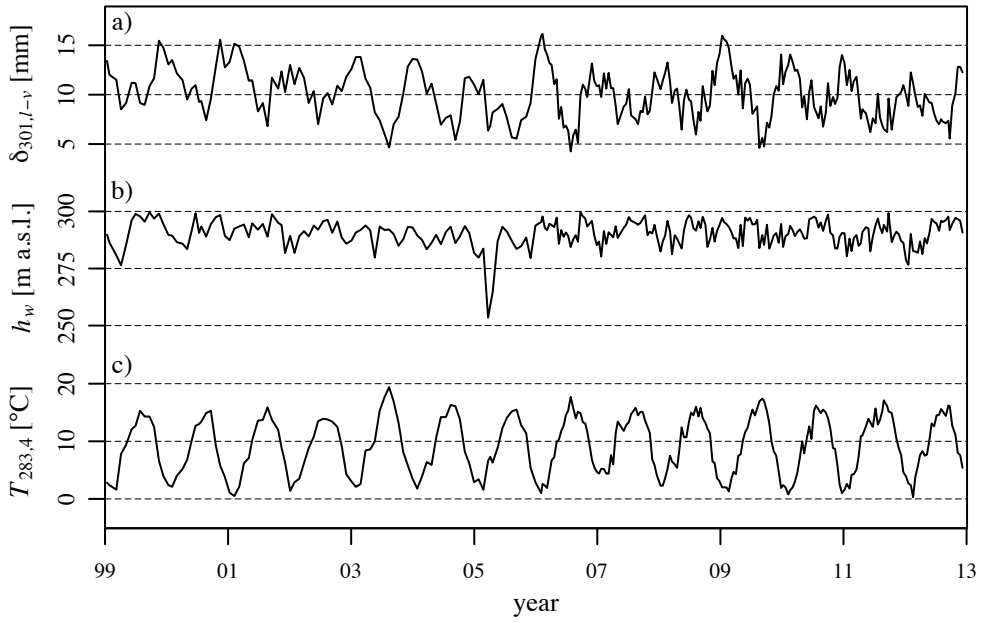

Fig. A.20 Time series of gravity dam G1 a) displacement $\delta_{301,l-v}$ in lake-valley direction at crest level, b) water level h_w and c) temperature $T_{283,4}$ 1.19 m away from the downstream boundary.

In Fig. A.20, the time series of the pendulum displacement at crest level in lake-valley direction, the water level and one concrete temperature on the downstream side are shown. The change of the measurement frequency from monthly to bi-weekly in 2006 is clearly recognisable. The displacement follows a seasonal pattern and does not show a trend that can be recognised at first sight. Due to the operation conditions, the reservoir level does not show a seasonal pattern and is almost always on a high level (> 280 m a.s.l.). In 2005, there was a reservoir lowering. The effect of this is not visible in the measured displacement. The temperatures show a seasonal pattern. For example, $T_{283,4}$ is shown in Fig A.20c. Furthermore, the heat wave of 2003 is clearly observable.

A.5.2 Gravity dam G2

The gravity dam G2 was built in the 1950s. Block no. 5 that was used for the analysis (Fig. A.21) has a height of 78 m. The upstream surface is south-west oriented and has an inclination of 1:0.025. The inclination of the downstream surface is varying, in average it is 1:0.71. Besides a seasonal storage, the reservoir is used for pumped storage operation.

The operator provided manually recorded data with monthly time steps from 2000 - 2015. In Fig. A.22a) the time series of the pendulum displacement on 289 m a.s.l., which is 13 m below the crest level, is shown. The seasonal pattern becomes clearly recognisable, for the water level too (Fig. A.22b). The data show that the water level of the reservoir was lowered in late 2004. However, this is not visible in the time series of the displacement. Due to the monthly measurement frequency and the measurement distance of 2 m from

the surface, the progress of the temperature $T_{272,4}$ is very smooth since high frequencies of the temperature variation are filtered out.

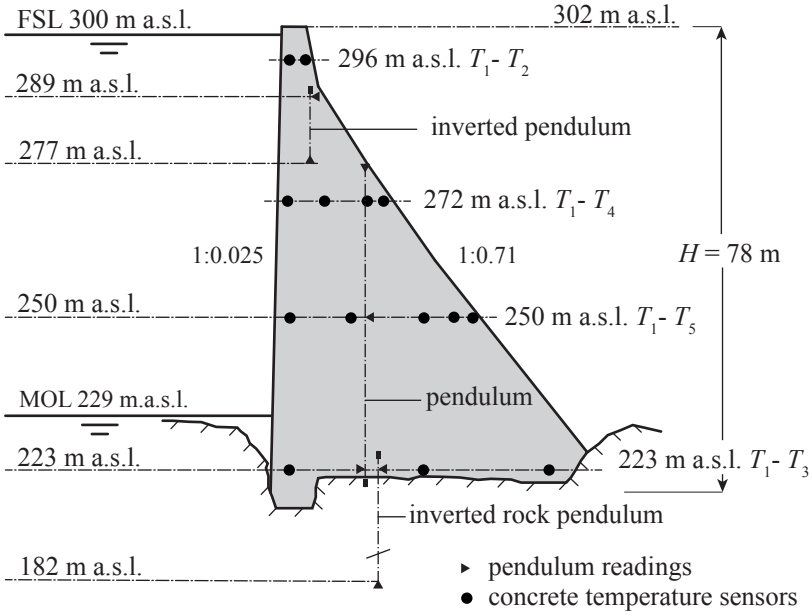

Fig. A.21 Cross section through block no. 5 of gravity dam G2.

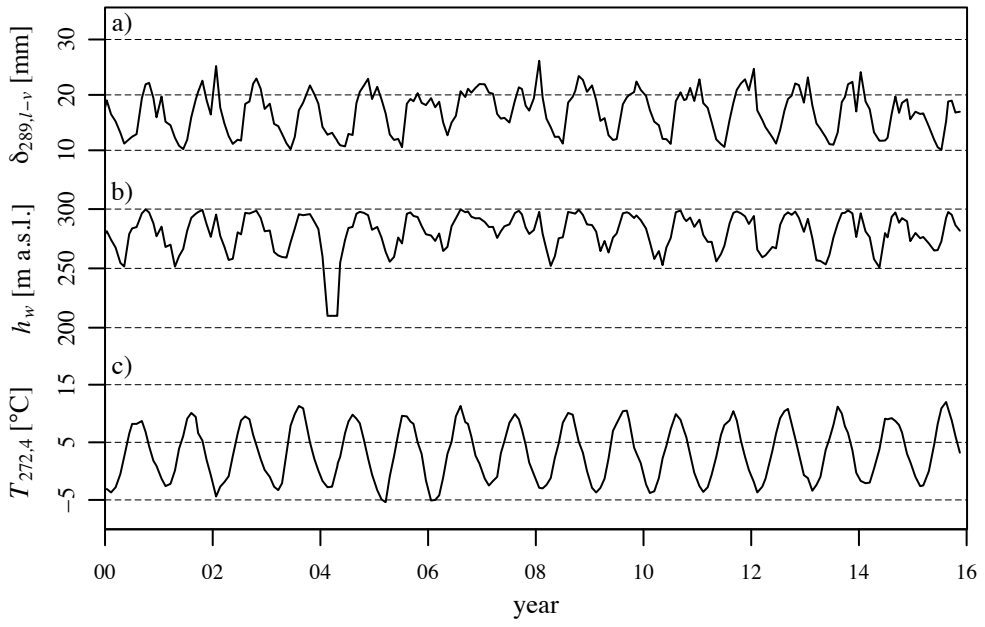

Fig. A.22 Measurement time series of gravity dam G2: a) displacement $\delta_{289.l-v}$ in lake-valley direction at 289 m a.s.l., b) water level, h_w c) temperature $T_{272,4}$ with a distance of 2 m from the downstream surface.

A.5.3 Arch dam A1

The 1980's built arch dam A1 has a height of 61 m and a crest length of 75 m. The positioning of the measurement equipment is shown in Fig. A.23. In the main section (pendulum line P1), the displacements are measured by the combination of a direct pendulum and an inverted rock pendulum on three levels in radial and tangential direction. In addition, a second direct pendulum (P2) is installed close to the orographic right abutment. The temperatures are recorded on four levels in the main section. There are 19 concrete temperature sensors and one water and air temperature sensor each. Time series from 1986 - 2014 are provided for this investigation. The measurement time steps were bi-weekly during the first 15 years of operation, then they were changed to monthly recordings. In addition, weekly measurements of the temperatures on 293 m a.s.l., the water level and the total displacement of pendulum P1 in radial direction were provided.

The reservoir is operated as daily storage with a water level always closed to the full supply level (Fig. A.24). The minimum operation level was never reached during the measurement period. Thus, the temperature change has the dominating effect on the displacement. Moreover, there is a clear trend into the upstream direction when looking at the raw data of P1 at crest level in radial direction (Fig. A.24a).

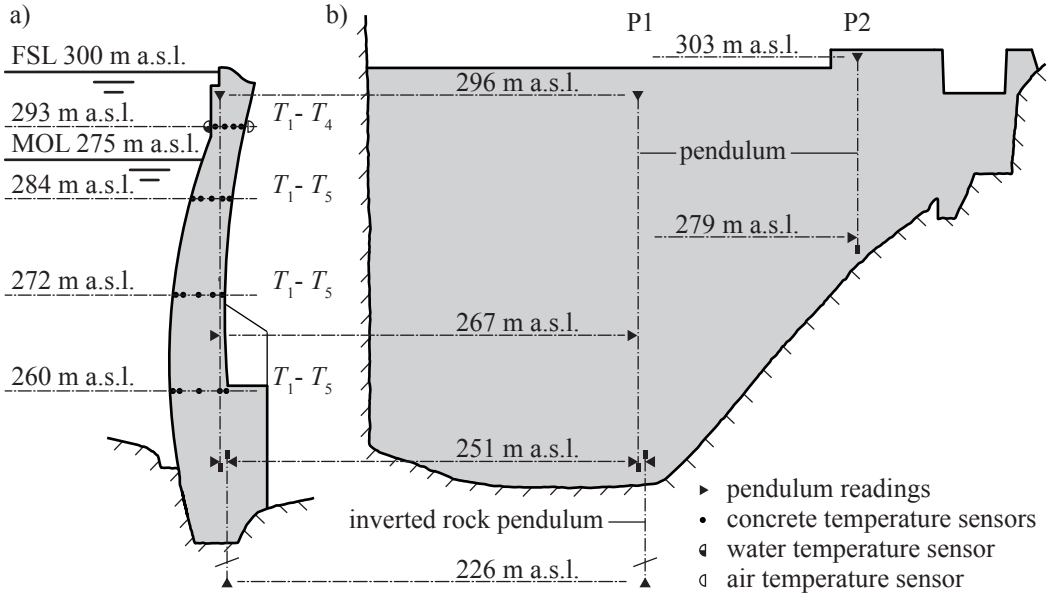

Fig. A.23 Measurement set up of arch dam A1 a) cross section of main section b) front view from upstream side.

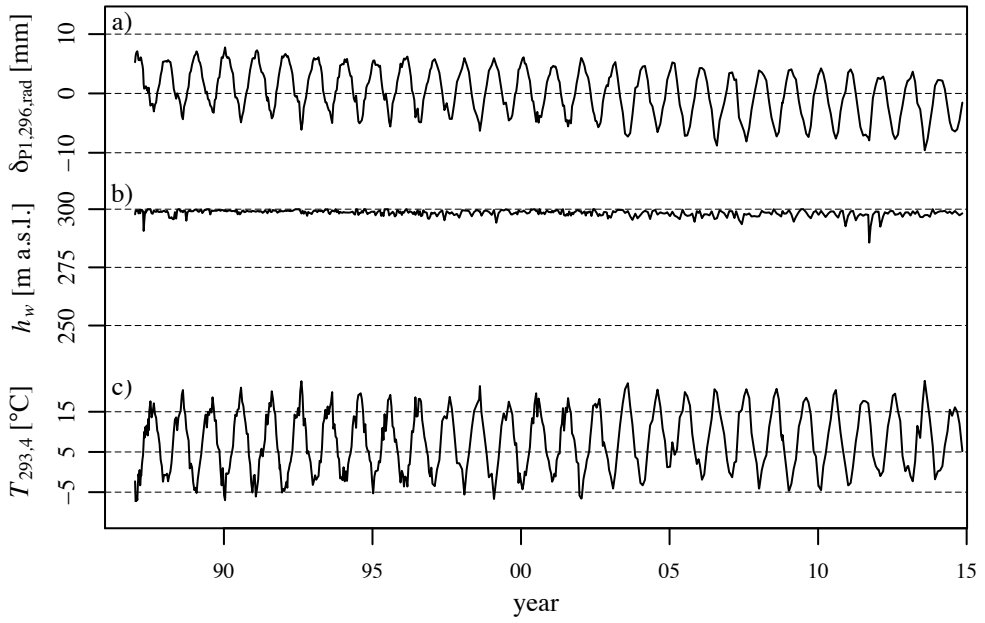

Fig. A.24 Time series of arch dam A1: a) displacement $\delta_{P1,296.rad}$ in radial direction at crest level (296 m a.s.l.), b) water level h_w and c) temperature $T_{293,4}$ with a distance of 0.20 m to the downstream surface.

A.5.4 Arch dam A2

The double curved arch dam A2 has a height of 180 m in the main section and a crest length of 554 m. A data set from 1976 until today with monthly measurement readings was provided by the operator. The displacement is measured by three pendulum lines (PII, PIII and PV) on several levels in radial and tangential direction (Fig. A.25). There are several temperature sensors on five levels.

Arch dam A2 was built in the 1970s. Since 2009, construction works for a large pumped storage power plant where the reservoir of arch dam A2 is used as a lower basin are taking place. For this reason, the reservoir was emptied to a lower level that was usual in spring time only beforehand (Fig. A.26b). The effect of these reservoir lowerings can be recognised in the pendulum displacement. In Fig. A.26a, the radial displacement of PIII at crest level is exemplarily shown.

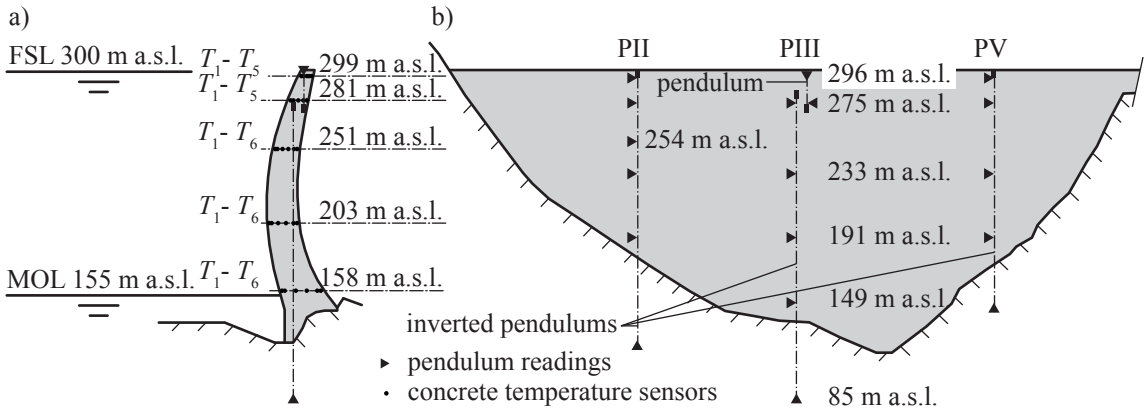

Fig. A.25 Measurement set up of arch dam A2: a) cross section of main section, b) front view from upstream side.

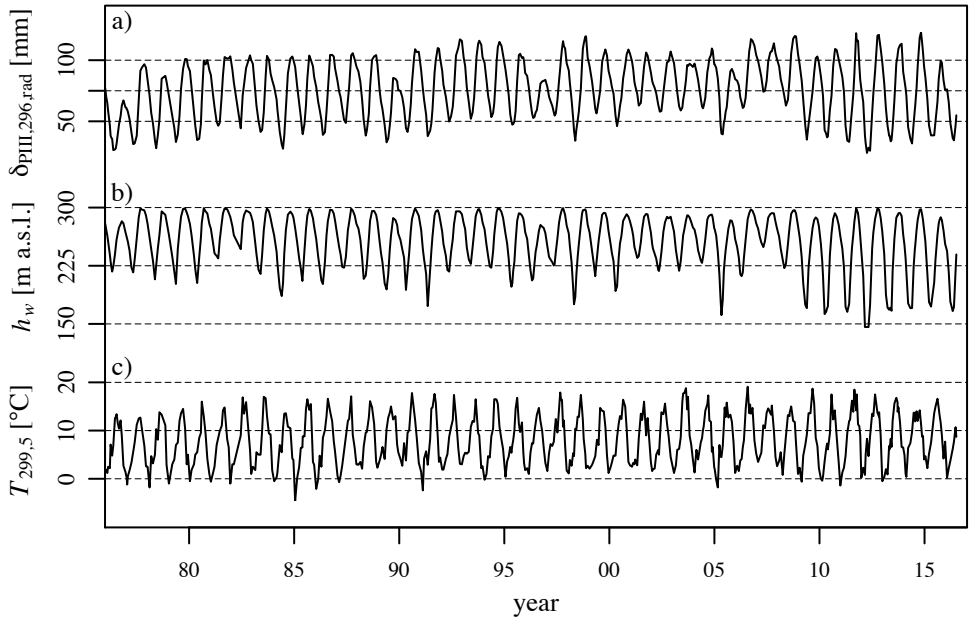

Fig. A.26 Time series of measurements of arch dam A2: a) displacement $\delta_{PIII,296.rad}$ in radial direction at crest level (296 m a.s.l.), b) water level h_w and c) temperature $T_{299,5}$ 0.50 m away from the downstream surface.

A.5.5 Arch dam A3

The arch dam A3 has a height of 111 m in the main section and a crest length of 320 m. The dam was built in the 1960s. The displacement is monitored by four pendulum lines with measurements in radial and tangential direction on several levels (Fig. A.27). All of them were provided by the operator. In Fig. A.28a the time series of pendulum P12 in radial direction at crest level is exemplary shown. A clear seasonal pattern can be recognised. In addition, the time series of the total drainage flow Q_{tot} measured at the bottom (Fig. A.28b), the water level (Fig. A.28c) and 12 temperature readings are provided. Nine

thermometers are placed in the concrete on three levels with three thermometers each. In addition, two water temperature (226 and 266 m a.s.l.) and one air temperature sensor are installed. All the measurements are taken 19 times per year with a time step between two and four weeks usually.

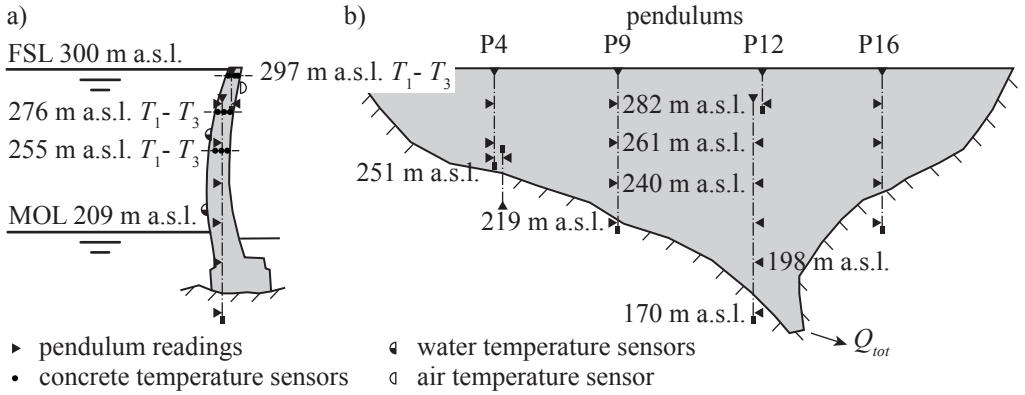

Fig. A.27 Measurement set up of arch dam A3: a) cross section of main section with pendulum line P12 and b) front view from upstream side.

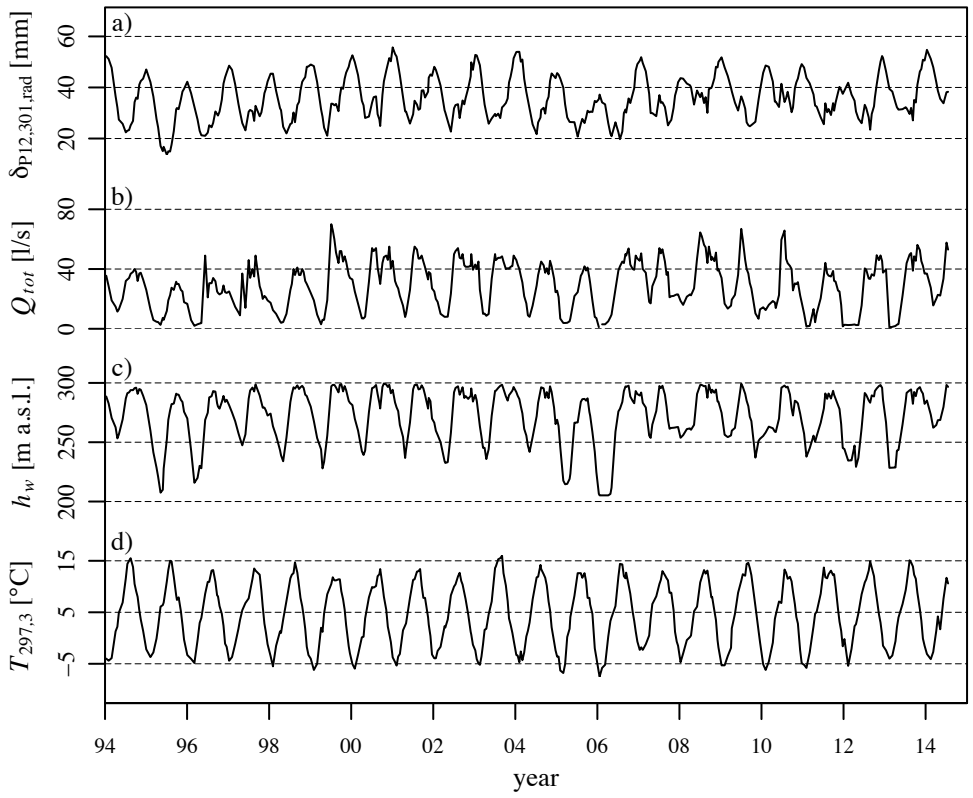

Fig. A.28 Measurement time series of arch dam A3: a) displacement $\delta_{P12,301.rad}$ in lake-valley direction at 301 m a.s.l., b) total drainage flow Q_{tot} at the dam toe, c) water level h_w and d) temperature $T_{299,3}$ with a distance of 0.88 m to the downstream surface.

A.5.6 Arch dam A4

The 1970's built arch dam A4 is 131 m high in the main section and it has a crest length of 725 m (Fig. A.29). The data set reaches over seven years from 1992 - 1998. Despite the short time span, many recordings are available since the measurements are taken daily. The provided data set comprises of a pendulum line measured displacement at crest level (Fig. A.30a), the water level (Fig. A.30b) and six time-series of temperature readings on two levels (Fig. A.30c).

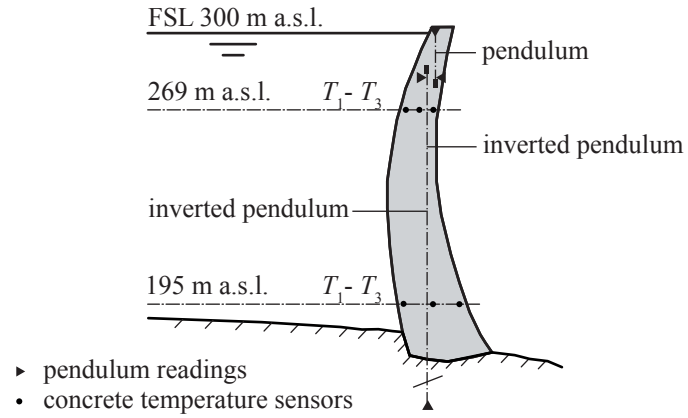

Fig. A.29 Cross section of arch dam A4.

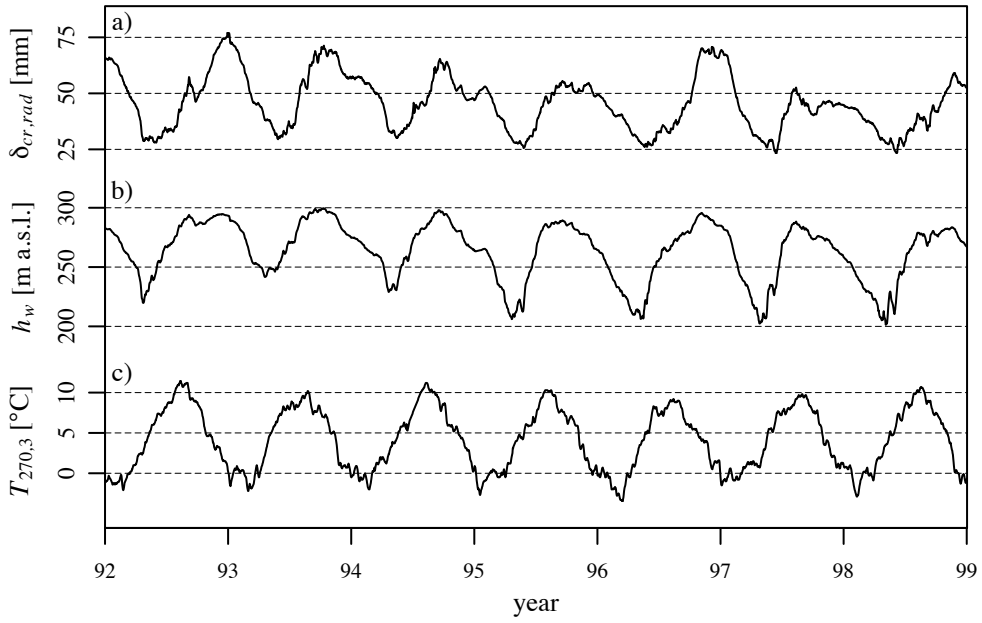

Fig. A.30 Time series of arch dam A4: a) displacement $\delta_{cr,rad}$ in lake-valley direction at crest level, b) water level h_w and c) temperature $T_{269,3}$ 1.5 m away from the downstream boundary.

A.5.7 Arch-gravity dam AG1

The as yearly storage reservoir operated arch-gravity dam AG1 was built in the 1950's. The height in the main section is 130 m and the crest length measures 363 m. The displacement of the dam is monitored by three pendulums (Fig. A.31) on several levels. Furthermore, the water level and the concrete temperature on four levels is measured. The data set from 1999 - 2014 provided by the operator contains bi-weekly measurement recordings. Whereas the water level and the temperature (Fig. A.32a and b) show a clear seasonal pattern, the pendulum displacement does not (Fig. A.32c).

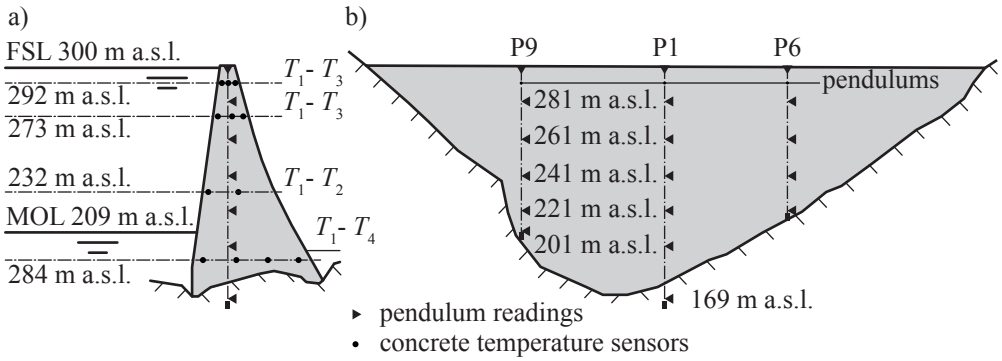

Fig. A.31 Cross section of arch dam A4.

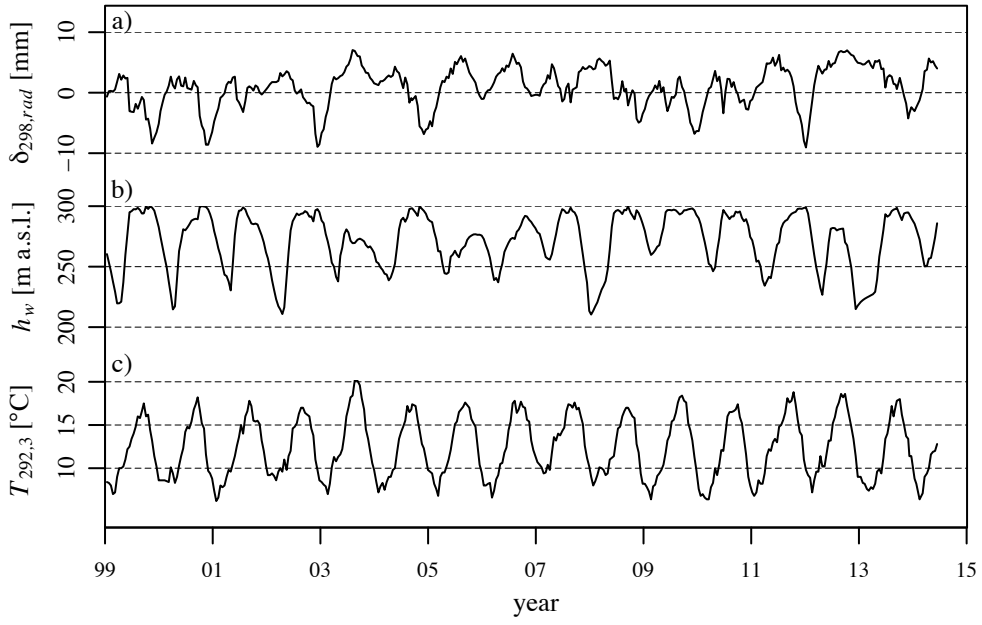

Fig. A.32 Measurement time series of arch-gravity dam AG1: a) displacement $\delta_{P1,302,rad}$ in radial direction at crest level, b) water level h_w and c) temperature $T_{292,3}$ with a distance of 2.2 m from the downstream boundary.

A.5.8 Hollow gravity dam HG1

The hollow gravity dam HG1 was built in the 1950s. There are two other reservoirs in the upper catchment area but a tributary flows into the reservoir. The main use of the dam is for pumped storage and flow regulation. Measurement data from 1999 - 2014 with monthly recordings were provided for this analysis. There are 14 temperature sensors, all of them are located in the upper part of the dam (Fig. A.33). As for gravity dam G2, the progress of the temperature measurement is distinctively seasonal and quite smooth due to the monthly measurement frequency and the distance from the boundary. However, the water level (Fig. A.34b) does not show a clear seasonal pattern. Since the displacement, measured by two regular and one rock pendulum, shows a clear seasonal pattern, the temperature seems to play a major effect. Furthermore, there is a clear visible irreversible trend in the displacement at crest level (Fig. A.34a).

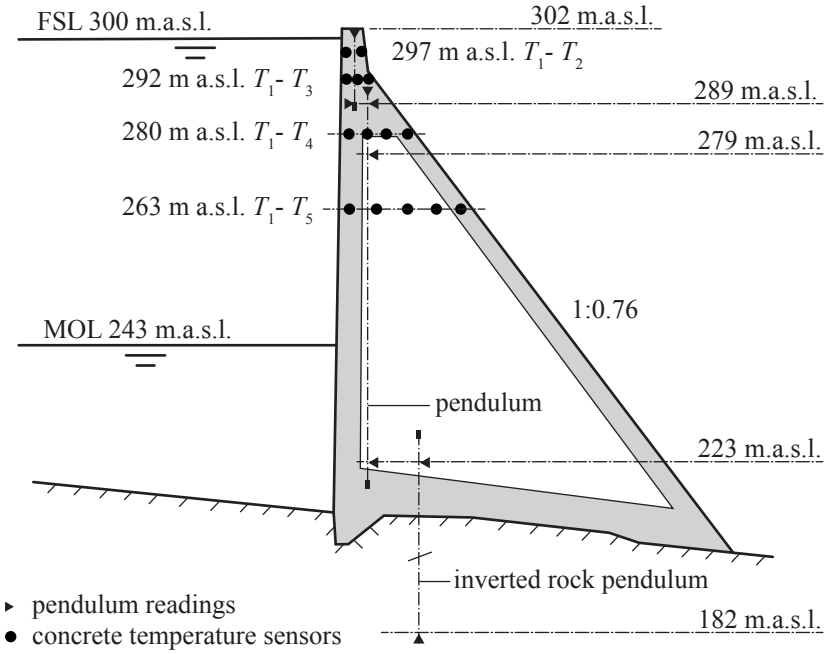

Fig. A.33 Cross section of hollow gravity dam HG1

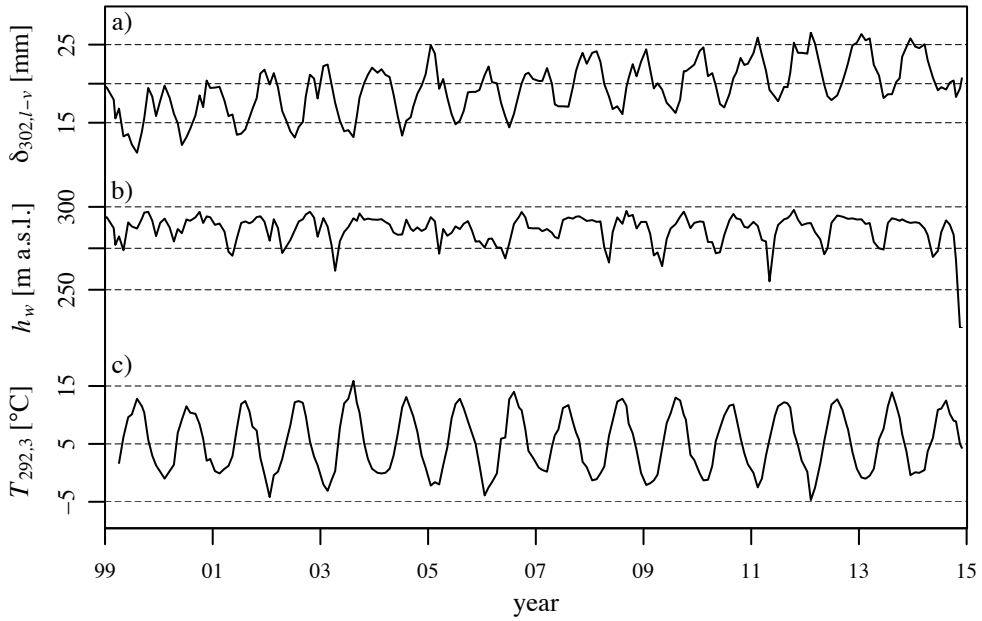

Fig. A.34 Measurement time series of hollow gravity dam HG1: a) displacement $\delta_{302,l-v}$ in lake-valley direction at crest level, b) water level h_w and c) temperature $T_{292,3}$ that is 1.3 m away from the downstream surface.

A.6 Behaviour analysis

A.6.1 Observation prediction comparison

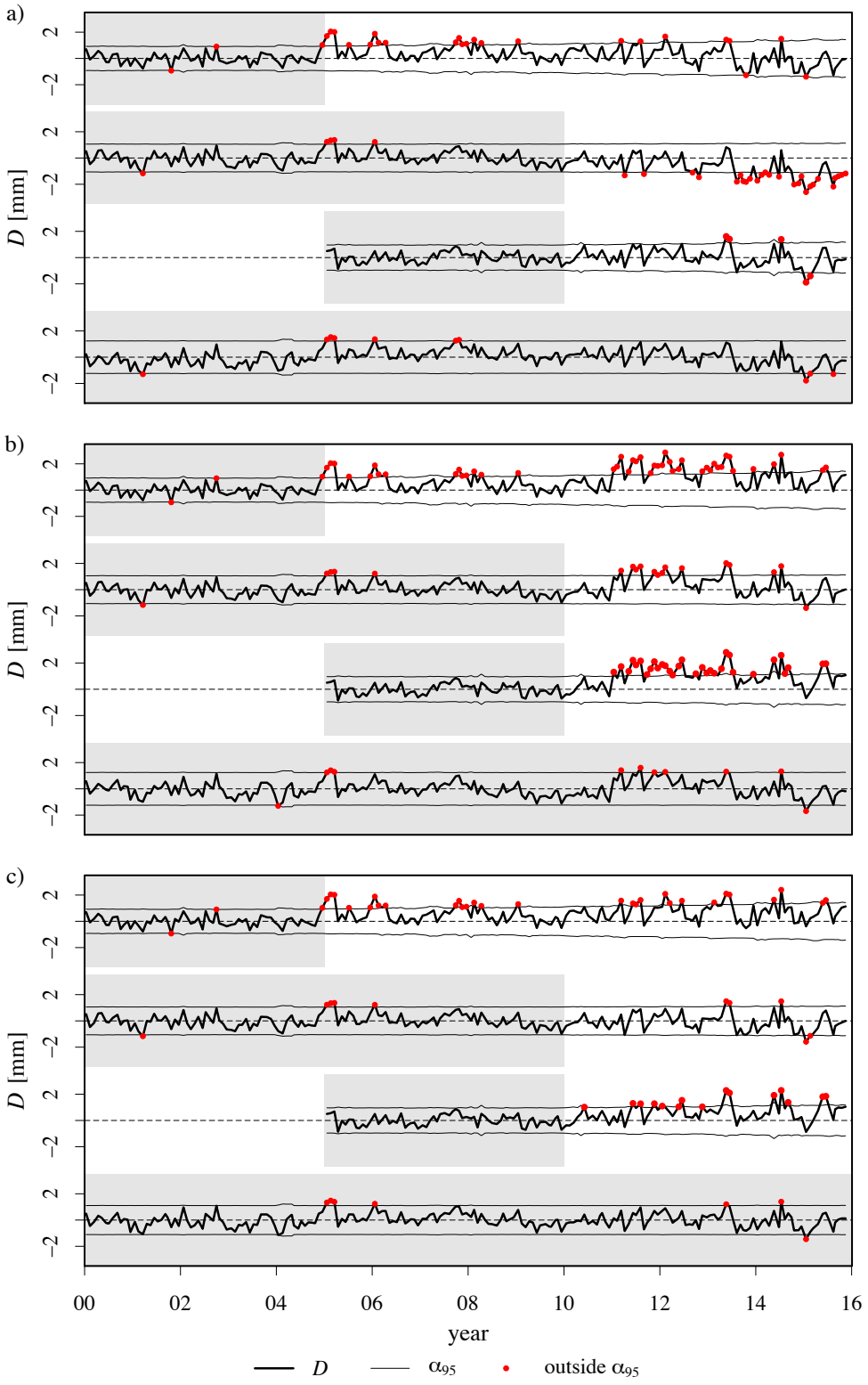

Fig. A.35 Observed differences D of the HST model for gravity dam G2 for different calibration periods shown by the grey background. The differences that are larger than the estimated prediction band α_{95} are shown by red dots: a) original data; b) original data with added shift of 1.2 mm on the 1.1.2006 to the pendulum displacement; c) original data with added drift of 0.2 mm/a after 1.1.2006.

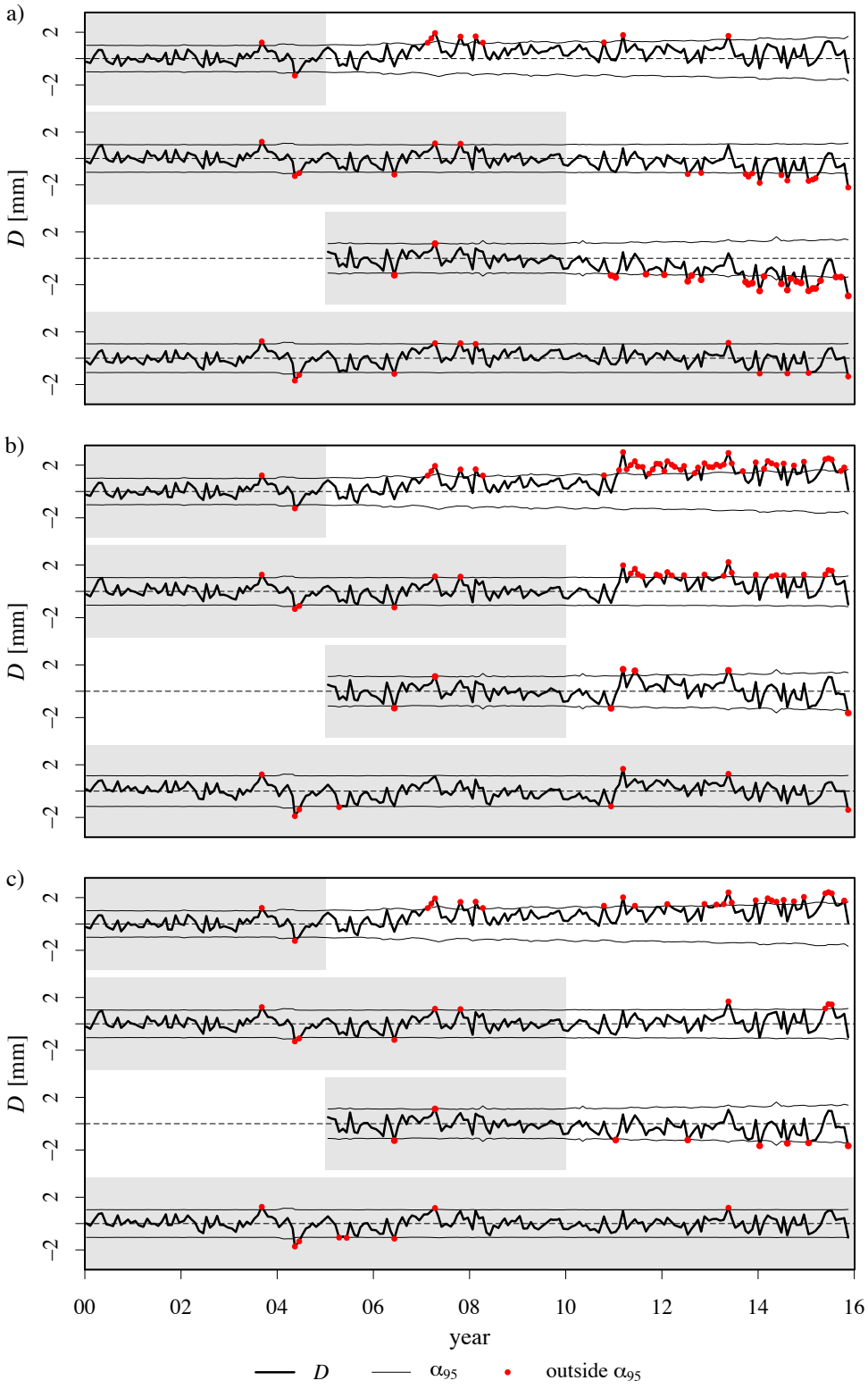

Fig. A.36 Observed differences D of the HTT model for gravity dam G2 for different calibration periods shown by the grey background. The differences that are larger than the estimated prediction band α_{95} are shown by red dots: a) original data; b) original data with added shift of 1.2 mm on the 1.1.2006 to the pendulum displacement; c) original data with added drift of 0.2 mm/a after 1.1.2006.

A.6.2 Adjusted behaviour indicator

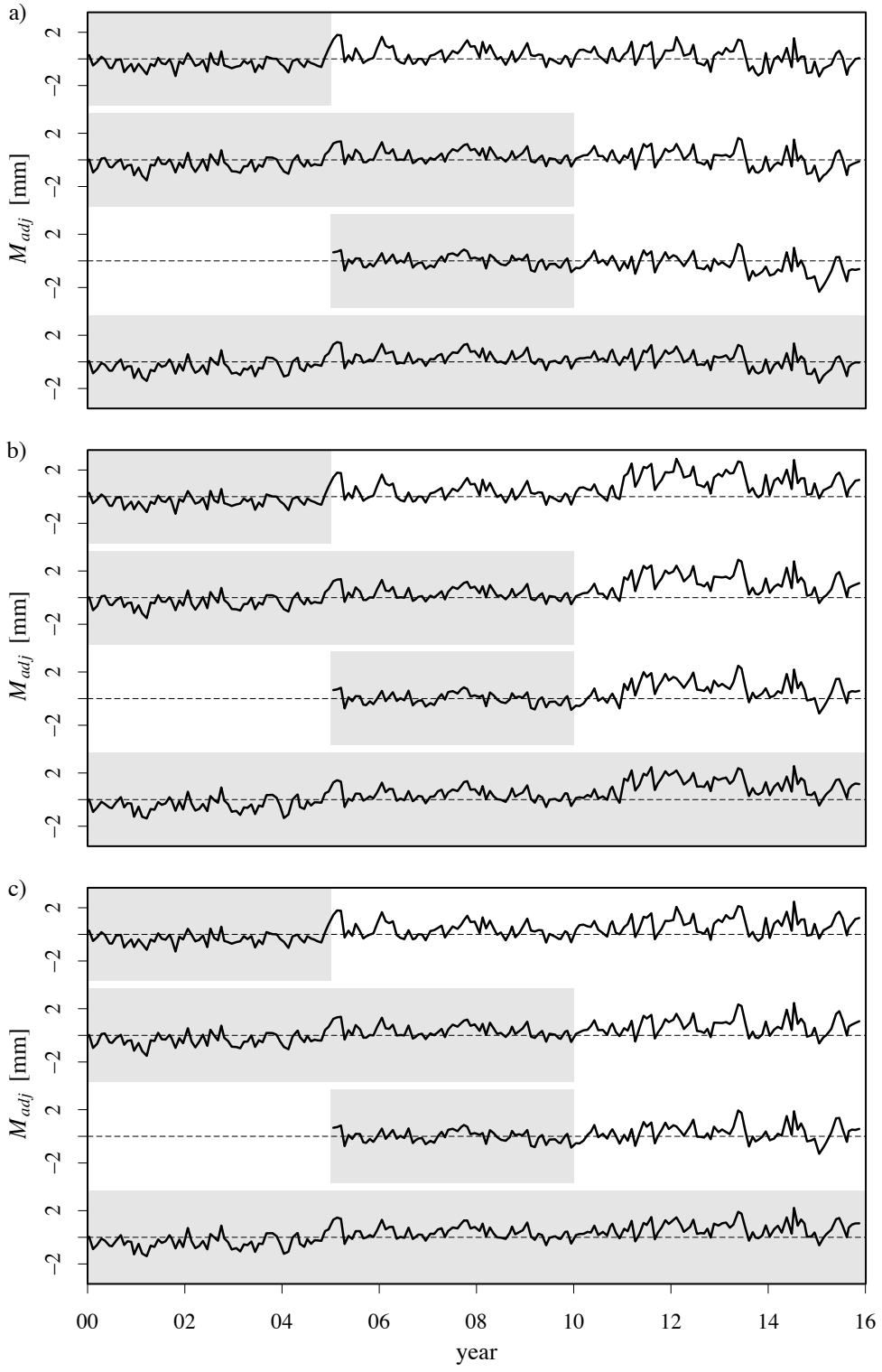

Fig. A.37 Observed adjusted behaviour indicator M_{adj} of the HST model for gravity dam G2 for different calibration periods shown by the grey background: a) original data; b) original data with added shift of 1.2 mm on the 1.1.2011 to the pendulum displacement and c) original data with added drift of 0.2 mm/a after 1.1.2010.

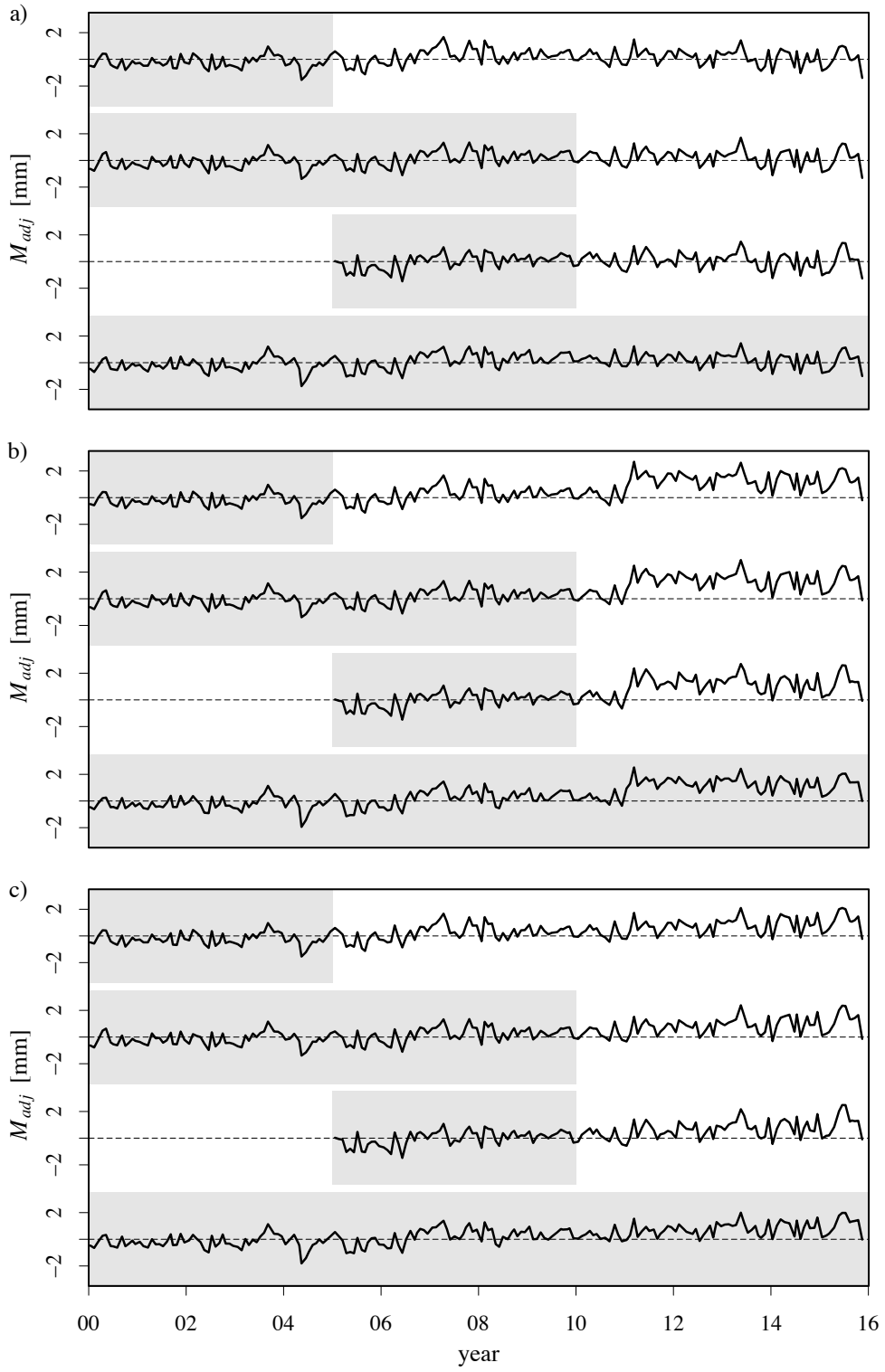

Fig. A.38 Observed adjusted behaviour indicator M_{adj} of the HTT model for gravity dam G2 for different calibration periods shown by the grey background: a) original data; b) original data with added shift of 1.2 mm on the 1.1.2011 to the pendulum displacement and c) original data with added drift of 0.2 mm/a after 1.1.2010.

A.6.3 Ridge regression

Table A.3 Results of hypothesis test done by MLR to find behaviour change for different magnitudes of abnormal behaviour
(*** p<0.001; ** p<0.01; * p<0.05; . p<0.1).

dam		drift					shift					season				
	model	0.50	0.75	1.00	1.25	1.50	0.50	0.75	1.00	1.25	1.50	0.50	0.75	1.00	1.25	1.50
G1	HTT_{dir}	*	**	***	***	***		*	**	***	***			*	**	***
	HTT_{T_m,T_d}	*	**	***	***	***		*	**	***	***			*	**	***
G2	HTT_{dir}	*	*	**	***	***		.	*	**	***				*	**
	HTT_{T_m,T_d}	*	**	***	***	***		.	*	**	***			.	*	**
A1	HTT_{dir}	*	**	***	***	***		*	**	**	***			*	**	***
	HTT_{T_m,T_d}	*	***	***	***	***		*	**	***	***				*	*
A2	HTT_{dir}		*	**	***	***			*	**	**				*	**
	HTT_{T_m,T_d}		*	**	***	***		.	*	**	**			*	**	***
A3	HTT_{dir}	.	**	***	***	***		.	*	**	**				*	**
	HTT_{T_m,T_d}	*	**	***	***	***		.	*	**	***				*	**
AG1	HTT_{dir}	*	***	***	***	***	.	*	**	***	***	.		*	***	***
	HTT_{T_m,T_d}	*	***	***	***	***	.	*	***	***	***	.		**	***	***
HG1	HTT_{dir}	.	**	***	***	***		.	*	**	***			.	*	**
	HTT_{T_m,T_d}	.	**	***	***	***		.	*	**	***			.	*	**

A.6.4 Principal component regression

Table A.4 Results of hypothesis test done by PCR to find behaviour change for different magnitudes of abnormal behaviour
(*** p<0.001; ** p<0.01; * p<0.05; . p<0.1).

dam		drift					shift					season				
	model	0.50	0.75	1.00	1.25	1.50	0.50	0.75	1.00	1.25	1.50	0.50	0.75	1.00	1.25	1.50
G1	HTT_{dir}	*	**	***	***	***		.	**	**	***			*	**	**
	HTT_{T_m,T_d}	*	**	***	***	***		*	**	***	****			*	**	***
G2	HTT_{dir}	.	*	***	***	***		.	*	**	***			.	*	**
	HTT_{T_m,T_d}	.	**	***	***	***		.	*	**	**			.	*	**
A1	HTT_{dir}		*	**	***	***			*	*	**				*	*
	HTT_{T_m,T_d}	.	**	***	***	***		.	*	**	***			.	*	**
A2	HTT_{dir}		*	**	***	***			*	**	**				*	*
	HTT_{T_m,T_d}		*	**	***	***			*	**	**				.	*
A3	HTT_{dir}	.	**	***	***	***			*	**	**				*	*
	HTT_{T_m,T_d}	.	**	***	***	***			*	**	**				*	*
AG1	HTT_{dir}	*	***	***	***	***	.	*	**	***	***	.		*	***	***
	HTT_{T_m,T_d}	*	***	***	***	***	.	*	***	***	***	.		**	***	***
HG1	HTT_{dir}	.	**	***	***	***		.	*	**	***			.	*	**
	HTT_{T_m,T_d}	.	**	***	***	***		.	*	**	***			.	*	**

A.7 Case studies

A.7.1 Arch dam A2, measurement data

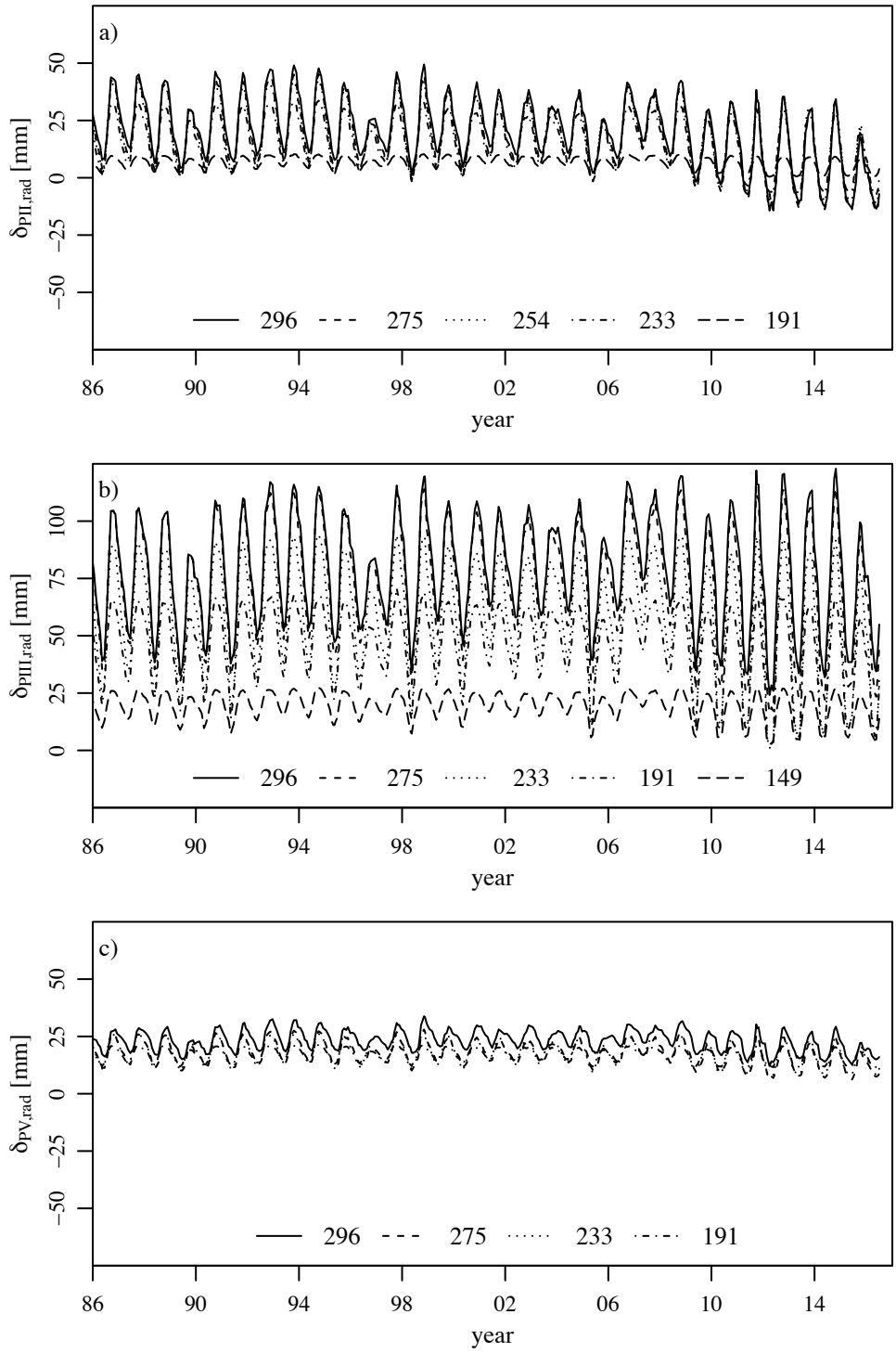

Fig. A.39 Radial displacement of arch dam A2; a) pendulum PII; b) PIII; c) PV.

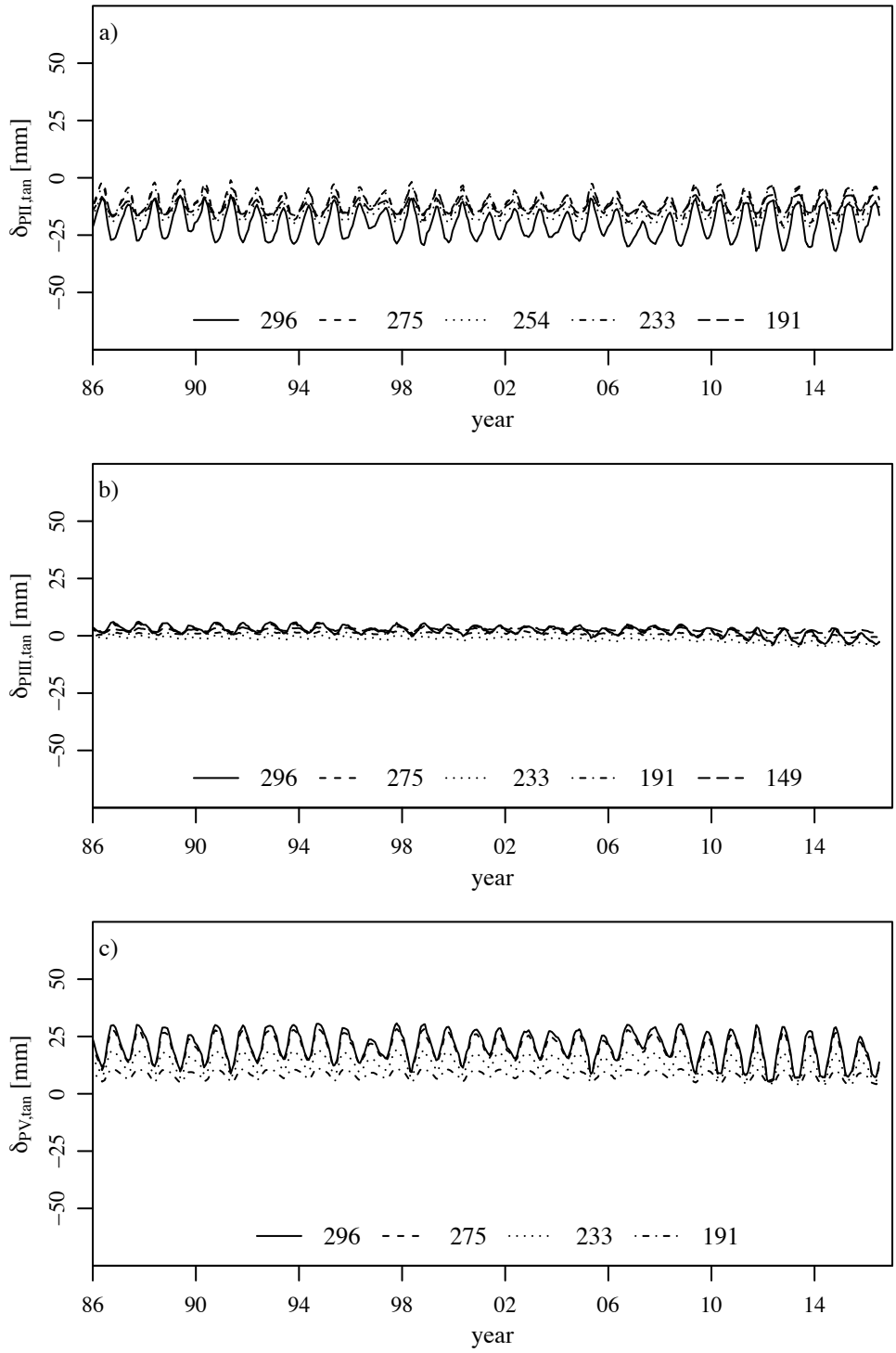

Fig. A.40 Tangential displacement of arch dam A2; a) pendulum PII; b) PIII; c) PV.

A.7.2 Arch dam A2, calculated displacements (output beam model)

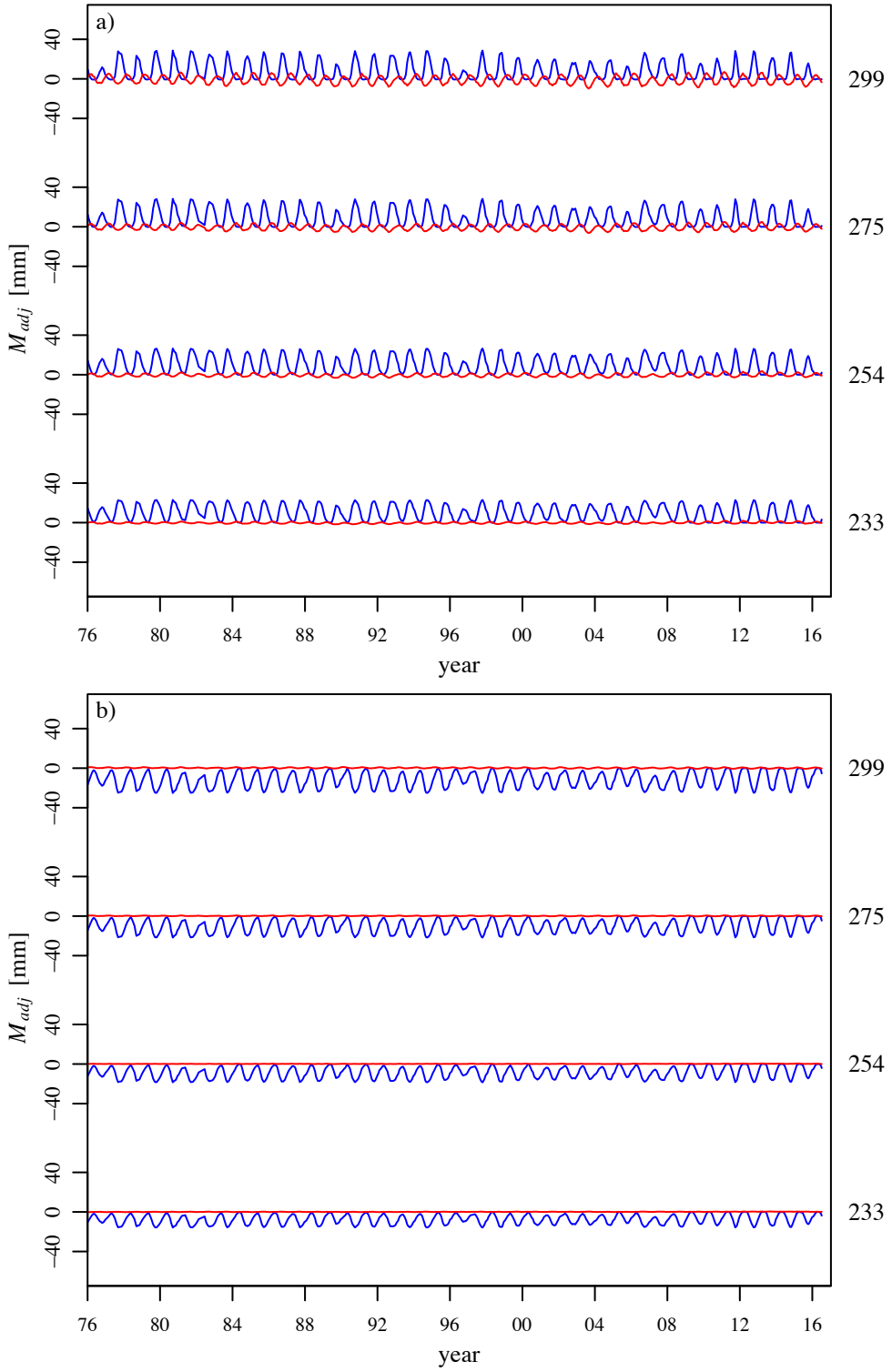

Fig. A.41 Displacements of pendulum PII calculated by beam model: a) radial (blue); b) tangential (red).

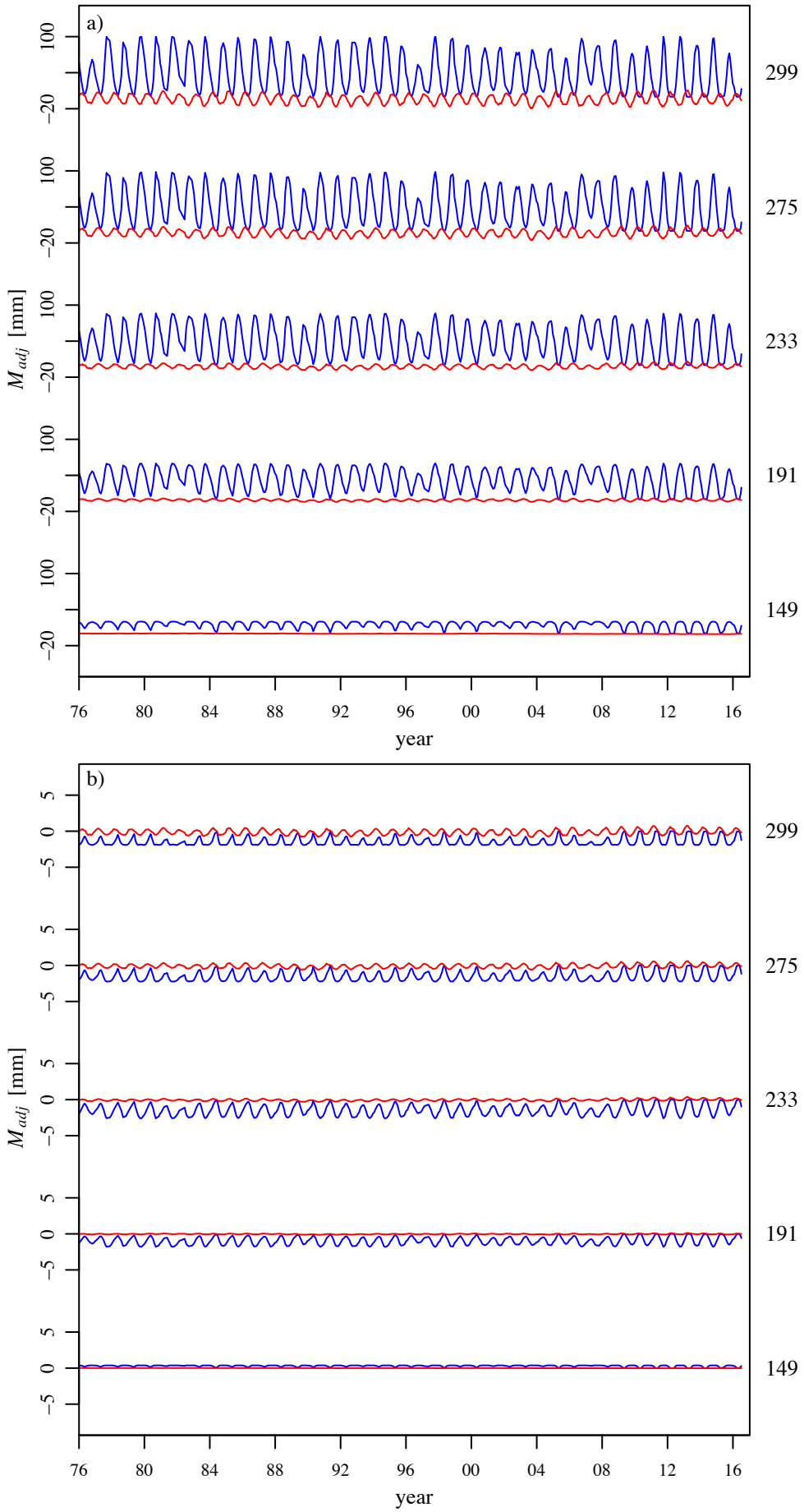

Fig. A.42 Displacements of pendulum PIII calculated by beam model: a) radial (blue); b) tangential (red)

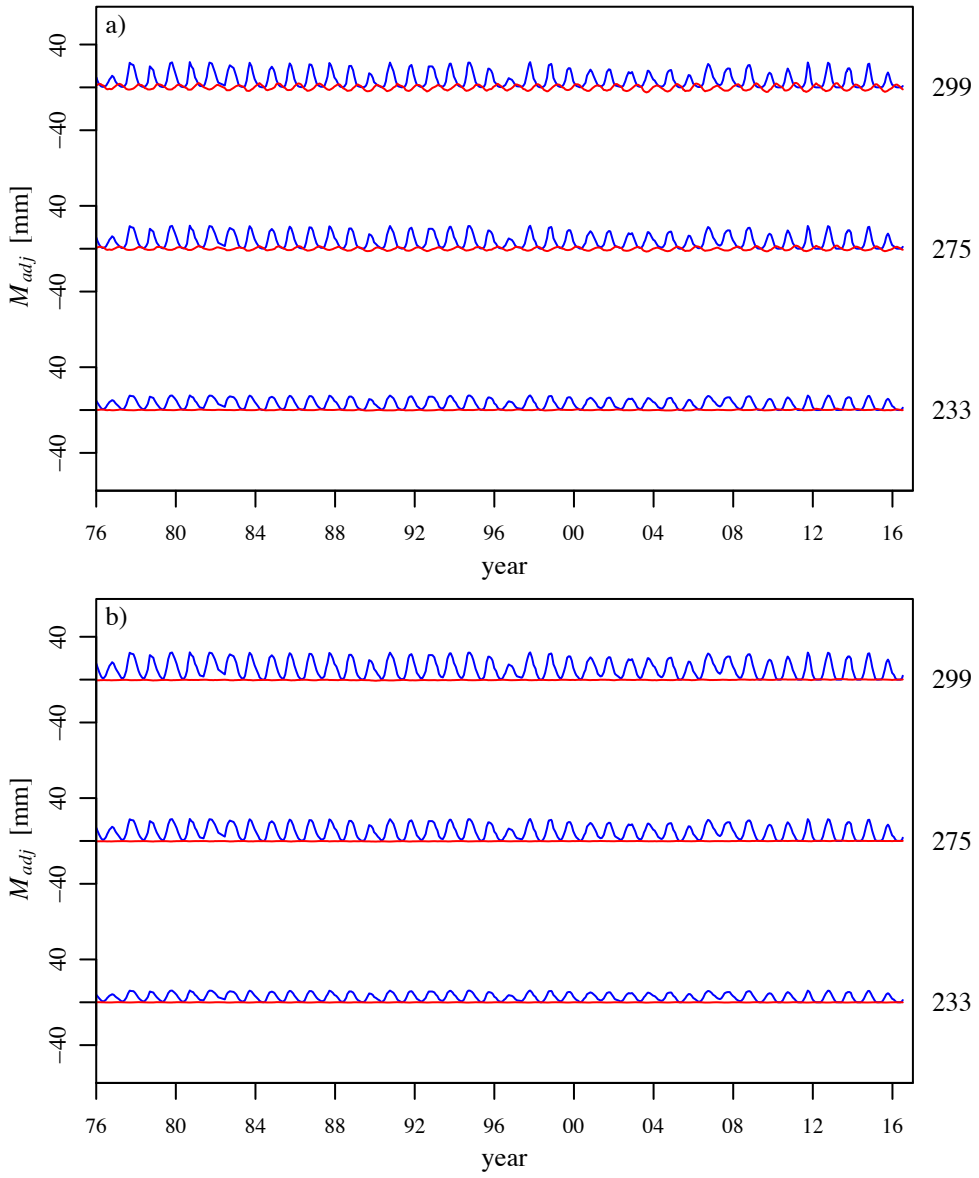

Fig. A.43 Displacements of pendulum PV calculated by beam model: a) radial (blue); b) tangential (red)